About Journal

The University of Sistan and Baluchestan entered into strategic partnership with Iranian Association of Electrical and Electronic Engineers (IAEEE) to publish the **International Journal of Industrial Electronics Control and Optimization (IECO)**. The IECO is a refereed international journal which presents to the international scientific community important results of work in these fields, whether in the form of modeling simulation, analysis, fundamental research, development, application, design or real-time implementation. The scope of IECO is broad, encompassing all aspects of Industrial Electronics, Control and Optimization.

Note: International Journal of Industrial Electronics, Control and Optimization (IECO) has qualified to **ACADEMIC RESEARCH JOURNAL (ELMI-PAJOHESHI)** status certified by the ministry of Science, Research and Technology of Iran (No. 231566/3/18 dated 1396/10/09), and is published by the University of Sistan and Baluchestan through a formal partnership (No. 952/2/1500 dated 1395/11/04) with Iranian Association of Electrical and electronic Engineers (IAEEE) in order to develop scientific and research cooperation.

Aims and Scope

International Journal of Industrial Electronics, Control and Optimization (IECO) is a Peer reviewed journal of advanced and state-of-the-art in the science and engineering of Industrial Electronics, Control and Optimization. Its Scope encompasses the applications of Industrial Electronics, power systems, control, optimization and computational intelligence for the enhancement of industrial and manufacturing system and processes. The scope of the journal include the following:

I. Industrial Electronics

- *Low and high power converters*
- *Renewable energy*
- *Drive control techniques*
- *Techniques for advanced power semiconductor devices*
- *Power quality and utility applications*
- *Communications*
- *Flexible AC Transmission Systems (FACTS)*
- *Control in power electronics*
- *Electromagnetic and thermal performance of electronic power converters*
- *Motion control, robotics, sensors and actuators*
- *Fault detection and diagnosis*
- *Power systems*
- *Factory automation, communication, and computer networks*

II. Control

- *Adaptive control*
- *Control of process systems*
- *Control theory*
- *Data processing*
- *Design of control systems*
- *Hybrid systems*
- *Identification and observation*
- *Intelligent systems*
- *Model-predictive control*
- *Optimal control*
- *Robust control*
- *Fractional order systems*

III. Optimization

- *Ant Colony*
- *Chaos Theory*
- *Evolutionary Computing*
- *Fuzzy Computing*
- *Hybrid Methods*
- *Immunological Computing*
- *Neuro Computing*

- *Particle Swarm*
- *Probabilistic Computing*
- *Rough Sets*
- *Wavelet*

International Journal of Industrial Electronics, Control and Optimization © 2021 IECO
Vol. 4, No. 4, pp. 377-385, Sep (2021)

A New and Very Fast Fault Detection and Classification Method Based on a Traveling Wave in Transmission Lines

Iman Mousaviyan[1], Seyyed Ghodratollah Seifossadat[2,†], and Mohsen Saniei[3]

[1, 2, 3] Department of Electrical Engineering, Faculty of Engineering, Shahid Chamran University of Ahvaz, Ahvaz, Iran

ABSTRACT

This study introduces a single-ended method to detect the protection zone and distinguish faults occurring in the back of the relay in the transmission lines and then provides an algorithm to classify different types of faults, including a lightning strike on phases and shield wire. Accordingly, using the Wavelet Transform (WT), the first class of Traveling Wave (TW) current is separated at the beginning of all bus-connected lines. The faulty line and the protection zone are selected based on the relations governing the radiation and reflection. Then, given the features and relations extracted from these waves, the faults caused by lightning strikes on the transmission line and conventional faults are classified, considering the mutual induction between TWs on the transmission line phases. This is essential and helpful for a transmission line with single-phase tripping and auto-reclosing mechanisms. Over 1100 faults with varying conditions and locations are implemented on a 100-km line with a voltage level of 230 kV in the PSCAD software to evaluate and test the proposed method. The results of this heavy simulation confirmed the validity, speed, and accuracy of the proposed method.

Article Info

Keywords:
Auto-Reclosing, Fault Classification, High-speed Relay, Lightning, Single Pole Tripping, Transmission Line Protection, Traveling Wave, Wavelet Transform.

Article History:
Received 2021-04-26
Accepted 2021-08-15

I. INTRODUCTION

The operation of transmission lines entails protecting them against all kinds of faults within the shortest possible time. The protection of transmission lines includes determining the protection zone, separating the faulty line from the rest of the grid, and interrupting the power transmission process. The effect of interruptions in high voltage transmission lines, which are mainly more critical, is followed by other impacts and consequences such as the whole grid instability and sometimes blackout. Therefore, fault correction methods without losing the entire power transmission process or minimizing the interruption period are considered. Accordingly, a process called fault classification (FC) and fault phase selection (FPS) is conducted before sending the command to the protection equipment. Then, Single Pole Tripping (SPT) or Auto Reclosing operation is implemented. Regarding the importance of speed and Traveling Wave application in protecting transmission lines, it should be noted that as the fault current flows, a force proportional to the square of the fault current amplitude enters the phase conductors and equipment installed in the substations. On the other hand, the maximum fault current amplitude occurs in the first cycle after the fault; therefore, the protection system needs to detect and make the right decision before this peak [1].

The impedance measurement, artificial intelligent network (AIN), traveling wave, or combinations are used to perform protection, FC, and FPS [2]. TW has gained a special place compared to other methods due to the importance of fault

†**Corresponding Author**: gh.seifossadat@scu.ac.ir
Tel: +98-9166182789, Department of Electrical Engineering, Faculty of Engineering, Shahid Chamran University of Ahvaz, Ahvaz, Iran

detection and classification time in protecting the transmission lines and high-speed microprocessors' availability in recent decades. Conventional FC methods such as [3] based on the principal component and those that apply the AIN to increase accuracy lengthen the processing time because of the time-consuming collection and smartification process, making them applicable in off-line methods [4]. Reference [2] uses TW for FC; however, it should be noted that if the ignored mutual induction between the generated TWs is taken into account, the proposed decision table would not be applicable. Moreover, the lightning strike on the transmission lines is neglected in FC.

Ref [5] uses fault current at 220 kV network with a 177.4 km transmission line in the PSCAD/EMTDC. This study presents a new FC and Fault Detection (FD) algorithm using a fuzzy-neuro of less than 10ms. In [6], FD and FC are based on an analysis of the fault current and voltage at a 1.2 kHz sampling frequency with WT and ANNs. Like [6], Ref [7] uses WT and ANN to extract TW from the fault current and voltage for FD/FC (with a 200 kHz sampling rate and different mother wavelets); therefore, the proposed algorithm of this study tested for more than 3900 cases. In [8], with WT and with linear discriminant analysis extract plus the analysis of TW in the fault current within a 0.25 cycle sample for FD/FC. This study claims that improved relay reaches for FD and FC. Unlike [6] and [7], this study uses only the fault current to reach a decision. In [9], the FD and FC plan introduces for static variable compensator (SVC) compensated line, based on SSCII with a 1 kHz sampling rate. Also [10] and [11] protect compensated transmission line using game theory and traveling wave.

Using the current TW separated by WT from the main waveform, this paper examines the protection and fault classification process in the transmission line after determining the protection zone. Accordingly, unlike most studies such as [12], [13], [14], [15], which use current and voltage TW, a method is proposed that only uses the current TW to determine the fault location behind the relay. After detecting the faults in the protection zone, the FC process is implemented using the current TW extracted features at the relay site and considering the mutual induction between the phases to send the most appropriate command according to the proposed algorithm. Moreover, lightning strikes on the transmission line under two different states (lightning strike to phase or shield wire) are considered another class of faults in the proposed algorithm, the subject that none of the study such as mention in introduction discuses about. The proposed method's validity is tested on a single-circuit transmission line with a length of 100 km in a 230kv network under more than 1100 faults in five different zones, inception angle, and fault resistance.

II. BASIC PRINCIPLE

If a fault happens in the transmission line, a TW is generated with various features depending on the fault type and flows to both ends. Accordingly, the fault types are investigated, and the relations associated with TW radiation and reflection are reviewed. Numerous methods are also applied to extract high-frequency TWs, one of the most powerful of which is the wavelet transform that its mathematical relations and the performance are discussed in section (II-C).

A. TW Fault Classification

a) Single-Line to Ground Fault (SLG): This fault happens when one of the transmission line phases is connected to the ground (by resistance) directly or indirectly. Accordingly, the phase faults current increases while the current does not change in the other two phases. However, in terms of TW, when a single-phase to ground fault occurs, TW takes place in the fault zone and the faulty phase. However, no TW is generated in the other two phases [2]. Given the mutual induction between the line phases at the beginning of the line, where the relays are located, TW is present on all three phases. The TWs received at the beginning of the line enjoys two essential features; first, the induced TW amplitude in the other two phases is equal (given that the transmission line phases have regular permutations), and second, their polarity is the opposite of the faulty phase, Fig. 1(A).

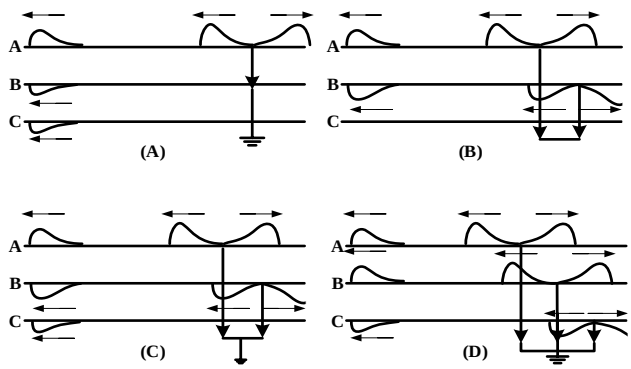

Fig. 1. Fault type base on Traveling Wave

b) Phase-to-Phase Fault: If the two phases of the transmission line are connected, the current of these two phases will be identical with opposite signs, and the current will be intact in the third phase [16]. However, the generated TW has an equal amplitude and inverse polarity in the faulty phases and fault zone. The same waves are received at the beginning of the line (with attenuation caused by losses in the transmission line). More importantly, the TW in the third phase is not received at the beginning of the transmission line. TWs are generated in the third phase because of inducing the other two phases, but they have a zero output because of equal amplitude and inverse polarity, Fig. 1(B).

c) Phase to Phase to Ground (or LLG Fault): since the fault

current flowing in the two phases in the two faulty phases is not equal, the generated amplitude of TW is not the same [2], [16]. Therefore because of mutual induction, TW is generated in the healthy line and thus, TW will exist at the beginning of the line on all three phases (Fig. 1(C)).

d) Three-Phase Fault (and ground): According to Fig. 1(D), when a three-phase fault occurs, TW is generated in each of the three phases based on the voltage range of each phase at the fault moment, and there is TW with different amplitudes at the beginning of the line in each of the three phases.

e) Lightning: Another class of faults that occur in transmission lines is the lightning strike on these lines, which statistically plays the most significant role [17]. In this study, the equation of lightning current is considered as Equ. (1), [18], [19].

$$I = A \times ((B.e^{-Ct}) - (D.e^{-Ct})) \quad (1)$$

The lightning strike on the transmission line is studied under two conditions. First, lightning strikes one of the phases directly and leads to a severe current flow in that phase(Shielding failure). Receiving TW at the beginning of this line makes this mode similar to the single-phase to ground short circuit as you can see in Table I. In the second case, lightning strikes the shield wire, induces a current in the phases. Based on the performed simulations, TW is received on three phases at the beginning of the line with similar polarity and amplitude. But in some cases, if the ground resistance of the tower is high, it will lead to flashover [20].

According to the above discussion and the obtained data from TW analysis, the features and specifications of all fault types are classified in Table I.

TABLE I
TW SPECIFICATION OF DIFFERENT FAULT'S

Fault type			i_A	i_B	i_C
Single Phase to Ground		AG	i_A^T	$-Mi_A^T$	$-Mi_A^T$
		BG	$-Mi_B^T$	i_B^T	$-Mi_B^T$
		CG	$-Mi_C^T$	$-Mi_C^T$	i_C^T
Phase to Phase		AB	i_A^T	$-i_A^T$	0
		AC	i_A^T	0	$-i_A^T$
		BC	0	i_B^T	$-i_B^T$
ABC and Phase to Phase to Ground			i_A^T	i_B^T	i_C^T
Lightning	To Phase	A	i_A^T	$-Mi_A^T$	$-Mi_A^T$
		B	$-Mi_B^T$	i_B^T	$-Mi_B^T$
		C	$-Mi_C^T$	$-Mi_C^T$	i_C^T
	To Shield Wire		i_M^T	i_M^T	i_M^T

As is seen in Table I, in single phase to ground faults, because of the mutual induction (in that M is mutual induction coefficient and T is an abbreviation for TW, so i_A^T means: current TW of phase A), two phases have equal amplitude and opposite polarity to the faulty phase just the same as when lightning strikes one of the phases, so we discuss this item in section III. Also in phase to phase faults, according to circuit equations, the same amplitude with opposite polarity TW generate in faulty phases but in the third one not received any TW.

B. TW and their equations

As a fault occurs in the transmission line, the TW voltage and current are generated in that zone and flow to the ends of the line, at a speed close to the speed of light. The amplitude of the generated TW is proportional to that of the voltage at the fault zone one moment before the fault occurs (V_F). The magnitude of TW, voltage, and current are as follows [14], [13]:

$$V_1 = \frac{-Z_C}{Z_C + 2R_F} V_F \quad (2)$$

$$i_1 = -\frac{V_1}{Z_C} = \frac{1}{Z_C + 2R_F} V_F \quad (3)$$

where R_F is the fault resistance and Z_C is the characteristic impedance of the faulty line. According to Fig. 2, a part of the generated TW is reflected in the fault zone by reaching the two line ends, and the other part is transferred towards the network (lines) connected to bus A. The radiation and reflection coefficients of TW current are obtained as follows:

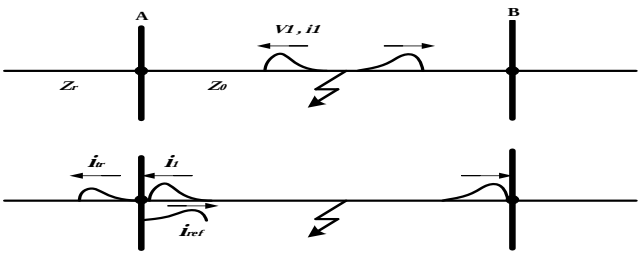

Fig. 2. Initial Traveling Wave on Transmission line

$$K_{ref}^i = \frac{Z_0 - Z_r}{Z_0 + Z_r} \rightarrow i_{ref} = K_{ref}^i \times i_1 \quad (4)$$

$$K_{tr}^i = \frac{2Z_0}{Z_0 + Z_r} \rightarrow i_{tr} = K_{tr}^i \times i_1 \quad (5)$$

If more than one line is connected to bus A (Fig. 3), the above relations will be re-written as follows:

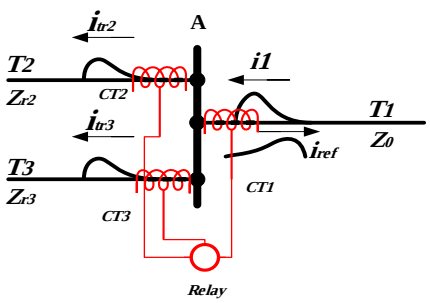

Fig. 3. Traveling Wave on bus A

$$i_{tr2} = \frac{2Z_{eq}}{Z_0 + Z_{eq}} \cdot \frac{Z_0}{Z_{r2}} \cdot i_1 \quad (6)$$

$$i_{tr3} = \frac{2Z_{eq}}{Z_0 + Z_{eq}} \cdot \frac{Z_0}{Z_{r3}} \cdot i_1 \quad (7)$$

where Z_{eq} is the equivalent impedance of T2 and T3.

C. Wavelet Transform (WT)

The Fourier series is applied to analyze the constituent harmonics of a signal; however, it cannot distinguish between the inception and disappearance of different harmonics. WT is one of the mathematical transformations capable of providing a time-frequency signal analysis. WT is formed by combining the low and high-pass filters in terms of frequency content, which could divide the frequency band of the input signal into two parts at each stage [21], [22].

The high-pass filter's output is the details or high-frequency harmonics, and that of the low pass filter is considered an approximation of the input signal. If the intended signal $f(n)$ has discrete data, the performance of the discrete WT (DWT) is expressed as follows:

$$A_{2^j}^d.f(n) = \sum_k h_k.A_{2^{j-1}}^d.f(n-2^{j-1}k) \quad (8)$$

$$W_{2^j}^d.f(n) = \sum_k g_k.A_{2^{j-1}}^d.f(n-2^{j-1}k) \quad (9)$$

where $A_{2^j}^d.f(n)$ is the signal approximation coefficients and $W_{2^j}^d.f(n)$ is the detail coefficients (high frequency) at the level of2^j, and h_k and g_k re the applied high and low-pass filters' coefficients in WT.

III. Proposed Algorithm

The proposed method in this article has two main parts. In the first part, the faulty line is detected among all the bus-connected lines, and in the second part, the type of fault and faulty phases are determined. Then, the fault zone is easily calculated using the existing relations and TW velocity.

A. Determining the faulty transmission line

For example, consider bus A in Fig. 3, which is connected to three lines. If a fault occurs on line T1, TW is generated and flows to bus (A) based on the TW behavior. As the TWs reach this bus, a part of them is reflected to the fault point, and the other part is transferred to the other two lines.

It is worth noting that the received TW through CT1 is equal to the sum of the radiated waves in the fault zone and reflected from the bus, that is:

$$i_{CT1}^{TW} = i_1 + i_{ref} \quad (10)$$

According to section II-B, the received TW amplitude by CT2 and CT3 is equal to:

$$i_{CT2}^{T.W} = \frac{2Z_{eq}}{Z_0 + Z_{eq}} \times \frac{Z_0}{Z_{r2}} \times i_1 \quad (11)$$

$$i_{CT3}^{T.W} = \frac{2Z_{eq}}{Z_0 + Z_{eq}} \times \frac{Z_0}{Z_{r3}} \times i_1 \quad (12)$$

where ($Z_r^{eq} = Z_2 \parallel Z_3$), and according to the circuit laws:

$$i_{CT1}^{T.W} = i_{CT2}^{T.W} + i_{CT3}^{T.W} \quad (13)$$

In other words, if TW is measured on the three lines connected to bus A and the sum of the two values is equal to the third, the faulty line will be detected by examining the conditions of the Equ. (13). This work has two main advantages. First, using a relay device allows protecting any number of bus-connected lines, which leads to significant savings and makes it possible to use a relay as the backup for the rest of the line's relays. The second major advantage of this method is to detect the protection zone and separate the out-of-zone and the fault location behind the relay. It should be noted that studies such as [12]- [15] use the TW voltage to determine these faults, which is a difficult task due to the limited frequency band of the voltage transformers [16], [14].

B. Fault classification

After identifying the faulted line (based on Equ. (13)), in order to distinguish phase to phase and three phase faults, the algebraic sum of current TWs is calculated on all three phase. If the algebraic sum of current TWs wasn't zero and the received TW polarity is precisely equal on each of the three phases, the fault is caused by a lightning strike on the protective lines (shield wire) above the transmission line. Furthermore, in some cases, it may cause a back flashover. If the amplitude of current TW is precisely the same, flashover has not occurred. Nevertheless, in some cases, a short time after the lightning strikes the shield wire, back flashover occurs, so depending on the type of flashover, the studied algorithm detects SLG (as shown in Fig.5) or another type of fault, and if the received TW polarity isn't equal fault is SLG or shield failed.

Suppose the ratio of received TW amplitude of the 1st level in the two phases is equal to $i_{ph1}/i_{ph2} = 1$, but the TW amplitude of the third phase has more amplitude, and polarity is inverse. In this case, the fault is a single-phase type or shield failed, and the faulty phase is the one with a higher amplitude. To distinguish between these two types of faults, the ratio between the details of the first and second WT levels must be calculated. If this ratio is less than TH, then shield failure occurs elsewhere, and SLG fault accrues. In this study, TH is set at 0.3.

If received current TW on phases have different amplitude ((iA/iB) or (iA/iC) or (iB/iC) ≠1) phase-to-phase to ground (LLG) fault occurs. However, identifying the phases under fault in LLG faults is not easy because, in less than 30% of cases, the fault may occur between two phases whose current polarity is similar. In this case, due to the mutual induction, high-amplitude current TW occurs in the healthy phase, and so it will be challenging to detect faulty phases.

For more details, consider the following three phases voltage waveform (Fig.4); if LLG fault occurs between two phases in the dotted zones, the polarity of the current TW generate become similar, and therefore the polarity of the induced current TW in the healthy phase is similar and add together. In such cases, the detection of faulty phases is very

complicated.

Therefore, to detect the phases involved in the LLG faults, define a pilot function (PF) with the following specifications for each phase, when the absolute voltage of each phase is less than half of the nominal value and the value of the pilot function of that phase remains equal to on for T/6 s. for example, phase (a) pilot function is defined as follows:

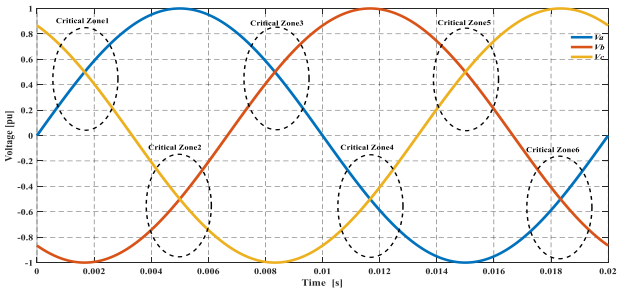

Fig. 4. Critical Zone on three phase's voltage waveform.

$$P.F = \begin{cases} 1 & if\ [|V_a| - 0.5 \times V_n^{max}] < 0 \\ 0 & if\ [|V_a| - 0.5 \times V_n^{max}] > 0 \end{cases} \quad (14)$$

According to the above explanations, LLG fault detection is divided into two categories. IF the average absolute magnitude of (detail level 1) current TW is greater than the third one AND pilot function (PF) of the phase with the least amount of current TW is zero, THEN the fault occurred between those two phases, and if this condition does not apply, fault accrues in the critical zone. For identifying these LLG faults, the polarity of voltage (at 60Hz) should be checked, and faults accrued between phases with similar polarity.

If the algebraic sum of TW is zero and the TW amplitude of a phase is zero and the ratio of received TW amplitude on the other two phases is $i_{ph1}/i_{ph2} = -1$, the fault is phase to phase type, and the faulty phases have TW. In reality, a TW is induced in the faultless phase with minimal amplitude due to the phase conductors' complete dissimilarity. The maximum amplitude of these TWs is related to the fault at the end of the line, and it is possible to obtain a threshold for it. If none of the above conditions is met and the received TW is present on each of the three phases, the fault is of the three-phase type.

According to the above explanations, Fig. 5 indicates the proposed algorithm for classifying the fault types and specifying the faulty phases. Note that, in Fig. 5 all of the i_A, i_B and i_C are details of the first level of WT.

It should be noted that the proposed method uses the TW amplitude of the current obtained from the relay without using any time-consuming calculations. This increases the proposed algorithm's effectiveness and reduces the decision time in single-phase cut-off operations, which is vital in this regard.

IV. Simulation Studies

This research is conducted on a single-circuit three-phase line with a length of 100 km in a network with a voltage of 230 kV, and 60 Hz frequency in PSCAD software (Fig. 6). Since the proposed algorithm is based on high-frequency TW analysis, the Frequency-Dependent (Phase) model is selected for transmission line analysis, which is highly similar to a real line and has a wide range of frequency bands of different parameters.

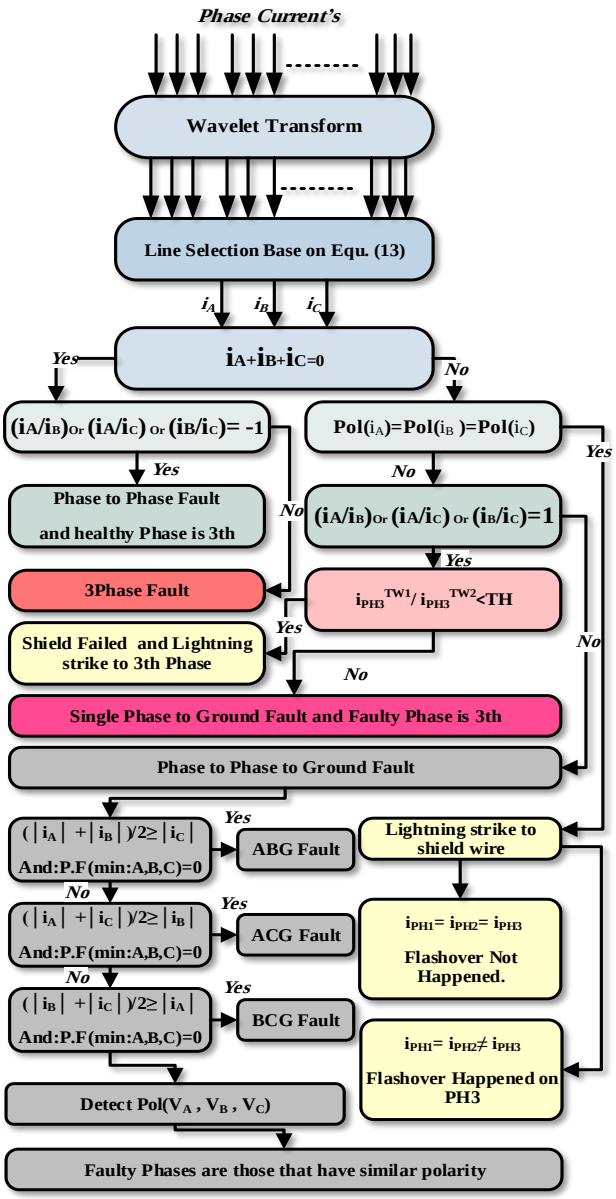

Fig. 5. Propose Flowchart for FC

The CTs with a conversion ratio of 5/1600 based on the Lucas model is used to extract TW from the line current [23]. Moreover, the sampling frequency is 500 kHz, and the details of the first level of WT (by selecting the mother wavelet db4) are used.

A wide variety of faults are analyzed in 3 different location with various fault resistance and inception angle to check the validity of the algorithm presented in this research, a small part

of which is presented below:

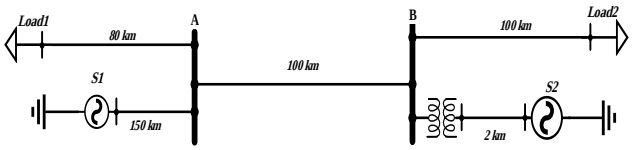

Fig. 6. Simulated network

A. *Single-phase to ground fault (SLG)*

These faults are the most probable ones statistically [17]. According to Table I and Fig. 5, when a single-phase to ground fault happens, the faulty phase's received TW amplitude is higher than two other phases and it has an inverse polarity, also the TW amplitude ratio of the other two phases equals one. Fig. 7 shows the single-phase to ground fault in phase A at a distance of 60 km from bus A (in Fig. 6) under two fault resistances of 1 and 50Ω.

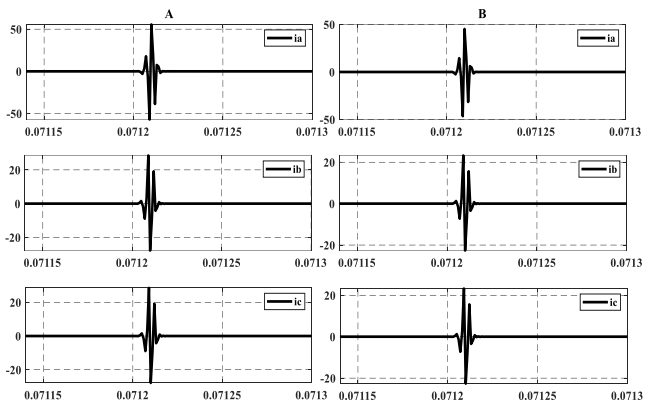

Fig. 7. Current TW Fault in 60km (A): R_f=1Ω, (B): R_f=50Ω

As the proposed algorithm is sorted based on the first received TW class and decisions, the equipment saturation problem in faults close to the bus will not arise. Table II includes information about some single-phase to ground faults at different distances, fault inception angles, and fault resistances.

TABLE II
RESULT OF SLG FAULT IN DIFFERENT CONDITION

$\lvert i_a^{TW}\rvert$	$\lvert i_b^{TW}\rvert$	$\lvert i_c^{TW}\rvert$	Time-ms	Fault Type	Fault location	Fault-Res	$\frac{\lvert i_a^{TW}\rvert}{\lvert i_b^{TW}\rvert}$	$\frac{\lvert i_a^{TW}\rvert}{\lvert i_c^{TW}\rvert}$	$\frac{\lvert i_b^{TW}\rvert}{\lvert i_c^{TW}\rvert}$
74	36	36	55	AG	30km	1	2/07	2/07	1
61	30	30	63	AG	30km	50	2/07	2/07	1
15	30	15	55	BG	30km	1	0/48	1	2
15	31	15	63	BG	30km	50	0/48	1	2/07
21	21	44	55	CG	30km	1	1	0/48	0/48
14	14	30	63	CG	30km	50	1	0/48	0/48
58	31	31	55	AG	60km	1	1/89	1/89	1
48	25	25	63	AG	60km	50	1/89	1/89	1
18	18	33	55	CG	60km	1	1	0/53	0/53
12	12	22	63	CG	60km	50	1	0/53	0/53

B. *Phase to phase fault*

According to section III-B, if the single-phase TW magnitude is zero (or very small) and the received TW amplitude on the other two phases is -1, the phase-to-phase fault takes place (Table III).

TABLE III
PHASE TO PHASE FAULT WITH 10Ω FAULT RESISTANCE

$\lvert i_a^{TW}\rvert$	$\lvert i_b^{TW}\rvert$	$\lvert i_c^{TW}\rvert$	Time-ms	Fault Type	Fault_loc
78/52001	78/52001	4/74E-07	63	AB	60km
70/91948	70/91948	4/74E-07	71	AB	60km
74/96908	4/73E-07	74/96908	63	AC	60km
58/43128	4/73E-07	58/43128	71	AC	60km
2/12E-09	3/550927	3/550927	63	BC	60km
2/12E-09	12/4882	12/4882	71	BC	60km
58/66404	58/66404	4/74E-07	55	AB	90km
63/07616	63/07616	4/74E-07	63	AB	90km
62/98396	4/73E-07	62/98396	55	AC	90km
2/12E-09	9/682649	9/682649	71	BC	90km

C. *Three-phase and phase-to-phase to ground faults*

The algebraic sum of the received TW at the beginning of the line is calculated to detect these faults. According to the algorithm, if the sum of the current TW is zero, a three-phase (and ground) fault happens(or two-phase fault as previously described), otherwise, it is the phase-to-phase to ground fault. If LLG fault occurs, current TWs are received at the beginning of the line on all three phases, and in most conditions, the faulty phases have a larger amplitude, but as mentioned above, when the voltage of the faulty phases is in the critical zone, the amplitude of the TW on a healthy phase is sometimes more significant than the faulty phases. Fig.7 shows the waveform of voltage, current, and current TW of these two types. Table IV contains BCG fault data at a distance of 60km; the red line in Table IV indicates the LLG faults in the critical zone. In the proposed algorithm shown in Fig.5, voltage polarity at the main frequency is used to detect faults occurring in the critical zone.

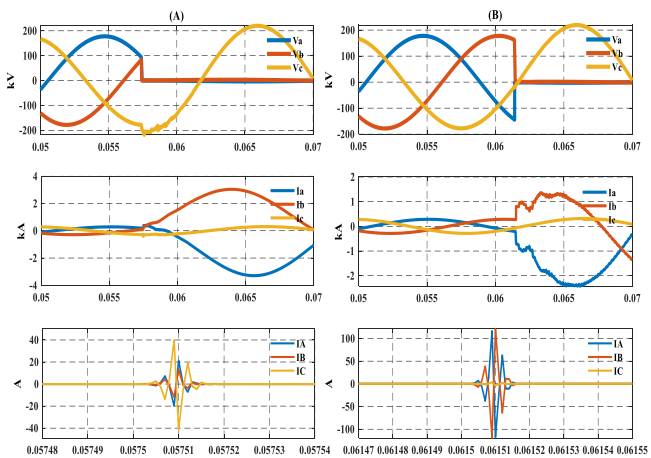

Fig. 7. 24 (A): ABG fault at 0.0574 [s] in critical zone, (B): ABG fault at 0.614 [s]

TABLE IV
BCG FAULT AT 60KM WITH 1Ω FAULT RESISTANCE

i_a^{TW}	i_b^{TW}	i_c^{TW}	Fault Time
-27/75	+4.13	-19.86	5/50E-02
-32.84	+28.77	-59.05	5/58E-02
+28/00	+62/22	-87/82	5/66E-02
+19/83	+88/23	-107/36	5/74E-02
+9/49	+102/99	-111/65	5/82E-02
-0/79	+111/96	-111/24	5/90E-02

D. Lightning

Two cases may arise in terms of the lightning strike on the transmission lines, discussed in section (II-A). If the lightning strikes one of the line phases, Fig. 8 and Fig. 9-A, the situation at the beginning of the line is like a single-phase to ground fault. However, the received TW amplitude can be much more than a single-phase to ground fault based on the lightning strength. Fig. 8 presents the received currents and TW amplitude at the beginning of the line after a lightning strike on one of the phases within a distance of 60 km.

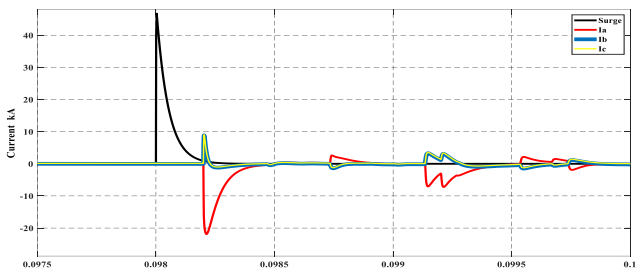

Fig. 8.Lightning strikes to phase A and Phase Current receive at beginning TL

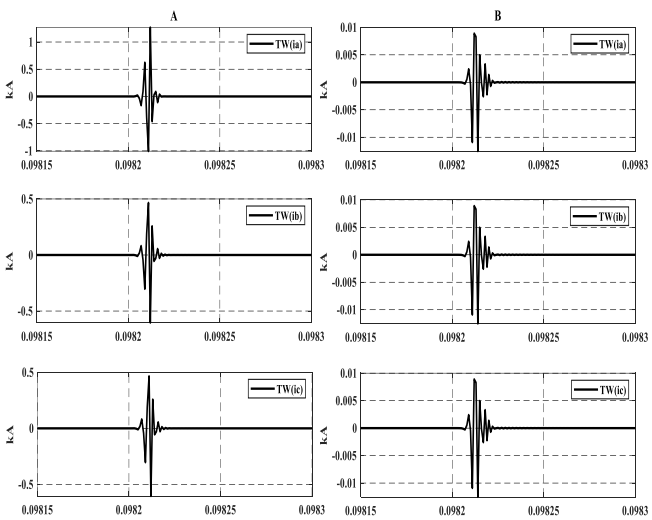

Fig. 9.Lightning strikes A: to phase (a), B: to Shield Wire

If lightning strikes the shield wire above the line, the induced currents in the three lines are quite similar to each other (given that the line is totally transposed) Fig. 9-B. In this case, if the ground resistance of one of the towers close to the place of the lightning strike is high a flashover may occure between one of the phases and the tower. In this case, depending on the location of the flashover, the amplitude of the induced TWs is slightly disturbed or it is seen as an SLG fault by the proposed algorithm.

E. Close in Faults

One of the modes that challenge the FC algorithms is remarkably close faults. However, our proposed method uses the first set of TWs; hence there will be no problem with the saturation of measuring equipment. As shown in Table V, the proposed method has an excellent ability to detect close-in faults.

TABLE V
SIMULATION RESULTS FOR CLOSE-IN FAULTS WITH 10Ω FAULT RESISTANCE

i_a^{TW}	i_b^{TW}	i_c^{TW}	Fault Type	Fault Loc	Fault Time
+207	-0.05	-0.05	AG	0.02km	0.0614 s
+75	-0.74	-0.74	AG	0.5km	0.062 s
-141.19	+141.19	-1.13 E-09	AB	0.02km	0.059 s
+12.48	-4.12 E-07	-12.48	AC	0.03km	0.052 s
-160.42	+255.59	-0.04	ABG	0.03km	0.052 s
+281	-201	-80	ABCG	0.03km	0.054 s

F. The effect of noise on the proposed algorithm

The effect of noise in traveling wave protection can be divided into two categories:

a) Interfere with algorithm activation

b) Failure to correctly identify the type of faults

To activate the process of protection (that involves fault detection, classification and location), the amplitude of TW should be selected according to the maximum expected noise level in the transmission line.

To investigate the effect of noise on the proposed fault classification algorithm, some random Gaussian white noise with SNR 20dB is added to phase current, for example, the results for an SLG fault are shown in Fig. 10.

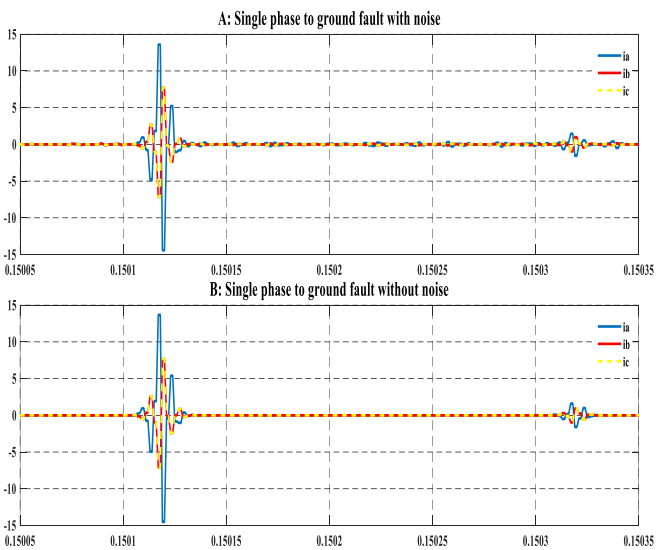

Fig. 10.Single phase to ground fault in 30km with and without noise

According to the results, the proposed algorithm has correct performance in the presents of white Gaussian noise.

III. CONCLUSIONS

Ignoring the fault-induced TW mutual induction challenges the performance and ultra-high-speed protection algorithms of transmission lines. Moreover, the lightning strike on the line and neglecting such situations as another class of faults cause the relays to send wrong commands. Therefore, given the above cases and separating fault behind the relay faults, this study proposed a fast, reliable, and simple method without heavy mathematical calculations by applying the first TW current class. The results of performed simulations that only a small part of them are presented in this study show that the proposed method is not sensitive to fault resistance and inception angle and has good performance for transmission lines with recloser and single-phase cut-off mechanism. Moreover, given the frequency band limitation of PTs, only the TW current is used for the algorithm's decision-making.

REFERENCES

[1] M. Bollen, "Travelling-wave-based protection of double-circuit lines,"*IEE Proceedings C-Generation, Transmission and Distribution*, vol. 140, no. 1, pp. 37-47, Jan. 1993.

[2] X. Dong,, W. Kong and T. Cui, "Fault Classification and Faulted-Phase Selection Based on the Initial Current Traveling Wave," *IEEE Transactions on Power Delivery*, vol. 24, no. 2, pp. 552-559, Apr. 2009.

[3] M. Biswal ,"Faulty phase selection for transmission line using integrated moving sum approach,"*IET Science, Measurement & Technology*, vol. 10, no. 7, p. 761 – 767, Oct. 2016.

[4] K. Chen, C.Huang and J. He, "Fault detection, classification and location for transmission lines and distribution systems: a review on the methods," *High Voltage*, vol. 1, no. 1, pp. 25 - 33, Apr. 2016.

[5] H. Wang and W. Keerthipala, "Fuzzy-neuro approach to fault classification for transmission line protection," *IEEE Transactions on Power Delivery*, vol. 13, no. 4, pp. 1093 - 1104, Oct. 1998.

[6] K.M. Silva, B.A. Souza and N.S.D. Brito, "Fault detection and classification in transmission lines based on wavelet transform and ANN," *IEEE Transactions on Power Delivery*, vol. 21, no. 4, pp. 2058 - 2063, Oct. 2006.

[7] C. Hong and S. Elangovan, "A B-Spline Wavelet Based Fault Classification Scheme for High Speed Protection Relaying," *Electric Machines & Power Systems*, vol. 28, no. 4, pp. 313-324, Nov. 2010.

[8] A. Yadav and A. Swetapadma, "A novel transmission line relaying scheme for fault detection and classification using wavelet transform and linear discriminant analysis," *Ain Shams Engineering Journal*, vol. 6, no. 1, pp. 199-209, Mar. 2015.

[9] O. H. Gupta and M. Tripathy, "An Innovative Pilot Relaying Scheme for Shunt-Compensated Line," *IEEE Transactions on Power Delivery*, vol. 30, no. 3, pp. 1439 - 1448, 2015.

[10] M. Khalili, F. Namdari and E. Rokrok, "A fault location and detection technique for STATCOM compensated transmission lines using game theory," *IET Generation, Transmission & Distribution*, vol. 15, no. 11, pp. 1688-1701, Feb. 2021.

[11] M. Khalili, F. Namdari and E. Rokrok, "Traveling wave-based protection for TCSC connected transmission lines using game theory," *International Transactions on Electrical Energy Systems*, vol. 30, no. 10, Aug. 2020.

[12] M. Khalili, F. Namdari and E. Rokrok, "Traveling wave-based protection for SVC connected transmission lines using game theory," *International Journal of Electrical Power & Energy Systems*, vol. 123, p. 106276, Dec. 2020.

[13] P. Jafarian and M. Sanaye-Pasand, "A Traveling-Wave-Based Protection Technique Using Wavelet/PCA Analysis," *IEEE Transactions on Power Delivery*, vol. 25, no. 2, pp. 588 - 599, Apr. 2010.

[14] S. Hasheminejad, S. G. Seifossadat, M. Razaz and M. Joorabian, "Ultra-high-speed protection of transmission lines using traveling wave theory," *Electric Power Systems Research*, vol. 132, pp. 94-103, Mar. 2016.

[15] D. Wang, H. Gao, G. Zou and S. Luo, "Ultra-high-speed travelling wave directional protection based on electronic transformers," *IET Generation, Transmission & Distribution*, vol. 11, no. 8, pp. 2065-2074, May. 2017.

[16] S. Hasheminejad, S. G. Seifossadat, M. Razaz and M. Joorabian, "Traveling-wave-based protection of parallel transmission lines using Teager energy operator and fuzzy systems," *IET Generation, Transmission & Distribution*, vol. 10, no. 4, pp. 1067-1074, Mar. 2016.

[17] B. Chen, "Fault Statistics and Analysis of 220-kV and Above Transmission Lines in a Southern Coastal Provincial Power Grid of China," *IEEE Open Access Journal of Power and Energy*, vol. 7, pp. 122 - 129, Feb. 2020.

[18] O. G. S. ,. K. D. K.T.M.U.Hemapala, "Techno-economic feasibility of lighting protection of overhead transmission line with multi-chamber insulator arrestors," *Development Engineering*, vol. 3, pp. 100-116, May. 2018.

[19] M. Hou, H. Gao, S. Zhang and F. Wang, "Simulation study on lightning protection of distribution transformer with zinc oxide arrester," in *5th International Conference on Electric Utility Deregulation and Restructuring and Power Technologies (DRPT)*, pp. 1763-1767, 2015.

[20] Y. Han, L.Tang, L. Li, Q. He, Y. Hao and S. Yao, "Influence of Lightning Flashover Criterion on the Calculated Lightning withstand Level of±800kV UHVDC Transmission Lines at High Altitude," *IEEE Transactions on Dielectrics and Electrical Insulation*, vol. 22, no. 1, pp. 185-191, Feb. 2015.

[21] N. Ghaffarzadeh, "A New Method for Power Quality Events Detection and Classification using Discrete Wavelet Transform and Correlation Coefficients," *International Journal of Industrial Electronics, Control and Optimization (IECO)*, vol. 4, no. 1, pp. 47-57, Jan. 2021.

[22] M. Farshad and J. Sadeh, "Transmission line fault location using hybrid wavelet-Prony method and relief algorithm," *International Journal of Electrical Power & Energy Systems*, vol. 61, pp. 127-

136, Oct. 2014.

[23] S.Hasheminejad, S.G.Seifossadat and M.Joorabian,"New travelling-wave-based protection algorithm for parallel transmission lines during inter-circuit faults,"*IET Generation, Transmission & Distribution*, vol. 11, no. 16, pp. 3984-3991, Nov. 2017.

[24] X. Li, A. Dyśko and GraemeM, "Traveling Wave-Based Protection Scheme for Inverter-Dominated Microgrid Using Mathematical Morphology," *IEEE TRANSACTIONS ON SMART GRID*, vol. 5, no. 5, pp. 2211-2218, Aug. 2014.

Iman Mousaviyan was born in 1983 in Shahrekord, Iran. He received the B.Sc. and the M.Sc. degree in power engineering from Shahid Chamran University of Ahvaz, Ahvaz, Iran, in 2005 and 2008 respectively. He is currently working towards his PhD degree in the Department of Electrical Engineering, Shahid Chamran University of Ahvaz, Ahvaz, Iran. His research interests are fault location, power system protection, Traveling wave, and power quality assessment.

Seyyed Ghodratollah Seifossadat was born in Ahvaz, Iran, on August 28, 1963 and received the B.Sc. degree in electrical engineering from the Iran University of Science and Technology (IUST), Tehran, in 1989 and the M.Sc. degree in electrical engineering from the Ferdosi University of Mashhad, Mashhad, Iran, in 1992 and the Ph.D. degree from IUST in 2006. Currently, he is a Professor with the Department of Electrical Engineering, Shahid Chamran University of Ahvaz, Iran, where he has been since 1992. His research interests are power system protection, fault location, power electronics, electric machinery, FACTS devices, and power quality assessment.

Mohsen Saniei born 1966 in Dezful, Iran, graduated in B.Sc of Electrical Engineering from Ferdowsi University of Mashhad, Iran, in 1989, and M.Sc from Tarbiat Modarres University, Tehran, Iran, in Electrical Engineering in 1992, and Phd in Strathclyde University, Glasgow, UK in Electrical Engineering in 2004. He is now associate professor of Electrical Engineering department of Shahid Chamran University of Ahvaz, Iran. His interests are in power system analysis, control and operation, Microgrid managemen.

IECO

This page intentionally left blank.

International Journal of Industrial Electronics, Control and Optimization © 2021 IECO
Vol. 4, No. 4, pp. 387-396, Sep (2021)

A New Event-Triggered Consensus Control for Microgrids

Razieh Heidari[1], Alimorad Khajehzadeh[2,†], and Mahdiyeh Eslami [3]

[1,2,3] Department of Electrical Engineering, Kerman Branch, Islamic Azad University, Kerman, Iran

ABSTRACT

This paper studies an adaptive event-triggered consensus problem for heterogeneous multi-agent systems considering the time delay of the communication network. An event-triggered interval is here considered as a specific delay and unified round trip time (RTT) delay. Furthermore, an efficient optimal predictive-based coordination control strategy is introduced for balancing the non-ideal behaviors of communication channels. The efficiency of the proposed method for controlling network-based multi-agent systems with coupled subsystems is evaluated in two stages. In the first stage, the very method is implemented on two coupled continuous stirred tank reactors while in the second one, it is used to control the voltage and current of a DC microgrid consisting of several distributed generation units. To prevent the unessential utilization of communication resources, the transfer of information does not occur in this mechanism unless a specific event is triggered. The simulation results show that despite being non-ideal and time-delayed communication channels, the proposed technique is capable of improving the performance of power grids.

Article Info

Keywords:
Adaptive event-triggered control, Microgrids, Multi-agent systems, Network-based control system, Time delay

Article History:
Received 2020-11-30
Accepted 2021-06-29

I. INTRODUCTION

Today, because of the tendency to replace renewable energy sources with fossil fuels and also the appearance of different distributed generation sources, traditional electric grids are rapidly changing with the use of microgrids because, in addition to providing their own loads with their DGs, microgrids can support the main grid during peak hours when the grid load increases sharply and the heavy loading disrupts the power grid [1]. Microgrids are controllable units composed of distributed generation sources, loads, energy storage sources, and control devices that are interconnected by power lines [2]. They are generally divided into three categories: Alternative Current (AC), Direct Current (DC), and hybrid AC-DC [3]. The standard microgrid model used for residential, commercial, and industrial applications is AC. Although DC power systems cannot solve some challenges of AC microgrids such as reactive power management, frequency control, synchronization, etc., they exhibit such advantages as availability of efficient converters, appropriate interfacing of batteries and DC energy sources, minimal power losses, and an ever-growing number of DC loads, making this type of microgrids attractive [4-7].

Current sharing and voltage regulation are the two main control challenges of DC microgrids. The optimal voltage regulation strategy leads to the desired output voltage of each microgrid while the other strategy, called the current sharing control strategy, causes the current to be equally distributed among all microgrids [8]. Hierarchical control has been proposed in several articles for these two purposes [9]. Although centralized controllers have a constant voltage and suitable current distribution, when the size of the grid increases, the grid load will also greatly increase and a failure in a single point may lead to the malfunction of the entire grid [10]. This is the main reason for the preference of decentralized and distributed controllers over centralized ones.

[†]Corresponding Author: khajehzadeh@iauk.ac.ir
Tel: +98-34-31321029, Fax: +98-34-31320051,
Department of Electrical Engineering, Kerman Branch, Islamic Azad University, Kerman, Iran

Droop controllers as a communication-less method may lead to voltage deviation from the reference value. Therefore, Zhao and Dörfler [11] combined a secondary control layer with consensus algorithms with a droop controller to control voltage deviations. In distributed control, each subsystem can receive information from its neighbors. This feature can improve system performance and has made many researchers interested in using scalable control strategies, especially for splitting current [11-14]. Despite the benefits of distributed controls, the exchange of information between subsystems on large networks may create a heavy communication burden in the communication network. To prevent unnecessary use of communication resources and reduce the frequency of information transmission and save energy consumption, event-triggered control (ETC) techniques have been introduced in recent researches [15-18]. In these techniques, each subsystem transmits its information according to certain event-triggering conditions via the communication network and the data transmission will only be done when the event-triggering condition occurs. So, communication costs are significantly reduced in these approaches [19]. Han et al. [20] proposed a distributed nonlinear ETC scheme for the current sharing and voltage regulation on an electrical grid model with a DC microgrid.

Research on ETC technology has proposed an efficient method called Adaptive Event Trigger Control (AETC) [21-25]. In these approaches unlike traditional ETC algorithms, some control parameters are adjusted according to the line signal to reduce the method's conservativeness. In the field of MASs, many have been conducted AETC. For example, Zou and Xiang [26] investigated the arrangement control for networked MASs by AETC. Yang et al. [27] examined the issue of the consensus for MASs by combining AETC with predictive control methods. Especially, in heterogeneous MASs, the output consensus problem and also a fully distributed ETC strategy with an AETC are presented in [21].

In most of the research works reviewed, some important behavior in the networked HMASs, such as the strong interaction among subsystems, is not taken into account in the design of adaptive event-triggered consensus controllers. Moreover, the impact of network latency on the communication connections among subsystems is another significant aspect in networked HMASs rarely considered in the literature.

Little work on the design of network-based multifactor power system controllers has considered the non-ideal behavior of the telecommunication network in interconnected communications between subsystems, which is another motivation for the present study.

Furthermore, new industrial distributed systems are regarded as large multi-agent systems. So, the challenging problems listed for network-based multi-agent systems occur in network-based distributed systems integrated with coupled sub-system [22]. Since few studies have been conducted on the design of network-based multi-agent power system controllers with considering the non-ideal behavior of the telecommunication network in interconnected communications among subsystems, it can be accounted as another motivation for the present research. Another goal of the present work is to examine the control of network-based interconnected systems via the proposed approach. In this regard, in the first case study, the proposed method is applied to two connected stirred tank reactors with subsystems strongly connected while in the second case, a DC microgrid model including various DG units and state-space model is considered to achieve the benefits of reducing network communication costs and improving security by controlling the voltage and current of DGs by the proposed adaptive event-triggered consensus controller. The main sections are as follows:

i) Proposing an AETC scheme for discrete-time MASs besides an adaptive event-triggered communication scheme to reduce the frequency of data transmission.

ii) Developing an efficient PD-like optimal control protocol for heterogeneous MASs as well as designing a PD-like predictive controller.

iii) Deriving the stability condition of network-based MASs considering random round-trip time (RTT) delays.

iv) Implementing the proposed method onto two connected stirred tank reactors with subsystems strongly connected for confirming the efficiency of the very approach.

v) Implementing the proposed method on a DC microgrid with five distributed generation units for gaining the proposed method advantages besides controlling the voltage and current of the microgrid.

The rest of this paper is organized as follows. Section II introduces the model of the studied system with some necessary assumptions and definitions. Section III presents the new event-triggered conditions besides the proposed PD-like predictive control scheme and the stability and consensus are analyzed for whole systems. Finally, the simulation verification and the conclusions are provided in Sections IV and V, respectively.

II. PROBLEM FORMULATION

The general linear discrete-time description of MASs can be considered as follows:

$$x_i(k+1) = H_i x_i(k) + G_i u_i(k+1) \quad (1)$$

where $x_i(k)$ and $u_i(k)$are the states and inputs of the ith agent, respectively and H_i and G_i are the system matrices of the ith agent, respectively.

Before proceeding, it is necessary to express some assumptions and definitions as bellow:

Assumption 1: The pair (H_i, G_i) is controllable and the

states can be measurable.

Assumption 2: The communication delay is bounded via τ_{max}, and the maximum amount of event-triggered time interval is δ_{max} [28].

Definition 1: The consensus problem of HMASs is that the different subsystems keep the consensus of the states while reducing the data transmission frequency and considering networks' constraints, i.e.

$$\lim_{k\to\infty}\left|x_i(k)-x_j(k)\right|=0 \tag{2}$$

According to the definition of ETC, the controller will be in the following form:

$$u_i(k)=u_i\left(k_t^i\right), k\in\left\lfloor k_t^i, k_{t+1}^i\right) \tag{3}$$

where k_t^i is the triggering time of the ith agent, and k_{t+1}^i stands for the next event-triggered time. We have:

$$k_{t+1}^i=inf\{k: k>k_t^i, g_i(k)>0\} \tag{4}$$

where $g_i(k)=e_i^T(k)We_i(k)-R_i(k)x_i^T(k)Wx_i(k)$, which is explained in the next section.

III. Main Results

A. The Developed Adaptive Event-Triggered Based Control

In the following, two adaptive event-triggered techniques are developed to store the communication network bandwidth or energy. Commonly, if the ratio of state error of the ith agent to its current state will be greater than a predefined value, the state data can be transferred. However, in the MASs' network topology, there is a high probability that only event-triggered mechanisms exist between agents, not the agent itself. Thus, an adaptive event-trigger control (AETC) is developed in this paper based on the states of entire agents.

Case 1: The proposed adaptive event-triggered strategy is as follows:

$$e_i^T(k)We_i(k)>R_i(k)x_i^T(k)Wx_i(k) \tag{5}$$

$$R_i(k)=\frac{R_i(k-1)}{1+e_i^T(k)We_i(k)} \tag{6}$$

where $e_i(k)=x_i(k)-x_i\left(k_t^i\right)$..

Lemma 1. For the condition (5) and the initial values $R_i(0)\in(0,1)$, the following inequality is satisfied for all $k\in N$

$$0\le R_i(k)\le R_i(0)<1 \tag{7}$$

Proof: To prove, firstly, consider $k=1$, thus we have:

$$R_i(1)=\frac{R_i(0)}{1+e_i^T(1)We_i(1)}\le R_i(0) \tag{8}$$

Then, given $k>1$, the quadratic term $e_i^T(k)We_i(k)$ in Equ. (5) will be semi-definite, i.e., $e_i^T(k)We_i(k)\ge 0$. As a result, we have:

$$R_i(k)=\frac{R_i(k-1)}{1+e_i^T(k)We_i(k)}\le R_i(k-1) \tag{9}$$

which results in $0\le R_i(k)\le R_i(0)<1$ if one chooses the appropriate $R_i(0)$. So, the proof is completed.

Case 2: In the research of ETC, the objects are usually network-based control systems, whose controllers are connected with sensors and actuators through non-ideal communication channels. However, in most MASs, the state of the agent itself can be obtained in real-time, and the state of the neighbor agent is transferred via the communication network. Only event-triggered communication between agents is considered. As a result, the triggering condition (5) is not suitable and appropriate for this case and a new efficient condition for this case is developed as follows:

$$e_{ij}^T(k)We_{ij}(k)>R_{ij}(k)x_j^T(k)Wx_j(k) \tag{10}$$

$$R_{ij}(k)=\frac{R_{ij}(k-1)}{1+e_{ij}^T(k)We_{ij}(k)} \tag{11}$$

where $e_{ij}(k)=x_i(k)-x_i\left(k_t^{ij}\right)$ and k_t^{ij} are the triggering communication time from the ith agent to the jth agent. It is clear that the triggering condition of case 2 becomes condition (5) if $i=j$. In other words, condition (5) is a special case of condition (10).

B. The PD-like Predictive Controller

The proposed method is a combination of the PD control based on predictors. Since predictors are used to simultaneously estimate the delayed states, the use of the delayed information is avoided. Thus, the performance degradation due to communication time delay can be alleviated. In this regard, to achieve consensus among heterogeneous agents modelled by deferent systems, an optimal coordination control protocol, which consists of two parts, is proposed. The first part is the proportional part, which can be obtained by various methods, such as pole placement, LQR, and so on [29]. The second part is the predictive term, which is to be designed as follows.

Consider the following controller:

$$u_i(k)=K_ix_i(k)+v_i(k) \tag{12}$$

where K_i is the proportional parameter matrix and $v_i(k)$ is the optimal prediction of the controller. By substituting Equ.

(12) in Equ. (1), we obtain:

$$x_i(k+1) = (H_i + G_iK_i)x_i(k) + G_iv_i(k) \tag{13}$$

To calculate the prediction term $v_i(k)$, the following cost function is introduced.

$$\sum g_{ij}\left(x_i(k+1) - x_j(k+1)\right)^2 + c_i{v_i}^2(k) \tag{14}$$

where $\Gamma = [g_{ij}]$ is the adjacency matrix, $g_{ij} = 1$ if $i \neq j$, otherwise $g_{ij} = 0$. Also, c_i denotes the weighting factor.

The minimization of the cost function (14) leads to:

$$\frac{\partial \sum_{i=1}^{N} J_i(k)}{\partial v_i(k)} = 0 \tag{15}$$

By substituting the relevant formulas in the formulas (15), we obtain:

$$\begin{aligned} &G_i^T \textstyle\sum_{j=1}^{N} g_{ij}\left(x_i(k+1) - x_j(k+1)\right) - \\ &G_i^T \textstyle\sum_{j=1,j\neq i}^{N} g_{ij}\left(x_j(k+1) - x_i(k+1)\right) + \\ &c_iv_i(k) = 0 \end{aligned} \tag{16}$$

Furthermore, the above formula can be rewritten as follows:

$$\begin{aligned} &G_i^T \textstyle\sum_{j=1}^{N} g_{ij}\left((H_i + G_iK_i)x_i(k) + G_iv_i(k) - \right. \\ &\left.(H_j + G_jK_j)x_j(k) - G_jv_j(k)\right) - \\ &G_i^T \textstyle\sum_{j=1,j\neq i}^{N} g_{ji}\left(\left(H_j + G_jK_j\right)x_j(k) + G_jv_j(k) - \right. \\ &\left.(H_i + G_iK_i)x_i(k) - G_iv_i(k)\right) + c_iv_i(k) = 0 \end{aligned} \tag{17}$$

Merging the same items leads to

$$\begin{aligned} &G_i^T \textstyle\sum_{j=1}^{N} g_{ij}\left(G_iv_i(k) - \right. \\ &\left.G_iv_j(k)\right) + G_i^T \textstyle\sum_{j=1,j\neq i}^{N} g_{ji}\left(G_iv_i(k) - \right. \\ &\left.G_iv_j(k)\right) + c_iv_i(k) = -\left(G_i^T \textstyle\sum_{j=1}^{N} g_{ij}\left((H_i + \right.\right. \\ &\left.G_iK_i)x_i(k) - \left(H_j + G_jK_j\right)x_j(k)\right) + \\ &G_i^T \textstyle\sum_{j=1,j\neq i}^{N} g_{ji}\left(\left(H_i + G_iK_i\right)x_i(k) - \left(H_j + \right.\right. \\ &\left.\left.G_jK_j\right)x_j(k)\right)\Big) \end{aligned} \tag{18}$$

Moreover, the following form can be obtained.

$$\sum_{j=1}^{N} b_{ij}v_i(k) = -\sum_{j=1}^{N} a_{ij}x_i(k) \tag{19}$$

where
$\omega = \sum_{j=1}^{N} g_{ij} + \sum_{j=1,j\neq i}^{N} g_{ji}$, $b_{ii} = \omega G_i^T G_i + c_iI_{ii}$, $b_{ij} = -\left(g_{ij} + g_{ji}\right)G_i^T G_j$, $a_{ii} = \omega G_i^T(H_i + G_iK_i)$, $a_{ij} = -\left(g_{ij} + g_{ji}\right)G_i^T\left(H_i + G_jK_j\right)$.

Furthermore, we have the matrix I_{ii} in which the element of the ith row and ith column is one and other elements are zero.

The compact form of the above formula can be written as follows:

$$Bv(k) = -Ax(k) \tag{20}$$

where $B = \{b_{ij}\}$ and $A = \{a_{ij}\}$.
Then, the prediction term of the controller for the whole systems is

$$v(k) = -B^{-1}Ax(k) \tag{21}$$

where
$v(k) = [v_1^T(k)\ v_2^T(k) \dots\ v_N^T(k)]^T$, $x(k) = [x_1^T(k)\ x_2^T(k) \dots\ x_N^T(k)]^T$
For the agent i, the prediction of the controller is as follows:

$$v_i(k) = I_{ii}v(k) = -I_{ii}B^{-1}Ax(k) \tag{22}$$

Then, the controller law (12) can be rewritten as

$$\begin{aligned} u_i(k) &= K_ix_i(x) + v_i(k) \\ &= K_ix_i(x) - I_{ii}B^{-1}Ax(k) \end{aligned} \tag{23}$$

According to the structure of the agent and its communication strategy, the controller law is obtained with the ETC.

$$u_i(k) = K_ix_i(x) + v_i\left(k_t^i\right), \qquad k \in \left[k_t^i, k_{t+1}^i\right) \tag{24}$$

Since the introduction of the network may cause delays in communication between agents, a PD-like predictive controller is proposed to actively compensate for the delay and achieve the consensus eventually. Combining Equ. (13) and Equ. (24), the predictions of state are given as

$$\begin{aligned} \hat{x}_i\left(k_t^i + 1\middle|k_t^i\right) &= (H_i + G_iK_i)\hat{x}_i\left(k_t^i\middle|k_t^i\right) \\ &\quad + G_i\hat{v}_i\left(k_t^i\middle|k_t^i\right) \\ &= (H_i + G_iK_i)\hat{x}_i\left(k_t^i\middle|k_t^i\right) \\ &\quad + G_iI_{ii}B^{-1}A\hat{x}\left(k_t^i\middle|k_t^i\right) \end{aligned} \tag{25}$$

Which can be described in an aggregated form as Equ. (26).

$$\begin{aligned} \hat{x}_i\left(k_t^i + 1\middle|k_t^i\right) &= \tilde{H}\hat{x}\left(k_t^i\middle|k_t^i\right) - \tilde{G}B^{-1}H\hat{x}\left(k_t^i\middle|k_t^i\right) \\ &= \phi\hat{x}\left(k_t^i\middle|k_t^i\right) \\ \hat{x}_i\left(k_t^i + d(k)\middle|k_t^i\right) &= \phi\hat{x}\left(k_t^i + d(k) - 1\middle|k_t^i\right) \\ &= \phi^{\bar{\tau}}\hat{x}\left(k_t^i\middle|k_t^i\right) \\ \hat{x}_i\left(k_t^i + \bar{\tau} + \bar{p}\middle|k_t^i\right) &= \phi\hat{x}\left(k_t^i + \bar{\tau} + \bar{p} - 1\middle|k_t^i\right) \\ &= \phi^{\bar{\tau}+\bar{p}}\hat{x}\left(k_t^i\middle|k_t^i\right) \end{aligned} \tag{26}$$

where
$\hat{x}_i\left(k_t^i\middle|k_t^i\right) = x_i\left(k_t^i\middle|k_t^i\right) = x_i\left(k_t^i\right)$, $\hat{v}_i\left(k_t^i\middle|k_t^i\right) = v_i\left(k_t^i\right)$, $\tilde{H} = diag(\bar{H}_1\ \bar{H}_2 \dots\ \bar{H}_N)$, $\tilde{G} = diag(\bar{G}_1\ \bar{G}_2 \dots\ \bar{G}_N)$, $\bar{H}_i = H_i + G_iK_i$, $\phi = \tilde{H} - \tilde{G}B^{-1}A$ and $\bar{\tau}$ are the upper bound of the communication delay.

We design a function to denote the relationship between the current time, trigger time, and delay. In the suggested scheme,

the event-triggered time interval is considered a particular delay and included in the round-trip time (RTT) delay.

$$k_t^i = k - \tau(k) - l = k - d(k) l = 0,1,\dots,\bar{p} \tag{27}$$

where $\bar{p}$ is the upper bound of the event-triggered interval.

Afterward, the prediction part of the controller of agent i can be expressed as

$$\begin{aligned} \hat{v}_i\left(k_t^i+1\middle|k_t^i\right) &= -I_{ii}B^{-1}H\hat{x}\left(k_t^i+1\middle|k_t^i\right) \\ &\vdots \\ \hat{v}_i\left(k_t^i+d(k)\middle|k_t^i\right) &= -I_{ii}B^{-1}H\hat{x}\left(k_t^i+d(k)\middle|k_t^i\right) \\ &\vdots \\ \hat{v}_i\left(k_t^i+\bar{\tau}+\bar{p}\middle|k_t^i\right) &= -I_{ii}B^{-1}H\hat{x}\left(k_t^i+\bar{\tau}+\bar{p}\middle|k_t^i\right) \end{aligned} \tag{28}$$

Based on the trigger condition and (27), we can easily get

$$\hat{v}_i\left(k_t^i+\tau(k)+l\middle|k_t^i\right) = \hat{v}_i(k|k-d(k)) \tag{29}$$

Then, the PD-like predictive controller is

$$\begin{aligned} u_i(k) &= K_i x_i(k) + \hat{v}_i(k|k- \\ d(k)) &= K_i x_i(k) + I_{ii}B^{-1}A\phi^{d(k)}x\left(k_t^i\middle|k_t^i\right) \end{aligned} \tag{30}$$

After that, the purpose is to find the stability condition and design the suitable controller so that the above systems become ultimately stable and achieve the consensus among agents.

According to the structure of the control system we designed, the current state $x_i(k)$ is available, i.e. $\hat{x}_i\left(k_t^i+\bar{\tau}+\bar{p}\middle|k_t^i\right) = x(k)$, then

$$\begin{aligned} x_i(k+1) &= \bar{H}_i x_i(k) + G_i\hat{v}_i(k|k-d(k)) = \\ \bar{H}_i x_i(k) &+ G_i I_{ii}B^{-1}A\phi^{d(k)}x\left(k_t^i\middle|k_t^i\right) \end{aligned} \tag{31}$$

The compact form can be written as

$$\begin{aligned} x(k+1) &= \tilde{H}x(k) - \tilde{G}B^{-1}A\phi^{d(k)}\hat{x}\left(k-\right. \\ &\left. d(k)\right) \end{aligned} \tag{32}$$

Moreover, the compact form predictions of the state is that

$$\begin{aligned} \hat{x}(k) &= \tilde{H}\hat{x}(k-1) - \tilde{G}B^{-1}A\hat{x}(k-1) \\ &\vdots \\ \hat{x}(k+d(k)+1) &= \tilde{H}\hat{x}\left(k-d(k)\right) - \\ \tilde{G}B^{-1}A\hat{x}&\left(k-d(k)\right) \\ &\vdots \\ \hat{x}(k-\bar{\tau}-\bar{p}+1) &= H\hat{x}(k-\bar{\tau}-\bar{p}) - \\ \tilde{G}B^{-1}A\hat{x}&(k-\bar{\tau}-\bar{p}) \end{aligned} \tag{33}$$

Equ. (32) and Equ. (33) can be expressed as

$$X(k+1) = \Lambda X(k) \tag{34}$$

where

$$(k) = \begin{bmatrix} x(k) \\ \hat{x}(k-1) \\ \vdots \\ \hat{x}\left(k-d(k)\right) \\ \hat{x}(k-\bar{\tau}-\bar{p}) \end{bmatrix},$$

$$\Lambda = \begin{bmatrix} \tilde{H} & 0\cdots & \tilde{G}B^{-1}A\phi^{d(k)} & 0_{Nn\times(\bar{\tau}-\bar{p}-d(k))Nn} \\ 0 & \phi & \cdots & 0_{Nn\times(\bar{\tau}-\bar{p}-d(k))Nn} \\ \vdots & \vdots & \ddots & \vdots \\ 0 & 0 & \cdots & 0_{Nn\times(\bar{\tau}-\bar{p}-d(k))Nn} \\ 0 & 0 & \cdots & \phi_{0_{\bar{\tau}-\bar{p}-d(k)}} \end{bmatrix}$$

Theorem 1. The stability and consensus performance of systems (34) is achieved if the Eigenvalues of matrix Λ are within the unit circle.

Proof: For a stochastic switching system, each sub-matrix of its systems' matrix is stable, then the whole system is stable [30]. Using the pole placement approach and the presented method we can choose the suitable $\mathrm{K_i}$ such that $\bar{H}_i = H_i + G_i K_i$ will be stable, Thus, as $\emptyset = \tilde{H} - \tilde{G}B^{-1}A$, it makes that the Eigenvalues of matrix $\emptyset$ will be within the unit circle. As a result, all sub-matrixes of Λ are stable, and then the system can be ensured to be stable. The proof is completed.

IV. Simulation Studies

Here, we consider two coupled continuous stirred tank reactors (CSTRs) as a case study. The nonlinear dynamic description of the CSTR model is considered as described in [31]. Moreover, the value of process parameters and operating steady states are given in Table I. The system has two coupled sub-systems that are interacted through their states. The sampling interval is chosen as $T_s = 0.0025\ h$. As a result, the nominal discrete-time linear state-space can be presented in the following form:

$$\begin{aligned} \bar{x}_{k+1}^1 &= A^{11}\bar{x}_k^1 + B^1 u_k^1 + A^{12}\bar{x}_k^2, \qquad \bar{y}_k^1 = C^1\bar{x}_k^1 \\ \bar{x}_{k+1}^2 &= A^{22}\bar{x}_k^2 + B^2 u_k^2 + A^{21}\bar{x}_k^1, \qquad \bar{y}_k^2 = C^2\bar{x}_k^2 \end{aligned} \tag{35}$$

where

$\bar{x}_k^1 = \begin{bmatrix} \frac{T_1 - {T_1}^S}{{T_1}^S} \\ \frac{C_{A_1} - C_{A1}^S}{C_{A1}^S} \end{bmatrix}$, $\bar{x}_k^2 = \begin{bmatrix} \frac{T_2 - {T_2}^S}{{T_2}^S} \\ \frac{C_{A_2} - C_{A2}^S}{C_{A2}^S} \end{bmatrix}$, $u_k^1 = \begin{bmatrix} \frac{Q_{r1} - Q_{r1}^S}{Q_{r1}^S} \\ \frac{C_{A0} - C_{A0}^S}{C_{A0}^S} \end{bmatrix}$, $u_k^2 = \begin{bmatrix} \frac{Q_{r2} - Q_{r2}^S}{Q_{r2}^S} \\ \frac{C_{A03} - C_{A03}^S}{C_{A03}^S} \end{bmatrix}$, $A^{11} = \begin{bmatrix} 1.0488 & 0.0117 \\ -0.1614 & 0.8786 \end{bmatrix}$, $A^{12} = \begin{bmatrix} 0.0920 & 0.0007 \\ -0.0093 & 0.0895 \end{bmatrix}$, $B^1 = \begin{bmatrix} 0.0036 & 0.0002 \\ -0.0003 & 0.0281 \end{bmatrix}$, $C^1 = [1 \quad 0]$, $A^{22} = \begin{bmatrix} 0.9113 & 0.0026 \\ -0.0359 & 0.8706 \end{bmatrix}$, $A^{21} = \begin{bmatrix} 0.0870 & 0.0006 \\ -0.0081 & 0.0714 \end{bmatrix}$, $B^2 = \begin{bmatrix} 0.0029 & 0.0001 \\ -0.0001 & 0.0567 \end{bmatrix}$, $C^2 = [1 \quad 0]$.

In addition, an additive state disturbance is considered as

$w_k^i \in \mathbb{W}^i$ where $\mathbb{W}^i = \{w^i \subseteq \mathbb{R}^2 || w^i|_\infty \leq 0.01\}$ and the output disturbance is $v_k^i \in \mathbb{V}^i$ where $\mathbb{V}^i = \{v^i \subseteq \mathbb{R}^1 || v^i|_\infty \leq 0.01\}$.

TABLE I
DEFINITIONS OF PROCESS VARIABLES

Variable	Definition
$F_0,\ F_r,\ F_3$	Flow rate of fresh A, flow rate of recycled A from reactor 2, flow rate of additional fresh stream feeding pure A
F_1, F_2	Effluent flow rate from reactors 1, 2
$C_{A1},\ C_{A2}$	Molar concentration of A in reactors 1, 2
T_1, T_2	Temperatures in reactors 1, 2
T_0, T_{03}	Feed stream temperatures to reactors 1, 2
Q_{r1}, Q_{r2}	Heat input rate into reactors 1, 2
$C_{A0},\ C_{A3}$	Inlet reactant concentration of reactors 1, 2
V_1, V_2	Reactor volume of reactors 1, 2
$\Delta H_j,\ k_j,\ E_j$ for $j = 1,2,3$	Enthalpies, pre-exponential constants, and activation energies of the three reactions
ρ_s, R, c_p	Heat capacity, gas constant, and density of fluid in the reactor

The induced time-varying delays of communication channels, which connect the local control units of two CSTRs to each other, are created randomly between 1 and 14 time steps (i.e., 126 seconds). The main objective of the designed control scheme is to regulate the system to the unstable (open loop) steady-state employing the suggested approach. The initial state for the system is chosen as $(537.3704\ ,\ 0.8342\ ,\ 340.0798, 3.5519)^{\mathrm{T}}$. Moreover, the simulation horizon is considered 0.6 hour.

In the following, some simulations are done to compare the proposed method and a resilient event-triggered output feedback control approach developed in [32] and two AETC schemes adopted from [20] and [22]. Furthermore, Q_{r1}, Q_{r2}, C_{A0} and C_{A03} are assumed to be constrained by $|Q_{r1}| \leq 1.4 \times 10^6 kJ/h$, $|Q_{r2}| \leq 1.8 \times 10^6 kJ/h$, $0 \leq C_{A0} \leq 6 kmol/m^3$ and $0 \leq C_{A03} \leq 4\ kmol/m^3$, respectively. Moreover, the random induced delays of communication channels connecting the local control units of subsystems are changing between 1 to 14 steps. The initial state $(T_1^0\ (K), C_{A1}^0 (kmol/m^3), T_2^0 (K),\ C_{A2}^0 (kmol/m^3))^T$ for the plant is chosen as $(412.9470\ ,\ 1.8367\ ,\ 384.4043, 1.5951)^{\mathrm{T}}$. In all simulation studies, the initial conditions are the same and the simulation horizon is considered as one hour.

The trajectories of state obtained via the suggested approach and other approaches adopted from [32], [21], and [23] are depicted in Figs. 1-4. Moreover, the trajectories of input obtained via the suggested approach and other approaches adopted from [32], [21], and [23] are depicted in Figs. 5-8. As can be concluded from these figures, the proposed method gives a more appropriate performance of stability and consensus in comparison to other applied approaches.

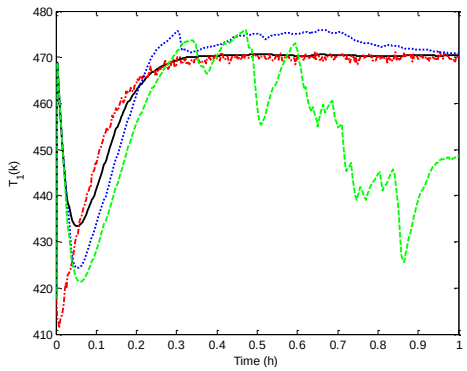

Fig. 1. The trajectories of state of the closed-loop system obtained via the suggested approach (solid lines) and resilient event-triggered output feedback control [32] (dashed-dotted lines), AETC approach presented in [21] (dotted lines), and AETC approach presented in [23] (dashed lines).

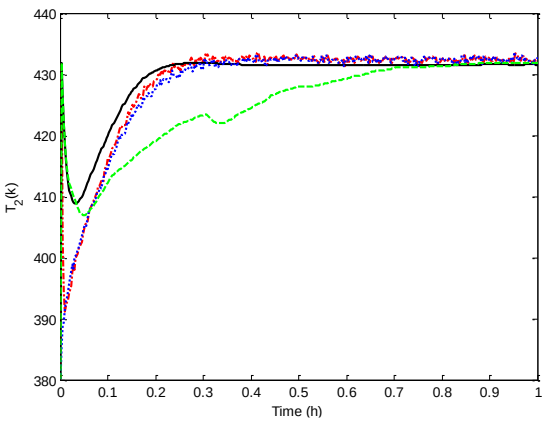

Fig. 2. The trajectories of state of the closed-loop system obtained via the suggested approach (solid lines) and resilient event-triggered output feedback control [32] (dashed-dotted lines), AETC approach presented in [21] (dotted lines), and AETC approach presented in [23] (dashed lines).

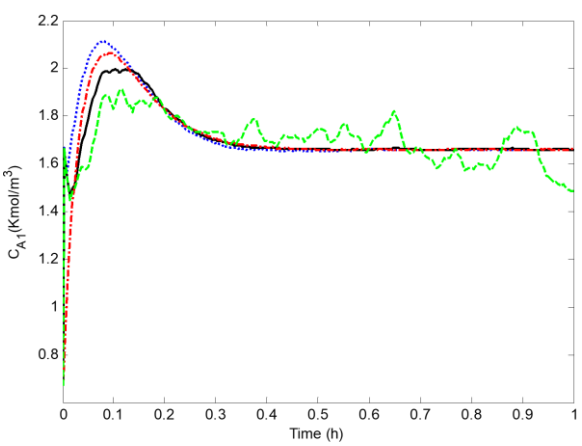

Fig. 3. The trajectories of state of the closed-loop system obtained via the suggested approach (solid lines) and resilient event-triggered output feedback control [32] (dashed-dotted lines), AETC approach presented in [21] (dotted lines), and AETC approach presented in [23] (dashed lines).

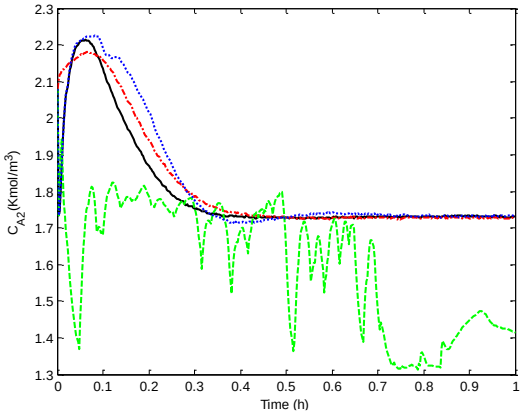

Fig. 4. The trajectories of state of the closed-loop system obtained via the suggested approach (solid lines) and resilient event-triggered output feedback control [32] (dashed-dotted lines), AETC approach presented in [21] (dotted lines), and AETC approach presented in [23] (dashed lines).

To show the efficiency of the proposed consensus control method for microgrids, this section uses an MG system model presented in [33] to control current sharing and voltage regulation. Fig. 9 shows that the DGU i has a complete hierarchical control in communication with its neighbors. All information about system modeling is mentioned in [33] in detail. It should be noted that the proposed event-triggered consensus control method that can also consider time delay is replaced with the one presented in [33]. Fig. 10 shows the graphs belonging to the studied MG including 5 DGUs, and as shown in the very figure, the physical and communication graphs are directional and non-directional, respectively. Scaling factors for DGUs are defined as $I_1^s = 1, I_2^s = 4, I_3^s = 2, I_4^s = 4, I_5^s = 1$.

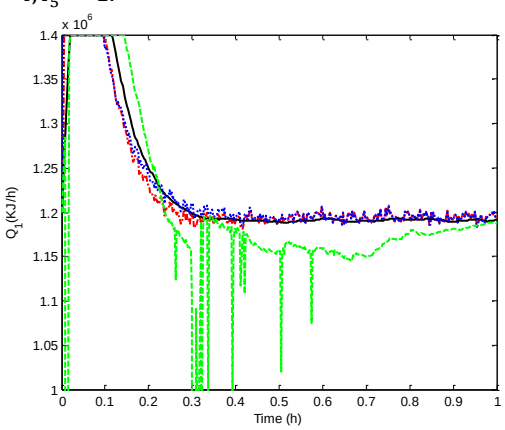

Fig. 5. The trajectories of input of the closed-loop system obtained via the suggested approach (solid lines) and resilient event-triggered output feedback control [32] (dashed-dotted lines), AETC approach presented in [21] (dotted lines), and AETC approach presented in [23] (dashed lines).

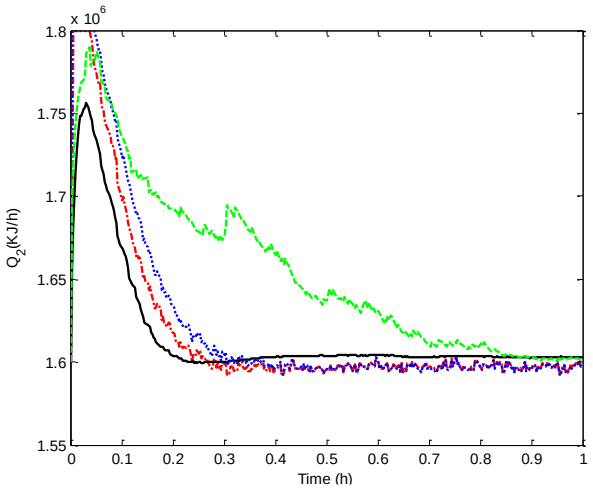

Fig. 6. The trajectories of input of the closed-loop system obtained via the suggested approach (solid lines) and resilient event-triggered output feedback control [32] (dashed-dotted lines), AETC approach presented in [21] (dotted lines), and AETC approach presented in [23] (dashed lines).

The reference voltage among the DGUs is set to $\bar{V}_{ref} = [40{,}50{,}48{,}42{,}46]^T$. The piece-wise constant load currents of DGUs numbered from 1 to 5 are considered as shown in Fig. 11. The electrical parameters belonging to DGs and primary control gains are given in [34] while sampling periods and secondary voltage control gains are stated in [33]. Fig. 12 depicts the voltage regulation for PCCs and current sharing calculated using the proposed event-triggered consensus control method. According to the results, It can be seen that the data transfer rate of DGs is higher in the proposed method than in the one introduced in [33].

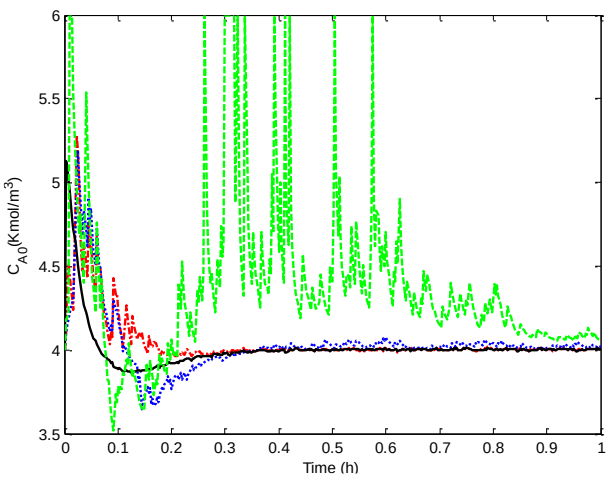

Fig. 7. The trajectories of input of the closed-loop system obtained via the suggested approach (solid lines) and resilient event-triggered output feedback control [32] (dashed-dotted lines), AETC approach presented in [21] (dotted lines), and AETC approach presented in [23] (dashed lines).

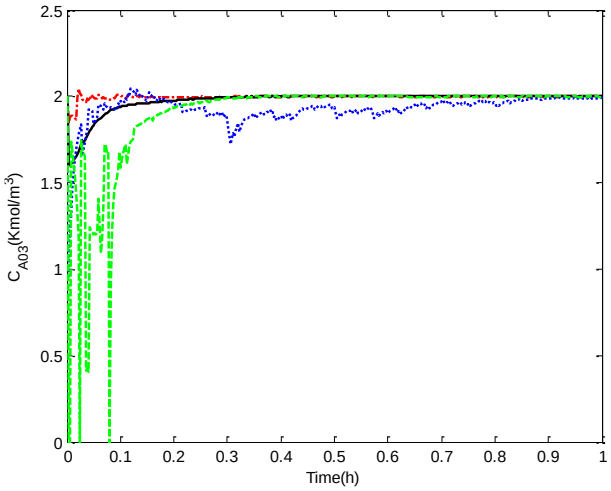

Fig. 8. The trajectories of input of the closed-loop system obtained via the suggested approach (solid lines) and resilient event-triggered output feedback control [32] (dashed-dotted lines), AETC approach presented in [21] (dotted lines), and AETC approach presented in [23] (dashed lines).

V. Conclusions

In this paper, the consensus problem of network-based heterogeneous multi-agent systems is evaluated by proposing an AETC algorithm. So, by considering the state information of agent i and other agents, an efficient AETC strategy is proposed to save the communication energy and reduce the frequency of data transmission, which are the main advantages of the proposed AETC approach. Moreover, the event-triggered time interval is considered a special delay and compensated by the predictive method. The optimal control is, furthermore, employed to design the PD-like predictive coordination controller. The condition for ensuring stability and consensus has been given. Finally, the developed method is applied successfully for the control of a network-based interconnected system with considering time delay.

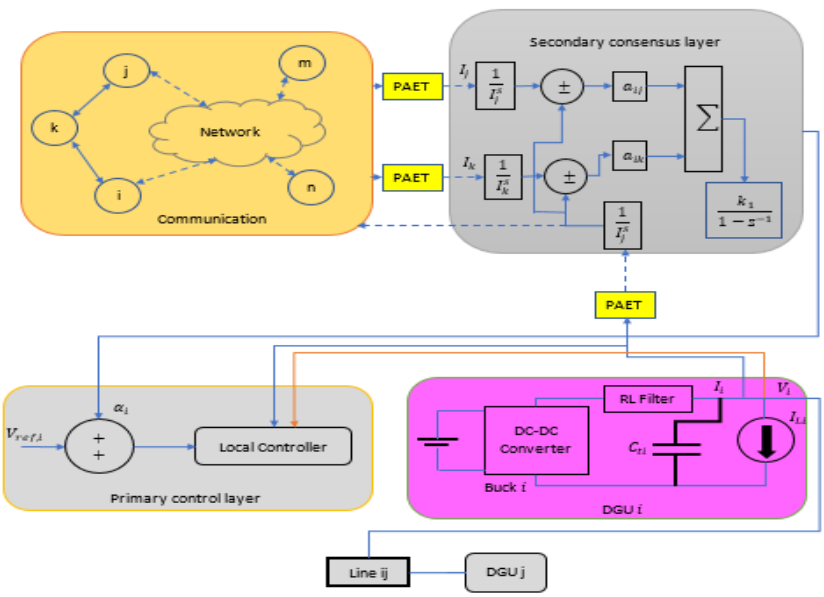

Fig. 9. The i_{th} DGU having complete hierarchical control in communication with its neighbors.

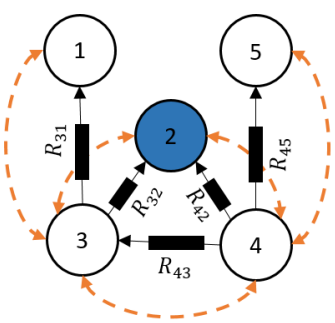

Fig. 10. Physical and communication graphs of a DC microgrid composed of 5 DGUs.

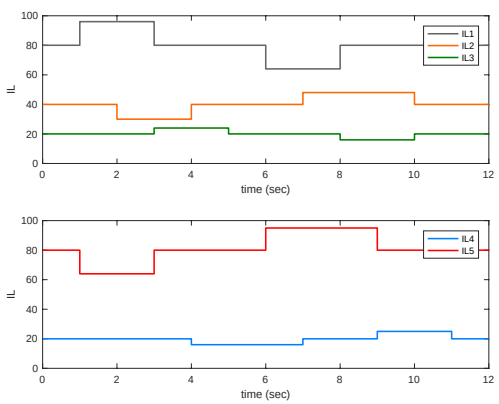

Fig. 11. The local load currents of the DGUs 1-5.

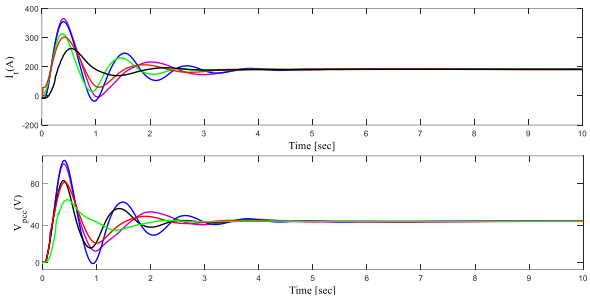

Fig. 12. The voltage regulation, current sharing, and average PCCs voltage of DGUs.

REFERENCES

[1] M. Vosoogh, M. Rashidinejad, A. Abdollahi, and M. Ghaseminezhad, "Efficient Networked Microgrid Management Considering Plug-in Electric Vehicles and Storage Units," *International Journal of Industrial Electronics Control and Optimization*, Vol. 4, No. 2, pp. 245-255, 2021.

[2] M. Ahmadi Kamarposhti, "Optimal Control of Islanded Micro grid Using Particle Swarm Optimization Algorithm," *International Journal of Industrial Electronics Control and Optimization*, Vol. 1, No. 1, pp. 53-60, 2018.

[3] Y. Jafarian, A. Karimi, and H. Bevrani, "Secondary Voltage Control in a Hybrid Microgrid," *International Journal of Industrial Electronics Control and Optimization*, Vol. 2, No. 3, pp. 221-232, 2019.

[4] E. Planas, J. Andreu, J. I. Gárate, I. Martínez de Alegría, and E. Ibarra, "AC and DC technology in microgrids: A review," *Renewable and Sustainable Energy Reviews*, Vol. 43, No. C, pp. 726-749, 2015.

[5] E. Unamuno and J. Barrena, "Hybrid ac/dc microgrids Part I: Review and classification of topologies," *Renewable & Sustainable Energy Reviews*, Vol. 52, pp. 1251-1259, 2015.

[6] D. Hammerstrom, "AC Versus DC Distribution SystemsDid We Get it Right?," *2007 IEEE Power Engineering Society General Meeting*, pp. 1-5, 2007.

[7] E. Unamuno and J. Barrena, "Hybrid ac/dc microgrids Part II: Review and classification of control strategies," *Renewable & Sustainable Energy Reviews*, Vol. 52, pp. 1123-1134, 2015.

[8] S. Trip, M. Cucuzzella, X. Cheng, and J. Scherpen, "Distributed Averaging Control for Voltage Regulation and Current Sharing in DC Microgrids," *IEEE Control Systems Letters*, Vol. 3, No. 1, pp. 174-179, 2019.

[9] J. M. Guerrero, J. C. Vasquez, J. Matas, L. G. d. Vicuna, and M. Castilla, "Hierarchical Control of Droop-Controlled AC and DC Microgrids—A General Approach Toward Standardization," *IEEE Transactions on Industrial Electronics*, Vol. 58, No. 1, pp. 158-172, 2011.

[10] L. Meng, T. Dragicevic, J. Roldán-Pérez, J. C. Vasquez, and J. M. Guerrero, "Modeling and Sensitivity Study of Consensus Algorithm-Based Distributed Hierarchical Control for DC Microgrids," *IEEE Transactions on Smart Grid*, Vol. 7, No. 3, pp. 1504-1515, 2016.

[11] J. Zhao and F. Dörfler, "Distributed control and optimization in DC microgrids," *Automatica*, Vol. 61, No. C, pp. 18–26, 2015.

[12] C. De Persis, E. R. A. Weitenberg, and F. Dörfler, "A power consensus algorithm for DC microgrids," *Automatica*, Vol. 89, pp. 364-375, 2018.

[13] P. Prabhakaran, Y. Goyal, and V. Agarwal, "Novel Nonlinear Droop Control Techniques to Overcome the Load Sharing and Voltage Regulation Issues in DC Microgrid," *IEEE Transactions on Power Electronics*, Vol. 33, No. 5, pp. 4477-4487, 2018.

[14] M. Cucuzzella, S. Trip, C. D. Persis, X. Cheng, A. Ferrara, and A. v. d. Schaft, "A Robust Consensus Algorithm for Current Sharing and Voltage Regulation in DC Microgrids," *IEEE Transactions on Control Systems Technology*, Vol. 27, No. 4, pp. 1583-1595, 2019.

[15] Y. Batmani, M. Davoodi, and N. Meskin, "Event-Triggered Suboptimal Tracking Controller Design for a Class of Nonlinear Discrete-Time Systems," *IEEE Transactions on Industrial Electronics*, Vol. 64, pp. 8079-8087, 2017.

[16] Z. Wu, Y. Xu, R. Lu, Y. Wu, and T. Huang, "Event-Triggered Control for Consensus of Multiagent Systems With Fixed/Switching Topologies," *IEEE Transactions on Systems, Man, and Cybernetics: Systems*, Vol. 48, No. 10, pp. 1736-1746, 2018.

[17] M. Davoodi, N. Meskin, and K. Khorasani, "Event-Triggered Multiobjective Control and Fault Diagnosis: A Unified Framework," *IEEE Transactions on Industrial Informatics*, Vol. 13, pp. 298-311, 2017.

[18] C. Peng, J. Zhang, and H. Yan, "Adaptive Event-Triggering ${H}_{¥infty }$ Load Frequency Control for Network-Based Power Systems," *IEEE Transactions on Industrial Electronics*, Vol. 65, pp. 1685-1694, 2018.

[19] T. Shi, T. Tang, and J. Bai, "Distributed event-triggered control co-design for large-scale systems via static output feedback," *J. Frankl. Inst.*, Vol. 356, pp. 10393-10404, 2019.

[20] R. Han, L. Meng, J. M. Guerrero, and J. C. Vasquez, "Distributed Nonlinear Control With Event-Triggered Communication to Achieve Current-Sharing and Voltage Regulation in DC Microgrids," *IEEE Transactions on Power Electronics*, Vol. 33, No. 7, pp. 6416-6433, 2018.

[21] S. Yuan, C. Yu, and J. Sun, "Adaptive event-triggered consensus control of linear multi-agent systems with cyber attacks," *Neurocomputing*, Vol. 442, pp. 1-9, 2021.

[22] H. Wang, B. Xue, and A. Xue, "Leader-following consensus control for semi-Markov jump multi-agent systems: An adaptive event-triggered scheme," *Journal of the Franklin Institute*, Vol. 358, No. 1, pp. 428-447, 2021.

[23] Y. Cui, M. Fei, and D. Du, "Event-triggered cooperative compensation control for consensus of heterogeneous multi-agent systems," *Iet Control Theory and Applications*, Vol. 10, pp. 1573-1582, 2016.

[24] X. Ge and Q. Han, "Distributed Formation Control of Networked Multi-Agent Systems Using a Dynamic Event-Triggered Communication Mechanism," *IEEE Transactions on Industrial Electronics*, Vol. 64, No. 10, pp. 8118-8127, 2017.

[25] X. Yin, D. Yue, S. Hu, and H. Zhang, "Distributed adaptive model-based event-triggered predictive control for consensus of multiagent systems," *International Journal of Robust and Nonlinear Control*, Vol. 28, No. 18, pp. 6180-6201, 2018.

[26] W. Zou and Z. Xiang, "Event-triggered distributed containment control of heterogeneous linear multi-agent systems by an output regulation approach," *International Journal of Systems Science*, Vol. 48, No. 10, pp. 2041-2054, 2017.

[27] R. Yang, H. Zhang, G. Feng, H. Yan, and Z. Wang, "Robust cooperative output regulation of multi-agent systems via

adaptive event-triggered control," *Automatica*, Vol. 102, pp. 129-136, 2019.
[28] h. chahkandi nejad, M. Farshad, and R. Havangi, "Designing Indirect Adaptive Multiple Controller for LTI Systems with Large Time Varying and Unknown Delay in Control Input Based on Online Estimation of Delay by Kalman filtering," *International Journal of Industrial Electronics Control and Optimization*, Vol. 4, No. 1, pp. 1-11, 2021.
[29] S. Rahmati and H. Eliasi, "Robust Decentralized Model Predictive Control for a Class of Interconnected systems," *International Journal of Industrial Electronics Control and Optimization*, Vol. 3, No. 3, pp. 327-336, 2020.
[30] E.-K. Boukas, *Stochastic Switching Systems*, 1 st ed., Birkhäuser Basel, 2006.
[31] Y. Sun and N. H. El-Farra, "Quasi-decentralized model-based networked control of process systems," *Computers & Chemical Engineering*, Vol. 32, No. 9, pp. 2016-2029, 2008.
[32] A. Sinha and R. K. Mishra, "Control of a nonlinear continuous stirred tank reactor via event triggered sliding modes," *Chemical Engineering Science*, Vol. 187, pp. 52-59, 2018.
[33] M. Mola, N. Meskin, K. Khorasani, and A. Massoud, "Distributed Event-Triggered Consensus-Based Control of DC Microgrids in Presence of DoS Cyber Attacks," *IEEE Access*, Vol. 9, pp. 54009-54021, 2021.
[34] M. Tucci, L. Meng, J. M. Guerrero, and G. Ferrari-Trecate, "Plug-and-play control and consensus algorithms for current sharing in DC microgrids," *IFAC-PapersOnLine*, Vol. 50, No. 1, pp. 12440-12445, 2017.

Razieh Heidari received her B.S.c in Electronic engineering from Islamic Azad University of Zahedan Branch, Zahedan, Iran, in 2007, M.Sc. degree in Electrical-power engineering from Sistan **&** Balochestan University, Zahedan, Iran, in 2014. She is now studying in PhD degree in power system engineering at Islamic Azad University of Kerman Branch, Kerman, Iran. She has been working as laboratory expert in the faculty of power engineering, in Islamic Azad University of Zahedan Branch, Zahedan, Iran since 2009. Her research interests are power electronic, distributed control of power systems, renewable energy resource integration, and application of optimization in power systems.

Alimorad Khajehzadeh received his B.Sc. in Electronic Engineering from Sistan & Balochestan University, Zahedan, Iran, in 1994, M.Sc. in Electrical Engineering from Tabriz University, Tabriz, Iran, in 1996, and Ph.D. from University of Technology Malaysia (UTM) in 2011, in Electrical Engineering. Since 2012, he has been an Assistant Professor at Department of Electrical Engineering, Science and Research Branch, Islamic Azad University, Kerman, Iran. His research interests include power electronic, optimization technique in power system, and artificial intelligence.

Mahdiyeh Eslami received her B.Sc. from Shahid Bahonar University of Kerman, Iran, in 2000, M.Sc. from Iran University of Science and Technology (IUST), Tehran, Iran, in 2004, and Ph.D. from National University of Malaysia (UKM) in 2012, all in Electrical Engineering. From 2012 to 2013, she was a Postdoctoral Research Fellow with the Power Research Group at National University of Malaysia. She has authored and co-authored more than 70 journal and conference articles. Since 2012, she has been an Assistant Professor at Department of Electrical Engineering, Science and Research Branch, Islamic Azad University, Kerman, Iran. She is a Member of IEEE, and Power System Society (PES). Her research interests include optimization technique in power system stability and FACTS devices.

International Journal of Industrial Electronics, Control and Optimization © 2021 IECO
Vol.4, No. 4, pp. 397-407, Sep (2021)

Green Micro-Grid Operation Constrained to Reliability and Flexibility Indices in the Presence of Distributed Generations and Energy Storage Systems

Seyed Arman Shirmardi[1], Mahmood Joorabian[2,†], and Hassan Barati[3]

[1,3] Department of Electrical and Computer Engineering, Dezful Branch, Islamic Azad University, Dezful, Iran
[2] Department of Electrical and Computer Engineering, Faculty of Engineering, Shahid Chamran University of Ahvaz, Ahvaz, Iran

ABSTRACT

This paper presents microgrid (MG) operation constrained to the reliability, flexibility, and environment indices in the presence of distributed generations (DGs) and energy storage systems (ESSs). The proposed scheme minimizes the total expected operating cost of MGs and DGs. It is also subject to alternating current (AC) power flow equations of MGs, constraints of operation, reliability, and flexibility of MGs, and operation model of power sources and storage devices. Stochastic programming is incorporated to model uncertainties of load, energy price, the active power of renewable energy generation, availability of MG equipment, sources, and storage devices. Following on, a hybrid solver formed by combining an artificial bee colony (ABC) and a sine-cosine algorithm (SCA) is adopted to achieve the optimal solution with approximate conditions of the unique ultimate response. Eventually, the suggested scheme is implemented on a 69-bus radial MG, where the numerical results confirm the capability of the scheme in improving the operation, reliability, flexibility, and environment status of the MG.

Article Info

Keywords:
Clean microgrid operation, Flexibility index, Hybrid evolutionary algorithm, Reliability index, Stochastic programming.

History:
Received 2021-02-16
Accepted 2021-07-30

Nomenclature

Indices and sets

h, n, s	Indices of operation hour, bus, scenario
l	Auxiliary index denoting a bus
ref	Slack bus
Ω_H, Ω_B, Ω_S	The set of operation hour, the set of MG buses, and the set of scenarios
Ω_R	The set of buses including renewable DGs

Variables

C	The sum of the expected operating cost of the MG and DGs ($)
$EENS$	Expected energy not-supplied in per-unit (p.u.)
P^{DG}, Q^{DG}	Active and reactive power of the DG (p.u.)
P^{DL}, Q^{DL}	Active and reactive power flowing through the distribution line (p.u.)
P^{DS}, Q^{DS}	Active and reactive power flowing through the distribution substation (p.u.)
$P^{E,D}$,$P^{E,C}$, Q^{E}	Discharge and charge active power of the ESS and reactive power of the ESS (p.u.)
P^{NS}	Load not-supplied (p.u.)
V, β	Voltage magnitude (p.u.) and angle (rad)
y	A binary variable denoting the operation status of the ESS in the charge and discharge mode

†Corresponding Author: mjoorabian@scu.ac.ir
Tel: +98-9161183017, Department of Electrical Engineering, Faculty of Engineering, Shahid Chamran University of Ahvaz, Ahvaz, Iran

Constants

a^{DL}, a^{DS}, a^{DG}, a^{E}	Availability of the distribution line, distribution substation, DG, and ESS
CR, DR	Charge and discharge rate of the ESS (p.u.)
$EENS^{max}$	Maximum value of expected energy not-supplied (p.u.)
EM^{max}	Maximum environmental pollution (kg)
E^{min}, E^{max}	Minimum and maximum storable energy in the ESS (p.u.)
G^{DL}, B^{DL}	Conductance and susceptance of the distribution line (p.u.)
IM	Incidence matrix of buses and the distribution line
PF^{min}	Minimum power factor
$P^{DG,m}$	Maximum active power generation by the renewable DG (p.u.)
P^{L}, Q^{L}	Active and reactive power of consumers (p.u.)
$S^{DG,m}$	Maximum capacity (size) of the DG (p.u.)
$S^{DL,m}$	Capacity of the distribution line (p.u.)
$S^{DS,m}$	Capacity of the distribution substation (p.u.)
$S^{E,m}$	Capacity of the ESS charger (p.u.)
V^{min}, V^{max}	Minimum and maximum permissible values of voltage magnitude (p.u.)
V_{ref}	The voltage of the slack bus
γ^{DS}, γ^{DG}	Coefficient of the total pollution of NO_x, CO_2, and SO_2 for supplying energy from the upstream network and DGs (kg/MWh)
η^{C}, η^{D}	Charge and discharge efficiency of the ESS
κ, χ, υ	Coefficients of the fuel cost function of the non-renewable DG respectively in \$, \$/MWh, and \$/MWh^2
π	The probability of occurrence of the scenario
ρ	Energy price (\$/MWh)
ΔF	Flexibility tolerance (p.u.)

I. Introduction

To reduce the environmental pollution caused by fossil fuel consumption, the utilization of distributed generations (DGs) at the consumption site has gained attention [1]. Renewable DGs produce negligible pollution and impose low operating costs. Thus, their application at consumption sites, such as distribution networks and microgrids (MGs), has been considered [2]. However, since the active power of these sources is uncontrollable and their active power generation relies on climatic conditions, it is expected that the results of day-ahead and real-time operations of a network in the presence of these sources differ due to the weather forecast error [3]. Therefore, the balance of generation and consumption in the network is possibly not established in exchange for real-time operation, which is considered as low flexibility status of the network [3, 4]. To address this issue, it is recommended to use non-renewable DGs and energy storage systems (ESSs) that are controllable along with renewable DGs [4]. Pollution coefficients of these sources and ESSs are smaller than the power supply from the upstream network [1]. Also, DGs and ESSs are generally distributed at different points across the network, so operating (reliability) indices such as voltage profiles (expected energy not supplied) are expected to be more favorable than those of power flow studies (power supply only via the upstream network) [3, 4]. Finally, to achieve the mentioned goals, it is necessary to implement an appropriate management system in the network. Therefore, it is predicted that the status of several network technical indices is improved by establishing a power management system (PMS) in a network, such as MG, and by optimal operation management of DGs and ESSs [5].

Various researches have been carried out in the field of operation of distribution networks and MGs. In [6], the effect of active and reactive power management of electric vehicles (EVs) in the parking lot on operation indices of distribution networks, such as energy loss and voltage profile, is investigated. It is formulated in a nonlinear optimization problem form and the linear approximation model (LAM) is used to achieve the optimal solution. Next, based on the results obtained in [6], a significant computational error is obtained for the design variables per linearization of the problem so that it is about 3% for active and reactive power. Also, due to the simultaneous management of active and reactive power of EVs in the network, a large number of EVs can be supplied by a distribution network in addition to minimizing energy loss and obtaining a smooth voltage profile. To improve the operation indices of the distribution network in the presence of a large number of photovoltaics (PVs), planning (sitting and sizing) of batteries in the distribution network is presented in [7]. The results indicate the ability of battery energy management in enhancing the status of distribution network operation indices. Note that batteries in [7] have been used as a source of flexibility improvement for a distribution network with PVs, but a mathematical model for evaluation of the flexibility level and status is not presented. This issue is also present in [8], where the authors incorporate demand response (DR) and battery as a source of flexibility in a wind system, while it does not provide a numerical index for flexibility. In [9], the simultaneous operation of several MGs is formulated by minimizing their operating cost as an objective function and the optimal power flow (OPF) equations as constraints of the problem. Similar to [7], robust optimization is incorporated in [9] to model uncertainties of load and renewable power. In [10], MG energy management is studied in two islanded and grid-connected modes to minimize energy costs and environmental pollution in the presence of responsive loads. In [11], the OPF model of several MGs connected to the grid is constrained by the voltage stability in the presence of DGs and DR. Based on the results presented in [11], simultaneous energy management of sources and responsive loads in the MG can create a safe margin for the bus voltages. Ref. [12] introduces the optimal

operation model of MGs in the presence of sources, ESSs, and DR, which incorporates grey wolf optimization (GWO) to achieve the optimal solution. In [13], a non-hybrid evolutionary algorithm (NHEA), named Porcellio Scaber algorithm (PSA), is employed to achieve the optimal solution of the MG energy management problem. Energy management of a multi-carrier MG connected to a network is described in [14]. This MG has electrical and thermal networks, so it is OPF with electrical and thermal power flow. Optimal operation of the distribution network with DGs and thermal blocks including boilers and combined heat and power (CHP) system is discussed in [15]. This design is in the form of multi-objective optimization and minimizes environmental pollution, energy loss, and the function of voltage deviations subject to OPF equations, the operation model of DGs, and the mentioned thermal block. It then uses the firefly algorithm to find the optimal solution. In [15], non-renewable DGs are exploited as a source of flexibility of a network with renewable sources, but similar to [7, 8], the mathematical model of flexibility is not presented. Finally, a summary of the recent research works is listed in Table I.

TABLE I
TAXONOMY OF RECENT RESEARCH WORKS

Ref.	Indices					Mathematical model of flexibility	Solver
	Economic	Operation	Reliability	Pollution	Flexibility		
[6-7]	Yes	Yes	No	No	No	No	LAM
[8]	Yes	Yes	No	No	No	No	MA
[9]	Yes	Yes	No	No	No	No	MA
[10]	No	Yes	No	Yes	No	No	MA
[11]	No	Yes	No	No	No	No	MA
[12-14]	No	Yes	No	No	No	No	NHEA
[15]	No	Yes	No	Yes	No	No	NHEA
Proposed scheme	**Yes**	**Yes**	**Yes**	**Yes**	**Yes**	**Yes**	**HEA**

MA: Mathematical approach, HEA: Hybrid evolutionary algorithm

Based on the literature presented and Table I, the following main research gaps related to the MG operation problem can be mentioned:

- In most researches, one or two indices, such as operational and economic indices, are generally considered in the problem of energy/power management of distribution networks and MGs. Nonetheless, this does not guarantee that other indices will be improved. For instance, to minimize the cost of power purchase from the upstream network imposed on the MG, high amounts of energy injected by DGs and ESSs are required, although it causes overvoltage in the network.
- Most research also mentions the use of flexibility sources such as ESS along with renewable DGs to enhance system flexibility, but a numerical index for it is rarely available in the literature. Yet, its magnitude is required to evaluate the status of an index in a system, and this is obtained by mathematical modeling of the problem.
- The MG energy management problem has generally a nonlinear framework for which some studies such as [1-3] adopt the LAM. This case leads to a significant computational error. Some other researches utilize NHEAs or suitable mathematical solutions for nonlinear problems. Nevertheless, such solvers do not provide a unique optimal solution.

To compensate for these research gaps, this paper presents MG's operation subject to reliability and flexibility indices in the presence of DGs and ESSs to provide clean energy. The scheme is based on an optimization problem whose objective function aims to minimize the total expected cost of power purchase by the MG from the upstream network and the expected cost of DGs. Constraints include AC power flow (AC-PF) equations; operation, reliability, flexibility, and environmental constraints of the MG; and formulation of DGs and ESSs operation. This scheme is subject to uncertainties of load, active power generation of renewable DGs, energy cost, and availability of network equipment, DGs, and ESSs. Therefore, the paper incorporates stochastic programming based on a combination of Monte Carlo simulation (MCS) and simultaneous backward method (SBM) to model the mentioned uncertainties. Then, a combination of an artificial bee colony (ABC) and a sine-cosine algorithm (SCA) is used to explore the optimal solution. Since decision variables are updated in two different processes by the algorithm, it is expected to reach approximate conditions of the unique final response. Eventually, the contributions of the proposed scheme are summarized as follows:

- Achieving a mathematical model for evaluating MG's flexibility;
- Simultaneous modeling of operation, reliability, economics, flexibility, and environmental indices of the MG; and
- Achieving the optimal solution with approximate conditions of the unique response by the hybrid ABC-SCA algorithm.

In the following, Section 2 presents the mathematical model of MG power management. Section 3 describes the problem-solving process based on the hybrid ABC-SCA algorithm. Numerical results and conclusions are expressed in Sections 4 and 5, respectively.

II. PROBLEM FORMULATION

In this section, the mathematical operation model of the MG subject to technical and environmental constraints is presented in the presence of DGs and ESSs. This scheme minimizes the total expected operating cost of MGs and DGs. It is also bound by AC-PF equations, operation, reliability, flexibility, and environmental constraints of the MG, and operation models of

DGs and ESSs. Details of this problem are provided below.

A) Objective function: Equation (1) indicates the objective function of the proposed problem, which has two parts. The first part represents the minimization of the expected cost of energy purchase by the MG from the upstream network [16], which is equal to the product of energy price and power received by the MG from the upstream network at any given time. In the second part of Eq. (1), the minimization of the expected cost of fuel or operation of DGs is considered, which follows the parabolic fuel cost-power curve of a DG [16].

$$\min \quad C = \sum_{s\in\Omega_S}\pi_s\sum_{h\in\Omega_H}\left(\begin{array}{l}\rho_{h,s}P^{DS}_{ref,h,s}+\\ \sum_{b\in\Omega_B}\left(\kappa_b+\chi_b P^{DG}_{b,h,s}+\upsilon_b\left(P^{DG}_{b,h,s}\right)^2\right)\end{array}\right) \tag{1}$$

B) *MG model*: The MG model is based on the AC-PF equations as given in (2)-(7) [1-2]. The active and reactive power balance in different MG buses is presented in (2) and (3). Also, active power and reactive power flowing through distribution lines are calculated by (4) and (5), respectively. Finally, (6) and (7) refer to voltage angle and magnitude of the slack bus, respectively. Note that, in this case, the MG is assumed to be connected to the upstream network via a distribution substation located on the slack bus. Therefore, variables P^{DS} and Q^{DS} are not zero only for the slack bus and are zero for other buses.

$$P^{DS}_{b,h,s}+P^{DG}_{b,h,s}+\left(P^{E,D}_{b,h,s}-P^{E,C}_{b,h,s}\right)+\sum_{l\in\Omega_B}IM_{b,l}P^{DL}_{b,l,h,s}=P^{L}_{b,h,s}-P^{NS}_{b,h,s}\qquad\forall b,h,s \tag{2}$$

$$Q^{DS}_{b,h,s}+Q^{DG}_{b,h,s}+Q^{E}_{b,h,s}+\sum_{l\in\Omega_B}IM_{b,l}Q^{DL}_{b,l,h,s}=Q^{L}_{b,h,s}\qquad\forall b,h,s \tag{3}$$

$$P^{DL}_{b,l,h,s}=\left\{\begin{array}{l}G^{DL}_{b,l}\left(V_{b,h,s}\right)^2-V_{b,h,s}V_{l,h,s}\\ \left(\begin{array}{l}G^{DL}_{b,l}\cos\left(\beta_{b,h,s}-\beta_{l,h,s}\right)+\\ B^{DL}_{b,l}\sin\left(\beta_{b,h,s}-\beta_{l,h,s}\right)\end{array}\right)\end{array}\right\}a^{DL}_{b,l,s}\qquad\forall b,l,h,s \tag{4}$$

$$Q^{DL}_{b,l,h,s}=\left\{\begin{array}{l}-B^{DL}_{b,l}\left(V_{b,h,s}\right)^2+\\ V_{b,h,s}V_{l,h,s}\left(\begin{array}{l}B^{DL}_{b,l}\cos\left(\beta_{b,h,s}-\beta_{l,h,s}\right)\\ -G^{DL}_{b,l}\sin\left(\beta_{b,h,s}-\beta_{l,h,s}\right)\end{array}\right)\end{array}\right\}a^{DL}_{b,l,s}\qquad\forall b,l,h,s \tag{5}$$

$$\beta_{ref,h,s}=0\qquad\forall h,s \tag{6}$$

$$V_{ref,h,s}=V_{ref}\qquad\forall h,s \tag{7}$$

C) *Technical and environmental constraints of the MG*: This part presents technical constraints of the network including operation (8)-(11) [5-7], flexibility (12), and reliability (13)-(14) constraints [17]. Operation constraint consists of limits of distribution lines and distribution substations (8) and (9), distribution substation power factor (10), and voltage magnitudes of buses (11). The MG flexibility limit is expressed in (12). Note that, according to [3], the results of day-ahead and real-time operation of a system with renewable sources differ due to their power generation forecast error. This will cause an imbalance of generation and consumption in that system under real-time operating conditions, which is take into account as the system's poor flexibility. To overcome this challenge and improve system's flexibility, small time-constant flexibility sources such as battery-type ESSs are used [4]. However, to ensure the desired optimal flexibility of the network, this index needs to be modeled in the proposed scheme. The limitation of changes in the active power received by MG from the upstream network for different scenarios is considered as (12) in this paper. The reason is that the unbalance between day-ahead and real-time operations will be minimal if the changes in active power are very low for different scenarios [3]. Hence, if the flexibility tolerance (ΔF) is zero, flexibility of 100% is accessible for the MG. Besides, reliability limitations of the MG are listed in (13) and (14). The constraint on the interrupted load due to the occurrence of an N − 1 event caused by the outage of a distribution line, distribution substation, DG, or ESS is presented in (13) [17]. Moreover, the expected energy not-supplied (EENS) of the MG is formulated in (14) for all of the above possible events [17]. In the end, the environmental constraint of the MG is modeled in (15), which has two parts. The first part refers to total NO_x, CO_2, and SO_2 emissions caused by the upstream power supply. Furthermore, the pollutants produced by DGs are calculated in the second part of this equation, where coefficient γ is the sum of NO_x, CO_2, and SO_2 pollution coefficients [18]. Noted that the proposed scheme has no limitation on being implemented on different networks such as an active distribution network or a MG. Another point is that parameter a^{DS} (Eq. (9)) in the proposed scheme refers to the accessibility of the MG connection to the upstream network. If it is 1, it means that the grid-connected mode is considered for the MG, and it is 0, it is operating in the islanded mode. This means the paper assumes that the MG is disconnected from the upstream network during critical conditions such as the occurrence of an N – 1 event. The reason is that an MG requires a strong backup source so that it could provide desired stable situation against the changes in the generation of renewable DGs and consumption load and this is accessible through connection to the upstream network. Also, assuming that the MG participates in the energy and ancillary services market, the grid-connected operation mode is needed. Thus, this operation mode is essential for MGs and this paper mainly focuses on this type of operation mode for MGs.

$$\sqrt{\left(P_{b,l,h,s}^{DL}\right)^2+\left(Q_{b,l,h,s}^{DL}\right)^2}\le S_{b,l}^{DL,m}\qquad \forall b,l \tag{8}$$

$$\sqrt{\left(P_{ref,h,s}^{DS}\right)^2+\left(Q_{ref,h,s}^{DS}\right)^2}\le S_{ref}^{DS,m}a_{ref,s}^{DS}\qquad \forall h,s \tag{9}$$

$$\frac{\left|P_{ref,h,s}^{DS}\right|}{\sqrt{\left(P_{ref,h,s}^{DS}\right)^2+\left(Q_{ref,h,s}^{DS}\right)^2}}\ge PF^{\min}\qquad \forall h,s \tag{10}$$

$$V_b^{\min}\le V_{b,h,s}\le V_b^{\max}\qquad \forall b,h,s \tag{11}$$

$$\left|P_{ref,h,s}^{DS}-P_{ref,h,s'}^{DS}\right|\le \Delta F\qquad \forall h,s\ne s' \tag{12}$$

$$0\le P_{b,h,s}^{ND}\le P_{b,h,s}^{L}\qquad \forall b,h,s \tag{13}$$

$$\overbrace{\sum_{s\in\Xi_S}\pi_s\sum_{h\in\Omega_H}\sum_{b\in\Omega_B}P_{b,h,s}^{NS}}^{EENS}\le EENS^{\max} \tag{14}$$

$$\sum_{s\in\Omega_S}\pi_s\sum_{h\in\Omega_H}\left(\gamma_{ref}\left|P_{ref,h,s}^{DS}\right|+\sum_{b\in\Omega_B}\gamma_b P_{b,h,s}^{DG}\right)\le EM^{\max} \tag{15}$$

D) *DG operation model*: In this part of the paper, the DG capacity constraint or the limit of simultaneous control of active and reactive power of DG is given by (16) [5]. Note that two renewable and non-renewable types of DGs are considered in this paper. In renewable DGs such as wind and PV systems, active power is always equal to the maximum active power generated by these sources in proportion to weather conditions [5]. This is modeled in (17). The active power of these sources is not generally considered to be controllable for minimizing energy cost and pollution, but its reactive power control capability has been used in this study [5]. Hence, these DGs follow two constraints (16) and (17). However, non-renewable DGs can control active and reactive power, so they only comply with constraint (16).

$$\sqrt{\left(P_{b,h,s}^{DG}\right)^2+\left(Q_{b,h,s}^{DG}\right)^2}\le S_b^{DG,m}a_{b,s}^{DG}\qquad \forall b,h,s \tag{16}$$

$$P_{b,h,s}^{DG}=P_{b,h,s}^{DG,m}a_{b,s}^{DG}\qquad \forall b\in\Omega_R,h,s \tag{17}$$

E) *ESS operation model*: The ESS operation model is formulated in (18)-(21) [2, 7]. Constraints (18) and (19) consider the ESS discharge and charge rate limits, respectively. Also, in these constraints, a binary variable y is used to observe the asynchronous operation of the ESS charge and discharge modes. Hence, if y is equal to unity (zero), the ESS is in the discharge (charge) mode and injects (receives) active power into (from) the MG. The limit of energy stored in the ESS is given by (20). Finally, the limit of size of the ESS charger in simultaneous control of active and reactive power is presented in (21).

$$0\le P_{b,h,s}^{E,D}\le DR_b y_{b,h}a_{b,s}^{E}\qquad \forall b,h,s \tag{18}$$

$$0\le P_{b,h,s}^{E,C}\le CR_b\left(1-y_{b,h}\right)a_{b,s}^{E}\qquad \forall b,h,s \tag{19}$$

$$E_b^{\min}\le E_b^{(0)}+\sum_{t=1}^{h}\left(\eta_b^C P_{b,h,s}^{E,C}-\frac{1}{\eta_b^{E,D}}P_{b,h,s}^{E,D}\right)\le E_b^{\max}\qquad \forall b,h,s \tag{20}$$

$$\sqrt{\left(P_{b,h,s}^{E,D}-P_{b,h,s}^{E,C}\right)^2+\left(Q_{b,h,s}^{E}\right)^2}\le S_b^{E,m}a_{b,s}^{E}\qquad \forall b,h,s \tag{21}$$

F) *Stochastic programming*: In the proposed scheme, parameters such as active and reactive load, P^L and Q^L, energy price, ρ, the maximum active power output of the renewable DG, $P^{DG,m}$, availabilities of the distribution line and distribution substation, DG and ESS, a^{DL}, a^{DS}, a^{DG} and a^E are uncertain. Therefore, in this paper, the stochastic programming method based on a combination of the MCS and the SBM [19] is utilized to model uncertainties of the problem (1)-(21). Following this method, the MCS first generates a large number of scenarios. In each scenario, uncertainties of P^L, Q^L, ρ, and $P^{DG,m}$ are determined according to their mean and standard deviation values [19]. Other uncertainties are also specified based on their forced outage rate (FOR) [17]. Next, for each scenario, the probability value of the first three uncertainty parameters is calculated based on the normal probability distribution function (PDF) [1]. To calculate the probability value of the parameter $P^{DG,m}$, beta/Weibull PDF is employed for PV/wind system [1]. For other uncertainty parameters, Bernoulli PDF is used to determine the probability of these uncertainties in each scenario [17]. The probability of each scenario is equal to the product of the probability of the uncertainty parameters mentioned in this scenario. Eventually, the SBM method used as a scenario reduction technique selects a certain number of scenarios with short distance from each other generated by the MCS. Details of this method are provided in [19].

III. METHODOLOGY

The problem presented in the previous section, (1)-(21), has a mixed integer non-linear programming (MINLP) framework. Therefore, the hybrid ABC [20] and SCA [21] algorithm is incorporated to cover the last research gap and achieve the optimal solution. This algorithm determines the values of decision variables including P^{NS} and P^{DG} for non-renewable DG, Q^{DG}, $P^{E,C}$, $P^{E,D}$, Q^E, and y based on the (22)-(28), respectively. Then, the values of dependent variables such as P^{DG} for renewable DG, P^{DS}, P^{DL}, Q^{DS}, Q^{DL}, V, and β are calculated according to the values of decision variables and constraints (2)-(7) and (17). In this section, the value of the first dependent variable is determined based on (17), then the

values of other dependent variables of AC-PF constraints, (2)-(7), are calculated based on the backward-forward method [22]. To estimate the technical and environmental limitations of MG, (8)-(12) and (14)-(15), DG size limit, (16), energy limit stored in the ESS and its charger capacity, (20)-(21), the penalty function technique is used [23]. This function for a constraint $a \le b$ is in the form of $\mu.\max(0, a - b)$ which is added to the objective function of the proposed problem, (1). In this equation, $\mu \ge 0$ represents Lagrangian multipliers, the value of which is determined similarly to a decision variable by the ABC-SCA algorithm. Next, the fitness function is equal to the sum of the objective function (1) and all the penalty functions resulting from constraints (8)-(12), (14)-(16), and (20)-(21).

$$P_{b,h,s}^{NS} \in Eq.(13) \quad \forall b,h,s \tag{22}$$

$$P_{b,h,s}^{DG} \in \left[0, S_b^{DG,m}\right] \quad \forall b \in \Omega_B - \Omega_R, h, s \tag{23}$$

$$Q_{b,h,s}^{DG} \in \left[0, S_b^{DG,m}\right] \quad \forall b,h,s \tag{24}$$

$$P_{b,h,s}^{E,D} \in Eq.(18) \quad \forall b,h,s \tag{25}$$

$$P_{b,h,s}^{E,C} \in Eq.(19) \quad \forall b,h,s \tag{26}$$

$$Q_{b,h,s}^{E} \in \left[0, S_b^{E,m}\right] \quad \forall b,h,s \tag{27}$$

$$y_{b,h} \in \{0,1\} \quad \forall b,h \tag{28}$$

Algorithm 1 ABC-SCA process

Initialization step

A- Generate random values for decision variables and Lagrangian multipliers according to constraints (22)-(28) and $\mu \ge 0$

B- Calculate the values of the dependent variables based on AC-PF constraints (2)-(7) and Eq. (17), where AC-PF equations are solved by the forward-backward power flow method

C- Calculate the fitness function that minimizes the sum of the objective function (1) and all penalty functions for constraints (8)-(12), (14)-(16), and (20)-(21)

Update decision variables and Lagrangian multipliers

for i = 1: I_{max}

1- Apply the ABC algorithm to calculate new values of decision variables and Lagrangian multipliers

2- Calculate dependent variables and fitness function according to steps B and C

3- Repeat steps 1 and 2 based on the SCA algorithm

end

Algorithm 1. Process of the ABC-SCA algorithm to solve the proposed formulation

The execution process of this solver is provided in Algorithm (1) and flowchart of Fig. 1. Accordingly, the solver initially generates a random value for decision-making variables and Lagrange multipliers proportional to constraints (22)-(28) and $\mu \ge 0$ for a certain number of populations such as *N*. Then, the values of dependent variables and the fitness function are calculated for *N* values of decision variables and Lagrange multipliers. Next, the updating process of the decision variables and Lagrange multipliers is performed based on the optimal value (minimum value for the proposed scheme based on (1)) of the fit function. In this section, first, the ABC process is executed, then the SCA operation is responsible for the update process. Finally, this operation continues until the convergence point for the proposed scheme is estimated. In this paper, it is assumed that the convergence point is available after a maximum number of iterations I_{max}.

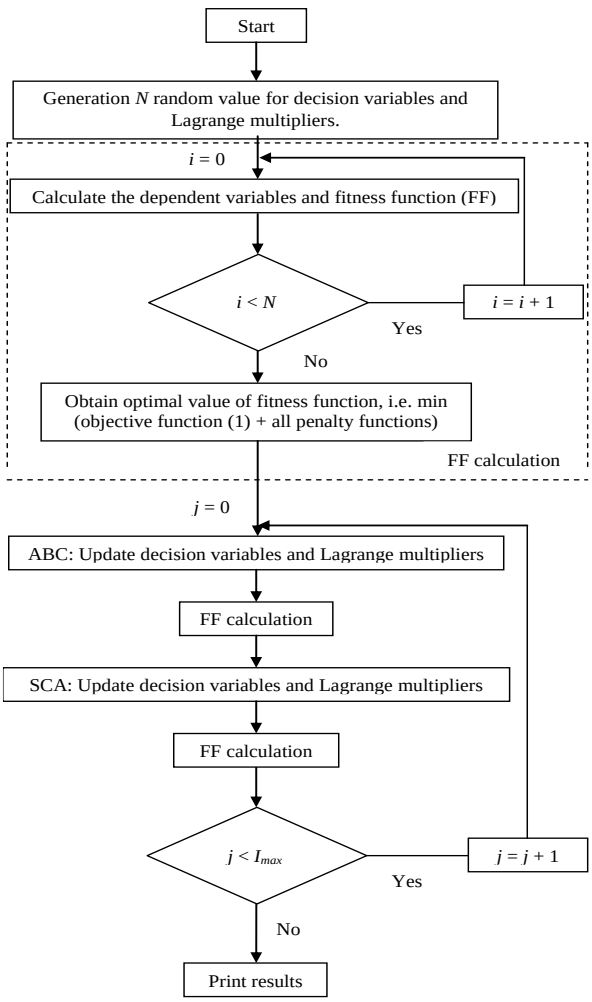

Fig. 1 Flowchart of the methodology for the proposed scheme

IV. NUMERICAL RESULTS

A. Case studies

In this section, the proposed problem is applied to the 69-bus radial MG [24-25]. This network has base power and base voltage of 1 MVA and 12.66 kV, respectively, and minimum power factor of the distribution substation is 0.9. Its permissible voltage range is between 0.9 p.u. and 1.1 p.u. Information of the distribution line and data of the peak load are provided in [24]. The daily load is equal to the product of the peak load and the daily load factor, as given in Fig. 2(a)

[26-27]. Load factor per hour is defined as the ration between the consumption power and the peak load, the value of which is between 0 and 1. Energy prices for three time periods, i.e. off-peak, 1:00-7: 00, middle-peak, 8:00-16:00, and 23:00-00:00, and peak, 17:00-22:00, are 16 $/MWh, 24 $/MWh, and 30 $/MWh, respectively [5]. The network consists of DGs of wind system (WS), photovoltaic (PV), and fuel cell (FC) types with sizes of 0.7 MVA, 0.7 MVA, and 1.2 MVA, respectively. The FCs are placed on buses 21 and 53, WSs are on buses 40 and 51, and PVs are located on buses 32 and 47. The daily active power profile of WS and PV is equal to the product of their size and the daily power rate, as presented in Fig. 2(b) [28, 29]. The coefficients κ, χ, and υ for renewable DGs such as WS and PV are zero, and for FC are equal to $ 100, 20 $/MWh, and 0.002 $/MWh^2, respectively. Also, the pollution coefficient for WS and PV is zero, is 2323.4523 kg/MWh for FC, and is 927.128 kg/MWh for power supply from the upstream network [18]. The network has battery-type (B) ESSs located on buses 32, 40, 47, and 51. The battery size is 5 MWh and has a charge/discharge efficiency of 0.95. Charge/discharge rate and charger sizes are 1.5 MW and 1.5 MVA, respectively. Minimum energy (initial energy) of 0.5 MWh is set for this ESS. FORs of distribution lines and substations are 1% and 0.1%, respectively, and FORs of DG and ESS are 1%. To achieve favorable flexibility, reliability, and environmental conditions, the terms ΔF, $EENS^{max}$, and EM^{max} are equal to 0.02 p.u., 2 MWh, and 25 tons, respectively. Finally, 1000 scenarios are generated by MCS for the uncertainties presented in Section 2, and then 40 of these scenarios are selected by the SBM.

B. Results

The proposed problem along with the mentioned solver is coded in MATLAB software environment, and the obtained numerical results are analyzed as follows.

A) *Analysis of the mentioned solver capability*: Table II reports the expected operating cost of MGs and DGs based on (1) calculated by ABC-SCA, ABC, SCA solvers, particle swarm optimization (PSO) [23], and Genetic Algorithm (GA) [23]. In this section, the population size (N) and the maximum number of convergence iterations (I_{max}) for the mentioned solvers are set 50 and 2000, respectively, and the rest of their adjustment parameters are selected according to [20-21, 23]. Also, to calculate the standard deviation of the final response of each algorithm, the problem solving is repeated 20 times by each solver. Finally, according to Table II, it is observed that the hybrid ABC-SCA algorithm obtains the lowest value for the operating cost of the proposed scheme, i.e. $1184.4, compared to other non-hybrid algorithms. This point is obtained at 628 convergence iterations and a computational time of 112.3 s for the ABC-SCA algorithm, while the optimum point in other algorithms is obtained for convergence iterations greater than 760 and computational time longer than 122 s. Another advantage of the hybrid ABC-SCA algorithm over other non-hybrid algorithms is that it has a low standard deviation. Hence, this solver has the approximate conditions of the final unique response compared to the other mentioned algorithms. Finally, the capability of the ABC-SCA solver presented in this section is a confirmation of the last research gap and the last contribution presented in Section 1.

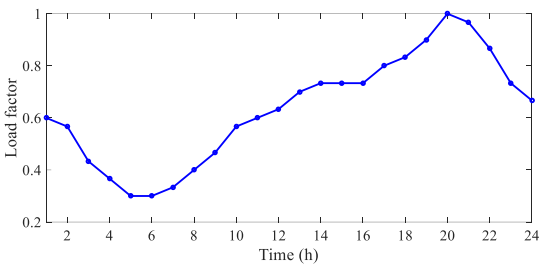

(a)

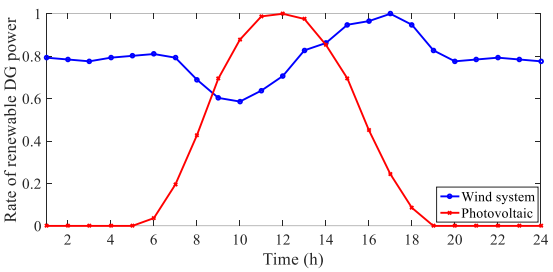

(b)

Fig. 2. The daily curve of the, (a) load factor [26-27], (b) rate of renewable DGs power [28, 29]

Table II
EXPECTED OPERATION COST CALCULATED BY DIFFERENT ALGORITHMS

Solver	Expected operation cost ($)	Convergence iteration	Calculation time (sec)	Standard deviation (%)
GA	1355.7	1511	154.8	2.95
PSO	1303.5	1346	141.2	2.13
SCA	1262.2	801	127.5	1.87
ABC	1249.1	761	122.4	1.55
ABC-SCA	1184.4	628	112.3	0.97

B) *Evaluation of the operation of sources and storage devices in the MG*: Figs. 3 and 4 show the daily active and reactive power curves of sources and storage devices, respectively. Comparing the results of Fig. 3 and the data of subsection 4.1 and Fig. 2, renewable sources such as WSs and PVs inject active power equal to their maximum capacity into the MG following the weather conditions during all operating hours because these sources have zero pollution coefficients and fuel costs according to subsection 4.1; thus, it is appropriate for these sources to inject high active power into the network to minimize the operating costs of the proposed

scheme and environmental pollution. In the case, FCs inject low active power into the network during off-peak hours 1:00-7:00 as shown in Fig. 3, but they inject active power equal to their maximum capacity into the MG at other operation hours. Note that the fuel price of FCs (coefficient χ) during 1:00-7:00 is higher than the energy price (reported in subsection 4.1); hence, consumers are supplied by the upstream network in accordance with the objective function (1). Nonetheless, since an FC is a source that can control its active power and is located at consumption points, it can improve flexibility, reliability, and the environmental conditions of the MG. Therefore, it is not switched off between 1:00-7:00. From 8:00 to 00:00, the energy price is higher than the FC fuel price. Consequently, to improve the operation, flexibility, reliability, and environmental conditions of the network, they inject high active power into the MG. In the following, according to Fig. 3, the batteries operate in the charge mode during off-peak hours due to low energy prices and receive active power from the network. At other times, they operate in discharge mode due to high energy prices, but a high percentage of their stored energy during 1:00-7:00 is injected into MG during peak hours, 17:00-22:00, to minimize the operating costs of the proposed scheme. Between 8:00-16:00 and 23:00-00:00, the batteries are not switched off and low active power is injected into the MG as shown in Fig. 3. As the battery can control its active power and is located at consumption points, its presence in the network can improve the reliability, environmental, and flexibility indices of the MG.

Based on the results reported in Fig. 4 and the data of Fig. 2, the daily reactive power curve of batteries, WSs, and PVs has the same format of changes as does the daily load profile. As a result, they feed a certain percentage of the MG reactive load every hour. The trend of changes of reactive power curve is as given in Fig. 2(a). Now, consumption reactive power of the network needs to be supplied by local sources distributed within the distribution network so that the voltage profile is improved in accordance with constraint (11) and power factor of the network is enhanced as per constraint (10). As a result, the curve of the mentioned elements will be almost similar to the load factor curve. Note that PVs can inject low reactive power into the network during 11:00-13:00, so that they cannot inject reactive power into the network at 12:00. This is because PVs inject active power close to S^{DG} to the network at these hours according to Fig. 3; hence, according to (16), they cannot inject high reactive power into the MG during these hours. This situation occurs for WSs between 16:00-17:00. Finally, it is observed from Fig. 4 that FCs are only able to inject reactive power into the network between 1:00 and 7:00, and their reactive power is zero at other times. During 1:00-7:00, FCs inject low active power into the network according to Fig. 3; thus, as per (16), they can inject reactive power into the network during these hours. Nevertheless, this is not the case for other hours. Moreover, according to Fig. 3, the amount of energy demanded by batteries and passive loads of the MG is high during 1:00-7:00. As a result, FCs inject high reactive power into the MG to prevent a large voltage drop in these conditions. Noted that Batteries are connected to the network generally via power electronics converters called chargers. In case a proper topology is used for the converter. i.e. the IGBT bridge, active power of the battery and reactive power of the charger can be controlled simultaneously [30]. Hence, in this case, the charger and battery together can play a role in active and reactive power management of the network. Moreover, active power of batteries, as given in Fig. 3, is between -3 MW and 3 MW (or p.u.) during operation hours, while the charging size of batteries as stated in subsection 4.1 is 6 MVA. Thus, the batteries' chargers can inject high reactive power into the network during the operation horizon. Consequently, based on the network demand and considering the voltage limitation, chargers inject reactive power into the network as illustrated in Fig. 4.

C) *Analysis of the economic and technical indices of the MG*: Fig. 5 presents the changes of the expected operating cost of the MG and DGs in accordance with the changes in the values of $EENS^{max}$, EM^{max}, and ΔF. As per Fig. 5(a), with increasing $EENS^{max}$ for EM^{max} = 25 tons and ΔF = 0.02 p.u., the operating cost decreases until it is a fixed value for $EENS^{max}$ ≥ 10 MWh. Furthermore, according to Fig. 5(b), for $EENS^{max}$ = 2 MWh and ΔF = 0.02 p.u., the operating cost decreases up to 37 tons with increasing EM^{max}, but it is a fixed value for EM^{max} ≥ 37 tons. Based on Fig. 5(c), for $EENS^{max}$ = 2 MWh and EM^{max} = 25 tons, the operating cost decreases with increasing the flexibility tolerance (ΔF) up to 0.12 p.u. Yet, for $\Delta F \geq 0.12$ p.u., the operating cost is always constant. It is worth noting that increasing the parameters $EENS^{max}$, EM^{max}, and ΔF means less importance of reliability, environmental conditions, and flexibility of the MG compared to the operating cost of the proposed scheme. Thus, under such conditions, sources and batteries will operate in a way that the operating cost is lower than that of a case with minimum values of $EENS^{max}$, EM^{max}, and ΔF.

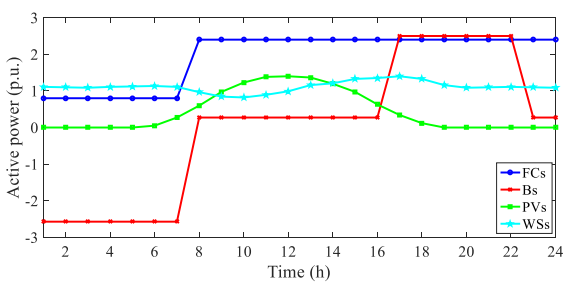

Fig. 3. Daily active power curve of sources and storages

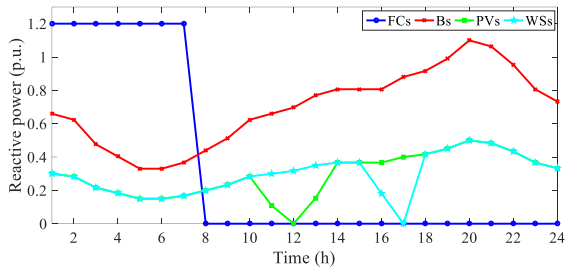

Fig. 4. Daily reactive power curve of sources and storages

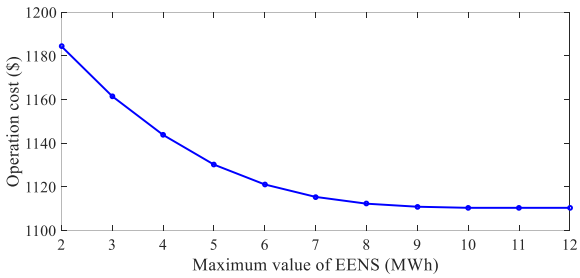

(a)

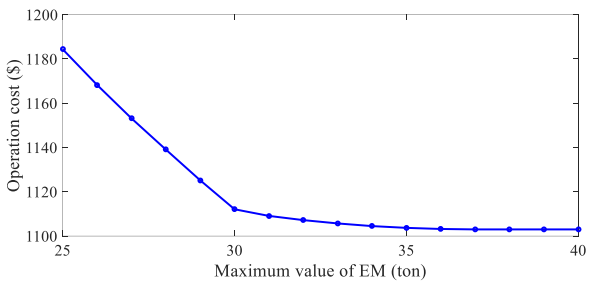

(b)

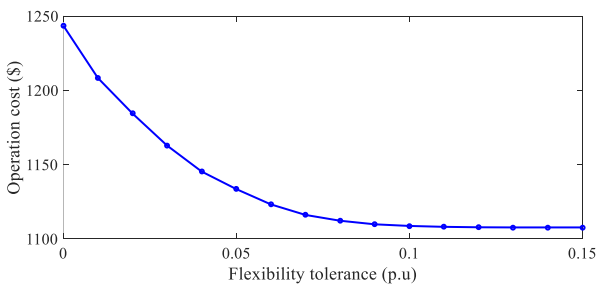

(c)

Fig. 5. Operating cost curve for (a) $EENS^{max}$ (EM^{max} = 25 tons, ΔF = 0.02 p.u.), (b) EM^{max} ($EENS^{max}$ = 2 MWh, ΔF = 0.02 p.u.), (c) ΔF (EM^{max} = 25 tons, $EENS^{max}$ = 2 MWh)

Table III tabulates the values of different technical indices for two case studies: power flow analysis (Case I) and the proposed scheme (Case II). Referring to this table, the pollution level, reliability, operating cost, energy loss, and maximum voltage drop in Case I have higher values than Case II. However, considering the flexibility of 100% for MG (ΔF = 0), the proposed scheme succeeds to reduce the aforementioned parameter values up to 51.2% ((51.1-25)/51.2), 95.9%, 34.2%, 33.7%, and 43.3% compared to Case I, while enhancing the technical and economic status of the network in comparison to Case I. Nonetheless, it should be noted that the percentage of improvement in operating cost, energy loss, and the maximum voltage drop is higher with increasing ΔF as per Table III but the values of reliability and environmental status of the MG are always constant for various values of ΔF. Additionally, the maximum overvoltage occurring in the MG in Case II, compared to Case I, is between 0.012 p.u. to 0.013 p.u. for different values of ΔF, although its value is always smaller than the permissible value of 0.1 (1.1− 1) p.u. It is noteworthy that, according to Table III, the maximum voltage drop occurs at bus 65 (the weakest bus in the 69-bus networks [24]) at hour 20:00 (the peak load hours based on Fig. 2(a)). Also, it is possible that the maximum over-voltage occurs at hours 17:00 (based on Fig. 3, the maximum active power of sources and batteries is injected to the network at this hour) at bus 2 (close to the reference bus).

Table III:

VALUE OF TECHNICAL INDICES FOR DIFFERENT CASES

Parameter	Case I	Case II		
		ΔF = 0 p.u.	ΔF = 0.01 p.u.	ΔF = 0.02 p.u.
Pollution (left side of Eq. (15)) in ton	51.2	25	25	25
EENS (MWh)	48.6	2	2	2
Operation cost ($)	1891.3	1243.6	1208.3	1184.4
Energy loss (MWh)	5.19	3.44	3.39	3.35
Maximum voltage drop (p.u.) (occurred in hour (.) and bus (.))	0.092 (20:00 - 65)	0.0522 (20:00 - 65)	0.0527 (20:00 - 65)	0.053 (20:00 - 65)
Maximum over-voltage (p.u.) (occurred in hour (.) and bus (.))	0 (-)	0.0129 (17:00 - 2)	0.0124 (17:00 - 2)	0.012 (17:00 - 2)

V. Conclusion

This paper presents the operation of MGs in the presence of DGs and ESSs considering the limitations on reliability, pollution status, and network flexibility. This scheme minimizes the total expected operating cost of MGs and DGs as the objective function. Its constraints also include MG's AC power flow equations; operation, reliability, flexibility, and environmental constraints of the MG; and operation model of sources and storage devices. Stochastic planning was adopted to model the uncertainties of renewable power, energy price, load, and availability of MG equipment, sources, and storage devices. Moreover, the hybrid ABC-SCA algorithm was exploited to solve the proposed problem. Eventually, based on the obtained numerical results, it was observed that the mentioned algorithm obtains a more optimal point than non-hybrid algorithms in a lower number of convergence iterations and shorter computational time. The least standard deviation, that is 0.97%, in the final response is also achieved by the suggested algorithm. Besides, the proposed scheme with

proper management of active and reactive power of sources and storage devices reduces the environmental status, reliability, operating cost, energy loss, and maximum voltage drop in MG by about 51.2%, 95.9%, 34.2%, 33.7%, and 43.3% compared to power flow studies by adopting flexibility of 100%.

It is possible that load change in the MG after islanding, or the transfer power changes in two modes of grid-connected mode and islanded one, or energy prices in these two modes changes, where these limits are considered in the future works.

REFERENCES

[1] A. Dini, S. Pirouzi, M.A. Norouzi, M. Lehtonen, "Grid-connected energy hubs in the coordinated multi-energy management based on day-ahead market framework," *Energy*, vol. 188, pp. 116055, 2019.

[2] J. Aghaei, S.A. Bozorgavari, S. Pirouzi, H. Farahmand, M. Korpås, "Flexibility Planning of Distributed Battery Energy Storage Systems in Smart Distribution Networks," *Iranian Journal of Science and Technology, Transactions of Electrical Engineering*, vol. PP, pp. 1-17, 2019.

[3] D. Wang, J. Qiu, L. Reedman, K. Meng, L.L. Lai, "Two-stage energy management for networked microgrids with high renewable penetration," *Applied Energy*, vol. 226, pp. 39-48, 2018.

[4] M. Vosoogh, and et al., "Efficient Networked Microgrid Management Considering Plug-in Electric Vehicles and Storage Units," International Journal of Industrial Electronics Control and Optimization, vol. 4, no. 2, pp. 245-255, 2021.

[5] H. Kiani, K. Hesami, A. Azarhooshang, S. Pirouzi, S. Safaee, "Adaptive robust operation of the active distribution network including renewable and flexible sources," *Sustainable Energy, Grids and Networks*, (accepted), 2021.

[6] S. Pirouzi, M.A. Latify, G.R. Yousefi, "Conjugate active and reactive power management in a smart distribution network through electric vehicles: A mixed integer-linear programming model," *Sustainable Energy, Grids and Networks*, vol. 22, pp. 100344, 2020.

[7] S.A. Bozorgavari, J. Aghaei, S. Pirouzi, A. Nikoobakht, H. Farahmand, M. Korpås, "Robust planning of distributed battery energy storage systems in flexible smart distribution networks: A comprehensive study," *Renewable and Sustainable Energy Reviews*, vol. 123, pp. 109739, 2020.

[8] A. Jamali *et al*., "Self-Scheduling Approach to Coordinating Wind Power Producers With Energy Storage and Demand Response," *IEEE Transactions on Sustainable Energy*, vol. 11, no. 3, pp. 1210-1219, July 2020.

[9] C. Zhang, Y. Xu and Z. Y. Dong, "Robustly Coordinated Operation of a Multi-Energy Micro-Grid in Grid-Connected and Islanded Modes Under Uncertainties," *IEEE Transactions on Sustainable Energy*, vol. 11, no. 2, pp. 640-651, April 2020.

[10] H. Razmi and H. Doagou-Mojarrad, "Comparative assessment of two different modes multi-objective optimal power management of micro-grid: grid-connected and stand-alone," *IET Renewable Power Generation*, vol. 13, no. 6, pp. 802-815, 29 4 2019.

[11] M. Nojavan and H. Seyedi, "Voltage Stability Constrained OPF in Multi-Micro-Grid Considering Demand Response Programs," *IEEE Systems Journal*, vol. 14, no. 4, pp. 5221-5228, Dec. 2020

[12] M. Haseeb, S. A. A. Kazmi, M. M. Malik, S. Ali, S. B. A. Bukhari and D. R. Shin, "Multi Objective Based Framework for Energy Management of Smart Micro-Grid," *IEEE Access*, vol. 8, pp. 220302-220319, 2020.

[13] H.E. Keshta, O.P. Malik, E.M. Saied, F.M. Bendary, A.A. Ali, "Energy management system for two islanded interconnected micro-grids using advanced evolutionary algorithms," *Electric Power Systems Research*, vol. PP, pp. 106958, 2020.

[14] S.M. Moghaddas-Tafreshi, S. Mohseni, M.E. Karami, S. Kelly, "Optimal energy management of a grid-connected multiple energy carrier micro-grid," *Applied Thermal Engineering*, vol. 152, pp. 796-806, 2019.

[15] R. Homayoun, and et al. "Multi-objective operation of distributed generations and thermal blocks in microgrids based on energy management system," *IET Generation, Transmission and Distribution*, (accepted), 2021.

[16] A. Shahbazi, J. Aghaei, S. Pirouzi, T. Niknam, M. Shafie-khah, J.P.S. Catalão, "Effects of resilience-oriented design on distribution networks operation planning," *Electric Power Systems Research*, vol. 191, pp. 106902, 2021.

[17] H.R. Hamidpour, J. Aghaei, S. Dehghan, S. Pirouzi, T. Niknam, "Integrated resource expansion planning of wind integrated power systems considering demand response programmes," *IET Renewable Power Generation*, vol. 13, no. 4, pp. 519-529, 2018.

[18] M. Nazari-Heris, S. Abapour, B. Mohammadi-Ivatloo, "Optimal economic dispatch of FC-CHP based heat and power micro-grids," *Applied Thermal Engineering*, vol. 114, pp. 756-769, 2017.

[19] A. Kavousi-Fard, A. Khodaei, "Efficient integration of plug-in electric vehicles via reconfigurable microgrids," *Energy*, vol. 111, pp. 653-663, 2016.

[20] D. Karaboga, B. Basturk, "On the performance of artificial bee colony (ABC) algorithm," *Applied Soft Computing*, vol. 8, pp. 687-697, 2008.

[21] K. Sarwagya, P.K. Nayak, S. Ranjan, "Optimal coordination of directional overcurrent relays in complex

distribution networks using sine cosine algorithm," *Electric Power Systems Research*, vol. 187, pp. 106435, 2020.

[22] P. R. Babu, C. P. Rakesh, G. Srikanth, M. N. Kumar, and D. P. Reddy, "A novel approach for solving distribution networks," *India Conference (INDICON), 2009Annual IEEE*, pp. 1-5, Dec. 2009.

[23] W. K. A. Najy, H. H. Zeineldin and W. L. Woon, "Optimal Protection Coordination for Microgrids With Grid-Connected and Islanded Capability," *IEEE Transactions on Industrial Electronics*, vol. 60, no. 4, pp. 1668-1677, April 2013.

[24] M.Q. Duong, and *et. al*., "Determination of Optimal Location and Sizing of Solar Photovoltaic Distribution Generation Units in Radial Distribution Systems" *Energies*, vol. 12, pp. 1-25, 2019.

[25] S. Abrisham-Foroushan-Asl, L. Bagherzadeh, S. Pirouzi, M.A. Norouzi, M. Lehtonen, "A new two-layer model for energy management in the smart distribution network containing flexi-renewable virtual power plant," *Electric Power Systems Research*, vol. 194, pp. 107085, 2021.

[26] A. Shahbazi, and et al. "Hybrid stochastic/robust optimization model for resilient architecture of distribution networks against extreme weather conditions," *International Journal of Electrical Power & Energy Systems*, vol. 126, pp. 106576, 2021.

[27] L. Bagherzadeh, and et al., "Coordinated flexible energy and self-healing management according to the multi-agent system-based restoration scheme in active distribution network," *IET Renewable Power Generation*, (accepted), 2021.

[28] S. Abrisham Foroushan Asl, M. Gandomkar, J. Nikoukar, "Optimal protection coordination in the micro-grid including inverter-based distributed generations and energy storage system with considering grid-connected and islanded modes," *Electric Power Systems Research*, vol. 184, pp. 106317, 2020.

[29] A. Rohani, M. Abasi, A. Beigzadeh, M. Joorabian, G.B. Gharehpetian, "Bi-level power management strategy in harmonic-polluted active distribution network including virtual power plants," *IET Renewable Power Generation*, vol. 15, no. 2, pp. 462-476, 2021.

[30] S. Pirouzi, and et al., "Power conditioning of distribution networks via single-phase electric vehicles equipped with Bidirectional Chargers," *IEEE Systems Journal*, vol. 13, no. 3, pp. 3433-3442, 2019.

Seyed Arman Shirmardi is a PhD student in power engineering at Department of Electrical Engineering, Dezful Branch, Islamic Azad University, Dezful, Iran. He is an expert in the technical office of the Khuzestan Hydropower Plant Installation, Repair and Maintenance Company. His research interests include smart grid, Micro-grid and renewable energy.

Mahmood Joorabian was born in Shooshtar, Iran, in 1961. He received his B.E.E degree from University of New Haven, CT, USA, M.Sc. degree in Electrical Power Engineering from Rensselaer Polytechnic Institute, NY, USA and Ph.D. degree in Electrical Engineering from University of Bath, Bath, UK in 1983, 1985 and 1996, respectively. He has been with the Department of Electrical Engineering at Shahid Chamran University as Senior Lecturer (1985), Assistant Professor (1996), Associate Professor (2004) and Professor (2009). His main research interests are fault location, facts devices, power system protection, power quality, and applications of intelligence technique in power systems.

Hassan Barati was born in Dezful, Iran, in 1969. He received the B.Sc. degree in electronic engineering from the Isfahan University of Technology, Isfahan, Iran, in 1993, the M.Sc. degree in electrical engineering from the Tabriz University, Tabriz, Iran, in 1996 and the Ph.D. degree in Electrical Engineering from Science and Research Branch, Islamic Azad University, Tehran, Iran, in 2007. Currently, he is an Associate Professor in the Electrical Engineering Department, Dezful Branch, Islamic Azad University, Dezful, Iran. His research interests are power systems operation & Reliability, restructured power systems, Micro-grids, Smart Grids, FACTS devices.

IECO

This page intentionally left blank.

International Journal of Industrial Electronics, Control and Optimization © 2021 IECO
Vol. 4, No. 4, pp.409-416, Sep (2021)

A New Method to Detect and Track the Resonance Frequency of Piezoelectric Transducers in Ultrasonic Power Supplies

Ebrahim Taghvayi Keshtkar [1] and Mohammad Reza Karafi [2]†

[1,2] Faculty of Mechanical Engineering, Tarbiat Modares University, Tehran, Iran

ABSTRACT

In this paper, a new method is developed to detect and track the resonance frequency of ultrasonic transducers. In order to have an acceptable performance of transducers, power supplies should be able to detect and track the resonance frequency. Different methods have been used for this purpose. In this research, the voltage of the transducer and the phase difference between the voltage and current are used to find the resonant frequency. The maximum voltage of a transducer is founded in a predefined frequency interval. Afterward, the minimum phase difference between the voltage and current is obtained in a smaller interval around it. The simultaneous use of the voltage and phase shift increases the accuracy and speed of the algorithm. Since the transducer's voltage variations are relatively large near the resonant frequency, it is a versatile parameter compared to the current used in other methods to indicate the resonance frequency. The algorithm is implemented within a microcontroller. An FPGA is used to generate accurate frequency using the Direct Digital Synthesis (DDS) method. The algorithm can detect the resonant frequency under free conditions. Applying force to transducers or emerging the transducer's head to the water changes the resonant frequency. The experimental tests showed that the algorithm could find and track the resonant frequency automatically under loading conditions.

Article Info

Keywords:
Ultrasonic Transducer, Tracking, Resonance Frequency, Power Supply
Article History:
Received 2021-02-16
Accepted 2021-07-30

I. INTRODUCTION

Ultrasonic transducers are widely used in today's industries [1]. In order to have maximum efficiency, power supplies should be able to detect and track the resonance frequency of transduces. Ultrasonic power supplies are used in cleaning, welding, mask sewing machine, and other manufacturing processes. Improvements and innovations in power supplies are still in progress [2] [3]. The resonance frequency would change while an ultrasonic transducer heats up or subjects to loads [4]. In addition, the precise control of the resonant frequency is essential since undesirable natural frequencies might be excited without tracking the frequency [5].

Different methods have been proposed for tracking the resonance frequency of ultrasonic transducers. Agbossou used the class-D power amplifier to excite piezoelectric transducers [6]. This power supply uses an analog integrated circuit to compare a sawtooth signal with a constant voltage to generate a PWM signal. Despite covering a wide range of frequencies, one crucial drawback is the lack of sufficient precision in the frequency generation. Gokcek [7], Lin [8], and Crivii [9] used the analog Phase-Locked Loop (PLL) for tracking and maintaining the resonance frequency. However, this method was not capable of detecting the resonance frequency under sudden and severe mechanical loads. Svilainis used the class-B power amplifier to excite an ultrasonic transducer [10]. The

†Corresponding Author: karafi@modares.ac.ir
Tel: +98(21)82884341 Fax: +98(21)82884341,
Faculty of Mechanical Engineering, Tarbiat Modares University, Tehran, Iran

signal distortion of the amplifier limits its application in high frequencies. Xiaoyi [11], Huang [12], and Chen [13] used the proportional or proportional-integral controller to find the frequency with the maximum current consumption. Wei-Hua [14] presented a frequency-tracking method using the Direct Digital Synthesizer (DDS) and a fine tracking using the PLL method. Shanli [15] used the maximum power consumption to find the resonance frequency. Longfei [16] implemented the resonance frequency detecting system using the phase difference for an ultrasonic cell destruction system. This system was not able to find the resonance frequency with changing loads. Jing-Shuang [17] designed an ultrasonic power supply and obtained the resonance frequency using a voltage-current phase correlation algorithm. Automatic resonance frequency tracking in this research was influenced by the system noise. Yokozawa [18] proposed the idea of controlling the output terminal impedance to control the resonance frequency. The impedance of the transducer can be changed using FETs which are parallel with piezoelectrics. Therefore, the resonance frequency becomes a function of the duty cycle of the FETs. This method can be used to change the resonance frequency of transducers; however, another method should be used to detect the resonant state. Fu [19] designed an ultrasonic power supply in a wide frequency range. In this power supply, the frequency was swept with a processor to obtain the maximum current amplitude. Using the Fast Fourier Transform (FFT), the new resonance frequency was detected from the phase-frequency characteristics. This power supply was not able to find new resonance frequencies with high and fast variations of loads.

The proposed algorithm of this paper uses the voltage and phase difference to find the resonant frequency. The simultaneous use of the maximum voltage and the minimum phase difference of voltage and current increases the accuracy and speed of the algorithm in comparison to other methods. Since the variations of the transducer's voltage are relatively large near the resonant frequency, it is versatile compared to the current to indicate the resonance frequency. If the transducer leaves its resonance state, the system sweeps the frequency and obtains a new frequency with the maximum piezoelectric voltage. Afterward, in a smaller interval around it, the frequency is swept again, and the minimum phase difference is achieved. Three types of tests, including applying loads to the transducer, immersing the head of the transducer into the water, and increasing the transducer's temperature, are conducted to evaluate the performance of the systems.

In this paper, the frequency response of a transducer is explained first. Then the hardware configuration of the system is described. After that, a flowchart of the algorithm used in the software is stated. Finally, experimental results are expressed.

II. Frequency Response of a Piezoelectric Ultrasonic Transducer

The most well-known transducers equivalent circuit is the Butterworth-Van Dyke model [20]. Fig. 1 shows the model.

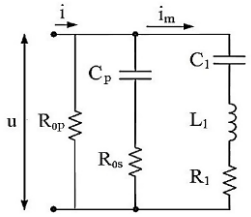

Fig. 1. Butterworth-Van Dyke Model for a Piezoelectric Ultrasonic Transducer.

In this model, i, i_m, and u are the input current, mechanical branch current, and the input voltage, respectively. C_p is the piezoelectric static capacitor, R_0p is the piezoceramic dielectric resistance, R_0s is the series resistance. The mechanical part of the transducer is modeled with a series RLC circuit in which the elements R_1, C_1, and L_1 are damping, stiffness, and the mass of the transducer, respectively. Thus, Eq. (1) expresses the total admittance of the equivalent circuit. In this equation R_0s is ignored.

$$\begin{aligned} Y &= G + jB \\ &= \frac{1}{R_{0p}} + \frac{R1}{\left(L_1\omega - \frac{1}{C_1\omega}\right)^2 + {R_1}^2} \\ &+ j\left(\frac{-\left(L_1\omega - \frac{1}{C_1\omega}\right)}{\left(L_1\omega - \frac{1}{C_1\omega}\right)^2 + {R_1}^2} C_p\omega\right) \end{aligned} \tag{1}$$

where G represents the conductance, and B is the susceptance. Using Eq. (2), the transducer's resonance frequency can be calculated according to Eq. (3).

$$Im(Y) = B = 0 \tag{2}$$

$$f_r = \frac{\sqrt{2C_1L_1C_p + {C_1}^2L_1 - {C_1}^2{R_1}^2C_p - \sqrt{M}}}{2\pi\sqrt{2{C_1}^2{L_1}^2C_p}} \tag{3}$$

The variable M in Eq. (3) is defined as follows.

$$\begin{aligned} M = {C_1}^3({R_1}^4{C_p}^2C_1 + {L_1}^2C_1 - 4{C_p}^2{R_1}^2L_1 \\ - 2C_1L_1C_p{R_1}^2) \end{aligned} \tag{4}$$

The resonance frequency of the mechanical branch is also expressed as follows.

$$f_{rs} = \frac{1}{2\pi\sqrt{L_1C_1}} \tag{5}$$

The difference between the resonance frequency in Eq. (3) and (5) is shown in Fig. 2. According to this figure, the overall resonance frequency of the transducer is approximately equal to the resonance frequency of the mechanical part, and the maximum transducer's current consumption occurs at this frequency.

$$|i| = u|Y| \tag{6}$$

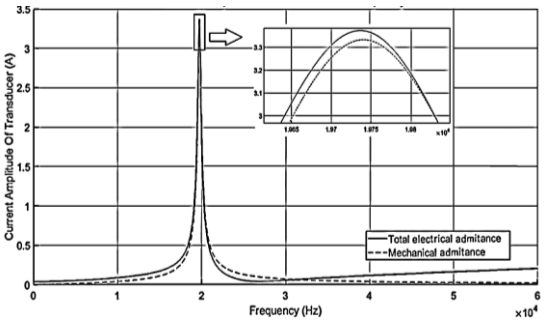

Fig. 2. Comparison of the resonance frequency of the whole transducer with the resonance frequency of the mechanical branch. Equivalent circuit parameters are u=100 V, R_0p=2.6 kΩ, C_p=6 nF, R_1=30 Ω, C_1=5 nF and L_1=13 mH.

III. HARDWARE CONFIGURATIONS OF THE SYSTEM

The system consists of a control unit, power unit, and signal sampling circuits. The control unit generates drive signals for the power unit based on feedback from the transducer. The connection between different parts of the system is shown in Fig. 3.

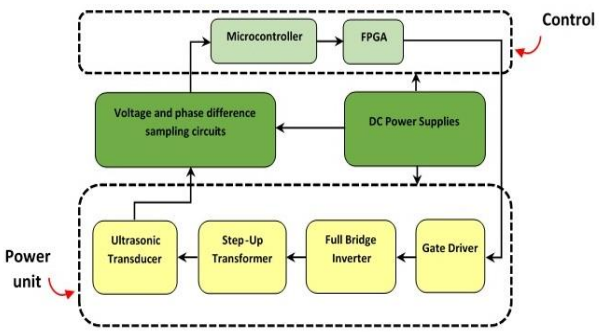

Fig.3. Block diagram of the system

Drive signals of the inverter are generated using a Field Programmable Gate Array (FPGA). Control commands are sent to the FPGA from a microcontroller. First, the piezoelectric voltage and the voltage-current phase difference are measured using sampling circuits. Afterward, they are sent to the microcontroller as feedbacks. Finally, the microcontroller sends a desired frequency command to the FPGA after processing and executing a control algorithm. The Direct Digital Synthesizer (DDS) method was used to generate the frequency. More information about the implementation of the system is provided in Appendix 1. Fig. 4 shows the driver circuits of the inverter.

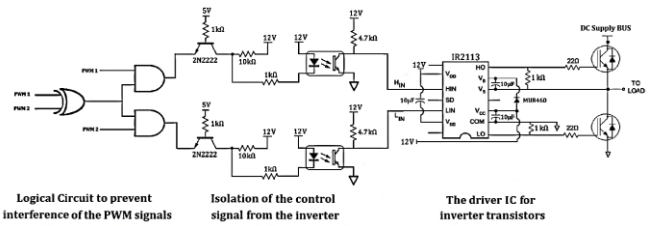

Fig. 4. The circuit for driving the inverter

The schematics of the inverter circuit, step-up transformer, and transducer are shown in Fig.5. The alternating signal generated by the inverter, transmitted to the transducer via a transformer. Connecting the transducer to the secondary of the transformer allows the output voltage to increase at the resonance frequency. If the load is directly connected to the output of the inverter, its voltage follows the inverter voltage.

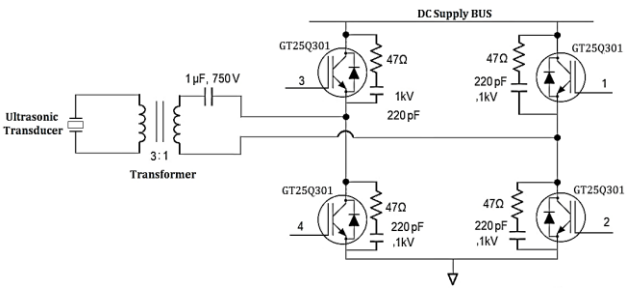

Fig. 5. Inverter circuit

Fig. 6 shows the sampling circuits to measure the voltage and phase difference.

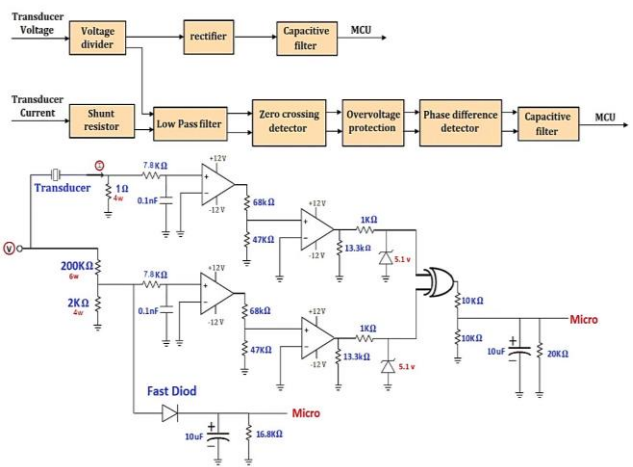

Fig. 6. Schematic of the sampling circuits

The first Analogue to Digital Converter (ADC1) of the microcontroller was used to acquire the voltage, and the second one (ADC2) was used for the phase difference.

3.1. The algorithm of the system

Fig. 7 shows a flowchart of the algorithm of the system.

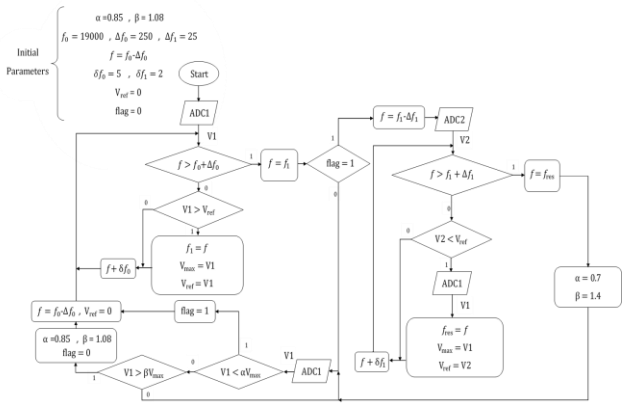

Fig. 7. The flowchart of the algorithm, V1 and V2 are the voltages read by ADC1 and ADC2 of the microcontroller respectively, α and β are predefined coefficients (α<1, β>1), Vmax is the maximum voltage of ADC1, f is the current frequency of the inverter

The initial parameters of Fig.7 are set in the microcontroller program. The algorithm searches and finds the resonance frequency, f_{res} . f_0 is the initial frequency, and Δf_0 is a large sweeping interval. When the system starts up, the frequency is swept from $f_0 - \Delta f_0$ to $f_0 + \Delta f_0$, with a predefined step of δf_0, and then the frequency with the maximum voltage is obtained. As loads are applied to the transducer, the resonance frequency changes. Therefore, the voltage of the transducer changes. The variable "flag" is an indicator to show loading conditions. If the variable is equal to one, it shows that the transducer is under loading conditions. If the new voltage of the ADC1 is lower than αVmax or greater than βVmax the algorithm starts to find a new resonance frequency, f_1. After the large sweep with the interval of Δf_0, to find the more accurate resonance frequency, a smaller interval Δf_1 is taken, and the frequency is swept from $f_1 - \Delta f_1$ to $f_1 + \Delta f_1$ with a smaller step of δf_1. The frequency with the minimum phase difference is obtained and adjusted in this stage. The small sweep is not conducted when the new voltage value of the ADC1 is greater than βVmax. This condition would generally occurs when the transducer be unloaded. When the transducer is loaded, the voltage at the resonance frequency is lower than free conditions. In this case, the algorithm may run searching loops frequently due to small voltage changes, which is not appropriate and made the system unstable. Therefore, to reduce the sensitivity of the algorithm, in this case, the values of α and β are chosen smaller and larger compared to previous values, respectively. The initial values of α and β are 0.85 and 1.08, respectively, and their values became 0.7 and 1.4 after adjusting the frequency under loading conditions, respectively.

3.1.1 Sensitivity of the algorithm

After the first start, the large sweep is done, and the resonant frequency is founded. After that, the algorithm is sensitive to changes in the ADC1 voltage. If V1< 0.85 Vmax or the ADC1 voltage decreases 15%, then the algorithm senses that the transducer is under loading conditions (flag=1). Therefore the large sweep is done again, and the maximum voltage, Vmax, has been founded. Then the small sweep is conducted, and the minimum voltage of ADC2 is founded. In this stage, the value of α and β have been changed. Since the voltage of the transducer is smaller under loading conditions, therefore α is changed to a smaller value of 0.7. In this condition, if V1< 0.7 Vmax or the ADC1 voltage decreases 30%, the algorithm runs a new sweep. In other words, the sensitivity of the algorithm under loading conditions is set less than free conditions. This is due to deviations of the transducer voltage under loading conditions. When the voltage V1> 1.08Vmax (or the ADC1 voltage increases 8%), then the algorithm senses that the transducer is unloaded (flag=0). Therefore a large sweep is conducted, and a new resonance frequency is detected. The coefficient β at loading condition is 1.4. Therefore, when the ADC1 voltage increases by 40%, the algorithm senses the unloading in this situation.

3.2. Implementation of the System

The Xilinx FPGA spartan6 XC6SLX9 chip with 50MHz clock frequency, 64MB of flash memory and 256MB of RAM, and A STM32F303VCT6 microcontroller with an ARM® cortex®-M4 processor, with the maximum clock frequency of 72 MHz, 256 kB of flash memory, and 48 kB of RAM are employed. C codes of the microcontroller are written in the Keil uVision5 software. Fig. 8 shows the experimental setup.

Fig. 8. Experimental setup

IV. Experimental Tests

To evaluate the performance of the system, the transducer is tested under different conditions of free, mechanical loadings, immersion in 25 ° C water, and immersion in boiling water, according to Fig. 9.

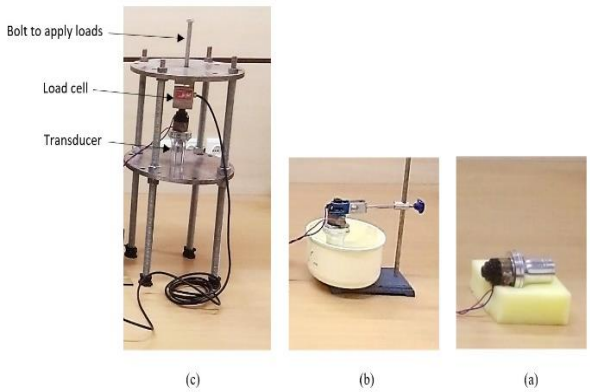

Fig. 9. The transducer under different test conditions, (a) free conditions, (b) head immersion in the water, (c) mechanical loading

The diagram of the current envelope of the transducer and the excitation frequency versus time are shown in Fig.10. After switching on the power supply, the excitation frequency is swept, and the maximum voltage is founded. The maximum current of the transducer is shown in Fig.10. The frequency is set on the maximum current consumption of the transducer. The resonant frequency under free conditions is 18860 Hz, and its maximum current is about 1.6 A.

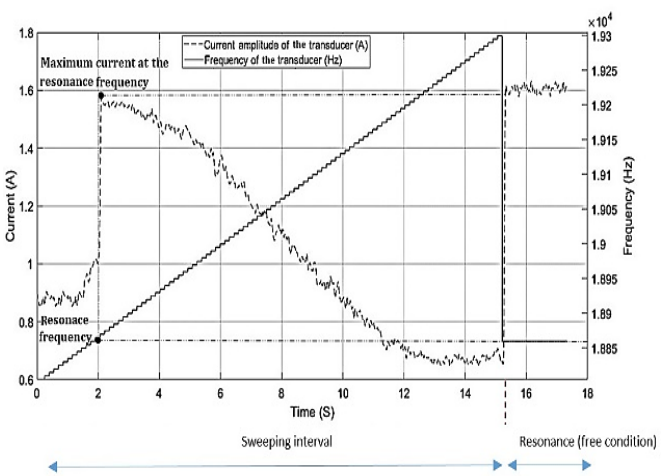

Fig. 10. Frequency sweeping to detect the resonance frequency of the transducer

By applying loads, the resonant frequency changes, and the algorithm conducts a new sweep. A DBBP-100 load cell manufactured by Bongshin Company, South Korea, is used to measure forces. Fig. 11 illustrates the operation of the algorithm under loading conditions.

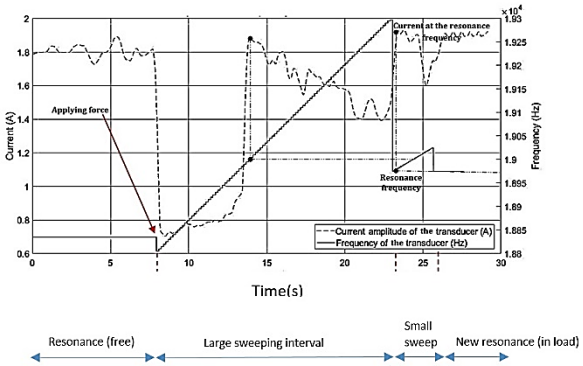

Fig. 11. Frequency sweeping of the system to detect the resonance frequency under a 35 kg load

According to Fig.11, the transducer is in the resonant state from zero to 8 seconds. Its current is about 1.8A in this situation. At the eighth second, a 35 kg force is applied to the transducer. Therefore the voltage of the transducer reduces, and the algorithm starts a large sweep. The large sweep ends at the 23rd second. Then the small sweep is conducted through the next 3 seconds. The maximum current of the transducer in this interval is about 1.9 A, and its new resonant frequency is 18975 Hz. However, its resonant frequency under free conditions was 18840 Hz. Increasing the resonant frequency is due to the increase of mechanical stiffness.

In the immersion tests, the transducer is first in its resonance frequency under a free condition. The resonant frequency in this condition is about 18830 Hz, and the consumption current is about 1.5A. The resonance frequency of the transducer changes as its head is immersed in the water. At around 7.5s, the head of the transducer is immersed 14mm into 25 °C water. Fig. 12 shows the performance of the system in this test.

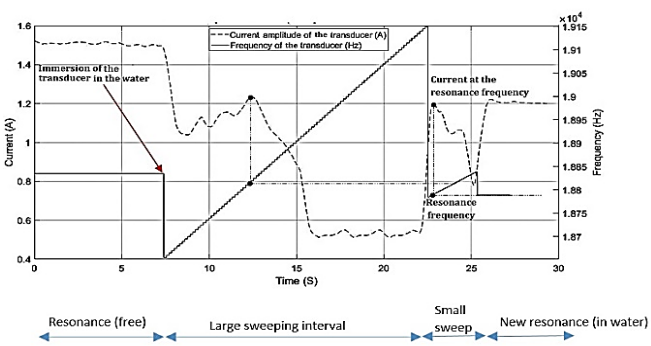

Fig. 12. Operation of the system in the immersion test

According to Fig.12, after the immersion of the transducer, the algorithm conducts the two sweeps and finds a new resonant frequency of 18770 Hz. The consumption current in this

condition is about 1.2 A.

Similar tests are conducted in different heights of the immersion and forces applied to the transducer. Table 1 summarizes the results of the tests.

TABLE I
RESULTS OF THE EXPERIMENTAL TESTS OF THE SYSTEM

Type of tests	Test conditions	Resonance frequency (Hz)	Changing the current amplitude after tuning (mA)
Free	unloaded	18860	<50
Mechanical loading	35kgf	18975	<50
	45kgf	19081	<50
	55kg	19181	<50
Head immersion in the water at 25 °C	14mm	18881	<50
	34mm	18902	<50
	60mm	18939	<50
Head immersion in boiling water	14mm	18789	<50

The resonant frequency of the transducer is 18860 Hz under free conditions. Applying mechanical loads or immerging the transducer in the water increases the resonant frequency because of increasing the mechanical stiffness. However, the resonant frequency decreases as the temperature rises. This is due to the mechanical expansion and the material properties changes of piezoelectrics. After finding the new resonance frequency, the current amplitude of the transducer had a deviation lower than 50mA.

V. CONCLUSION

In this paper, a new method was developed to detect and track the resonance frequency of transducers. Piezoelectric voltage and the phase difference between the voltage and current were used to find the resonance frequency. Simultaneous use of the maximum voltage and the minimum phase difference increased the accuracy and speed of the algorithm in comparison to other methods. The developed algorithm conducted two sweeps with different intervals and steps. The first one was a larger sweep with a course step, and the second one was a smaller one with a fine step. In the first sweep, the maximum voltage was founded, and in the second one, the minimum phase difference was set. The performance of this system was tested experimentally. The system could detect and track the resonance frequency automatically under free and different loading conditions. After finding the new resonance frequency, the current amplitude had a deviation lower than 50mA. The algorithm was sensitive to changing the transducer's voltage. The resonant frequency of transducers increased with applying mechanical loads or immersion in 25 °C water. The more mechanical was the loads or immersion heights, the more resonant frequency would be. However, increasing the transducer's temperature decreased the resonant frequency. These were the typical variations of the resonant frequency of ultrasonic transducers under loading conditions. The speed of the algorithm could be faster to compensate for rapid changes in mechanical loads.

APPENDIX

A.1. Frequency Generator Unit

The Direct Digital Synthesizer (DDS) method is used to generate the frequency. A 32-bit binary number is generated by the microcontroller as an input. The procedure of loading the binary number on the FPGA is shown in Fig. A.1. The 32-bit data is separated into two 16 bits (high and low bits) and loaded on a multiplexer through a data bus of Data_0 through Data_15. The control bit of l_h_d specifies which group of data are stored on flip-flops (registers). After storing the data on the flip-flops, a clock is triggered, and the data is transferred to the final flip-flop (register). The 32-bit binary number is used as the input of an adder.

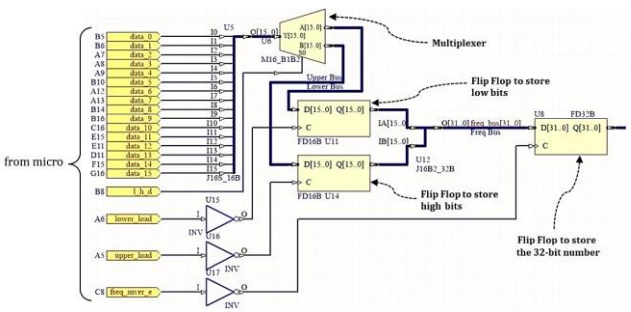

Fig. A.1. Loading of the 32-bit binary number from the microcontroller to the FPGA

An adder adds the 32-bit binary number with each clock pulse while an overflow occurs. The period of the elapsed time to overflow is represented by the parameter T. The inverse of this period is the adder's overflow frequency. If in each clock pulse, the adder output adds with the number N, the overflow period of the adder is expressed by Eq. (A.1), and the overflow frequency is expressed by Eq. (A.2).

$$T = \frac{2^{32}\frac{1}{f_s}}{N} \tag{A.1}$$

$$f_{out} = \frac{1}{T} = \frac{f_s}{2^{32}}N \tag{A.2}$$

The frequency resolution in this method is equal to $\frac{f_s}{2^{32}}$. The left 8 bits (higher bits) of the output of the adder are chosen to generate the desired frequency. These 8 bits change from 0 to 255 during each overflow period. Fig. A.2 illustrates how to use the higher 8 bits of the adder's output. This 8-bit number is used to compare with predefined numbers.

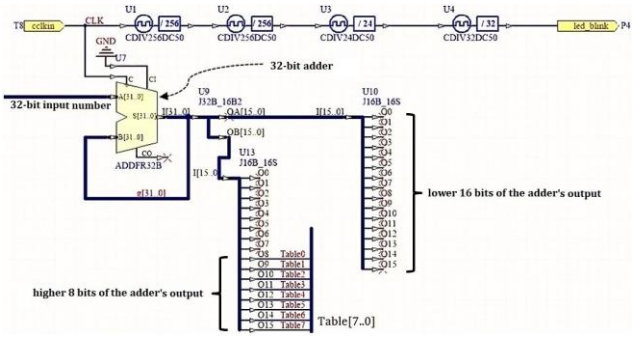

Fig. A.2. the higher 8 bits of the adder's output

To drive the inverter, two complementary PWM signals are required with a dead time. The two signals with the described features are generated using the circuit in Fig. A.3.

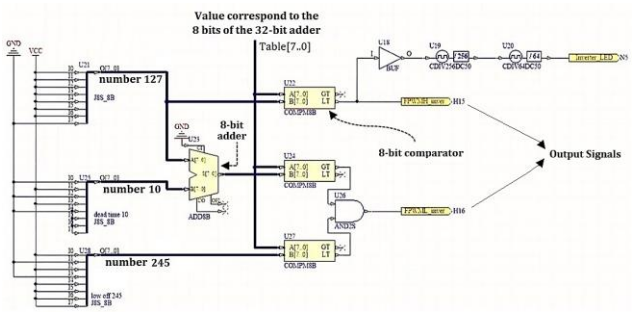

Fig. A.3. Conversion of the 8-bit data to the two complementary PWM signals

Three comparators and one adder are employed to generate the two PWM signals. The 8-bit number is inserted into the three comparators and compares with predefined binary numbers that determine the duty cycle, phase difference, and dead time. Table A.1 illustrates the logic used to generate signals.

TABLE A.1
THE LOGIC TO GENERATE THE TWO PWM SIGNALS WITH COMPARATORS

8-bit number		First signal	Second signal
≥ 0	< 117	1	0
≥ 117	≤ 127	0	0
> 127	< 245	0	1
≥ 245	≤ 255	0	0

Fig. A.4 shows the two PWM signals in one period.

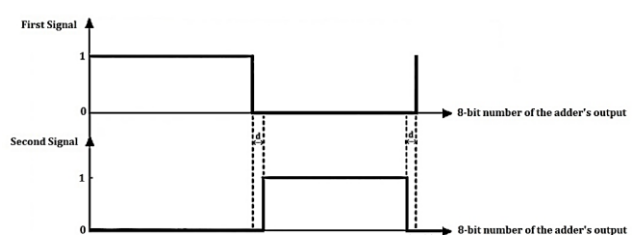

Fig. A.4. PWM signals used to drive the inverter

In this way, the frequency of the inverter can be controlled by changing the number N.

REFERENCES

[1] Ye Yao, Yue Pan, Shiqing Liu, "power ultrasound and its application: A state-of-the-art review," *Ultrasonics-sonochemistry*, vol.62, April. 2020.

[2] Kim K, Choi H, "High-efficiency high-voltage class F amplifier for high-frequency wireless ultrasound systems," *Plos one*, vol.16, No.3, 2021. https://doi.org/10.1371/journal.pone.0249034.

[3] Hamid Radmanesh, Masood Saeidi, "Linear Modelling of Six Pulse Rectifier and Designee of Model Predictive Controller with Stability Analysis," *International Journal of Industrial* Electronics, Control and Optimization, Vol.3, No.4, pp. 491-501, 2020.

[4] A. Ramos-Fernandez, "Automatic system for dynamic control of resonance in high power and high Q ultrasonic transducers," *Ultrasonics*, pp.151–156, 1985.

[5] T. Morita, "Miniature piezoelectric motors", *Sensors and Actuators A*, Vol.103, pp.291-300, 2003.

[6] Agbossou, Kodjo, "Class D amplifier for a power piezoelectric load," *IEEE transactions on ultrasonics, ferroelectrics, and frequency control*, Vol.47, No.4, pp.1036-1041, 2000.

[7] C. Gokcek, "Tracking the resonance frequency of a series RLC circuit using a phase locked loop, in control applications," *IEEE Conference*, Vol.1, pp.609–613, 2003.

[8] J. Lin., Y. Duan., H. Lin, "An Ultrasonic Motor Drive Using LLCC Resonant Technique," *30th Annual IEEE Power Electronics Specialists Conference*, Vol.2, pp.947-952, 1999.

[9] M. Crivii, M. Jufer, "DC to AC Converter for Piezoelectric Motors," *Proc. of EPE'99, Lausanne*, 1999.

[10] Svilainis et al., 2006. "Power amplifier for ultrasonic transducer excitation," *Ultragarsas Ultrasound*, Vol.58, No.1, pp.30-36, 2006.

[11] Jin Xiaoyi, Wu Weiyang, Sun Xiaofeng. "Operational Principle and Control of Series-Resonant Current-Source Mode High Frequency Link Sine-Wave Inverter," *Transactions of China Electro-Technical Society*, Vol.22, No.4, pp.100-106, 2007.

[12] Huang Ruhai, Xie Shaojun., "Double-Loop Digital Control Strategy Based on Proportional-Resonant Controller," *Transactions of China Electrotechnical Society*, pp.77-81, 2012.

[13] Chen Hongzhi, "Virtual Structure Design Method for Inverter Power Supply," *Transactions of China Electro-Technical Society*, pp.157-163, 2013.

[14] Wei-hua, W. U, "Research on the Frequency Automatic Tracking in Ultrasonic Power based on DDS-PLL," *Power Electronics 5*, Vol.42, No.5, pp.50-52, 2008.

[15] ZHANG Shanli., "High-power ultrasonic digital inverter power supply based on DSP," Ph.D. Dissertation, Jiangnan University, china, (2011)

[16] Xiao, Longfei, "Circuit design of intelligent frequency tracking for ultrasonic cell disruption system," *9th International Congress on Image and Signal Processing, BioMedical Engineering and Informatics (CISP-BMEI). IEEE*, pp.1611-1615, 2016.

[17] G. Jing-shuang, "A design of intelligent power ultrasonic supply," *Symposium on Piezoelectricity, Acoustic Waves,*

and Device Applications (SPAWDA). IEEE, pp.293-296, 2016.

[18] Yokozawa, H, "Dynamic control of transducer's resonant frequency via the controlling of electric terminal," *International Conference on Noise and Vibration Engineering and USD*, 2016.

[19] Fu, Yu, "A Design of Wide-range Frequency-tracking Ultrasonic Power Supply," *Journal of Physics: Conference Series*, Vol.1345, No.3, 2019.

[20] Domarkas, V. I., and R-J. Kažys, *Piezoelectric transducers from measuring devices,* Mintis, pp. 255, 1975.

EbrahimTaghvaee , was born in qazvin, Iran, in 1994. In 2015, He received the Bsc degree in power electronic Engineering from Imam Khomeini International University, Qazvin, Iran. In 2018 he received his Msc degree in Mechatronics Engineering from Tarbiat Modares University.

Mohammad Reza Karafi was born in Noshahr, Iran, in 1984. He received the Bsc degree in Mechanical Engineering from the Iran University of Science and Technology, Tehran, Iran, in 2006, and the Msc degree in Mechanical Engineering from Tarbiat Modares University, Tehran, Iran, in 2008, and Ph.D. degrees in Mechanical engineering from Tarbiat Modares University, Tehran, Iran, in 2013. In 2013, he joined the Department of Mechanical Engineering, Tarbiat Modares University, as a Faculty member. His current research interests include sensors and actuators, Mechatronics, Ultrasonic devises and power supplies.

International Journal of Industrial Electronics, Control and Optimization © 2021 IECO
Vol. 4, No. 4, pp. 417-431, Sep (2021)

Supervisory Controller Design for Power System Stability using Hybrid Automata Modeling

Fariba Forouzesh [1], Mahdiyeh Eslami [2,†], and Mehdi Jafari Shahbazzadeh [3]

[1,2,3] Department of Electrical Engineering, Kerman Branch, Islamic Azad University, Kerman, Iran

ABSTRACT

Power systems are categorized as nonlinear dynamical systems, and the importance and complexity associated with their stability have dramatically increased. Accordingly, the behavior of power systems can be characterized by interactions between continuous and discrete-event dynamics. This paper proposes a systematic approach to the design and analysis of a supervisory control scheme for power systems using the hybrid automata (HA) model. The proposed model for optimal controller application is derived, and the power system's overall behavior is modeled using HA to enhance its stability. Hybrid systems' formulation incorporates continuous dynamics as well as discrete switching behavior into a modeling and control framework, thus allowing a complete system description while crystallizing the concepts of safety into system design criteria. This study uses a power system (HA) model as a discrete event system (DES) plant and controller. In the proposed method, to present the hybrid model, the discrete events used include the presence and absence of disturbances and voltage control elements, fault, sudden load increase, capacitor bank, and under-load tap changer (ULTC) transformer. Voltage stability and control are investigated by the generators' rotor angle, bus voltage, eigenvalues, and the stability theory of the switched linear systems. Applications in voltage control, stability, and dynamic service restoration are presented on two benchmark power systems with 12 discrete states. The simulation results reveal the effective performance of the proposed supervisory controller model to enhance voltage stability in power systems.

Article Info

Keywords:
Discrete event, Hybrid Automata (HA), Modeling, Voltage Stability

Article History:
Received 2021-06-14
Accepted 2021-09-17

I. INTRODUCTION

To maintain the operating range of the equipment, stability and voltage control in power systems are inevitable and have been a major topic in this domain. In electrical distribution systems, for voltage stability, reactive power generation devices (e.g., static reactive power compensators), as well as under-load tap changer (ULTC), are utilized. In these cases, the ULTC transports the voltage within the acceptable range and, then, the static reactive power compensator is responsible for its precise control [1].

Various methods are adopted for voltage control and power system stability. Due to the power system's nonlinear behavior, hybrid modeling can be employed to design supervisory controllers. Power systems can be modeled with a hybrid automatic model because their behavior is described by interactions between continuous dynamics and discrete events [2]. HA modeling is suitable for simple power systems [2], [3]. Considering the discrete conduction mode of most electrical power system equipment used for switching, voltage regulation, etc., such as switches, which are discrete on or off [2], different methods of descriptive language (e.g. fuzzy logic, Petri net, automata) are applied to represent a DES system. Ref. [4] deals with the fault diagnosis of a linear continuous-variable dynamical system represented by a discrete state-space model. The proposed fault diagnoser is based on a special Petri Net called continuous-time delay Petri net (CTDPN). In general, stability is a feature of the power system that allows it to remain in the equilibrium

[†]**Corresponding Author** : m.eslami@iauk.ac.ir
Tel: +98-3431321029, Islamic Azad University Kerman, Iran.
Department of Electrical Engineering, Kerman Branch, Islamic Azad University, Kerman, Iran

mode under normal conditions and/or allows the system to reacquire an admissible mode under disturbance [1]. Stability is frequently discussed in terms of maintaining the performance of synchronous generators [1].

Since power generation in a power system is based on synchronous generators, all machines must be operated in synchronous mode or in harmony with one another to achieve satisfactory system performance. This aspect of stability is influenced by the dynamics of the generator's rotor angle equation [1]. Moreover, rotor angle stability and short-term voltage stability are closely linked to each other. In some cases, the loss of synchronism of any generator in the power system may lead to short-term voltage instability or collapse [5]. Therefore, the rotor angle must be checked via a certain threshold to ensure rotor angle stability [5].

When evaluating stability, it is essential to consider the system's behavior when it is operated under a transient disturbance [1]. The system must resist severe disturbances including a short circuit on a transmission line, loss of a generator or a large load, and/or loss of communication between two subsystems [1], [6]. The system's performance under disturbances is mainly influenced by the performance of its components [1], [6].

In [7], a controller design method has been developed using the hybrid automaton approach for a three-phase switch shunt active power filter (SAPF) supplied by a photovoltaic system and associated with the nonlinear load. In [8], besides designing a controller to coordinate the performance of two VSEs, including a ULTC-equipped transformer and static VAR compensator (SVC), problems related to the practical implementation of the controller are presented, and recommendations are made on transformer and compensator controller settings and synchronization between control systems; however, in this study, we used the hybrid modeling method to control and maintain voltage stability. The theory of discrete event systems (DES) monitoring is proposed to address power system problems such as challenges of controlling the voltage of ULTC-equipped transformers, which are extensively used in transmission systems to protect instantaneous load changes.

In [9], an innovative supervisor localization technique has been utilized to solve the voltage control problem in a distributed method that has a simpler and more transparent structure than the supervisory control method utilized in the present study. Moreover, the voltage decay in power systems is examined to study the voltage decay, and techniques related to voltage stability are summarized [10].

In [11], the role of distribution grid control against a steady voltage has been examined in a case study. Furthermore, in [12], a robust PI controller is designed to reach the desired control objective. The robustness of PI is guaranteed by the Lyapunov stability theory.

Methods available to analyze voltage stability include those based on power flow Jacobian matrix as the minimum eigenvalue [13], test function [14], tangent vector [15], Markov chain's probability [16], indices determined by Lagrange multipliers [17], Jacobian matrix singularity, small disturbance voltage stability (SDVS) [18], and bus voltage ranking index [19], [20].

Therefore, for an easier analysis of stability and voltage regulation, followed by the supervisory controller design, the automatic hybrid modeling formulation is employed in this paper. In this way, the space state and transfer function are obtained. After this step, system stability can be easily evaluated. In the proposed method, to present the hybrid model, discrete events, including the presence and absence of disturbances and voltage control elements, fault, sudden load increase, capacitor bank, and ULTC transformer, are used.

Herein, voltage stability is examined for five system modes. In Sections III and IV, first, two scenarios of Sm(F,T,C) and Sm(L,T,C) are defined in which definitions are presented for various system modes (Sm). The controller is designed by hybrid automata (HA) modeling in power systems under disturbance resulting from fault (F) and a sudden increase in load (L). The supervisory controller is designed using ULTC (T) and a capacitor bank (C). The discrete events system (DES) is presented, and then the overall HA modeling for each system consisting of 12 modes is performed.

The simulation results show that the voltage control process is implemented and examined by applying the disturbance caused by a fault and a sudden increases in load for a *WSCC* 9-bus and IEEE 30-bus system using Matlab and Digsilent; a supervisory controller is also designed in the presence of disturbance resulting from a three-phase fault to earth and a sudden increase in load. Finally, the voltage stability in the controller is examined using four approaches of "buses' voltage", "generators' rotor angle", "the eigenvalues of the system", and "the stability theory of the switched linear systems". Simulation results demonstrate that the proposed using HA modeling is easier and more accurate for power system voltage stability.

The rest of this paper is organized as follows: Section II describes the hybrid system and hybrid automata (HA). In Section III, voltage stability is examined for five system modes. Section IV presents the proposed HA modeling for two scenarios of Sm(F,T,C) and Sm(L,T,C). A supervisory controller for two scenarios is also designed. In Sections V and VI, simulation results are discussed. Finally, in Section VII, the conclusions derived from this work are presented.

II. HYBRID SYSTEMS

The introduction of the supervisory control theory (SCT) provided the necessary background for applying discrete event models (DEMs) to the processes of the physical world; consequently, a wide range of industrial systems, including

traffic control systems, manufacturing line systems in industrial plants, telecommunication systems, database systems, and electrical power systems have been studied [21]. A hybrid dynamic system is a system whose behavior is influenced by continuous and discrete dynamics. As an important feature of hybrid systems, some dynamics are time-driven while some are event-driven. In time-driven systems, the mechanism of the system mode change is based on differential equations where the modes vary over time. In event-driven and DES systems, changes in the system mode depend on the events that occur, not the time [21], [22].

The continuous system is usually a physical and natural system with a continuous behavior. The communication between two continuous and DES systems is facilitated by an interface and the use of communication signals. Some major types of hybrid dynamic systems include the HA machine, timed Petri nets, and switched systems [22].

A. Hybrid Automata (HA)

Hybrid automata (HA) machines provide a general modeling formulation for the analysis of hybrid systems. HA is utilized to model dynamic systems which include both continuous and discrete components [22].

HA can be expressed as an eight-parameter relation as follows [22]:

$$H = (Q, v, f, Init, Inv, \theta, G, R)$$

- Q is a limited set of discrete modes (control locations) of the system; $Q = \{q_1, ..., q_k\}$, $q \in Q$;
- v refers to a limited set of continuous states of the system, and X is the continuous state space;
- $\dot{x} = f(q, x)$ is the continues dynamics, and f denotes the functions related to the continues dynamics of the system $(q, x) \in Q \times v$;
- $Init \subseteq Q \times R^n$ is a set of the system's initial modes and conditions;
- $Inv : Q \to 2^{R^n}$ is the description of the characteristics of locations; it is, in fact, a prerequisite for staying in or passing the continuous modes of the system. As long as the prerequisite related to each location is mandatory, there is a continuous dynamic for that location and it can operate.
- $\theta \subset Q \times Q$ is the interface of the system's transitions graphically depicted as arcs between discrete modes.
- $G : \theta \to 2^{R^n}$ is the system guard prerequisite; it constrains the continuous dynamics' function. The prerequisite is applied to the arcs of the HA model.
- $R : \varepsilon \to 2^{R^n} \times 2^{R^n}$ resets the map to its initial mode.

Based on this mapping, one can find the location of the continuous state in the subset of the continuous state space that is not used in the power system [22].

III. Examining Voltage Stability of Power Systems Without a Controller

When evaluating stability, it is essential to consider system behavior when it is operated under a small or large transient disturbance. Disturbances applied to the grid in this study include:

I) Three-phase fault to Earth on the most sensitive bus of the grid

The most sensitive bus is sensitive to sudden voltage changes and makes the network/grid unstable.

II) A sudden increase in load

In this section, voltage stability is examined for five system modes:

- Under normal circumstances
- In the presence of a fault in the grid
- In the presence and absence of a fault and change in the tap changer
- In the presence and absence of a fault and a sudden increase in load
- In the presence and absence of a fault and a capacitor bank

The methods used to monitor system stability include:

a) The voltage of the busses [1], [23] and [24].
b) The rotor angle of generators [1], [23].
c) The eigenvalues of a system [1], [23] and [25].
d) The stability theory of the switched linear systems [26], [27] if the controller is present.

According to previous studies, in the absence of a controller, system stability is examined in three ways "a", "b" and "c", while in the presence of a controller, system stability is examined in four ways "a", "b", "c" and "d".

IV. Hybrid Automata Controller Design and Modeling

The purpose of designing a controller for a grid is to provide stability and voltage control. Controller inputs include the voltage of the most sensitive bus of the grid and ULTC.

i) The voltage of the most sensitive bus of the grid; the control of the ULTC T tap changer status is adjusted to the voltage of the most sensitive bus. The standard voltage deviation of buses is 5%, i.e. A bus voltage of $1.05 < V_{bus} > 0.95$ is standard and permitted [1], [28].

ii) The ULTC tap changer has state "3"; for each increase in the tap changer, a 3% increase in voltage is applied to the grid.

A bus voltage <0.95 indicates a voltage drop on the bus. Some important controller functions include:

• After applying the fault to the most sensitive bus, the system becomes unstable and a voltage drop occurs in the gird [23]. As a result, the tap changer first shifts from state 1 to state 2, and then (if the drop in voltage occurs again in the

system or under instability) shifts to state 3.

• If the tap changer is in state 3 and there is also a drop in voltage, or when the system is unstable, then the tap changer remains in state 3.

• The voltage of the most sensitive bus is > 1.05, $V_{bus} > 1.05$ and a stable system puts the capacitor bank out of the circuit.

• When the tap changer is in state 3 and the bus voltage is > 0.95, $V_{bus} > 0.95$, this indicates that there is no voltage drop in the system. Therefore, the tap changer returns to state 2. If there is no voltage drop again, the tap changer will return to state 1 (initial mode).

A. Modeling of HA and the performance of a supervisory controller under the disturbance caused by a three-phase fault to Earth

For HA modeling, discrete states of the system are first introduced; these are a combination of discrete events, including disturbance resulting from fault, in the presence and absence of a fault, in the presence and absence of voltage control elements such as a capacitive bank, and an increase and decrease in ULTC tap changer with three states (Table I).

TABLE I
DESs WITH THE SCENARIO OF SM (F, T, C)

Event Name	Value	Explanation of an event
F	1	Presence of a fault
	0	Lack of a fault
T	1	State of tap trans 1
	2	State of tap trans 2
	3	State of tap trans 3
C	1	Presence of a capacitor
	0	Lack of a capacitor

The power system is represented by the symbol S and the mode number m. If the combined modes of the system are defined as Sm(F,T,C) scenario, then all the combined states occurring for the system include 12 modes as presented in Table II.

TABLE II
SYSTEM MODES WITH SCENARIO SM (F,T,C)

Sm	F	T	C
S1	0	1	0
S2	0	1	1
S3	0	2	1
S4	0	3	1
S5	1	1	1
S6	1	2	1
S7	1	3	1
S8	0	2	0
S9	0	3	0
S10	1	1	0
S11	1	2	0
S12	1	3	0

Each mode has a specific continuous dynamic. For example, mode "S3" represents the continuous dynamics of the system with the presence of faults, the tap changer in status 2, and in the absence of capacitors in the grid.

According to Fig. 1, the system initially operates in the normal condition (initial state of the system S1) under a constant voltage and the desired amplitude (voltages of all buses are > 0.95). The system remains in the S1 state until the fault is applied to the system (i.e. F = 0); when the fault is applied to the most sensitive bus of the system (i.e. F = 1), the system tends to become unstable and shifts from S1 to S2. To improve the voltage of buses and the grid stability, the T tap changer increases again and shifts from status 1 to state 2, i.e. It shifts to state S3. In the event of instability, the T tap changer increases again and shifts from status 2 to state 3, i.e. It shifts to state S4. Constant system instability puts the capacitor bank into the circuit, i.e. The system shifts to state S7. After removing the fault (i.e. F = 0), the system shifts to state S12, and then, it reaches its initial state; it first puts the capacitor bank out of the circuit, and the system shifts to state S9; then, the T tap changer shifts from state 3 to state 2 while the system shifts to state S8; finally, the tap changer shifts to state 1, the system returns to its initial state, and the voltage of all buses reaches > 0.95. Fig. 1 displays the HA model of the closed-loop system..

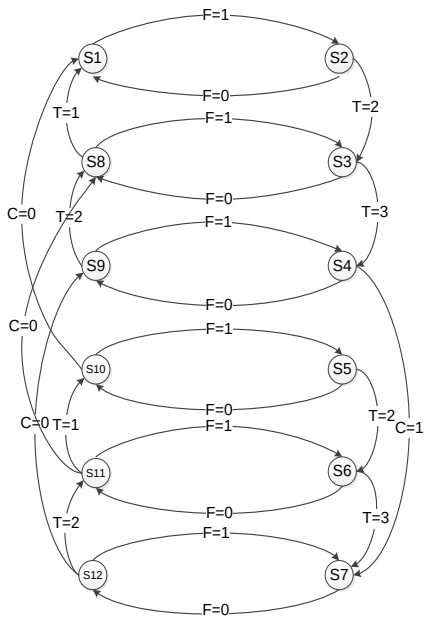

Fig. 1. HA model of the Sm(F,T,C) scenario

The HA model of the system is an eight-parameter [22] relation (Equ. (1)).

$$H = (Q, v, f, Init, Inv, \theta, G, R) \quad (1)$$

Q is a set of discrete states of the system as presented in Table II and in Equ. (2):

$$Q \in \{S1, S2, S3, S4, S5, S6, S7, S8, S9, S10, S11, S12\} \quad (2)$$

v is a set of continuous variables of the system as shown in Equ. (3) and defined in the DIgSILENT software [29]:

$$v \in \{phi, speed, psie, psiD, psiX, psiQ\} \quad (3)$$

Descriptions of continuous variables are provided in Table III.

TABLE III
CONTINUOUS VARIABLES [29]

Name of variables	Name of Unit	Explanation
Speed	p.u	speed
Phi	rad	Rotor angle
Psie	p.u	Exitation Flux
PsiD	p.u	Flux in D - Winding
Psix	p.u	Flux in X - Winding
psiQ	p.u	Flux inQ - Winding
Speed	p.u	speed

In steady-state systems, the eigenvalues are obtained by Modal Analysis in Digsilent. After that, the transfer function will be obtained.

The continuous dynamics of the system can be represented as $\dot{x} = A_i(x)$, including the continuous equations of each of the 12 states of the system. To obtain A_i in Equ. (4), given the eigenvalues corresponding to each state, the denominator of the transfer function for the system $P_i(S)$ is obtained by Equ. (5). Then, the matrices A of each state of the system are obtained by the canonical realization of its controller (explained in Appendix A).

$A_i \in \{A_1, A_2, A_3, \ldots, A_{12}\}$, $i = 1,2,...,12$ *and i* stands for the number of these states (4)

$$A_i = \begin{bmatrix} 0 & 1 & 0 & \ldots & 0 \\ 0 & 0 & 1 & \ldots & 0 \\ \vdots & \vdots & \vdots & \ldots & \vdots \\ 0 & 0 & 0 & \ldots & 1 \\ -a_0 & -a_1 & -a_2 & \ldots & -a_{n-1} \end{bmatrix}$$

$$P_i(S) = S^n + a_{n-1}S^{n-1} + \ldots + a_1 S + a_0 \quad (5)$$

n is the number of eigenvalues;

$$Inv \in \{F=0, F=1\} \quad (6)$$

Inv is expressed according to Equ. (6); for example, the system first operates in the normal condition (initial state; S1) under constant voltage and optimal amplitude. The initial state of the system is expressed as Init = S1.

System guards, under the same prerequisite intended for the HA arcs, are expressed as Equ. (7).

$$G \in \{F=0, F=1, C=0, C=1, T=1, T=2, T=3\} \quad (7)$$

B. Modeling of HA and the supervisory controller performance under disturbance caused by a sudden increase in load

For HA modeling, discrete states of the system are first introduced; these are a combination of discrete events, including disturbances caused by a sudden increase in load and without a sudden increase in load (normal condition for load), the presence and absence of voltage control elements such as a capacitive bank, and the increase and decrease of the ULTC tap changer with the three states (Table IV).

TABLE IV
DESS WITH THE SCENARIO SM(L, T, C)

Event name	Value	Explanation of an event
L	1	sudden increase of load
	0	Lack of a sudden increase of load
T	1	State of tap trans 1
	2	State of tap trans 2
	3	State of tap trans 3
C	1	Presence of a capacitor
	0	Lack of a capacitor

Combined modes of the system are defined as the Sm(L,T, C) scenario. Overall, all the combined modes occurring for the system constitute 12 separate modes (Table V).

TABLE V
SYSTEM MODES WITH SCENARIO SM(L,T,C)

Sm	L	T	C
S1	0	1	0
S2	0	2	0
S3	0	3	0
S4	0	1	1
S5	0	2	1
S6	0	3	1
S7	1	1	0
S8	1	2	0
S9	1	3	0
S10	1	1	1
S11	1	2	1
S12	1	3	1

The controller consists of 12 discrete modes, each with a special continuous dynamic. The system first operates in the normal condition (initial state of the system; S1) under constant voltage and optimal amplitude (all bus voltages are s > 0.95). After a sudden rise in load at one of the most sensitive loads of the grid, the system shifts to the S7 mode. To improve bus voltage and grid stability, the T tap changer increases and shifts from state 1 to state 2, i.e. The system shifts to state S8. If the bus voltage does not improve, the T tap changer will rise again and shift to state 3, i.e. The system shifts to state S9. Constant voltage drop puts the capacitor bank in the circuit, i.e. The system shifts to state S12. Improving the bus voltage puts the capacitor bank out of the circuit (C = 0); this causes the system to first shift to state S9 and then (if necessary) state S8; and finally, the T tap changer reaches status 1, i.e. The system shifts to state S7. HA modeling is performed for a scenario consisting of 12 system modes. The HA graph for the Sm(L,T,C) scenario is presented in Fig. 2.

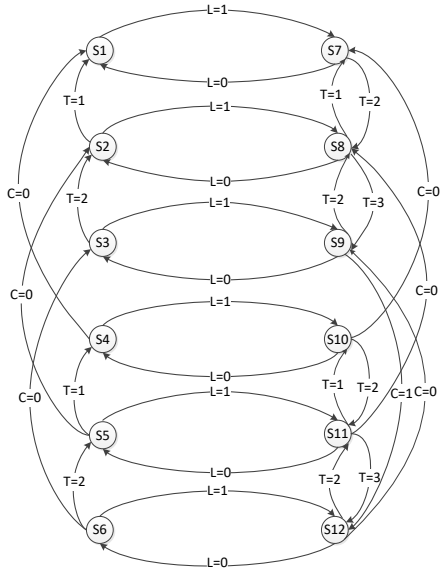

Fig. 2. HA model of the Sm(L,T,C) scenario

The continuous dynamics of the system can be represented as $\dot{x} = A_i(x)$, including the continuous equations of each of the 12 system states. To obtain A_i in Equ. (4), the denominator of the transfer function $P_i(S)$ for the system is obtained by Equ. (5). Subsequently, the matrices A of each state of the system are obtained by the canonical realization of its controller (Section A, and explained in APPENDIX A,).

$$Inv \in \{L=0 , L=1\} \quad (8)$$

Inv is expressed by Equ. (8). First, the system operates in a normal condition (initial state; S1). The system remains in the S1 state until a sudden rise in load is applied (i.e. L = 0). If there is a sudden increase in load in the system (L = 1) and when the tap changer is in status 3 and there is a capacitor (C = 1) i.e. in state S12, then the unstable system will remain in instability because the tap changer is in status 3 and the capacitor is available. Nevertheless, if a sudden increase in load is removed (L = 0), then the system shifts to state S6 and becomes stable. The initial state of the system is expressed as Init = S1. System guards are expressed as Equ. (9).

$$G \in \{ L=0, L=1,C=0 ,C=1 , T=1 , T=2 , T=3 \} \quad (9)$$

The hybrid modeling method applies to all power systems; for example, in this study, we implemented and simulated the method for the 9-bus power system.

V. Simulation Results for First Case Study

The power system studied is a standard WSCC 9-bus, three-machine system. Fig. 3 illustrates the status of machines and buses and all impedances and admittances (in p.u) [28]. The data of the system are given in APPENDIX A, TABLE XI.

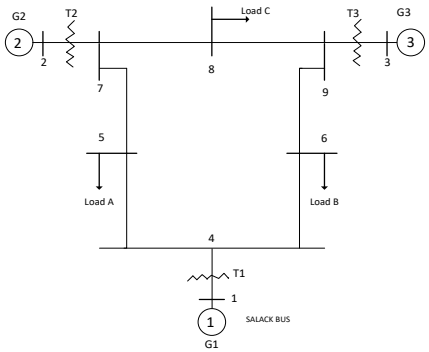

Fig. 3. standard WSCC 9-bus, three-machine system [28]

A. *Maintaining the 9-bus system's voltage without a controller*

The stability of the system is investigated for five modes, according to Sections III and B. According to [23], the fault was applied to bus 7 because it is the most sensitive bus to sudden voltage changes and can cause grid instability. The fault was applied to bus 7 at ts = 0.1 sec. It has been demonstrated that a sudden increase in load A will drive a voltage drop in the grid buses [24]. The stability of the system was investigated in the four manners presented in Section III. It was found that, in the stable mode, the system is unstable in all cases in the presence of a fault in bus 7 and will no longer be stable even in the presence of a capacitor bank. In steady-state, each system mode has its continuous equations and is considered as a discrete state for a hybrid system. The results of examining the stability of the 9-bus system are presented in Table VI.

TABLE VI
RESULTS OF EXAMINING THE STABILITY OF THE 9-BUS SYSTEM WITHOUT A CONTROLLER

States of system	Voltage of buses, p.u.	Stability of steady and transient state	Explanations
Normal system	$V_{bus} > 0.95$	Stable	No voltage drop
Increase of tap trans	$V_{bus} > 0.95$	Stable	No voltage drop
Activity of capacitor	$1.05 < V_{bus} > 0.95$	Stable	No voltage drop
Sudden increase of Loads	A few buses less than 0.95	Stable	Small voltage drop in buses
Five mentioned states with presence of fault	$V_{bus} < 0.95$	Instable	Severe voltage drop in the busses

B. *Simulation results and examining voltage control under a disturbance caused by a three-phase fault to Earth from the Sm(F,T,C) scenario*

Responses were evaluated by simulation in DIgSILENT. Under normal circumstances, the system maintains its steady state because no faults are applied to the system. The following events are applied to the system to monitor how the voltage is controlled. The ULTC tap controller is intended for

transformer T2.

Transformer T2 has a three-mode tap with a 3% rise in voltage at each phase of tap change. In t=3 sec, a three-phase fault-to-Earth fault is applied to the 7th bus for 1 second.

Capacitor placement is fulfilled via the genetic algorithm to minimize total loss. Load A is the optimal place to install the capacitor, where the grid has the least losses.

At t=4 sec, a 100MVar capacitor bank is applied to the grid in two 50MVar capacitance steps in the 5th busbar and close to Load A. Grid stability is now examined using a capacitor and a three-phase tap changer controller in the grid. System stability is evaluated by four approaches, including "buses' voltage", "generators' rotor angle", "the eigenvalues of a system", and "the stability theory of the switched linear systems".

I) Bus Voltage

When the fault is applied, the bus voltage drops; the bus voltage improves and the system reaches a stable mode after putting the capacitor in the grid (at t=4 sec), applying 107.17 MVar of reactive power into the grid and controlling voltage by changing the T2 tap changer (Fig. 4).

After applying the fault, the buses' voltage is improved by the ULTC supervisory closed-loop controller system (Table VII).

In [30], an energy margin constrained online coordinated voltage control (CVC) algorithm was defined. The energy function model was established based on the detailed device models that included the effects of shunt capacitor banks, reactive power output of generators, and under-load-tap-changers (ULTCs). To control the voltage, the control equipment was checked separately. The simulation results for the three-machine system showed that in CVC method, by applying the fault to bus 3, voltage controls were performed using each of the capacitor banks and ULTC [30]. The average voltage of bus 3 was 1.012 p.u and 0.82 p.u in the presence of capacitive banks and ULTC, respectively. In the HA method, the voltage of all buses was in the steady state and above 1p.u., so comparing the HA and CVC methods showed that the HA method was more effective in voltage improvement.

TABLE VII
BUSES' VOLTAGE OF SYSTEMS AND ITS SCENARIO SM(F,T,C)

Name of bus	normal system, p.u	without controller, fault in Bus 7, p.u	within ULTC and capacitor, Sm(F,T,C), p.u
Bus 1	1.04	0.717	1.04
Bus 2	1.025	0.194	1.025
Bus 3	1.025	0.202	1.025
Bus 4	1.063	0.595	1.043
Bus 5	0.996	0.565	1.044
Bus 6	1.013	0.417	1.042
Bus 7	1.026	0	1.04
Bus 8	1.016	0.063	1.035
Bus 9	1.032	0.153	1.043

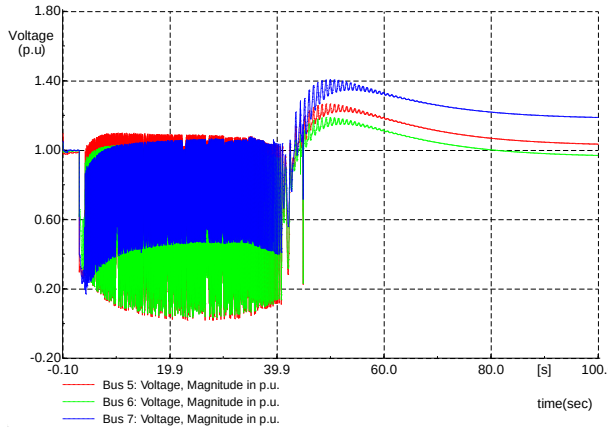

Fig. 4. Voltage of the system's buses 5, 6, and 7 after applying the fault, with a controller

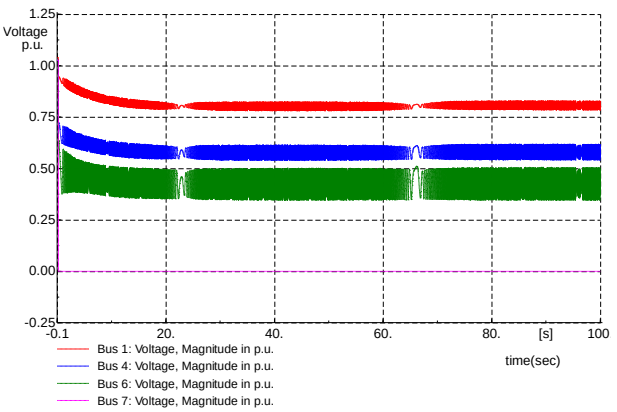

Fig. 5. Voltage of the system's buses 1, 5, 6, and 7 after applying the fault, without a controller

At t=3 sec, when the fault is applied to the 7th bus, the bus voltage drops, and the tap changer first shifts to status 2 and then status 3 (its highest level). From the 3rd sec to about 40th sec, when the capacitor is also applied to the grid, the bus voltage oscillates and the tap changer shifts from status 2 to status 3. After the 40th sec, the voltage of the system's buses improves and the tap changer returns to status 1, i.e. The voltage is controlled by the ULTC (Figs. 4 and 6).

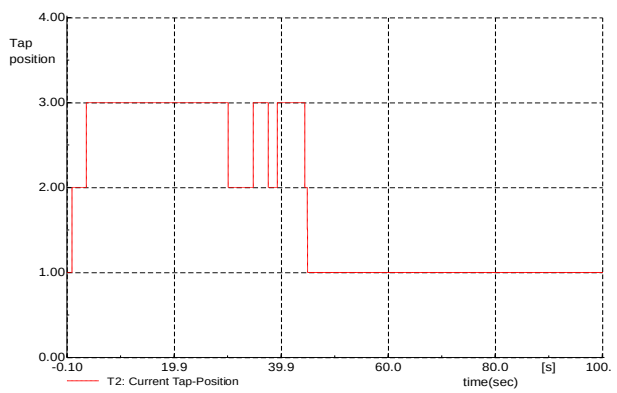

Fig. 6. Tap changer TC changes (T2), with a controller

II) Generator's rotor angle

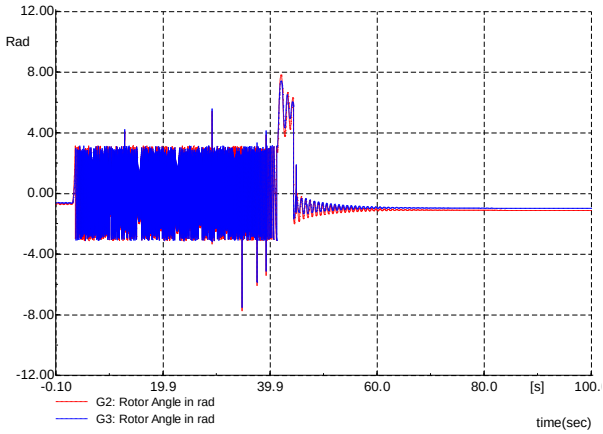

Fig. 7. Rotor angle of generator G3,G2, with a controller

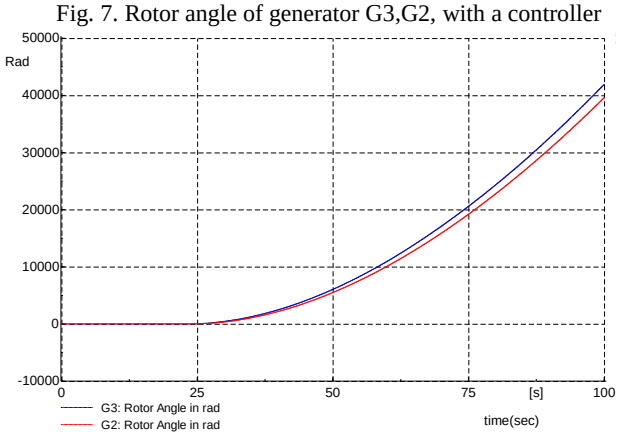

Fig. 8. Rotor angle of generator G3,G2, without a controller

Between t=3 sec, when the fault is applied to the 7th bus, to about the 40th sec, the rotor angle of the generators oscillates; after the 40th sec, the rotor angle of the generators will damp over time, indicating the stability of the system (Fig. 7).

III) The eigenvalues of a system

The eigenvalues of the system having a negative true root indicate the stability of the system at a steady state.

TABLE VIII
THE EIGENVALUES OF THE SYSTEM

Row	Eigenvalue	Row	Eigenvalue
1	0	10	-13.006
2	-55.519	11	-13.206
3	-37.196	12	-4.110
4	-0.744+j13.852	13	-2.805
5	-0.744-j13.852	14	-0.099+j0.049
6	-0.015+j9.409	15	-0.099+j0.049
7	-0.015-j9.409	16	-0.172
8	-15.217	17	-0.140
9	-11.704		

The results of controller simulation using the HA model, examining the voltage response of the buses, and considering the rotor angle of the generators show that the system is also stable in a transient state.

IV) The stability theory of the switched linear systems

According to theory 1 provided in [26] about the stability of a switched linear system, if some subsystems are stable while others are not, then to achieve overall stability, the duration of system operation in stable modes must be longer than the duration of operation in unstable modes; this depends on the system's working growth and decline rate in unstable and stable modes [26], [27]. According to the above theory and given that the system has a longer operating time in the stable mode, it can be conservatively concluded that the entire system is stable.

C. Simulation results and examining voltage control under disturbance caused by a sudden increase in load from the Sm (L,T,C) scenario

Responses were evaluated by simulation in DIgSILENT. A 9-bus power system was considered with a three-phase T2 tap changer and a 3% increase in voltage at each step of tap change.

A 100MVar reactive power compensation capacitor bank is applied to the grid in two 50MVar capacitance steps in the 5th busbar and close to Load A. After simulating at t=100 sec, at the 0.013th sec, the active power of load A increases by 25% while the reactive power of load A suddenly increases by 5%; the situation puts the capacitor bank into the circuit for reactive power compensation.

When the load rises suddenly, the buses' voltage first drops, and the tap changer shifts to status 3; after putting the capacitor bank into the circuit, the buses' voltage improves (reaches > 0.95 p.u.) and the tap changer returns to status 1 (Table IX).

The system stability is measured by four approaches, including "buses' voltage", "generators' rotor angle", "the eigenvalues of a system", and "the stability theory of the switched linear systems".

I) Buses Voltage

After performing load distribution calculations, the buses' voltage somewhat drops in the Sm(L,T,C) scenario due to disturbances; it is possible to address the problem using reactive power control equipment (Table IX).

TABLE IX
BUSES' VOLTAGE OF NORMAL SYSTEMS AND ITS SCENARIO SM-(L,T,C)

Name of bus	Voltage of bus, normal system, p.u	Voltage of bus, without controller, p.u	Voltage bus within Sm(L,T,C), p.u
Bus 1	1.04	1.006	1.008
Bus 2	1.025	0.92	0.957
Bus 3	1.025	0.91	0.973
Bus 4	1.063	0.98	0.999
Bus 5	0.996	0.933	0.983
Bus 6	1.013	0.91	0.979
Bus 7	1.026	0.964	0.983
Bus 8	1.016	0.90	0.972
Bus9	1.032	0.95	0.985

At t=0.013 sec, load A suddenly increases by 25%, the buses' voltage drops first and, at t=0.2 sec, the capacitor bank enters the circuit and leads to the application of -38.6MVar reactive power into the grid; this improves the buses' voltage (Fig. 9).

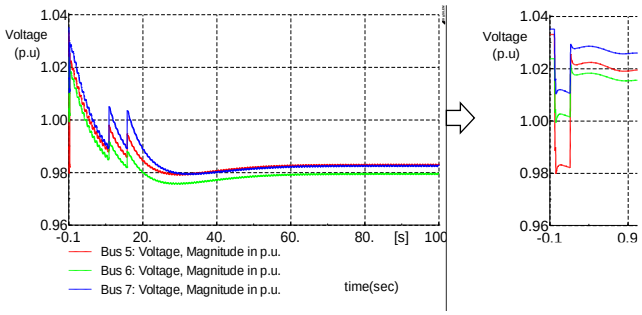

Fig. 9. Voltage of Bus 5, Bus 6, and Bus7 of the system, with a controller (zoom -0.1 to 1 second)

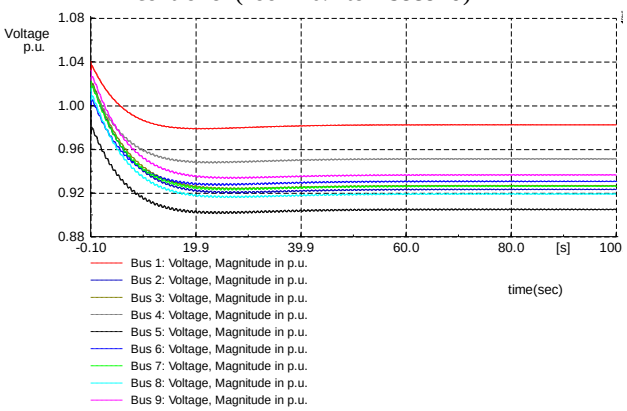

Fig. 10. Voltage of the system's buses, without a controller

As the buses' voltage drops, the tap changer shifts from status 1 to status 2 and then status 3. As the bus voltage improves while the capacitor is present, the tap changer remains in status 3 (Fig. 11).

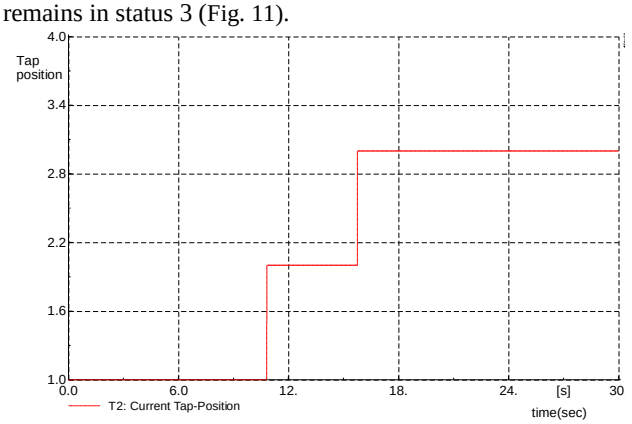

Fig. 11. Tap changer changes (T2), with a controller

II) Generators' rotor angle

At t=0.013 sec, the buses' voltage drops first and the rotor angle of the generators increases; then, the rotor angle of the generators dampens and converges while oscillating, indicating that the system is stable (Fig. 12).

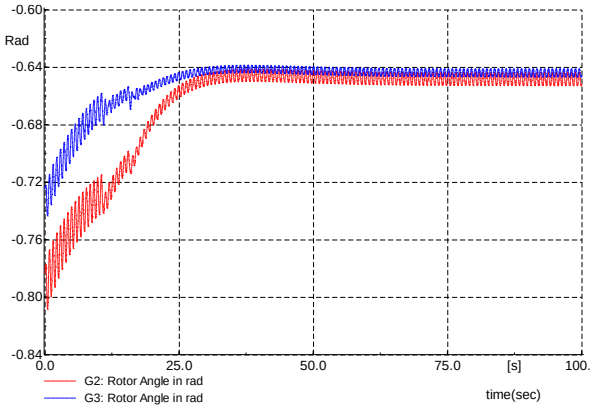

Fig. 12. Rotor angle of generators G2, G3, with a controller

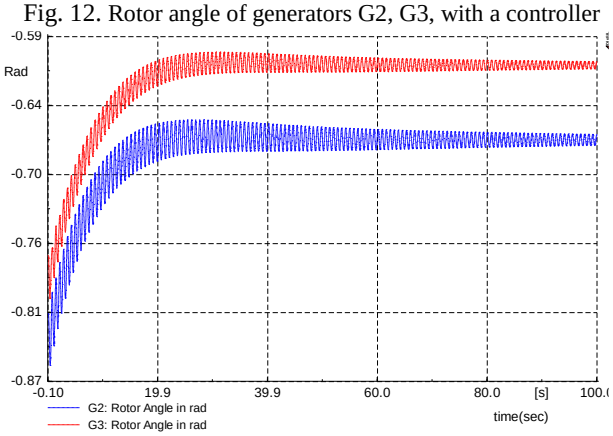

Fig. 13. Rotor angle of generators G2, G3, without a controller

III) The eigenvalues of a system

Considering the rotor angle of the generators as state variables, after calculations, 17 eigenvalues are obtained (Table X). The eigenvalues of the system having a negative true root indicate the stability of the system at a steady state.

TABLE X
THE EIGENVALUES OF THE SYSTEM

Row	Eigenvalue	Row	Eigenvalue
1	0	10	-12.98
2	-54.92	11	-13.2
3	-36.84	12	-3.92
4	-0.85+j13.81	13	-2.81
5	-0.85-j13.81	14	-0.2
6	-0.05+j9.29	15	-0.149
7	-0.05-j9.29	16	-0.108+j0.042
8	-15.20	17	-0.108-j0.042
9	-11.62	-	-

IV) The stability theory of the switched linear systems

As with paragraph IV of the controller, section B, according to prerequisite 1 in [26], and given that the duration of system operation in the stable mode is higher, it can be conservatively concluded that the entire system is stable.

VI. SIMULATION RESULTS FOR THE SECOND CASE STUDY

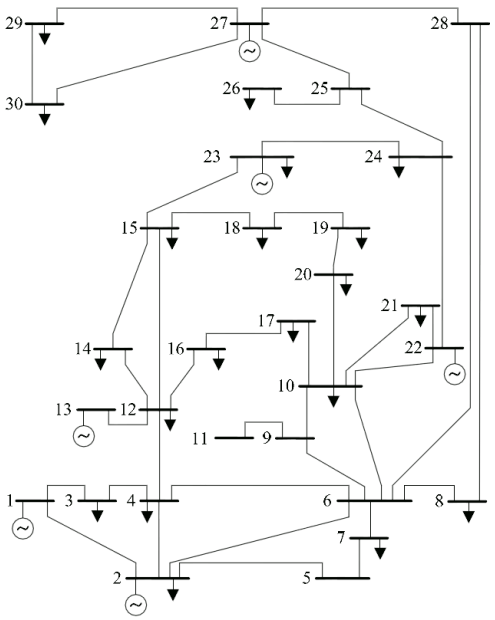

Fig. 14. IEEE 30-bus system [1]

the IEEE 30-bus system is illustrated in Fig. 14 with middle transmission lines, and the electrical property of each line is described by the model [1]. The simulation results of the stability analysis of the IEEE 30-bus system similar to the 9-bus system are presented in Table VI.

A. Simulation results and examining voltage control under a disturbance caused by a three-phase fault to Earth from the Sm(F,T,C) scenario

Responses were evaluated by simulation in DIgSILENT. The following events are applied to the system to monitor how the voltage is controlled. The ULTC controller is intended for transformer Trf4.

Transformer Trf4 has a three-mode tap with a 3% rise in voltage at each phase of tap change.

Capacitor placement is fulfilled via the genetic algorithm to minimize total loss. By running the algorithm, the optimal place for installing the capacitor bank is obtained in Bus 10 and Bus 24 where the capacity must be 19 and 4.3 Mvar, respectively, to compensate for the reactive power. After fulfilling the simulation for a 30-sec time horizon, a three-phase to ground fault during the period of 0.1-0.5 seconds is imposed on Bus 28.

The grid stability is now examined using a capacitor and a three-phase tap changer controller in the grid. The stability analysis of the system in the presence of the supervisory controller is investigated from four aspects: buses' voltage, generators rotor angle, eigenvalues of the system, and the stability theorem of switched linear systems.

I) Bus Voltage

When the fault is applied, the bus voltage drops; the bus voltage improves and the system reaches a stable mode after putting the capacitor in the grid (at t=0.1 sec), applying 19 and 4.3MVar reactive power into the grid, and controlling voltage by changing the Trf4 tap changer (Fig. 15).

After applying the fault, the buses' voltage is improved by the ULTC supervisory closed-loop controller system.

In [30], an energy margin constrained online coordinated voltage control (CVC) algorithm was defined. The energy function model was established based on the detailed device models that included the effects of shunt capacitor banks, reactive power output of generators, and under-load-tap-changers (ULTCs). The simulation results for the IEEE 30-bus system demonstrated that in CVC method, by applying the fault on lines 25–27 and lines 6-28, voltage controls were performed using the ULTC as well as both ULTC and capacitor [30]. In the HA method, the voltage of all the buses was in the steady state and above 1p.u., so comparing the HA and CVC methods represented that the HA method was more effective than the CVC method in voltage improvement (TABLE XI).

TABLE XI
COMPARISION OF COMPUTATION BUSES'VOLTAGE BY DEFFERENT METHODS FOR THE IEEE 30-BUS SYSTEM

		proposed method(HA)	CVC method[30]	
Name of bus	without controller, fault in Bus 28, p.u	within Sm(F,T,C), Capacitor and ULTC, p.u	ULTC, Line 25-27 tripping , p.u	Capacitor and ULTC, Line 6-28 tripping , p.u
Bus 05	0.16	1.03	1.01	1.01
Bus 06	0.08	1.032	1.01	1.02
Bus 07	0.11	1.035	1.01	1.01
Bus 08	0.1	1.032	1.00	1.01
Bus 23	0.08	1.031	1.01	1.01
Bus 24	0.07	1.037	0.99	1.025
Bus 26	0.04	1.021	0.98	1.012
Bus 28	0	1.02	1.01	1.001
Bus 30	0.03	1.02	1	0.99

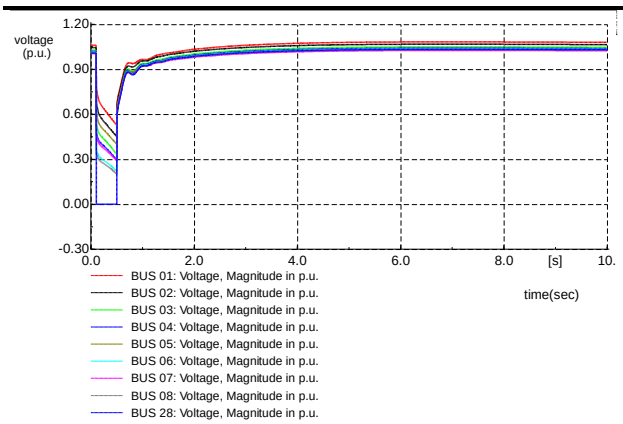

Fig. 15. Voltage of Bus 2 to Bus 8 and Bus 28 of the system, with a controller

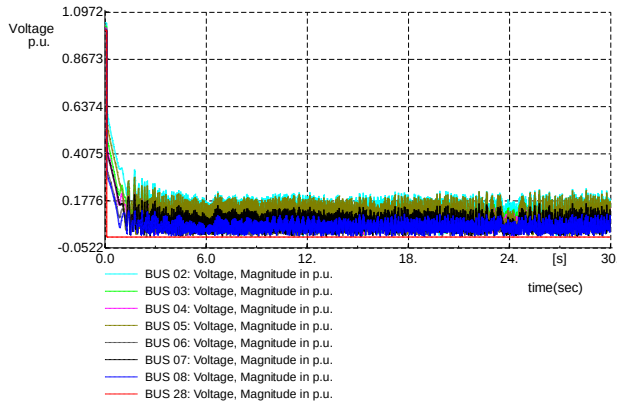

Fig. 16. Voltage of Bus 2 to Bus 8 and Bus 28 of the system, without a controller

Evidently, at t=0.1sec, when the fault is applied to Bus 28, the bus voltage drops, and the tap changer first shifts to status 2 and then status 3 (its highest level). Subsequently, the capacitor is also applied to the grid. The voltage of the system's buses improves and the tap changer returns to status 1, i.e. The voltage is controlled by the ULTC (Figs. 15 and17).

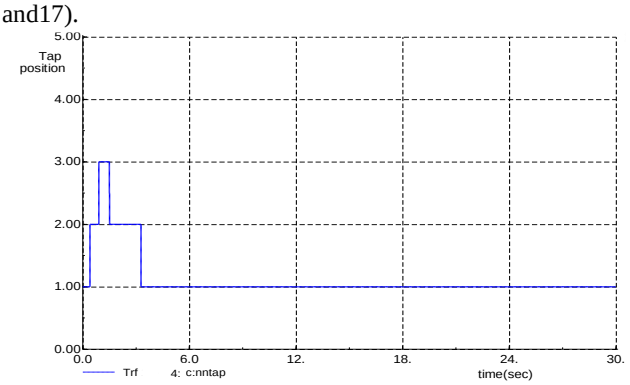

Fig. 17. Tap changer ULTC changes (Trf4)

II) Generators' rotor angle

At t=0.1 sec, the buses' voltage drops first and the rotor angle of the generators increases; then, the rotor angle of the generators dampens and converges while oscillating, indicating that the system is stable (Fig. 18).

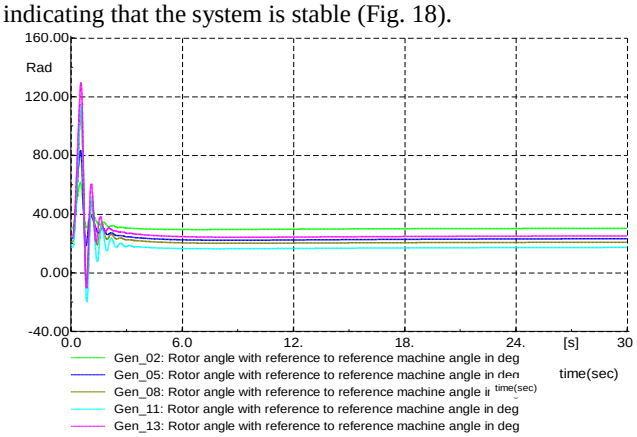

Fig. 18. Rotor angle of generators, with a controller

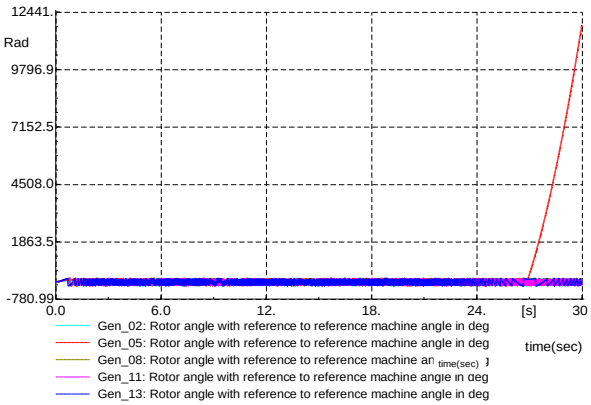

Fig. 19. Rotor angle of generators, without a controller

III) The eigenvalues of a system

Considering the rotor angle of the generators as state variables, after calculations, 36 eigenvalues are obtained. The eigenvalues of the system having a negative true root indicate the stability of the system at a steady-state, shown in APPENDIX A, Second Case Study.

Eigenvalues: $P_i(S)=0$ and i=1,2,3,...,12

IV) The stability theory of the switched linear systems

As with paragraph IV of the controller, Section B, according to prerequisite 1 in [26], and given that the duration of system operation in the stable mode is higher, it can be conservatively concluded that the entire system is stable.

B. Simulation results and examining voltage control under disturbance caused by a sudden increase in load from the Sm (L,T,C) scenario

The conditions of the presence of the capacitor in the system and the changes of the transformer tap (Tr4) to voltage control are the same as in Section A for the Sm (F, T, C) scenario.

After simulating at t=30 sec, at 0.1 sec, the active power of load 30 increases by 50% while the reactive power of load 30 suddenly increases by 10%, and load 02 increases by 30% while the reactive power of load 02 suddenly rises by 10%; this puts the capacitor bank into the circuit for reactive power compensation.

When the load suddenly increases, the buses' voltage first drops, and the tap changer shifts to status 3; after putting the capacitor bank into the circuit, the buses' voltage improves (reaches >0.95 p.u.) and the tap changer returns to status 1. As in Section A, system stability is measured by four approaches.

I) Buses' Voltage

After performing load distribution calculations, the buses' voltage somewhat drops in the Sm(L,T,C) scenario due to disturbances; it is possible to address the problem using reactive power control equipment.

At t=0.1 sec, load 30 suddenly increases by 50%, and load 02 rises by 30%, the buses' voltage drops first and, at t=0.1

sec, the capacitor bank enters the circuit; this improves the buses' voltage (Fig. 20).

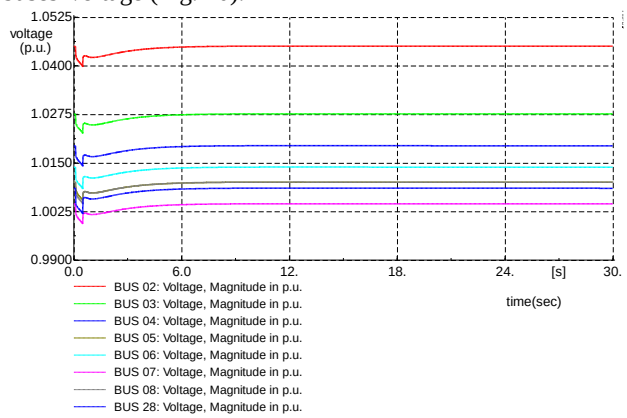

Fig. 20. Voltage of Bus 2 to Bus 8 and Bus 28 of the system, with a controller

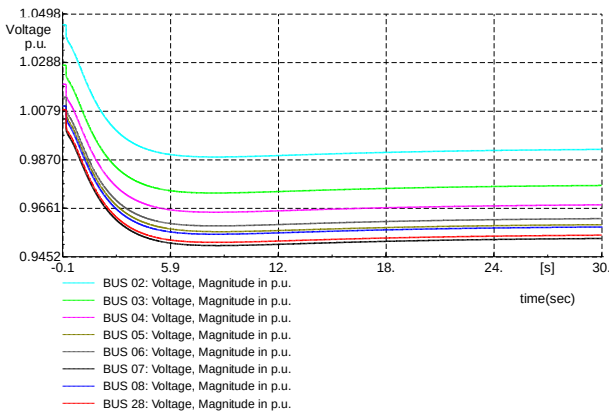

Fig. 21. Voltage of Bus 2 to Bus 8 and Bus 28 of the system, without a controller

As the buses' voltage drops, the tap changer shifts from status 1 to status 2. As the bus voltage improves while the capacitor is present, the tap changer returns to status 1. Fig. 22

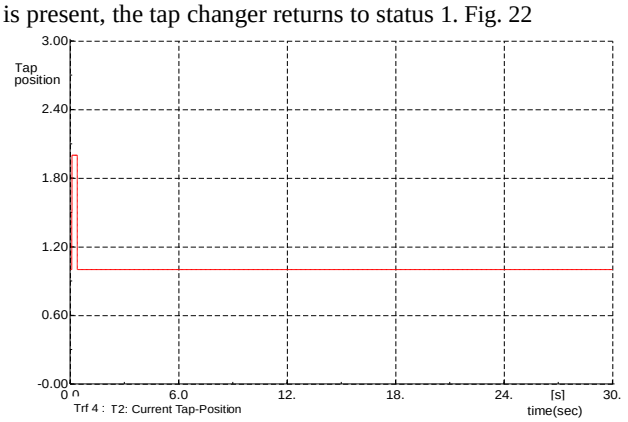

Fig. 22. tap changer ULTC changes(Trf4)

II) Generators' rotor angle

At t=0.1 sec, the buses' voltage drops first and the rotor angle of the generators decreases; then, the rotor angle of the generators reaches a constant value and the system becomes stable.

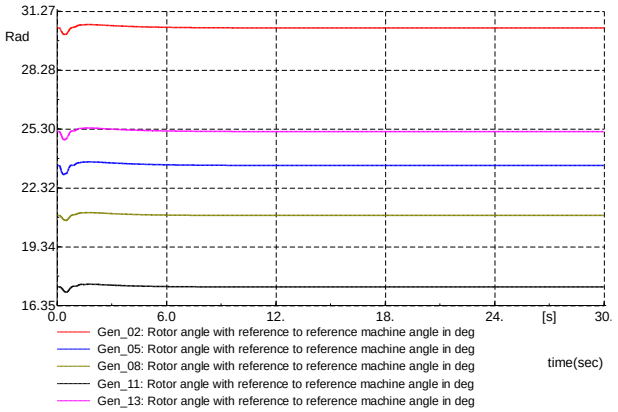

Fig. 23. Rotor angle of generators**,** with a controller

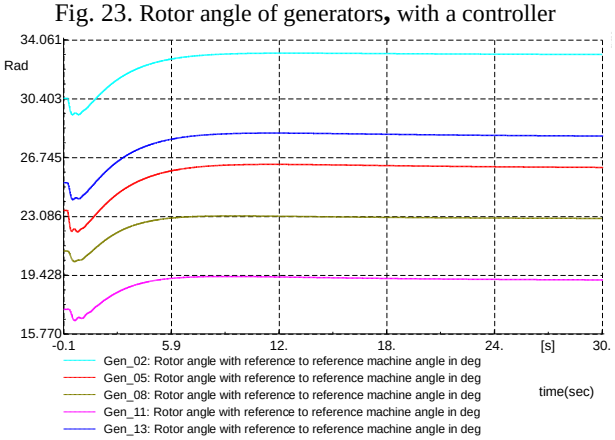

Fig. 24. Rotor angle of generators**,** without a controller

III) The eigenvalues of a system

Considering the rotor angle of the generators as state variables, after calculations, 36 eigenvalues are obtained. The eigenvalues of the system having a negative true root indicate the stability of the system at a steady-state, presented in APPENDIX A, Second Case Study.

Eigenvalues: $P_i(S)=0$ and i=1,2,3,...,12

IV) The stability theory of the switched linear systems

As with paragraph IV of the controller, Section B, according to prerequisite 1 in [26], and given that the duration of system operation in the stable mode is higher, it can be conservatively concluded that the entire system is stable.

VII. Conclusions

Herein, the power system was modeled with a new strategy. Discrete states were a combination of discrete events, including changes in the ULTC tap changer with three states, i.e. the presence and absence of a capacitor bank, presence and absence of disturbances resulting from a fault, and a sudden increase in load. In each case of disturbance, the overall behavior of the system was examined in 12 modes, each with specific continuous dynamics. The power system was then modeled as a hybrid automaton, and a closed-loop system was controlled using the ULTC tap changer and capacitor bank. Voltage control and stability were measured

by four approaches of “buses' voltage”, “generators’ rotor angle”, “the eigenvalues of a system”, and “the stability theory of the switched linear systems”.

The results revealed that the supervisory controller performs well on the control targets, directs the buses' voltage to the permissible range, and is resistant to changing parameters and applying disturbances, i.e. The system is stable in the transient and steady-state. This method applies to other power systems as well.

APPENDIX A

First Case Study: For example, to obtain A_1 matrix by using the eigenvalues of this system, $P_1(S)$ will be calculated as Equ. (10).

$$P_1(S)=s*(s+54.5824)*(s+36.6425)*(s+0.9081-13.7997i)*(s+0.9081+13.7997i)*(s+0.0776-9.2090i)*(s+0.0776+9.2090i)*(s+15.1974)*(s+11.5742)*(s+12.9647)*(s+13.2056)*(s+3.8289)*(s+2.8220)*(s+0.2284)*(s+0.1565)*(s+0.1121-0.0351i)*(s+0.1121+0.0351i) \quad (10)$$

After simplifying the coefficients of $P_1(S)$, they will be shown in Equ. (11) as follows.

$$P_1(S)=S^{17}+a_{16}S^{16}+...+a_1S+a_0 \quad (11)$$

The coefficients related to $P_1(S)$ in Equ. (11) including $a_1, a_2, ..., a_{16}$ will be calculated as presented in Equ. (12).

$$A_1=\begin{bmatrix} 0 & 1 & 0 & 0 & 0 & 0 & 0 & 0 & 0 & 0 & 0 & 0 & 0 & 0 & 0 & 0 & 0 \\ 0 & 0 & 1 & 0 & 0 & 0 & 0 & 0 & 0 & 0 & 0 & 0 & 0 & 0 & 0 & 0 & 0 \\ 0 & 0 & 0 & 1 & 0 & 0 & 0 & 0 & 0 & 0 & 0 & 0 & 0 & 0 & 0 & 0 & 0 \\ 0 & 0 & 0 & 0 & 1 & 0 & 0 & 0 & 0 & 0 & 0 & 0 & 0 & 0 & 0 & 0 & 0 \\ 0 & 0 & 0 & 0 & 0 & 1 & 0 & 0 & 0 & 0 & 0 & 0 & 0 & 0 & 0 & 0 & 0 \\ 0 & 0 & 0 & 0 & 0 & 0 & 1 & 0 & 0 & 0 & 0 & 0 & 0 & 0 & 0 & 0 & 0 \\ 0 & 0 & 0 & 0 & 0 & 0 & 0 & 1 & 0 & 0 & 0 & 0 & 0 & 0 & 0 & 0 & 0 \\ 0 & 0 & 0 & 0 & 0 & 0 & 0 & 0 & 1 & 0 & 0 & 0 & 0 & 0 & 0 & 0 & 0 \\ 0 & 0 & 0 & 0 & 0 & 0 & 0 & 0 & 0 & 1 & 0 & 0 & 0 & 0 & 0 & 0 & 0 \\ 0 & 0 & 0 & 0 & 0 & 0 & 0 & 0 & 0 & 0 & 1 & 0 & 0 & 0 & 0 & 0 & 0 \\ 0 & 0 & 0 & 0 & 0 & 0 & 0 & 0 & 0 & 0 & 0 & 1 & 0 & 0 & 0 & 0 & 0 \\ 0 & 0 & 0 & 0 & 0 & 0 & 0 & 0 & 0 & 0 & 0 & 0 & 1 & 0 & 0 & 0 & 0 \\ 0 & 0 & 0 & 0 & 0 & 0 & 0 & 0 & 0 & 0 & 0 & 0 & 0 & 1 & 0 & 0 & 0 \\ 0 & 0 & 0 & 0 & 0 & 0 & 0 & 0 & 0 & 0 & 0 & 0 & 0 & 0 & 1 & 0 & 0 \\ 0 & 0 & 0 & 0 & 0 & 0 & 0 & 0 & 0 & 0 & 0 & 0 & 0 & 0 & 0 & 1 & 0 \\ 0 & 0 & 0 & 0 & 0 & 0 & 0 & 0 & 0 & 0 & 0 & 0 & 0 & 0 & 0 & 0 & 1 \\ 0 & 5.2\times10^{9} & 1.45\times10^{11} & 1.57\times10^{15} & 7.88\times10^{13} & 1.748\times10^{13} & 4.64\times10^{13} & 1.008\times10^{12} & -1.57\times10^{11} & 1.91\times10^{10} & 1.81\times10^{9} & 1.33\times10^{8} & 7.65\times10^{8} & 3.29\times10^{5} & 9.51\times10^{3} & -1.29\times10^{13} & 153.39 \end{bmatrix} \quad (12)$$

Therefore, it is possible to calculate the matrixes of $A_{i\,17*17}$ for the other 11 states, which means $A_2, A_3, ..., A_{12}$.

TABLE XI
The Data of *WSCC* 9-bus system

Bus Number	Load (MW)	Load (MVar)	Generation (MW)	Generation (MVar)	Voltage Rated (KV)
1	0	0	0	0	16.5
2	0	0	163	0	18
3	0	0	85	0	13.8
4	0	0	0	0	230
5	125	50	0	0	230
6	90	30	0	0	230
7	0	0	0	0	230
8	100	35	0	0	230
9	0	0	0	0	230

Second Case Study: For example, to obtain A_1 matrix by using the eigenvalues of this system, $P_1(S)$ will be calculated as Equ. (13).

$$P_1(S)=s*(s+49.6660)*(s+49.0020)*(s+46.2050)*(s+44.8300)*(s+42.982)*(s+33.6960)*(s+27.7090)*(s+26.9620)*(s+25.1130)*(s+26.2520)*(s+26.0230)*(s+21.0290)*(s+2.9040-17.2170i)*(s+2.9040+17.2170i)*(s+2.2750-15.4000i)*(s+2.2750+15.4000i)*(s+2.9730-14.7630i)*(s+2.9730+14.7630i)*(s+2.1960-13.3710i)*(s+2.1960+13.3710i)*(s+2.5440-13.9090i)*(s+2.5440+13.9090i)*(s+4.6800)*(s+6.0610)*(s+5.2570)*(s+5.5200)*(s+5.8360)*(s+2.2940)*(s+0.1070)*(s+0.5870)*(s+0.4750)*(s+0.4600)*(s+0.3590-0.0060i)*(s+0.3590+0.0060i)*(s+0.3210) \quad (13)$$

After simplifying the coefficients of $P_1(S)$, they will be shown in Equ. (14) as follows.

$$P_1(S)=S^{36}+a_{35}S^{35}+...+a_1S+a_0 \quad (14)$$

The coefficients related to $P_1(S)$ in Equ. (14) including $a_1, a_2, ..., a_{35}$ will be calculated as presented in Equ. (15).

$$a_{35}=477.569$$
$$a_{34}=107.08*10^{3}$$
$$a_{33}=1.504*10^{6}$$
$$,...$$

$$A_1=\begin{bmatrix} 0 & 1 & 0 & \dots & 0 \\ 0 & 0 & 1 & \dots & 0 \\ \vdots & \vdots & \vdots & \dots & \vdots \\ 0 & 0 & 0 & \dots & 1 \\ -a_0 & -a_1 & -a_2 & \dots & -a_{35} \end{bmatrix} \quad (15)$$

Therefore, it is possible to calculate the matrixes of $A_{i\,36*36}$ for the other 11 states, which means $A_2, A_3, ..., A_{12}$.

ACKNOWLEDGMENT

We are grateful to the South of Kerman Electric Power Distribution Company and its personnel.

REFERENCES

[1] G. K. Fourlas, K. J. Kyriakopoulos, and C. D. Vournas, “Hybrid systems modeling for power systems,” *IEEE Circuits and Systems Magazine*, vol. 4, no. 3, pp. 16–23, 2004.

[2] I. A. Hiskens, “Power system modeling for inverse problems,” *IEEE Transactions on Circuits and Systems I: Regular Papers*, vol. 51, no. 3, pp. 539–551, 2004.

[3] S. Baniardalani, “Fault Diagnosis of Discrete-Time Linear Systems Using Continuous Time Delay Petri Nets,” *International Journal of Industrial Electronics Control and Optimization*, vol. 3, no. 1, pp. 81–90, 2020.

[4] P. Kundur, N. J. Balu, and M. G. Lauby, *Power system stability and control*, vol. 7. McGraw-hill New York, 1994.

[5] P. Fakhrooeian, M. Abedi, and P. Karimyan, "Optimal allocation and sizing of dynamic VAR support to improve short-term voltage stability considering wind farm and dynamic load model," International Journal of Industrial Electronics, Control and Optimization, vol. 1, no. 1, pp. 41–51, 2018.
[6] L. L. Grigsby, *Power system stability and control*. CRC press, 2016.
[7] Z. Hekss *et al.*, "Hybrid Automaton Control of Three Phase Reduced Switch Shunt Active Power Filter Connected Photovoltaic System," *IFAC-PapersOnLine*, vol. 53, no. 2, pp. 12847–12852, 2020.
[8] R. Malkowski, R. Kowalak, and J. Klucznik, "SVC and power transformers controllers coordination," in *2015 IEEE Eindhoven PowerTech*, 2015, pp. 1–5.
[9] D. A. Krishna and M. R. Sindhu, "Application of static synchronous compensator (STATCOM) to enhance voltage profile in IEEE standard 5 bus transmission system," *Indian Journal of Science and Technology*, vol. 9, no. 30, 2016.
[10] R. M. Larik, M. W. Mustafa, and M. K. Panjwani, "A statistical jacobian application for power system optimization of voltage stability," *Indonesian Journal of Electrical Engineering and Computer Science*, vol. 13, no. 1, pp. 331–338, 2019.
[11] P. Aristidou, G. Valverde, and T. Van Cutsem, "Contribution of distribution network control to voltage stability: A case study," *IEEE Transactions on Smart Grid*, vol. 8, no. 1, pp. 106–116, 2015.
[12] S. M. Hoseini, N. Vasegh, and A. Zangeneh, "Robust hybrid control of output power for three-phase grid connected PV system," International Journal of Industrial Electronics, Control and Optimization, vol. 2, no. 4, pp. 365–372, 2019.
[13] B. Gao, G. K. Morison, and P. Kundur, "Voltage stability evaluation using modal analysis," *IEEE transactions on power systems*, vol. 7, no. 4, pp. 1529–1542, 1992.
[14] H.-D. Chiang and R. Jean-Jumeau, "Toward a practical performance index for predicting voltage collapse in electric power systems," *IEEE Transactions on power systems*, vol. 10, no. 2, pp. 584–592, 1995.
[15] A. C. Z. De Souza, C. A. Canizares, and V. H. Quintana, "New techniques to speed up voltage collapse computations using tangent vectors," *IEEE Transactions on Power systems*, vol. 12, no. 3, pp. 1380–1387, 1997.
[16] M. Mohammadniaei, F. Namdari, A. P. Valadbeigi, and M. R. Shakarami, "A new method for analyzing the probability of voltage and frequency stability status based on Markov Chain," *International Journal of Electrical Power & Energy Systems*, vol. 125, p. 106500, 2021.
[17] M. O. N. Teixeira, I. D. Melo, and A. P. João Filho, "An optimisation model based approach for power systems voltage stability and harmonic analysis," *Electric Power Systems Research*, vol. 199, p. 107462, 2021.
[18] G. Wang, Z. Xu, and Z. Zhang, "Voltage stability analysis of power systems with a large number of non-synchronous machine sources connected," *International Journal of Electrical Power & Energy Systems*, vol. 131, p. 107087, 2021.
[19] W. Cigre, "Indices predicting voltage collapse including dynamic phenomena," *Task Force 38.02. 11 Report*, 1994.
[20] R. B. Prada, L. J. De Souza, and J. L. Vega, "The need for voltage stability analysis in voltage-controlled buses," *International Journal of Electrical Power & Energy Systems*, vol. 68, pp. 252–258, 2015.
[21] C. G. Cassandras and S. Lafortune, *Introduction to discrete event systems*. Springer Science & Business Media, 2009.
[22] J. Lunze and F. Lamnabhi-Lagarrigue, *Handbook of hybrid systems control: theory, tools, applications*. Cambridge University Press, 2009.
[23] F. Milano, "Three-dimensional visualization and animation for power systems analysis," *Electric Power Systems Research*, vol. 79, no. 12, pp. 1638–1647, 2009.
[24] M. A. Pai, P. W. Sauer, and R. K. Ranjan, "Robustness Of Steady-State Stability In Power Systems With Respect To Nonlinear Voltage Dependent Load Models."
[25] X.-H. Zong, Y. Zhang, and Z. Wu, "Probabilistic eigenvalue analysis for voltage stability," in *Zhongguo Dianji Gongcheng Xuebao(Proceedings of the Chinese Society of Electrical Engineering)*, 2006, vol. 26, no. 8, pp. 61–65.
[26] M. S. Alwan and X. Liu, "On stability of linear and weakly nonlinear switched systems with time delay," *Mathematical and Computer Modelling*, vol. 48, no. 7–8, pp. 1150–1157, 2008.
[27] A. Kundu and D. Chatterjee, "On stability of discrete-time switched systems," *Nonlinear Analysis: Hybrid Systems*, vol. 23, pp. 191–210, 2017.
[28] P. W. Sauer and M. A. Pai, "Power system dynamics and stability," *Urbana*, 1998.
[29] Di. PowerFactory, "Digsilent powerfactory 15 user manual," *DIgSILENT GmbH, May-2014*, 2013.
[30] Q.-Y. Liu, C.-C. Liu, and Q.-F. Liu, "Coordinated voltage control with online energy margin constraints," *IEEE Transactions on Power Systems*, vol. 31, no. 3, pp. 2064–2075, 2015.

Fariba Forouzesh, received her B.Sc. degree in Electronics Engineering from Islamic Azad university, Kerman, Iran in 1998, M.Sc. degree in Power System Control Engineering from Science and Research branch, Islamic Azad university, Boroujerd, Iran in 2012. She is currently Ph.D. Student of Power Systems in Islamic Azad university, Kerman, Iran. her main interest system stability, power quality, control applications in power electric industry and power system optimization.

Mahdiyeh Eslami, received her B.Sc. degree from Shahid Bahonar university of Kerman, Iran, in 2000, M.Sc. from Iran University of Science and Technology (IUST), Tehran, Iran, in 2004, and Ph.D. from National University of Malaysia (UKM) in 2012, all in Electrical Engineering. from 2012 to 2013, she was a Postdoctoral Research Fellow with the Power Research Group at National University of Malaysia. She has authored and co-authored more than 70 journal and conference articles. Since 2012, she has been an Assistant Professor at Department of Electrical Engineering. Science and Research Branch, Islamic Azad university, Kerman, Iran. her research interests include optimization technique in power system stability and FACTS devices.

Mehdi Jafari Shahbazzadeh, received his B.Sc. degree in Electronics Engineering and the M.Sc. degree in communication from Shiraz University, Iran, in 1991 and 1995 respectively. He received the Ph.D. degree in Electrical engineering from Science and Research branch, Islamic Azad university, Tehran, Iran in 2007. He is currently a professor with the department of Electrical engineering, where he is also the leader of Robotics group. His research interests include smart grids, compact modeling of GFET, HVDC of power systems, optimization and image processing.

IECO

This page intentionally left blank.

International Journal of Industrial Electronics, Control and Optimization © 2021 IECO
Vol. 4, No. 4, pp. 433-444, Sep(2021)

Reliability-Based Operation in Energy Hubs with Several Energy Networks

Alireza Malekijavan[1], Mehdi Aslinezhad[2,†], and Hamidreza Zaferani[3]

[1,2] Department of Electrical Engineering, Shahid Sattari Aeronautical University of Science and Technology, Tehran, Iran

[3] Department of Electrical Engineering, Tehransar-Sama College, Tehran

ABSTRACT

The paper presents reliability-based operation (RBO) of an energy hub consisting of electric vehicles (EVs) and a combined cooling, heating, power (CCHP) system in electricity, natural gas, and district heating networks. The proposed strategy aims to minimize the total expected operating and reliability costs of the mentioned energy networks as its objective functions. Furthermore, the problem is subject to optimal power flow (OPF) equations, reliability constraints, and a hub energy model including constraints of EV parking lots and CCHP. This strategy has a mixed-integer nonlinear programming (MINLP) model, so MILP will be used to achieve a unique optimal solution in less computational time for the proposed scheme. Moreover, the scheme includes uncertainties of the load, energy price, the demand of EVs, and equipment availability of the given systems, which are modeled using scenario-based stochastic programming (SBSP). Finally, the approach is implemented on a standard test system in the GAMS software environment. Then, according to the numerical results, it is observed that the mentioned outline can achieve optimal operating conditions and high reliability in energy systems if the EVs and CCHPs are optimally managed in the energy hub form.

Article Info

Keywords:
Combined cooling, heating and power system, Electrical vehicle parking lot, Energy hub, Reliability-based operation, Stochastic linear programming

Article History:
Received 2020-10-06
Accepted 2021-01-24

NOMENCLATURE

Indices and sets

e, Ξ_{BC}	Index and set of a bus in the electrical network
g, Ξ_{NG}	Index and set of a node in the natural gas network
h, Ξ_{NH}	Index and set of a node in the district heating network
j	Auxiliary index defined as a bus or a node
l, Ξ_L	Index and set of linearization segments in the conventional piecewise linear method
k, Ξ_K	Index and set of laterals of the regular polygon
ref	Slack bus
t, Ξ_{ST}	Index and set of simulation time
w, Ξ_{SC}	Index and set of scenarios

Variables

$Cost$	Total expected operation and reliability costs ($)
C^C	Cooling power of CCHP per unit (p.u)
$EENS$	Expected energy not-supplied (MWh or p.u)
E^{EV}	Stored energy in the battery of EVs in the parking lot (p.u)
G^C	Gas power of CCHP (p.u)
G^L	Gas power flowing through the pipeline (p.u)
G^S	Gas power of the natural gas station (p.u)
H^C	Heating power of CCHP (p.u)
H^L	Heating power flowing through the pipeline (p.u)
H^S	Heating power of the heat station (p.u)
P^C, Q^C	Active and reactive power of CCHP (p.u)
$P^{EV,B}$, $P^{EV,L}$	Battery power and active loss of EVs chargers in the parking lot (p.u)
$P^{EV,ch}$, $P^{EV,dech}$	Charging and discharging power of EVs (p.u)

†**Corresponding Author**: M.aslinezhad@ssau.ac.ir.
Tel: +982164032229, University of Science and Technology of Shahid Sattari Aeronautical, Tehran 1384663113, Iran

P^L, Q^L Active and reactive power flowing on distribution line (p.u)

P^{LNS}, G^{LNS}, H^{LNS} Active, gas, and heating power not-supplied (p.u)

P^S, Q^S Active and reactive power of distribution station (p.u)

Q^{EV} Reactive power of chargers of EVs in the parking lot (p.u)

T Temperature (p.u)

V, ΔV, θ Voltage magnitude (p.u), deviation (p.u), and angle (radian)

x Binary variable related to charging/discharging state of EVs in the parking lot

π, $\Delta\pi$ Gas pressure and deviation (p.u)

Constants

AL^E, AL^G, AL^H Incident matrix of buses and lines in the electrical networks, Incident matrix of nodes and pipelines in the natural gas networks, and Incident matrix of nodes and pipelines in the district heating network

a^p, a^q Coefficients of active and reactive power in the calculation equation of losses in chargers of EVs

c, $\dot{m}$ Specific heat capacity of water and mass flow rate of water through a pipeline

CR, DR Charging and discharging rates of EVs in the parking lot (p.u)

E^{Arr}, E^{Dep} Energy of EVs at arrival and departure time (p.u)

g, b Conductance and susceptance of distribution line (p.u)

G^{Cmax} Maximum gas capacity of CCHP (p.u)

G^D Gas demand power (p.u)

G^{Lmax} Maximum gas power allowed to flow through the pipeline (p.u)

G^{Smax} Maximum capacity of the natural gas station (p.u)

H^D Heat demand power (p.u)

H^{Lmax} Maximum heat power allowed to flow through the pipeline (p.u)

HR^C The ratio of cooling power to heating power in CCHP

H^{Smax} Maximum capacity of the heat station (p.u)

P^D, Q^D Active and reactive power demand (p.u)

S^{Cmax} Maximum allowed apparent power of CCHP (p.u)

S^{EVmax} Maximum allowed apparent power of chargers of EVs in the parking lot (p.u)

$sign(\pi_g, \pi_j)$ A constant value, which is 1 if π_g is greater than π_j , else is −1.

S^{Lmax} Maximum apparent power allowed to flow through the distribution line (p.u)

S^{Smax} Maximum capacity of the distribution station (p.u)

T^{min}, T^{max} Minimum and maximum allowed temperature (p.u)

V^{min}, V^{max} Minimum and maximum allowed voltage magnitude (p.u)

$VOLL$ Value of lost load ($/MWh)

η^C Efficiency of CCHP

κ Pipeline constant (p.u)

ν Probability occurrence of the scenario

π^{min}, π^{max} Minimum and maximum allowed pressure (p.u)

ρ^E, ρ^G, ρ^H Price of electrical, gas, and heat energy ($/MWh)

I. INTRODUCTION

Nowadays, authorities and organizations encourage energy consumers to utilize state-of-the-art technologies with low emissions to reduce environmental pollution. One of the most widespread technologies to reach this aim is electric vehicles (EVs), which obtain their kinetic energy from the energy stored in their batteries [1-2]. Moreover, the energy demand of EVs is generally supplied via connection to a power system, especially a distribution network [3]. Thus, it is predicted that the number of EVs available in a power system will increase to supply their power demand. Among the proposed technologies are distributed generations (DGs), which can improve operation indices such as voltage profile, energy loss, and distribution lines overloading [4]. Nevertheless, it should be noted that among various types of DGs, combined cooling, heating, and power (CCHP) systems can widely be used in power systems thanks to their high energy efficiency compared to other DGs [5]. Therefore, it is expected to establish an energy management system (EMS) by coordinating EV parking lots and CCHP systems in the form of energy hubs (in short: hubs) and collaboration of hub operators and energy network operators (ENOs) so as to increase energy efficiency, reach an optimal operation, and enhance reliability in energy networks.

Various research studies have been conducted in the field of hub operation in different energy networks. As stated in [6], hubs are expressed based on wind systems. In this reference, a combination of stochastic modeling and the information gap decision theory (IGDT) has been used to consider uncertainty parameters. It is noteworthy that in the IGDT method, the maximum radius of the uncertainty of parameters is obtained for the optimal solution of the problem. In [7], an economic-cooperative scheduling problem model is considered for energy hubs, in which each hub is considered an energy cooperative center. In [8], the constrained-chance optimization problem model is evaluated for a multi-carrier energy (MCE) system consisting of a hub. Ref. [9] presents a new model of hub that can, firstly, increase the use of clean energy and energy efficiency and achieve the goal of local energy consumption. Secondly, according to the interconnected hub framework, calling is carried out on the

internet of energy. Then, an energy distribution management strategy is designed for the hub using the compatibility theory. Finally, case studies show that the price adjustment mechanism with more than 500 hubs is stable, and the price adjustment tends to be a constant value after 15 times. Also, authors in [10] introduce a risk-constrained energy management strategy for hubs consisting of photovoltaics (PVs), compressed air energy storage (CAES), and demand response program (DRP). In this case, stochastic programming has been employed to model the uncertainty parameters of PVs and the load. Additionally, energy storage and demand response have been used to increase the flexibility of the hub in the presence of PV sources. The optimal bidding model of a hub with its participation in energy markets is stated in [11]. In another study, stochastic dynamic programming (SDP) has been used in [12] for optimal hub operation. In [13], the issue of hub participation in the distribution network based on the DRP is presented. Furthermore, a hub participation model is presented in [14] for electric and heating energy markets based on the price clearing model of the mentioned energies. The large hub operating model has been studied in [15] by considering different models of DRP. Ref. [16] provides the daily energy management model of electrical, heating, and gas microgrids in the presence of a hub. Authors in [17] mention the operation of a hub consisting of EVs and a combined heat and power system (CHP). The proposed scheme uses the capability of controlling the reactive power of CHPs and EVs to improve electrical network indices, such as voltage regulation of electrical buses. Also, in the given scheme, a robust model has been utilized to model the uncertainty parameters of consumption loads and EVs.

Based on the literature, it is observed that most research cases focus on the coordination of DGs and active loads (ALs), such as EVs, energy storage systems (ESSs), and DRP in distribution networks. However, in general, the coordination of EVs and CCHPs has rarely been considered in the literature. Yet, it should be noted that the use of EVs has grown significantly in recent years as it helps reduce air pollution. Moreover, CCHP is expected to have significant future benefits due to the simultaneous production of three energy forms and increased energy efficiency. Therefore, the coordination of these cases in the form of a hub can have suitable benefits for energy networks from economic, operational, reliability, flexibility, and security viewpoints. Above all, general research has focused on the operation of hubs in various energy networks and has evaluated the ability of hubs to improve the operation indices of these networks. Nonetheless, it is worth noting that hubs, which act as a local resource in energy grids, can play a role in improving other grid indices, one of the most important of which is reliability. However, this has less been a case in research on the proposed topic.

To compensate for the research gaps mentioned in this paper, the reliability-based operation (RBO) in electrical, natural gas, and district heating networks is presented as shown in Fig. 1. In the proposed scheme, the hub is intended for the aggregation of EV parking lots and CCHP. The suggested problem also undermines the total expected operating and reliability costs in the mentioned energy networks. This problem is also constrained by the power flow (PF) equations and technical and reliability constraints in the given energy networks, and the hub model, consisting of EV parking lots and CCHP. It is noteworthy that this problem has a mixed-integer nonlinear programming (MINLP) model. Therefore, the solvers of this problem can obtain the local optimal solution at high computation time provided that the final solution of each solvent is different. Hence, to achieve a unique optimal solution in low computation time, the mixed-integer linear programming (MILP) model is used for the proposed scheme in the next step. Furthermore, the introduced outline includes uncertainty in consumption loads, energy prices, EV parameters, and availability of energy grid equipment. Therefore, this paper presents scenario-based stochastic programming (SBSP) for modeling these uncertainty parameters, which is based on a combination of the Monte Carlo simulation (MCS) technique and the Kantorovich method. Contributions of this scheme can be summarized as:

- implementing simultaneous reliability and operation problems in electrical, natural gas, and district heating networks consisting of an energy hub;
- coordinating EV parking lots and CCHP in the form of an energy hub to increase energy efficiency and reduce the operation of batteries and chargers of EVs; and
- improving operation, economic, and reliability indices in energy networks using energy hub as a local energy source.

The paper is organized as follows. In Section II, the RBO model of the hub in energy networks is described. Section III provides a linearized model for the proposed problem. Sections IV and V present the numerical results and conclusions, respectively.

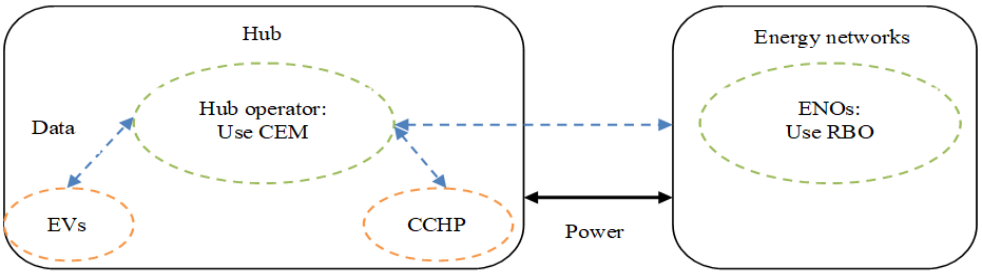

Fig. 1. The suggested scheme for RBO in energy networks in the presence of a hub

II. RBO OF THE HUB IN ENERGY NETWORKS

This section presents the problem of RBO of a hub consisting of an EV parking lot and CCHP in electrical, natural gas, and district heating networks. This minimization problem takes into account the total operating and reliability costs in the proposed networks as the objective function. The problem is also constrained to optimal power flow (OPF) equations, reliability limitation, CCHP equations, and EV parking lot constraints. Therefore, the problem is formulated as follows:

$$\min \quad Cost = \sum_{w\in\Xi_{SC}} \nu_w \sum_{t\in\Xi_{ST}} \left\{ \sum_{e\in\Xi_{BE}} \rho_t^E P_{e,t}^S + \sum_{g\in\Xi_{NG}} \rho^G G_{g,t}^S + \sum_{h\in\Xi_{NH}} \rho^H H_{h,t}^S \right\} + \overbrace{VOLL \times \sum_{w\in\Xi_{SC}} \nu_w \sum_{t\in\Xi_{ST}} \left\{ \sum_{e\in\Xi_{BE}} P_{e,t}^{LNS} + \sum_{g\in\Xi_{NG}} G_{g,t}^{LNS} + \sum_{h\in\Xi_{NH}} H_{h,t}^{LNS} \right\}}^{EENS} \quad (1)$$

Subject to:

$$P_{e.t.w}^{LNS} + P_{e.t.w}^{S} + P_{e.t.w}^{C} + \left(P_{e.t.w}^{EV.dch} - P_{e.t.w}^{EV.ch}\right) - P_{e.t.w}^{D} = \sum_{j\in\Xi_{BE}} AL_{e.j}^{E} P_{e.j.t.w}^{L} \quad \forall e.t.w \quad (2)$$

$$Q_{e.t.w}^{S} + Q_{e.t.w}^{C} + Q_{e.t.w}^{EV} - Q_{e.t.w}^{D} = \sum_{j\in\Xi_{BE}} AL_{e.j}^{E} Q_{e.j.t.w}^{L} \quad \forall e.t.w \quad (3)$$

$$P_{e.j.t.w}^{L} = g_{e.j}(V_{e.t.w})^2 - V_{e.t.w}V_{j.t.w}\{g_{e.j}\cos(\theta_{e.t.w} - \theta_{j.t.w}) + b_{e.j}\sin(\theta_{e.t.w} - \theta_{j.t.w})\} \forall e.j.t.w \quad (4)$$

$$Q_{e.j.t.w}^{L} = -b_{e.j}(V_{e.t.w})^2 + V_{e.t.w}V_{j.t.w}\{b_{e.j}\cos(\theta_{e.t.w} - \theta_{j.t.w}) + g_{e.j}\sin(\theta_{e.t.w} - \theta_{j.t.w})\} \forall e.j.t.w \quad (5)$$

$$\theta_{e,t,w} = 0 \qquad \forall e = ref, t, w \quad (6)$$

$$G_{g,t,w}^{LNS} + G_{g,t,w}^{S} - G_{g,t,w}^{D} - G_{g,t,w}^{C} = \sum_{j\in\Xi_{NG}} AL_{g,j}^{G} G_{g,j,t,w}^{L} \qquad \forall g,t,w \quad (7)$$

$$G_{g,j,t,w}^{L} = \kappa_{g,j}\, sign(\pi_{g,t,w}, \pi_{j,t,w}) * \sqrt{sign(\pi_{g,t,w}, \pi_{j,t,w})\left(\pi_{g,t,w}^2 - \pi_{j,t,w}^2\right)} \quad \forall g,j,t,w \quad (8)$$

$$H_{h,t,w}^{LNS} + H_{h,t,w}^{S} + H_{h,t,w}^{C} - H_{h,t,w}^{D} = \sum_{j\in\Xi_{NH}} AL_{h,j}^{H} H_{h,j,t,w}^{L} \qquad \forall h,t,w \quad (9)$$

$$H_{h,j,t,w}^{L} = c_{h,j}\dot{m}_{h,j}\left(T_{h,t,w} - T_{j,t,w}\right) \qquad \forall h,j,t,w \quad (10)$$

$$V_e^{\min} \le V_{e,t,w} \le V_e^{\max} \qquad \forall e,t,w \quad (11)$$

$$\left(P_{e,j,t,w}^{L}\right)^2 + \left(Q_{e,j,t,w}^{L}\right)^2 \le \left(S_{e,j}^{L\max}\right)^2 \qquad \forall e,j,t,w \quad (12)$$

$$\left(P_{e,t,w}^{S}\right)^2 + \left(Q_{e,t,w}^{S}\right)^2 \le \left(S_e^{S\max}\right)^2 \qquad \forall e,t,w \quad (13)$$

$$\pi_g^{\min} \le \pi_{g,t,w} \le \pi_g^{\max} \qquad \forall g,t,w \quad (14)$$

$$-G_{g,j}^{L\max} \le G_{g,j,t,w}^{L} \le G_{g,j}^{L\max} \qquad \forall g,j,t,w \quad (15)$$

$$0 \le G_{g,t,w}^{S} \le G_g^{S\max} \qquad \forall g,t,w \quad (16)$$

$$T_h^{\min} \le T_{h,t,w} \le T_h^{\max} \qquad \forall h,t,w \quad (17)$$

$$-H_{h,j}^{L\max} \le H_{h,j,t,w}^{L} \le H_{h,j}^{L\max} \qquad \forall h,j,t,w \quad (18)$$

$$0 \le H_{h,t,w}^{S} \le H_h^{S\max} \qquad \forall h,t,w \quad (19)$$

$$0 \le P_{e,t,w}^{LNS} \le P_{e,t,w}^{D} \qquad \forall e,t,w \quad (20)$$

$$0 \le G_{g,t,w}^{LNS} \le G_{g,t,w}^{D} \qquad \forall g,t,w \quad (21)$$

$$0 \le H_{h,t,w}^{LNS} \le H_{h,t,w}^{D} \qquad \forall h,t,w \quad (22)$$

$$0 \le P_{e,t,w}^{EV,dch} \le DR_{e,t,w}x_{e,t} \qquad \forall e,t,w \quad (23)$$

$$0 \le P_{e,t,w}^{EV,ch} \le CR_{e,t,w}\left(1 - x_{e,t}\right) \qquad \forall e,t,w \quad (24)$$

$$P_{e,t,w}^{EV,dch} - P_{e,t,w}^{EV,ch} = P_{e,t,w}^{EV,B} - P_{e,t,w}^{EV,L} \qquad \forall e,t,w \quad (25)$$

$$P_{e,t,w}^{EV,L} = a^p\left(P_{e,t,w}^{EV,dch} + P_{e,t,w}^{EV,ch}\right) + a^q Q_{e,t,w}^{EV} \qquad \forall e,t,w, Q_{e,t,w}^{EV} \ge 0 \quad (26)$$

$$E_{e,t,w}^{EV} = E_{e,t-1,w}^{EV} - P_{e,t,w}^{EV,B} \qquad \forall e,t,w \quad (27)$$

$$E_{e,t,w}^{EV} = E_{e,t,w}^{Arr} \qquad \forall e, t = \text{Arrival time}, w \quad (28)$$

$$E_{e,t,w}^{EV} = E_{e,t,w}^{Dep} \qquad \forall e, t = \text{Departure time}, w \quad (29)$$

$$\left(P_{e,t,w}^{EV,dch} - P_{e,t,w}^{EV,ch}\right)^2 + \left(Q_{e,t,w}^{EV}\right)^2 \le \left(S_{e,t,w}^{EV\max}\right)^2 \qquad \forall e,t,w \quad (30)$$

$$G_{g,t,w}^{C} = \frac{P_{e,t,w}^{C} + H_{h,t,w}^{C} + C_{h,t,w}^{C}}{\eta^c} \qquad \forall g,e,h,t,w \quad (31)$$

$$C_{h,t,w}^{C} = H_{h,t,w}^{C} HR^{C} \qquad \forall h,t,w \quad (32)$$

$$\left(P_{e,t,w}^{C}\right)^2 + \left(Q_{e,t,w}^{C}\right)^2 \le \left(S_e^{C\max}\right)^2 \qquad \forall e,t,w \quad (33)$$

$$0 \le G_{g,t,w}^{C} \le G_g^{C\max} \qquad \forall g,t,w \quad (34)$$

The objective function has two terms. The first term refers to the expected operation cost of electric, gas, and district heating substations [17], and the reliability cost in electrical, natural gas, and district heating networks is presented in the second term [18]. The reliability cost in the given equation is proportional to the product of the expected energy not supplied (EENS) and the value of lost load (VOLL) [18], in

which case, according to the second term in (1), the EENS is equal to the sum of the electric, gas and, heating loads not supplied on the operation horizon.

Constraints of the problem are given in (2)-(34), in which constraints (2)-(10) are related to PF equations in different energy networks. AC-PF constraints of the power distribution follow (2)-(6). These equations represent the active and reactive power balance at different buses, active and reactive power flowing through the distribution line, and the voltage angle value of the slack bus, respectively [1]. The gas power balance at different nodes and the gas flowing through the pipeline are proportional to constraints (7) and (8), respectively [17]. Moreover, PF equations of district heating network are also presented in constraints (9) and (10), which indicate the heating power balance at different nodes and the heat flowing through the pipeline, respectively [17]. In addition, technical or operational constraints of different energy networks are formulated in (11)-(19). The technical constraints of the electrical network, including the voltage limit of the buses, the limitation of the distribution line, and station capacities, are presented in (11)-(13), respectively [19]. Also, the pressure limit on the nodes and the capacity limit of the pipeline and the gas station in the natural gas network correspond to constraints (14)-(16), respectively. Finally, the limits on the temperature of the nodes, the capacity of the pipeline, and the heating station capacity proportional to the heating network are listed in (17)-(19). Constraints on reliability in electrical, natural gas, and district heating networks are provided in (20)-(22), respectively [18].

Constraints of the hub consisting of an EV parking lot and CCHP are given in (23)-(34). It is noteworthy that in the equations, it is assumed that there is cooling load only in the hub where it is supplied by CCHP. Also, EVs are connected to the network during the day after their last trip [1]. According to these cases, equations (23) to (30) will be equal to the constraints of the EV parking lot, which in turn represent the constraints concerning the charging and discharging rates of the EV batteries in the parking lot, the power balance in the EV parking lot, the calculation of EV charger power losses in the parking lot, the energy stored in the EV batteries in the parking lot, the initial and final energy amounts at the arrival and departure times for the EVs in the parking lot, and the charging capacity limit of the EVs in the parking lot, respectively [1]. It should be noted that the electrical network generally has inductive loads, so it is expected that the EV charger will operate in the capacitive mode. Therefore, the reactive power variable of EVs always has a positive value for (26). Note that in these equations, *CR*, *DR*, and S^{EVmax} are equal, to $\sum_{i=1}^{N_t} cr_i$, $\sum_{i=1}^{N_t} dr_i$, and $\sum_{i=1}^{N_t} cc_i$, respectively where *cr*, *dr*, and *cc* represent the charging rate, discharging rate, and charger capacity of an EV, respectively. N_t represents the number of EVs available in the parking lot at time *t*. Also, the E^{Arr} and E^{Dep} parameters can be calculated from $\sum_{i=1}^{NA} soc_i bc_i$ and $\sum_{i=1}^{ND} bc_i$, respectively in which *bc* and *soc* represent the battery capacity and state of charge (SOC) of an EV battery, respectively. *NA* and *ND* indicate the number of EVs at arrival and departure times, respectively [1]. Finally, the CCHP constraints are expressed in (31) to (34). The power balance in different parts of the CCHP is proportional to constraint (31). Additionally, the CCHP cooling power is generally a coefficient of its heating power, which is shown in equation (32). Capacity constraints of the CCHP in electrical and gas sectors correspond to (33) and (34), respectively. One should note that since the input limit of the CCHP (gas section) and one of its outputs (electrical section) is taken into account, the constraint of the heating and cooling section can be neglected in the CCHP problem model. Besides, in this case, it is assumed that the CCHP cooling power is consumed in the hub, so the cooling network model is not required in this formulation.

In the suggested problem, load (P^D, Q^D, G^D, and H^D), energy price (ρ^E, ρ^G, and ρ^H), parameters of the EV (*CR*, *DR*, S^{EVmax}, E^{Arr}, and E^{Dep}), and availability of energy network equipment such as distribution lines, pipelines, and stations are uncertain. Therefore, the SBSP is utilized in this paper to model these parameters. In this method, first, the MCS generates a high number of scenarios for load and energy prices corresponding to the normal probability distribution function (PDF) for EV parameters proportional to Rayleigh PDF [20], and for accessibility of equipment according to Bernoulli PDF [18]. Then, the Kantorovich method is used as a scenario reduction approach to achieve a lower number of scenarios with a higher probability of occurrence. This method selects scenarios that have a minimum distance to each other, but this statement describes an NP-hard set-covering problem that is too large in scale to be practical in many applications [21]. The Kantorovich method can obtain final scenarios in a shorter time than the other scenario reduction methods. Most details of this approach are described in [21].

III. LINEAR APPROXIMATE MODEL OF THE PROPOSED PROBLEM

The problem model presented in the previous section is an MINLP caused by nonlinear constraints (4), (5), (8), (12), (13), (30), and (33) and non-convex equations (4) and (5) [1, 17]. Since the hub operation problem in different networks is a complicated optimization problem, the solvers of this problem model cannot be expected to achieve a unique solution in low computation time. In other words, different solvers may reach different optimal solutions, impairing reliance on the solutions of these solvers [1]. To overcome this issue, it is recommended to linearize nonlinear equations.

To linearize equations (4) and (5), it should be noted that in a distribution network, in general, bus voltages are close to 1 p.u., so the voltage magnitude will be 1 + ΔV where ΔV denotes the voltage deviation. Furthermore, the voltage angle difference between the two ends of a distribution line is less than 6° (or 0.105 rad). Thus, $\cos\left(\theta_{e,t,w}-\theta_{j,t,w}\right)$ and $\sin\left(\theta_{e,t,w}-\theta_{j,t,w}\right)$ terms can be approximated by 1 and $\left(\theta_{e,t,w}-\theta_{j,t,w}\right)$, respectively. Therefore, linearized forms of constraints (4) and (5) and bus voltage limitations considering the above assumptions and neglecting ΔV^2, $\Delta V_e \Delta V_j$, and $\Delta V \times (\theta_e - \theta_j)$ will be as follows [17]:

$$P^L_{e,j,t,w} = g_{e,j}\left(\Delta V_{e,t,w}-\Delta V_{j,t,w}\right)-b_{e,j}\left(\theta_{e,t,w}-\theta_{j,t,w}\right) \qquad \forall e,j,t,w \tag{35}$$

$$Q^L_{e,j,t,w} = -g_{e,j}\left(\theta_{e,t,w}-\theta_{j,t,w}\right)-b_{e,j}\left(\Delta V_{e,t,w}-\Delta V_{j,t,w}\right) \qquad \forall e,j,t,w \tag{36}$$

$$V_e^{\min}-1 \le \Delta V_{e,t,w} \le V_e^{\max}-1 \qquad \forall e,t,w \tag{37}$$

To linearize (8), it is first rewritten as (38) where the auxiliary variable ξ can be calculated from $\left(\xi_{g,j,t,w}\right)^2 = sign(\pi_{g,t,w},\pi_{j,t,w})\left(\pi^2_{g,t,w}-\pi^2_{j,t,w}\right)$. However, this is a quadratic polynomial nonlinear equation that can be approximated to a linear equation using the conventional piecewise linearization method [1]. Based on this method, variables ξ and π are divided into several variables with a small range of changes, i.e. $\Delta\xi$ and $\Delta\pi$, the sum of which gives the values of ξ and π similar to constraints (39) and (40). Moreover, the square of each variable, such as ξ^2 (π^2), can be expressed as $\sum_{l\in\Xi_L} s^{\xi}_l \Delta\xi_l$ ($\sum_{l\in\Xi_L} s^{\pi}_l \Delta\pi_l$), where l and Ξ_L are the index and the set of linearized segments, and s denotes the piecewise slope. Consequently, the proposed quadratic polynomial equation is linearized as (41).

$$G^L_{g,j,t,w} = \kappa_{g,j}\, sign(\pi_{g,t,w},\pi_{j,t,w})\,\xi_{g,j,t,w} \tag{38}$$

$$\xi_{g,j,t,w} = \sum_{l\in\Xi_L}\Delta\xi_{g,j,t,w,l} \qquad \forall g,j,t,w \tag{39}$$

$$\pi_{g,t,w} = \pi_g^{\min} + \sum_{l\in\Xi_L}\Delta\pi_{g,t,w,l} \qquad \forall g,t,w \tag{40}$$

$$\sum_{l\in\Xi_L} S^{\xi}_l \Delta\xi_{g.j.t.w.l} = sign(\pi_{g.t.w}.\pi_{j.t.w})\left(\sum_{l\in\Xi_L} S^{\pi}_l(\Delta\pi_{g.t.w.l} - \Delta\pi_{j.t.w.l})\right) \forall g.j.t.w \tag{41}$$

Constraints (12), (13), (30), and (33) are in the form of a circular plane with a radius of S, i.e., $P^2+Q^2 \le S^2$. The plane can be approximated by a regular polygon [1] such that if the number of laterals is high, a more accurate approximation is reached. It is noted that the laterals of this regular polygon correspond to a straight line in the form of $P\times\cos\left(k\times\Delta\beta\right)+Q\times\sin\left(k\times\Delta\beta\right)=S$ where $\Delta\beta$ is the angle deviation equal to $360/n_k$ in which n_k represents the number of laterals of the regular polygon, and k is the index of linearization segments, which varies between 0 and $n_k - 1$ in set Ξ_k. Finally, the proposed regular polygon plane is the overlaps of planes $P\times\cos\left(k\times\Delta\beta\right)+Q\times\sin\left(k\times\Delta\beta\right)\le S$ if this equation is repeated for all values of k. Therefore, the linearized equations of constraints (12), (13), (30), and (33) are rewritten as:

$$P^L_{e,j,t,w}\cos\left(k\times\Delta\beta\right)+Q^L_{e,j,t,w}\sin\left(k\times\Delta\beta\right)\le S^{L\max}_{e,j} \qquad \forall e,j,t,w,k \tag{42}$$

$$P^S_{e,t,w}\cos\left(k\times\Delta\beta\right)+Q^S_{e,t,w}\sin\left(k\times\Delta\beta\right)\le S^{S\max}_{e} \qquad \forall e,t,w,k \tag{43}$$

$$\left(P^{EV,dch}_{e,t,w}-P^{EV,ch}_{e,t,w}\right)\cos\left(k\times\Delta\beta\right)+Q^{EV}_{e,t,w}\sin\left(k\times\Delta\beta\right)\le S^{EV\max}_{e,t,w} \qquad \forall e,t,w,k \tag{44}$$

$$P^C_{e,t,w}\cos\left(k\times\Delta\beta\right)+Q^C_{e,t,w}\sin\left(k\times\Delta\beta\right)\le S^{C\max}_{e} \qquad \forall e,t,w,k \tag{45}$$

As a result, the suggested linearized problem model in the form of an MILP that can be solved using conventional solvers such as CPLEX is as follows:

$$\min \quad Cost = \sum_{w\in\Xi_{SC}} \nu_w \sum_{t\in\Xi_{ST}} \left\{ \sum_{e\in\Xi_{BE}} \rho^E_t P^S_{e,t} + \sum_{g\in\Xi_{NG}} \rho^G G^S_{g,t} + \sum_{h\in\Xi_{NH}} \rho^H H^S_{h,t} \right\} + \overbrace{VOLL\times \sum_{w\in\Xi_{SC}} \nu_w \sum_{t\in\Xi_{ST}} \left\{ \sum_{e\in\Xi_{BE}} P^{LNS}_{e,t} + \sum_{g\in\Xi_{NG}} G^{LNS}_{g,t} + \sum_{h\in\Xi_{NH}} H^{LNS}_{h,t} \right\}}^{EENS} \tag{46}$$

Subject to:

Constraints (2), (3), (6), (7), (9), (10), (14)-(29), (31), (32), (34)-(45) (47)

IV. NUMERICAL RESULTS

4.1. Data

The proposed problem is applied to a system consisting of a 9-bus electric grid, a 4-node natural gas system, and a 7-node district heating network as shown in Fig. 2 [17]. The base values of power, voltage, pressure, and temperature in the given system are 1 MW, 1 kV, 10 bar, and 100°C, respectively, and the allowable range of voltage, pressure, and temperature is equal to [0.9, 1.1] p.u. The specifications of the distribution lines, pipelines, stations, and electrical loads are selected from [17]. Also, the daily curve of electricity, gas, and heating energy prices is illustrated in Fig. 3. In addition, the proposed system includes 7 hubs, the position of which is shown in Fig. 2. Each of the hubs, other than Hub 4, has 200 EVs, with the EV penetration level curve given in Fig. 4 [22], and other EV specifications such as charging/discharging rates, SOC, battery capacity, charger capacity, and more are proportional to the data selected from [1, 22]. Hubs 4, 6, and 7 have a CCHP with specifications as follows. The capacity of the input gas and the output electricity is 2.5 MW and 1 MW, respectively, the efficiency

ηc is 0.8, and it is assumed that 20% of its output heat capacity is used to cool the hub. In this section, the

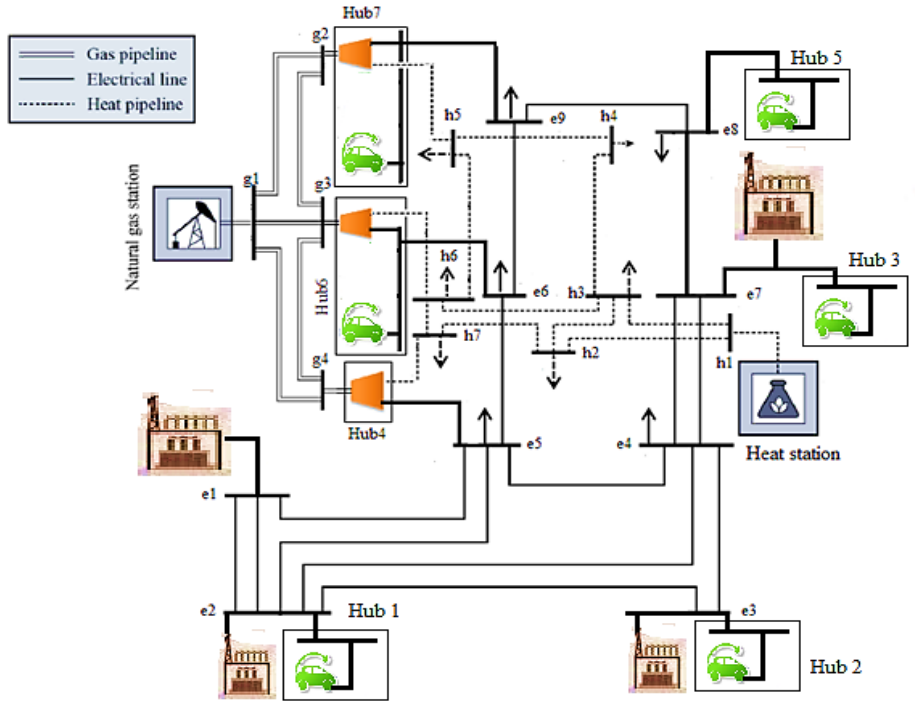

Fig. 2. The studied system [17]

standard deviation for uncertainties of load, energy price, and EV parameters is set at 10%. Regarding the uncertainty of accessibility of network equipment, this parameter depends on the forced outage rate (FOR), the amount of which is assumed to be 1% for all electrical network equipment and 0.5% for the equipment of other networks. Finally, the MCS generates 1000 scenarios for the mentioned uncertainties, and then the Kantorovich method selects 40 scenarios with a high probability of occurrence.

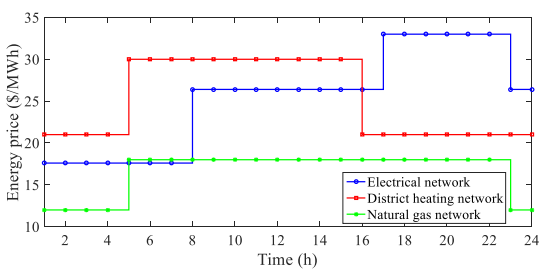

Fig. 3. The daily curve of energy price in different networks

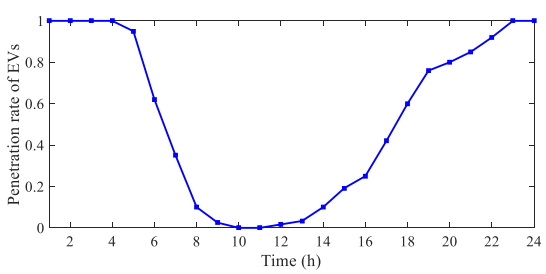

Fig. 4. The daily curve of EV penetration level [22]

4.2. Results

The problem is coded in the GAMS software environment and the CPLEX solver is then used to achieve the optimal solution [23].

A) The capability of the proposed linear model: In this section, it is assumed that the number of pieces in the conventional piecewise linear method is equal to 5, and also the circular plane is approximated by a regular 45-gon. The results of this section are presented in Table I. Accordingly, the solvers of the MINLP model, such as BONMIN, BARON, and KNITRO, produce different solutions for the proposed problem, where BONMIN can achieve a better solution (including lower result for the objective function and calculation time) versus other MINLP solvers. However, MILP solvers such as CPLEX, CBC, and CONOPT can achieve unique optimal solutions with the lowest calculation time in comparison to MINLP solvers. Based on Table I, it is observed that the computational error for active and reactive power is about 2.2%, and this value is about 0.5% for voltage. The computational error for the variables of gas and heat networks is very low; its value for gas power, pressure, heat power, and temperature is about 0.7%, 0.1%, and 0%, respectively.

TABLE I

RESULTS OF THE PROPOSED MILP AND MINLP MODELS

Results of different solvers			
Model	Solver	Cost ($)	Calculation time (s)
MINLP	BONMIN	5768.25	791.67
	BARON	6311.42	1023.22
	KNITRO	Infeasible	-
MILP	CPLEX	5399.13	12.31
	CBC	5399.13	15.78
	CONOPT	5399.13	18.92

Parameter	MINLP	MILP	Percentage of deviation
Solver	BONMIN	CPLEX	-
The sum of the expected active power of distribution stations in the operation horizon (p.u)	82.5451	82.4278	2.23
The sum of the expected reactive power of distribution stations in the operation horizon (p.u)	54.9965	56.2448	2.19
The sum of the expected gas power of gas stations in the operation horizon (p.u)	77.3520	76.8143	0.7
The sum of the expected heat power of heat stations in the operation horizon (p.u)	43.7935	43.7935	0
Average voltage magnitude (p.u)	0.9816	0.9765	-0.52
Average voltage angle (rad)	0.004034	0.004016	-0.448
Average pressure (p.u)	0.9290	0.9281	-0.1
Average temperature (p.u)	0.9347	0.9347	0
Computation time	791.67	12.31	-

TABLE II

The Expected Operation and Reliability Cost in Energy Networks for Different Case Studies

Energy management system		Expected operation cost ($)	Expected reliability cost ($)	Total cost ($)
UEM	EVs	6211.47	1612.31	7823.78
	CCHP	5783.43	1246.22	7029.65
CEM		4857.49	541.64	5399.13

TABLE III

Expected Values of Operation Indices in Different Energy Networks for Different Case Studies

Case	Energy loss (p.u) in the network of			Maximum deviation (p.u) of		
	Electrical	Gas	Heating	Voltage	Pressure	Temperature
I	4.1	0	2.1	0.103	0	0.112
II	3.8	0	2.1	0.086	0	0.112
III	2.7	1.7	1.4	0.053	0.086	0.074
IV	2.4	1.8	1.4	0.047	0.086	0.074

This indicates that the proposed MILP model has a very low computational error compared to the original MINLP model. It is also noteworthy that according to Table I, the computation time in the MILP model by the CPLEX solver is 12.31 s, while in the MINLP model, it is 791.67 s. This also proves the feasibility of the proposed problem in achieving the optimal solution in the shortest possible time. Therefore, according to the stated cases, the proposed MILP model will be a suitable alternative to the original MINLP model.

B) *Evaluating the coordination compatibility of the EV parking lot and CCHP in the form of a hub*: This section examines the coordination compatibility of the EV parking lot and CCHP in the form of a hub. To this end, two strategies have been performed. The first strategy focuses on the uncoordinated energy management (UEM) of these resources. In other words, in this strategy, the operation of energy networks has been carried out for only EV parking lot (the first case study) or CCHP (the second case study) as two separate problems. The second strategy is a coordinated energy management (CEM) plan that uses a hub form to coordinate the EV parking lot and CCHP. The results of this section are tabulated in Table II. Based on this, it is observed that the operation of different networks in the presence of only the EV parking lot has high operation and reliability costs, i.e., 6211.47$ and 1612.31$, compared to the other study case with UEM. In the case of the second study, the operation and reliability

costs decrease by about 6.9% and 22.7%, respectively, compared to the first case study because only the CCHP is responsible for energy production in this case. Nevertheless, in the first case study, EVs are in the form of active loads that, besides controlling network indices, must receive high energy to their travel in a day. However, it should be noted that in the CEM strategy, the energy hub has been able to reduce the operation and reliability cost to a large extent compared to the case studies of the first strategy such that it has reduced the operation (reliability) cost of energy networks by about 16% (56.5%) compared to the second case study in the first strategy. This indicates the ability of the energy hub as a framework for coordinated energy management between different sources and active loads in improving the economic costs of different energy networks.

Figs. 5 to 7 show the daily power injection curve of the hubs to different energy networks. The daily curves of their active and reactive power are shown in Fig. 5. Based on Fig. 5(a), it is observed that the hubs receive active power from 1:00 to 7:00 and 13:00 to 15:00 from the electrical network, but at other times, they can inject power into the network. This is due to the operation of the EV parking lot and CCHP as follows:

- EVs perform charging operations and receive a high amount of power from the network to minimize the operation cost of the electrical network and their own charging cost from 1:00 to 7:00 when the electricity price is the lowest based on Fig. 3. They also perform recharging operations from 12:00 to 16:00, when the charged energy level during these hours is low due to the low number of EVs connected to the electrical grid, as given in Fig. 4. The EVs then inject their stored energy into the network to improve operation indices such as voltage profiles and reduce electrical losses during peak hours, i.e., from 17:00 to 22:00, which correspond to high electrical energy price based on Fig. 3. This amount of energy is low because a low number of EVs have been able to perform the charging operation between 12:00 and 16:00, and it is also supposed that the initial energy of the EVs is low at the moment of connection to the network.
- CCHPs generally have four levels of produced active power based on Fig. 5(a). At the first level, from 5:00 to 7:00, they produce almost no power. From 8:00 to 15:00, according to the second level, they produce an active power of roughly 0.25 p.u. At the third level, they produce an active power of about 0.9 p.u. from 1:00 to 4:00. Finally, at the fourth level corresponding to 16:00-24:00, CCHPs generate an active power of about 1.8 p.u. At the first level, since the price of gas energy based on Fig. 3 is higher than the electricity price, according to Eq. (1), CCHPs are not inclined to produce active power to minimize the operation cost of the electrical network. At the second level, the price of heat energy has the highest value based on Fig. 3; hence, CCHPs are more inclined to produce heat, while producing less active power. In the third and fourth levels, the difference between electricity and gas prices has a positive value, so that this value is high for the fourth level. Therefore, CCHPs produce high power at the fourth level.

The daily curve of the reactive power of the hubs and their elements are presented in Fig. 5(b). It is observed that EVs produce high reactive power from 1:00 to 7:00 because, during these hours, the EVs receive a high level of active power from the network, referring to Fig. 5(a). Hence, it is predicted that if the reactive power of the hubs is not managed, bus voltages will drop sharply. Therefore, EVs and CCHPs generate high reactive power at these hours to regulate the voltage buses, so the hubs inject high reactive power into the network during these hours. At other times, CCHPs can maintain the bus voltages within their allowable range of 0.9 to 1.1 p.u. Also, since EVs based on Eq. (26) inject reactive power into the grid and increase charger losses and operation costs, it is not cost-effective to utilize reactive power in these situations. So, between 8:00 and 24:00, EVs do not generate reactive power. Finally, during these hours, the reactive power curve of the hubs will be equal to the reactive power curve of the CCHPs. Note that this indicates the advantage of coordination between EVs and CCHPs in the form of a hub such that if only EVs were present in the network, higher operation costs would have to be paid to manage the reactive power of the electrical network.

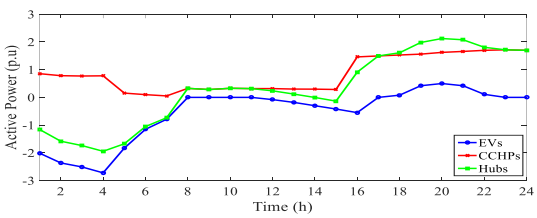

(a)

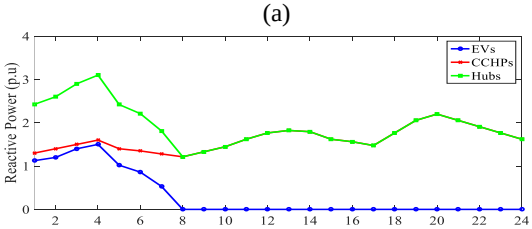

(b)

Fig. 5. The daily curve of hubs and their elements, (a) active power, and (b) reactive power

As is seen in Fig. 6, hubs inject higher amounts of heat power into the district heating network from 8:00 to 15:00, compared to other hours because, in these hours, the difference between heat and gas energy prices is higher than that between electrical and gas energy prices, as Fig. 3 presents. Consequently, CCHPs and/or hubs are more inclined to generate higher heat power. However, the contrary is true from 16:00 to 24:00. As a result, CCHPs are more inclined to generate active power (Fig. 5(a)), so their heat power will be lower during these hours. From 1:00 to 4:00, the heat power level, as shown in Fig. 6, is proportional to the ratio of the difference between heat and gas energy prices (22 – 12 = 10 $/MWh) to the difference between the electrical and gas energy prices (17.6 – 12 = 5.6 $/MWh). Finally, the daily gas power curve of hubs will be as Fig. 7, where its value is constant during all hours. This is due to the operation of CCHPs in electrical and heat sectors in proportion to Figs. 5 and 6.

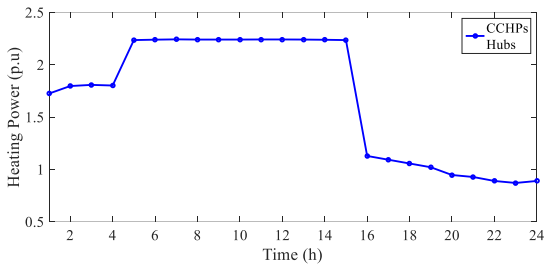

Fig. 6. The daily heat power curve of all hubs

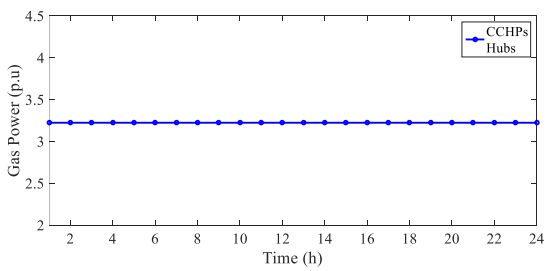

Fig. 7. The daily gas power curve of all hubs

C) Evaluation of capabilities of energy hub in energy networks: The results of the operation indicators of energy networks are listed in Table III in accordance with four different study cases, the details of which are as follows:

- Case I: Power flow analysis neglecting the hubs
- Case II: Proposed problem considering EVs only
- Case III: Proposed problem considering CCHPs only
- Case IV: Proposed problem considering hubs

Table III shows that electrical and heat energy losses in the first study have the highest values, namely, 4.1 and 2.1 p.u, compared to other case studies, respectively. This is also true for the maximum voltage and temperature deviation (maximum value of voltage or temperature deviation from 1p.u). Adding EVs to the first case study (Case II) reduces these indices, but the rate of decline is very low because EVs operate as active loads that have a higher consumption rate than their generation, referring to Fig. 5. Nevertheless, the addition of CCHPs to power grids (Case III) improves or reduces these indices to a high degree compared to Case II. Yet, in this case study, about 1.7 p.u gas energy loss appears and the maximum pressure deviation from zero increases to 0.086 p.u in Case I. Finally, in Case IV, which considers the hub, electrical and heat energy losses are reduced by about 41.5% and 33% compared to Case I, respectively. This reduction for maximum voltage and temperature deviations is about 54.3% and 33%, respectively. These features are created for the proposed strategy by causing 1.8 p.u gas energy loss and a maximum of 0.086 p.u pressure deviation.

The results of reliability in energy networks are proportional to Figs. 8 and 9. Fig. 8 evaluates the EENS changes for the VOLL variations. One can observe that increasing VOLL reduces EENS, until in VOLL of more than 80 $/MWh, the amount of EENS will be constant and equal to 5.41 p.u. In addition, Fig. 9 illustrates the expected operation and reliability cost changes in terms of the VOLL. As can be seen in this figure, an increase in VOLL increases the operation cost, while for a VOLL value of higher than 80 $/MWh, it is fixed at 4857.49$ because, in these conditions, the amount of EENS based on Fig. 8 has a constant value. The expected reliability cost in VOLL is 20 $/MWh, which has the highest value according to the EENS value in Fig. 8, but in other VOLL values, its value decreases. Additionally, although in the VOLL values of more than 80 $/MWh, the expected operation cost and EENS have fixed values, the expected reliability cost increases with increasing VOLL because the cost, based on Eq. (1), is equal to the product of EENS and VOLL.

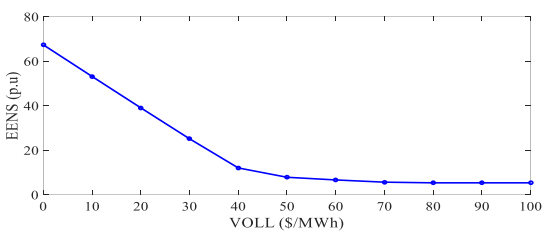

Fig. 8. The EENS curve in terms of VOLL

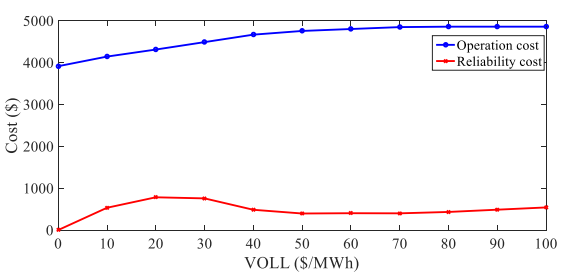

Fig. 9. Expected operation and reliability cost curve in terms of VOLL

V. CONCLUSIONS

The paper presented an RBO of hubs in electrical, natural gas, and district heating networks, where the hub is a framework for coordinating EV parking lots and CCHP. The problem considers the total expected operation and reliability costs of the energy networks provided that OPF constraints, the reliability limitation, and the constraints of the hub with EV parking lots and CCHP are taken into account in these networks. Then, the linearized model of the proposed scheme was employed to determine the optimal solution. Moreover, the SBSP method was utilized to model the uncertainty of the load, energy price, EV parameters, and accessibility of network equipment. Finally, considering the numerical results, it was observed that the linearized problem model was able to obtain the unique optimal solution with a maximum computational error of 2.2% in a very short time compared to the main model of the problem. Furthermore, a coordinated energy management plan between EVs and CCHP in the form of a hub can reduce the operation and reliability cost by about 16% and 56.5%, respectively, compared to the uncoordinated energy management plan. Besides, the hub uses those resources with lower operating costs to manage power. Finally, considering the VOLL equal to 80 $/MWh for the given study system, energy networks with high reliability can be achieved.

REFERENCES

[1] S. Pirouzi, M.A. Latify, G.R. Yousefi, "Conjugate active and reactive power management in a smart distribution network through electric vehicles: A mixed integer-linear programming model," *Sustainable Energy*, Grids and Networks, (accepted), 2020.

[2] M. Ramzanzadeh, and et al. "Security-Constrained Unit Commitment in the Presence of Demand Response Programs and Electric Vehicles," *International Journal of Industrial Electronics*, Control and Optimization, vol. 3, no. 3, pp. 313-326, 2020.

[3] S. Pirouzi *et al*., "Power Conditioning of Distribution Networks via Single-Phase Electric Vehicles Equipped," *IEEE Systems Journal*, vol. 13, no. 3, pp. 3433-3442, 2019.

[4] Q. Zhou, Z. Tian, M. Shahidehpour, X. Liu, A. Alabdulwahab and A. Abusorrah, "Optimal Consensus-Based Distributed Control Strategy for Coordinated Operation of Networked Microgrids," *IEEE Transactions on Power Systems*, vol. 35, no. 3, pp. 2452-2462, 2020.

[5] F. Zhao, C. Zhang and B. Sun, "Initiative optimization operation strategy and multi-objective energy management method for combined cooling heating and power," *IEEE/CAA Journal of Automatica Sinica*, vol. 3, no. 4, pp. 385-393, 2016.

[6] A. Dolatabadi, M. Jadidbonab and B. Mohammadi-ivatloo, "Short-Term Scheduling Strategy for Wind-Based Energy Hub: A Hybrid Stochastic/IGDT Approach," *IEEE Transactions on Sustainable Energy*, vol. 10, no. 1, pp. 438-448, 2019.

[7] S. Fan, Z. Li, J. Wang, L. Piao and Q. Ai, "Cooperative Economic Scheduling for Multiple Energy Hubs: A Bargaining Game Theoretic Perspective," *IEEE Access*, vol. 6, pp. 27777-27789, 2018.

[8] D. Huo, C. Gu, K. Ma, W. Wei, Y. Xiang and S. Le Blond, "Chance-Constrained Optimization for Multienergy Hub Systems in a Smart City," *IEEE Transactions on Industrial Electronics*, vol. 66, no. 2, pp. 1402-1412, 2019.

[9] Y. Yu, T. Zhang, Y. Du and Q. Shao, "Energy hub model for energy management in energy internet," *The Journal of Engineering*, vol. 2019, no. 9, pp. 5432-5438, 2019.

[10] M. Jadidbonab, A. Dolatabadi, B. Mohammadi-Ivatloo, M. Abapour and S. Asadi, "Risk-constrained energy management of PV integrated smart energy hub in the presence of demand response program and compressed air energy storage," *IET Renewable Power Generation*, vol. 13, no. 6, pp. 998-1008, 2019.

[11] T. Zhao, X. Pan, S. Yao, C. Ju and L. Li, "Strategic Bidding of Hybrid AC/DC Microgrid Embedded Energy Hubs: A Two-Stage Chance Constrained Stochastic Programming Approach," *IEEE Transactions on Sustainable Energy*, vol. 11, no. 1, pp. 116-125, 2020.

[12] S. Moazeni, A. H. Miragha and B. Defourny, "A Risk-Averse Stochastic Dynamic Programming Approach to Energy Hub Optimal Dispatch," *IEEE Transactions on Power Systems*, vol. 34, no. 3, pp. 2169-2178, 2019.

[13] M. Majidi and K. Zare, "Integration of Smart Energy Hubs in Distribution Networks Under Uncertainties and Demand Response Concept," *IEEE Transactions on Power Systems*, vol. 34, no. 1, pp. 566-574, 2019.

[14] R. Li, W. Wei, S. Mei, Q. Hu and Q. Wu, "Participation of an Energy Hub in Electricity and Heat Distribution Markets: An MPEC Approach," *IEEE Transactions on Smart Grid*, vol. 10, no. 4, pp. 3641-3653, 2019.

[15] D. Zhang and T. Liu, "A Multi-Step Modeling and Optimal Operation Calculation Method for Large-Scale Energy Hub Model Considering Two Types Demand Responses," *IEEE Transactions on Smart Grid*, vol. 10, no. 6, pp. 6735-6746, 2019.

[16] H. Reza Massrur, T. Niknam and M. Fotuhi-Firuzabad, "Day-ahead energy management framework for a networked gas–heat–electricity microgrid," *IET Generation, Transmission & Distribution*, vol. 13, no. 20, pp. 4617-4629, 2019.

[17] H.R. Zafarani, S.A. Taher, M. Shahidehpour, "Robust operation of a multicarrier energy system considering EVs and CHP units," *Energy*, vol. 192, pp.1-12, 2020.

[18] H.R. Hamidpour, J. Aghaei, S. Pirouzi, S. Dehghan, T. Niknam, "Flexible, reliable, and renewable power system resource expansion planning considering energy storage systems and demand response programs," *IET Renewable Power Generation*, vol. 13, no. 11, pp. 1862-1892, 2019.

[19] M.A. Norouzi, J. Aghaei, S. Pirouzi, T. Niknam, M. Lehtonen, "Flexible operation of grid-connected microgrid using ES," *IET Generation, Transmission & Distribution*, (accepted), 2020.

[20] B. Khorramdel, H. Khorramdel, and J. Aghaei., "Voltage security considerations in optimal operation of BEVs/PHEVs integrated microgrids," *IEEE Trans on Smart Grid.*, vol. 26, no. 2, pp. 12-23, 2014.

[21] J. Aghaei, M. Barani, M. Shafie-khah, A.A.S.d.l. Nieta, and J.P.S. Catalão, "Risk-constrained offering strategy for aggregated hybrid power plant including wind power producer and demand response provider," *IEEE*

Transactions on Sustainable Energy, vol. 7, no. 2, pp. 513-525, 2016.
[22] S. Pirouzi, J. Aghaei, T. Niknam, H. Farahmand, M. Korpås, "Exploring prospective benefits of electric vehicles for optimal energy conditioning in distribution networks," *Energy*, vol. 157, pp. 679-689, 2018.
[23] Generalized algebraic modeling systems (GAMS). [Online]. Available: http://www.gams.com.

Alireza Malekijavan received his B.Sc. degree from the Shahid Sattari Aeronautical University of Science and Technology, Iran, and his M.Sc. degree from Khajenasir, Tehran, Iran, and his Ph.D. degree from Khajenasir University, Tehran, Iran. His current research interests include high-frequency circuit design and intelligent signal processing.

Mehdi Aslinezhad received his B.Sc. degree from the Shahid Sattari Aeronautical University of Science and Technology, Iran in 2003, his M.Sc. degree from Islamic Azad University, Tehran, Iran in 2010, and his Ph.D. degree from Kashan University, Iran in 2019. His current research interests are turbine monitoring, transformer monitoring, and sensors.

Hamidreza Zafarani received his B.Sc. and M.Sc. degrees from Islamic Azad University, Tehran, Iran in 2010 and his Ph.D. degree from Kashan University, Iran in 2020. His current research interests include the application of power electronics in renewable energy systems and electrified railway systems, restructured market, distributed generation, smart grid, electrical vehicles, reactive power control, power quality management, and compensation systems such as SVC, UPQC, FACTS devices.

International Journal of Industrial Electronics, Control and Optimization IECO
Vol. 4, No. 4, pp. 445-451, Sep (2021)

Determining Optimal Value of Pole Arc to Pole Pitch Ratio to Increase Average Torque and Decrease Unbalance Magnetic Force in Hybrid Electrical Vehicle

Alireza Hoseinpour [1,†] and Ahmad Khajeh[2]

[1]Faculty of Electrical Engineering, University of Zabol, Zabol, Iran
[2] Faculty of Electrical and Computer Engineering, University of Sistan and Baluchestan, Zahedan, Iran

ABSTRACT

In this paper, the effects of magnetization patterns on the performance of Hybrid Electrical Vehicle (HEV) are investigated. HEVs have three magnetic field sources: armature winding, permanent magnets, and field winding. To initiate the investigation, the magnetic field distributions produced by these three sources are obtained. By using the magnetic field distributions, the machine is analyzed under no-load and on-load conditions, and the operational indices, such as self and mutual inductance, cogging-, reluctance- and instantaneous torque, and unbalance magnetic force (UMF) in x- and y direction are calculated. Various magnetization patterns are considered to investigate their influences on the performance of the machine. This step was done with Maxwell software. Furthermore, instantaneous torque and magnitude of UMF are expressed in terms of pole arc to pole pitch ratio by using artificial intelligence. The optimal of the pole arc to pole pitch ratio to maximize the average of instantaneous torque and minimize the magnitude of UMF by some multi-objective algorithms is also computed. The modeling and optimization are performed by MATLAB Software.

Article Info

Keywords: Auxiliary winding, Hybrid excitation synchronous machine, Multi-objective optimization, Permanent magnet.

Article History:
Received 2021-07-14
Accepted 2021-09-23

I. INTRODUCTION

The permanent magnet synchronous machines (PMSMs) are widely used in industry due to their high efficiency and torque to volume ratio. Despite their advantages, their flux control capabilities are limited due to the constant permanent magnet flux, especially in surface-mounted PMSMs [1]. To overcome this weakness, it is recommended to use PMSMs with an auxiliary excitation. These machines are named hybrid excitation synchronous machines (HESMs). Therefore, they can be utilized as HEV. These machines have been used in propulsion applications [2] and three-wheel electrical vehicles [3]. Moreover, they can be equipped with a modular magnetic-shunting rotor [4].

HESMs are divided into two types: series HESMs (SHESMs) and parallel HESMs (PHESMs) [5-8]. In SHESMs, the magnet flux and the auxiliary winding (AW) flux pass through the same path, which leads to less iron losses [5]. The machines can operate in the flux-enhancing mode when the fluxes are in the same directions, and if the fluxes are in the opposite directions, the machine is in the flux-weakening mode of operation. In SHESMs, there is a higher probability of demagnetization because the whole AW flux passes through the magnet, and the flux controllability is reduced due to the low permanent magnet permeability [5], [7-8]. In PHESMs, the risk of demagnetization is reduced and, controllability is increased. However, the iron losses are increased because the flux routes of excitation sources are different [5], [8].

[†]**Corresponding Author**: a.hoseinpour@uoz.ac.ir
Tel: +98-9153409088, University of Zabol
Faculty of Electrical Engineering, University of Zabol, Zabol, Iran

If both field sources are placed in the stator, not only there is no need for retaining the sleeve but also the heat is easier removed. However, the mutual torque is not generated, and the end winding effects are considerable [9]. Some of the structures of the machine [10-11] limit the available space for the winding, so the diameter of the stator should be high. Therefore, the torque to volume ratio reduces [12].

If the magnet is on the rotor and the AW is in the stator, the reluctance and the mutual torque are produced. To reduce iron losses, the external rotor structure can be used [13].

If both field excitation sources are located on the rotor [14], mutual, and reluctance torque components are generated. This machine can be employed in constant power applications [12] with speed variations. However, the existence of brushes and retaining sleeves is the disadvantage of this structure [11].

Therefore, a series HESM in which both excitation sources are in the rotor is selected as HEV. Three structures are suggested that both of the rotor excitations are located in the rotor: spoke [15], buried [16], and surface mounted (SM) [17]. Among these three types, only the SM one is a series hybrid excitation synchronous machine, so it is chosen. The structure of a SHESM is shown in Fig. 1.

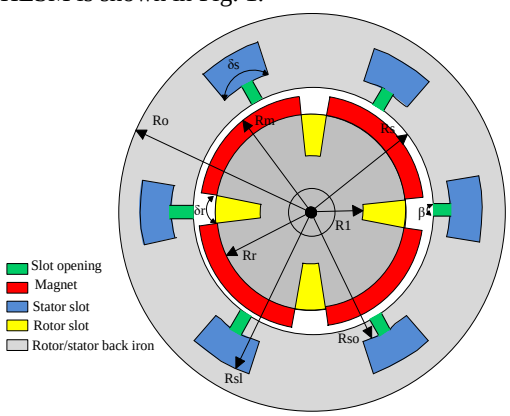

Fig 1. Configuration of SHESM.

Various types of magnetization patterns are reported for PMSMs [18] among which radial magnetization (RM), parallel magnetization (PM), and Halbach magnetization (HM) are more popular. The type of magnetization pattern highly influences the magnetic flux density distribution. Therefore, the performance of the machine is significantly affected by the magnetization pattern. HSEM has been analyzed with a parallel magnetization pattern in [17]. In the present paper, three types of magnetization (RM, PM, and HM) are considered, and the SHESM is analyzed for open-circuit and under load modes of operation.

To model the magnet, there are some methods, such as splitting the magnet into some pieces [19]. However, the Fourier series model was used in tangential and radial directions [20].

In addition, there are two different layouts for stator winding. The first one is non-overlapping, and the second one is overlapping. Moreover, the non-overlapping type is divided into alternate-teeth wounds and all-teeth wounds [20]. It is assumed that the armature winding is a non-overlapping alternate-teeth wound for the SHESM.

In this paper, first, the method of calculating the magnetic field has been explained for a magnetostatic. Then, the torque, inductance, and UMF have been determined for a rotating SHESM. To evaluate the effects of the magnetization pattern on the machine performances, three types of magnetization are simulated, and the results are compared. Finally, the influence of the pole arc to pole pitch ratio on torque and UMF is analyzed.

II. Analysis of SHESM

A. Calculation of flux density

Ampere and Gauss laws are used to obtain the magnetic field in the machine.

$$\nabla \times \boldsymbol{H} = \boldsymbol{J} \quad (1)$$

$$\nabla . \boldsymbol{B} = 0 \quad (2)$$

Where $\boldsymbol{J}$, $\boldsymbol{H}$, and $\boldsymbol{B}$ are current density, magnetic field intensity, and magnetic flux density, respectively.

Equation (3) states the relationship between $\boldsymbol{B}$ and $\boldsymbol{H}$ in the magnetized area.

$$\boldsymbol{B}=\mu_0\mu_{rm}\boldsymbol{H}+\mu_0\boldsymbol{M} \quad (3)$$

Where μ_0, μ_{rm}, and $\boldsymbol{M}$ are permeability of free space, the relative permeability of magnet, and magnetization vector, respectively.

Substituting relation (3) in the Ampere's law yields:

$$\nabla \times \boldsymbol{B} = \mu_0\mu_r\boldsymbol{J} + \mu_0\nabla \times \boldsymbol{M} \quad (4)$$

Where μ_r is the relative permeability of winding space. Given that the $\nabla.\boldsymbol{B} = 0$, thus flux density is Curl of another quantity which is called the vector magnetic potential. Therefore,

$$\boldsymbol{B} = \nabla \times \boldsymbol{A} \quad (5)$$

Replacing equation (5) in (4) and considering that $\nabla.\boldsymbol{A} = 0$, the following relation is obtained:

$$\nabla^2\boldsymbol{A} = -\mu_0\mu_r\boldsymbol{J} - \mu_0\nabla \times \boldsymbol{M} \quad (6)$$

In regions where there is current but no magnetization (e.g., winding regions), the following relation can be written.

$$\nabla^2\boldsymbol{A} = -\mu_0\mu_r\boldsymbol{J} \quad (7)$$

In regions where there is magnetization but no current (e.g., magnet), we will have the following relation.

$$\nabla^2\boldsymbol{A} = -\mu_0\nabla \times \boldsymbol{M} \quad (8)$$

In regions where there is neither current nor magnetization (e.g., air-gap region), the Laplace equation can be written.

$$\nabla^2\boldsymbol{A} = 0 \quad (9)$$

These equations are solved numerically in Maxwell software by finite element method [21]; thus flux density is calculated.

B. Energy calculation

The magnetic energy of a system is given by the following expressions. The expressions represent total values of energy for the volumes taken into account. Note that the integrals

have simpler expressions if the material property of the object considered is a linear one. In the case of linear material properties, magnetic energy and co-energy values are identical ($w = w_c$).

$$w = w_c = \int_V \left(\int_0^B \boldsymbol{H}.d\boldsymbol{B} \right) dV \tag{10}$$

where V is the volume of the machine.

C. UMF calculation

The radial and tangential forces are calculated by Maxwell stress tensor. First, the flux density should be computed then the mentioned magnetic pull is obtained by the following relations.

$$f_r = \frac{1}{2\mu_0}\left({B_r}^2 - {B_\theta}^2\right) \tag{11}$$

$$f_\theta = \frac{1}{\mu_0} B_r B_\theta \tag{12}$$

These equations can be transformed into the Cartesian system.

$$f_x = f_r \cos(\theta) - f_\theta \sin(\theta) \tag{13}$$

$$f_y = f_r \sin(\theta) + f_\theta \cos(\theta) \tag{14}$$

Then, the x- and y components of UMF are determined with the integration of these magnetic pulls in the middle of the air gap by formulas numbers (15) and (16). Finally, the magnitude of UMF is calculated based on them by (17).

$$F_x = \int_{-L/2}^{L/2} \int_{-\pi}^{\pi} f_x r \, d\theta \, dz = L \int_{-\pi}^{\pi} f_x r \, d\theta \tag{15}$$

$$F_y = \int_{-L/2}^{L/2} \int_{-\pi}^{\pi} f_y r \, d\theta \, dz = L \int_{-\pi}^{\pi} f_y r \, d\theta \tag{16}$$

$$F_r = \sqrt{F_x^2 + F_y^2} \tag{17}$$

D. Torque calculation

The instantaneous torque ($\boldsymbol{T_{inst}}$) is computed by $\boldsymbol{T} = \boldsymbol{r} \times \boldsymbol{F}$ as follows.

$$\boldsymbol{r} = r a_r$$

$$\boldsymbol{F} = F_r a_r + F_\theta a_\theta$$

$$T_{inst} = r \times F = (r a_r) \times \int_{-\frac{L}{2}}^{\frac{L}{2}} \int (f_r a_r + f_\theta a_\theta) \, dl \, dz = \frac{L}{\mu_0} \int r \, B_\theta B_r \, dl a_z \tag{18}$$

The instantaneous torque has three components. The first one is cogging torque, the second one is reluctance torque, and the last one is mutual torque. In order to compute cogging torque magnet and AW are active, and stator excitation is inactive. In contrast, just armature winding should be excited to calculate reluctance torque. Mutual torque is achieved by the interaction between field- and armature excitation.

E. Inductance calculation

The mutual inductance between two phases is computed by the following equation.

$$w_{ij} = \frac{1}{2} L_{ij} I^2 \rightarrow L_{ij} = \frac{2w_{ij}}{I^2} \tag{19}$$

Where w_{ij} is the energy stored in the magnetic field linking conductor i with conductor j. I is the current in conductor i. In order to set the self-inductance of a phase, just consider i instead of j as bellow

$$w_{ii} = \frac{1}{2} L_{ii} I^2 \rightarrow L_{ii} = \frac{2w_{ii}}{I^2} \tag{20}$$

III. SIMULATION RESULTS

A. MODELING OF SHESM

According to Fig. 3, the center of the magnet is aligned with the first slot of the stator, and the layout of the stator winding is an alternate-teeth wound. The characteristic of the machine is presented in Table I, and three types of magnetization for the magnets are considered. The machine's rotor moves in the dynamic analysis, and the torque, the mutual inductance of stator phases, and the UMF are calculated.

The spatial angle is chosen as the horizontal axis in the Figs of this section. In the following, inductance, torque, and UMF are computed for this machine.

The mutual inductances, between stator phases, are independent of the type of magnetization, and depend on the configuration of the stator coil and the machine dimensions. The individual flux linkage of each phase is more than the coupling flux with other phases; thus the self-inductance value is more than mutual inductances. Further, the stator self-inductance is a function of the rotor position because it includes a slot. Since the angle between phases is 120 degrees, so the two-phase mutual inductance is negative. These points are clearly visible in Fig. 4.

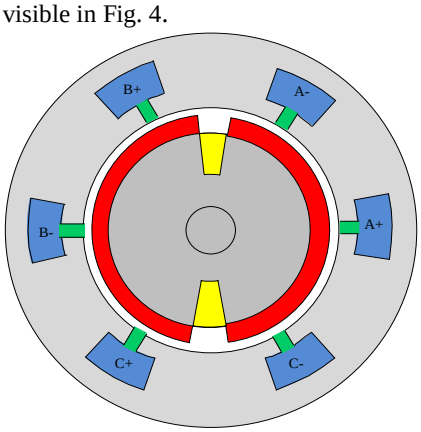

Fig. 3 The structure of SHESM.

TABLE I
Parameters of the SHESM.

Parameters	symbols	Values	Parameters	symbols	Values
Number of pole-pairs	p	1	Stator-slot span angle	δ_s	0.6283 rad
Number of stator-slots	Q_s	6	Stator-slot-opening span angle	β	0.4398 rad
Number of rotor-slots	Q_r	2	Rotor-slot span angle	δ_r	0.4712 rad
Outer radius of machine	R_o	105 mm	Pole arc to pole pitch ratio	α	0.85
Outer radius of the stator-slots	R_{sl}	81.5 mm	Permanent magnet remanence	B_{rem}	1 T
Outer radius of the stator-slot-opening	R_{so}	62.9 mm	Relative recoil permeability of magnets	μ_{rm}	1.05
Staor bore radius	R_s	57.5 mm	Cross sectional area of wire in stator and rotor	A_c	1.2 mm^2
Magnet Radius	R_m	56 mm	Rotor current	I_r	10 A
Rotor back-iron radius	R_r	50 mm	Stator peak current	I_m	14.14 A
Inner rotor-slot radius	R_1	26.5 mm	Number of stator coil winding turns	N_{ts}	422
Motor axial length	L	90 mm	Number of rotor coil winding turns	N_{tr}	212

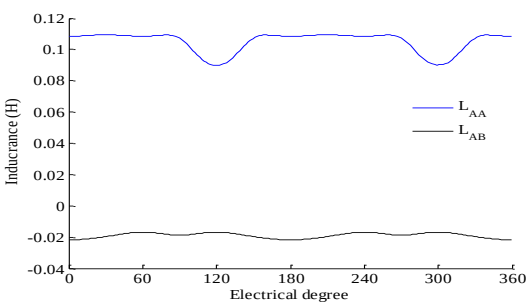

Fig.4. Self and mutual inductances.

The instantaneous torque includes three components; reluctance-, cogging-, and mutual torque. In this SHESM, the reluctance torque is produced by armature excitation; thus it is independent of the magnetization. Despite the reluctance torque, the cogging and mutual torque, in which the excitation resources of the field have the main influence, are affected by the magnetization type. Therefore, the instantaneous torque is affected by the magnetization patterns.

Reluctance torque is shown in Fig. 5.a. By comparison of the presented Figs for cogging torque in Fig. 5.b, HM has the lowest cogging torque, so from this point of view, it is more desirable.

The average amounts of T_{inst} for RM, PM, and HM are 34.68, 29.88, and 27.37 N.m., respectively. Therefore, radial magnetization produces higher torque, but it is not recommended for applications where the torque ripple is important.

The unbalanced magnetic forces can be divided into two components along the x and y axes. The two components of three magnetization patterns are shown in Figs 6.a and 6.b. The magnitude of the force, which is calculated from equation 17 is shown in Fig. 6.c. It can be deduced from Fig. 6 that the HM produces less UMF.

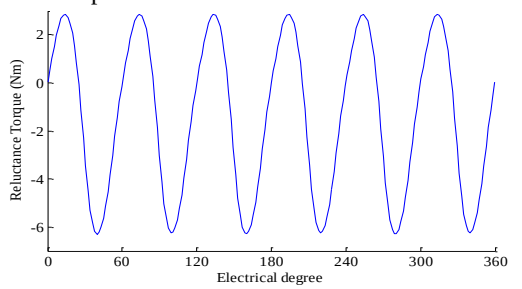

a

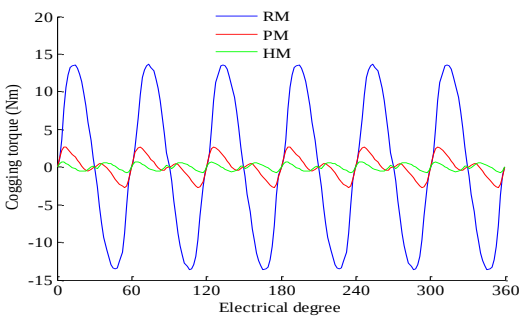

b

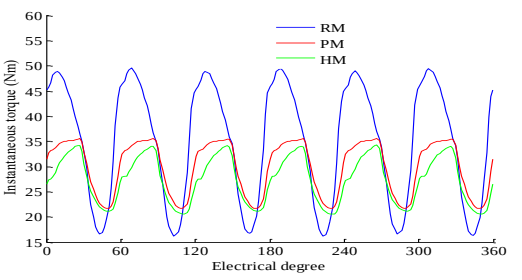

c

Fig.5. a) Reluctance torque. b) Cogging torque due to three magnetization patterns. c) Instantaneous torque for RM, PM, and HM.

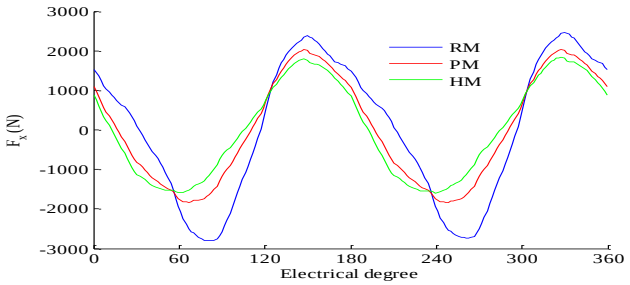

a

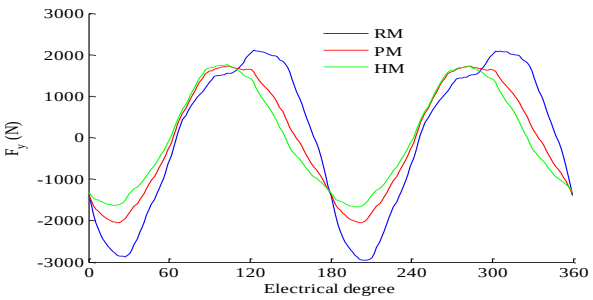

b

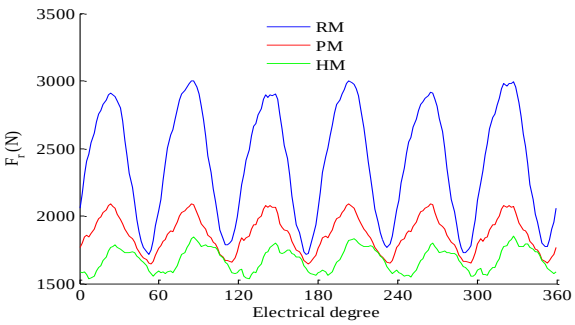

c

Fig.6. a) UMF in x direction. b) UMF in y direction. c) The magnitude of UMF.

B. OPTIMAL DESIGN

In this section, the effect of the pole arc to pole pitch ratio on the SHESM performance, denoted by α, is investigated. Indeed, the impact of changes of α on the average instantaneous torque (T_{ave}) and the magnitude of UMF (F_r) are demonstrated. Magnet is the main field source, and rotor winding is the auxiliary field source which causes that α be greater than 0.5. Moreover, the magnetization type is considered to be RM, and rotor current density is constant.

Table.II presents T_{ave} for several values of α. As well, Fig.7 shows T_{ave} versus α, and it is clear that a second-degree polynomial can be fitted to it as follows

$$T_{ave} = -54.3571\alpha^2 + 74.0257\alpha + 10.9297 \quad \text{Nm} \qquad (21)$$

TABLE. II.
Average torque

α	0.95	0.85	0.75	0.65	0.55
T_{ave}	32.15	34.68	35.85	36.01	35.24

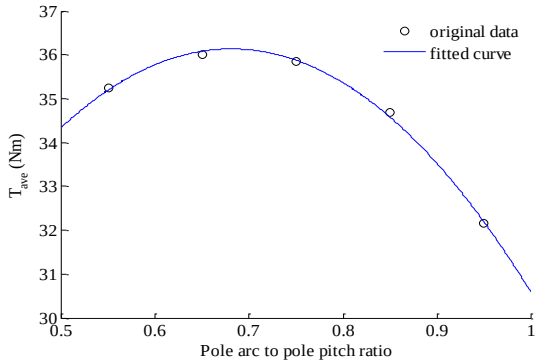

Fig. 7.T_{ave} versus α

According to equation (21) the maximum of the T_{ave} is achieved by α=0.6809 is 36.13. If SHESM is simulated by mentioned α the average torque is 36.07.

After that, the influence of pole arc to pole pitch ratio on the magnitude of UMF will be analyzed. According to Table.III, decreasing the value of α leads to decreasing in F_r average (F_{ra}). Therefore, from this point of view, the reduction of α is suitable. It can also be fitted grade 3 polynomial for the relation between F_{ra} with α as presented in (22)

$$F_{ra} = -21.1166\alpha^3 + 42.1964\alpha^2 - 25.2142\alpha + 6.3 \quad KN \qquad (22)$$

TABLE. III.
Changes of F_{ra} due to α

α	0.95	0.85	0.75	0.65	0.55
F_{ra}	2341	2416	2255	1986	1735

Now, two expressions obtained for the average torque and F_{ra}must be optimized simultaneously. Given that, the goal is to minimize, so instead of torque, its inverse is considered. In fact, we are faced with a two-objective optimization problem as follows:

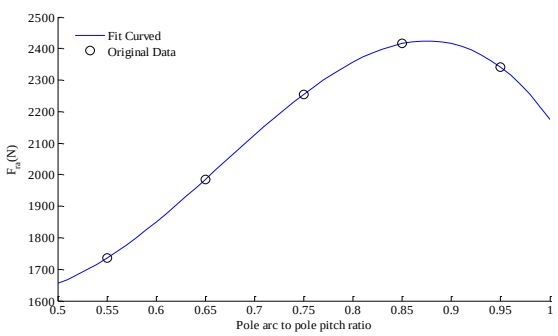

Fig. 8.pF_{ra} versus α

Min (1/Tave, Fr) (23)

$1/T_{ave}$=1/(-54.3571α^2+74.0257α+10.9297) (24)

F_r=-21.1166α^3+42.1964α^2-25.21421α+6.3 (25)

s.t 0.50<a<1 (26)

If the mentioned multi-objective problem is optimized with the NSGA-II, PESA-II, and MPSO algorithm, the obtained

Pareto fronts as shown in Fig. 9a to 9c. The results are very close, so the optimal point of Pareto front will be achieved by fuzzy Max-Min [22] algorithm in MPSO Pareto front, which is

$$\alpha = 0.5335 \quad (27)$$

$$T_{ave} = \frac{1}{0.0286} = 34.965 \quad (28)$$

$$F_{ra} = 1702 \quad (29)$$

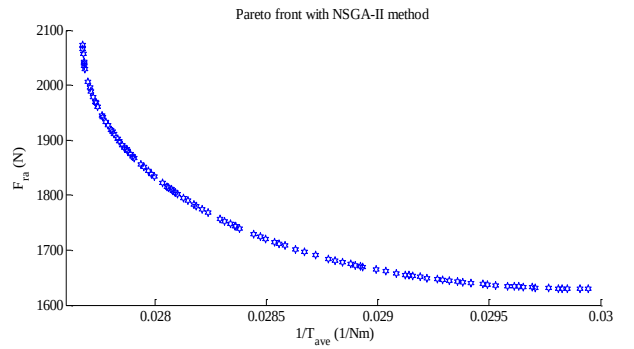

(a)

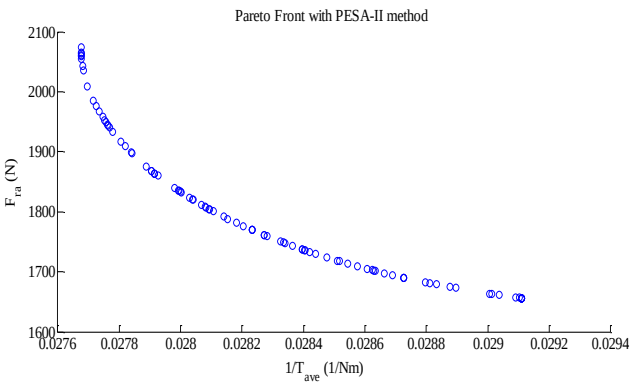

(b)

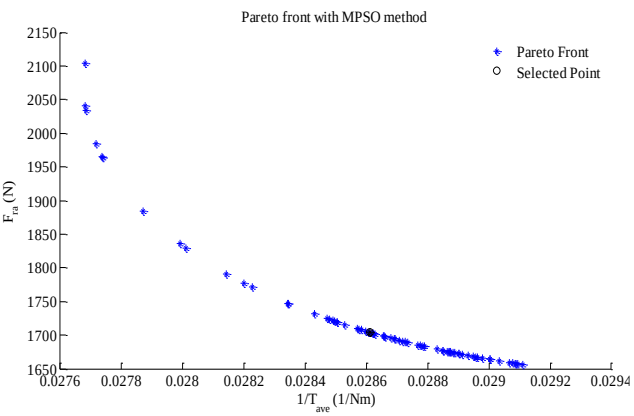

(c)

Fig. 9. Pareto front for both objective (magnitude of UMF and inverse of instantaneous torque) a) NSGA-II b) PESA-II c) MPSO

If the SHESM is simulated for obtained pole arc to pole pitch ratio, the instantaneous torque diagram will be as shown in Fig. 11. Furthermore, the curve of UMF in x - and y direction, and its magnitude are drowned in Fig11.

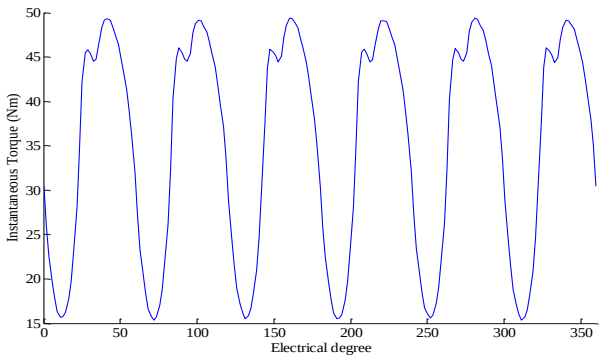

Fig. 10. Instantaneous torque

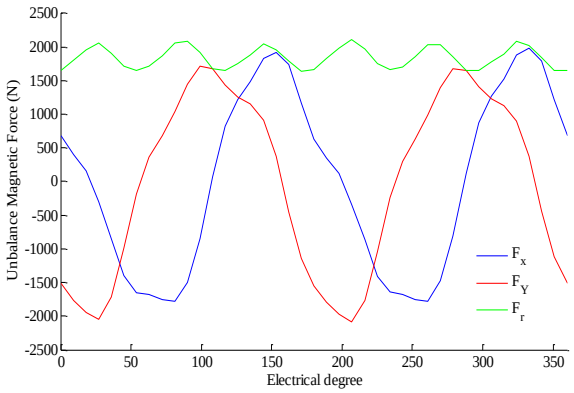

Fig. 11: Unbalance magnetic force

CONCLUSIONS

In this paper, a SHESM was introduced, and the effect of different magnetization patterns was evaluated on its performance. High average instantaneous torque is achieved with radial magnetization, while low cogging torque, torque ripple, and UMF are obtained with Halbach magnetization. Moreover, increasing average instantaneous torque and decreasing magnitude of UMF can be achieved by determining the pole pitch to pole are ratio properly.

REFERENCES

[1] A. Hosseinpour, M. Mardaneh and A. Rahideh "*Investigation of the Effects of Different Magnetization Patterns on the Performance of Series Hybrid Excitation Synchronous Machines*" Progress In Electromagnetics Research M, Vol. 64, 109–121, 2018.

[2] C. Wang, Z. Zhang, Y. Liu and H. Gao, "*Mechanical Design and Analysis of a High-Torque Modular Hybrid Ecitation Synchronous Machine for Electric Vehicle Propulsion Applications* "IEEE Transactions on Vehicular Technology, Vol. 69, Is. 9, 2020.

[3] A. Shah Mohammadi and J. P. F. Trovão, " *System-Level System-Level Optimization of Hybrid Excitation Synchronous Machines for a Three-Wheel Electric Vehicle* "IEEE Transactions on Transportation Electrification, Vol. 6, Is. 2, 2020.

[4] Y. Liu, Z. Zhang, C. Wang and H. Gao, "Optimization and Performance Improvement of a Hybrid Excitation Synchronous Machine with Modular Magnetic-Shunting Rotor", *IEEE Transactions on Industrial Electronics*, Vol. 67, Is. 6, 2020.

[5] Y. Amara, S. Hlioui, Rachid Belfkira, G. Barakat and M. Gabsi "Comparison of open circuit flux control capability of a series double excitation machine and a parallel double excitation machine" *IEEE Trans. Veh. Technol.*, vol. 60, no. 9, Nov 2011.

[6] Y. Wang and Z. Deng "Hybrid excitation topologies and control strategies of stator permanent magnet machines for DC power system" *IEEE Trans. Ind. Elec.*, vol. 59, no. 12, 2012.

[7] W. Geng, Z. Zhang, K. Jiang and Yangguang Yan, "A new parallel hybrid excitation machine: permanent-magnet/variable-reluctance machine with bidirectional field-regulating capability*" IEEE Trans. Ind. Elec.*, vol. 62, no. 3, Mar. 2015.

[8] K. Kamiev, J. Pyrh¨onen, J. Nerg,V. Zaboin and J. Tapia "Modeling and testing of an armature-reaction-compensated (PM) synchronous generator" *IEEE Trans. Energy Convers*., vol. 28, no. 4, Dec. 2013.

[9] X. Zhu, M. Cheng, W. Hua, J. Zhang, and W. Zhao, "Design and analysis of a new hybrid excited doubly salient machine capable of field control," in *Conf. Rec. IEEE IAS Annu. Meeting*, Tampa, FL, USA, 2006, vol. 5,pp. 2382–2389.

[10] W. Hua, M. Cheng, and G. Zhang, "A novel hybrid excitation flux switching motor for hybrid vehicles," *IEEE Trans. Magn.*, vol. 45, no. 10,pp. 4728–4731, Oct. 2009.

[11] R. L. Owen, Z. Q. Zhu, and G. W. Jewell, "Hybrid-excited flux-switching permanent-magnet machines with iron flux bridges," *IEEE Trans. Magn.*, vol. 46, no. 6, pp. 1726–1729, Jun. 2010.

[12] Z. Zhang, S. Ma, J. Dai and Y. Yan "Investigation of Hybrid Excitation Synchronous Machines With Axial Auxiliary Air-Gaps and Non-Uniform Air-Gaps" *IEEE Trans. Ind Appl.*, vol. 50, no. 3, May/Jun. 2014.

[13] L. Xiaogang and T. A. Lipo, "A synchronous/permanent magnet hybrid AC machine," *IEEE Trans. Energy Convers.*, vol. 15, no. 2, pp. 203–210, Jun. 2000

[14] A. Hosseinpour, M. Mardaneh and A. Rahideh "Two-dimensional analytical model for double field excitation synchronous machines" IET Generation, Transmission & Distribution , Vol. 15, Is. 6, pp. 1081-1093, 2021.

[15] S. I. Kim, J. Cho, S. Park, T. Park and S. Lim "Characteristics comparison of a conventional and modified spoke-type ferrite magnet motor for traction drives of low-speed electric vehicles " *IEEE Trans. on Ind. Appl.*, vol. 49, no. 6, pp. 2516-2523, 2013.

[16] K. Kamiev, J. Nerg, J. Pyrhönen, V. Zaboin, and J. Tapia "Feasibility of an armature-reaction-compensated permanent-magnet synchronous generator in island operation" *IEEE Trans. Ind. Elec.*, vol. 61, no. 9, Sep. 2014.

[17] H. Bali, Y. Amara, G. Barakat, R. Ibtiouen and M. Gabsi "Analytical modeling of open circuit magnetic field in wound field and series double excitation synchronous machines" *IEEE Trans. Magn.*, vol. 46, no. 10, Oct. 2010.

[18] A. Rahideh , M. Mardaneh , and T. Korakianitis "Analytical 2-D Calculations of Torque, Inductance, and Back-EMF for Brushless Slotless Machines With Surface Inset Magnets" *IEEE Trans. Magn.*, Vol. 49, no. 8, pp.1-12, Aug. 2013.

[19] V. Z .Faradonbeh, A. Rahideh, M. M. Ghahfarokhi, E. Amiri, A. D. Aliabad, G.A Markadeh,"Analytical Modeling of Slotted, Surface Mounted Permanent Magnet Synchronous Motors with Different Rotor Frames and Magnet Shapes" IEEE Transactions on Magnetics, Vol. 57, Is. 1, 2021.

[20] A. Rahideh and T. Korakianitis, "Analytical magnetic field calculation of slotted brushless permanent-magnet machines with surface inset magnets," *IEEE Trans. Magn.*, vol. 48, no. 10, pp. 2633–2649, Oct.2012.

[21] M. Ghods, Z. Nasiri-Gheidari, and H. Oraee " Performance Analysis of Permanent Magnet Vernier Generator under Mechanical Faults" *International Journal of Industrial Electronics, Control and Optimization*, Vol. 1, No. 2, pp. 121-131, 2018.

[22] G. Xiao, T. Zhu, Y. Chen and X. Yang "*Linear Searching Method for Solving Approximate Solution to System of Max-Min Fuzzy Relation Equations With Application in the Instructional Information Resources Allocation*" IEEE ACCESS, vol. 7, pp. 65019-65028, 2019.

Alireza Hoseinpour was born in Zabol, Iran in 1985. He received his B.Sc. degree with honors from Sistan and Baluchestan University of Zahedan, Iran in 2007. In 2010, he received his M.Sc. degree from the Ferdowsi University of Mashhad, Iran and Ph.D. degree in 2018 from the Shiraz University of Technology all in electrical engineering. Following receipt of the Ph.D. degree, he joined the University of Zabol, Iran. His main research interests are wind turbine, renewable energy, permanent magnet synchronous machine drive, four-switch three-phase inverter, power electronic, and design of hybrid electrical vehicle.

Ahmad Khajeh was born in Zabol, Iran in 1982. He received the B.Eng. degree from Sistan and Baluchestan University, Zahedan, Iran, in 2004 and the M.Eng. and Ph.D. degrees from the Amirkabir University of Technology and Ferdowsi University of Mashhad, Iran in 2007 and 2014, all in electrical engineering, respectively. Currently, he is an Assistant Professor with the Faculty of Electrical and Computer Engineering, University of Sistan and Baluchestan, Zahedan, Iran. His current research interests include power electronics, wind power, adjustable speed drives, and photovoltaic system.

IECO

This page intentionally left blank.

International Journal of Industrial Electronics, Control and Optimization © 2021 IECO
Vol. 4, No. 4, pp. 453-464, Sep (2021)

Optimal Charging/Discharging Control of Electric Vehicle Charging Station Considering Grid Resiliency

Emad Hadian[1] , Hamidreza Akbari[2†], Mehdi Farzinfar[3], and Seyed Amin Saeed[4]

[1,2,4] Department of Electrical Engineering, Yazd Branch, Islamic Azad University, Yazd, Iran
[3] School of Engineering, Damghan University, Damghan, Iran

ABSTRACT

Management and control of charging/discharging of Electric vehicles (EVs) with the aim of profitability for the Distribution System Operator (DSO) and the private sector is one of the challenges in operating Electric vehicles Charging Stations (EVCS). This paper proposes a novel methodology for optimal planning of charging/discharging of the hybrid wind- EVCS which on the one hand, lead to correction of the load curve and on the other hand, improves the grid resilience in extreme weather conditions. In the proposed methodology, since the weather based outages lead to consumer interruptions, the idea of profit sharing between DSO and EVCS owner is proposed to incentivize the owner to implement the obtained charging/discharging schedule. To this end, firstly, a Monte-Carlo based stochastic framework for forecasting probability of weather based line outages and also modelling uncertainties is devised. Then, a resilience-oriented multi-objective optimization algorithm is presented that, while coordinating operation of the wind turbine, EV management and Demand Response Programs (DRP), the profits of both EVCS and DSO are maximized during daily operation planning. The resiliency improvement of the proposed method is evaluated by using ΦΛΕΠ metrics. The obtained optimal results prove effectiveness of the proposed method in increasing resiliency and benefits for all players.

Article Info

Keywords:
Control of Charging/Discharging, Electric Vehicle, Extreme Weather Condition, Multi-Objective Optimization, Resilience

Article History:
Received 2021-01-12
Accepted 2021-09-24

I. INTRODUCTION

The growing use of Electric Vehicles (EVs) within the grid is one of the interesting topics in the concept of smart grid, particularly, as EVs can be integrated in as mobile demand or Energy Storage (ES). However, the accidental and unplanned connection of EVs to the distribution network is a challenge for operation of the power system [1, 2]. In this regard, the idea of constructing and planning EV Charging Stations (EVCS), as per the V2G capability of EVs, has been implemented. In fact, EVs are parked within the EVCSs when not in use [3]. In this way, EVs can be modeled as a load that consumes a power from the network while charging, and as an energy storage device, which is discharged to feed the stored energy back into the grid [4, 5].

Another recent topic is to equip the EVCSs with Distributed Energy Resources (DER), and in this way, DERs can be operated to inject energy into the EVCS and network. This interesting topic has attracted attentions in the recent years, so that, solar, wind, and hybrid wind-solar powered charging stations have been studied and realized. In the most cases, the EVCS is linked to the distribution network and can supply its energy from both grid and renewable resources (DERs) [6-10]. In this regard, charging/discharging strategies of the EVs, and especially the adopted programs under which the EV is posed in charging/discharging conditions, are among main challenges of operating the EVCS. Moreover, integration of the DERs and EVCSs requires coordination of DERs generation and EVs charging/discharging behavior. In other words, lack of suitable methods for EVs management

† **Corresponding Authors:**, h.akbari@iauyazd.ac.ir
Department of Electrical Engineering, Yazd Branch, Islamic Azad University, Tel: +98-3531872742, Fax: +98-3538215034

may lead to unexpected events such as feeder congestion, increasing active power losses, voltage drop, decreasing economic profits and reliability [11]. Various researches have been conducted in response to such challenges, among which the following can be mentioned. In [12, 13] a stochastic method, based on Monte Carlo simulation, for modelling the probabilistic nature of the EVs, like daily travel distance, charging pattern is presented.

Technical issues on scheduling, controlling and operating of EVs are reviewed in [14]. In [15] charging/discharging schedule of EVs is simply presented based on the market price, however, it does not consider the effect of presented schedule on load profile of the network. In [16, 17], considering all available opportunities, optimal coordination of DERs and EVs for the purpose of load shaving during peak load hours, reducing active power losses and voltage drop is done. In [18, 19], with the purpose of reliability improvement the charging program of the EVs is modeled, However, the discharging schedule of EVs is not studied. Therefore, it can be concluded that the most optimal program is obtained when the benefits of the EVCS (or EV) owner and the Distribution System Operator (DSO), are considered simultaneously. This issue is discussed in paper [20] and a method to share the benefits of the program implementation is proposed.

In all above mentioned papers, charging/discharging programs are mainly devised regardless of resiliency of the grid, which is one of the drawbacks of the existing researches. In fact, such programs are only presented with the aim of flattening load curve of the network, while in case of natural disasters; charging/discharging behavior of the EVCS must be changed to improve resilience of the network. In the power systems, the grid resiliency is defined as ability of the network to prepare, survive, and rapidly recover itself in face of unforeseen events, like extreme weather conditions, as it has effects on outage rate of lines [21-23]. It should be noted that development and implementation of the charging/discharging program with the aim of improving network resilience can reduce Energy Not Supplied (ENS) to an acceptable level and thus reduce cost of the DSO [24].

On the other hand, wind speed may affect scheduling of the wind turbines. Thus, in addition to investigating effect of extreme weather (like thunder) on the grid resilience, changes in wind turbine generation should also be considered. Comprehensive challenges in DERs scheduling and forecasting wind effects on outage rates can be found in [25-27].

In the context of the grid resilience improvement, various methods such as Demand Response Programs (DRP) [28, 29], DER utilization, network reconfiguration methods [30] have been proposed. However, in the matter of the EVCS, particularly integrated with DERs, developing an optimal and proportionate charging/discharging schedule can effectively improve network resilience. A risk-based operational planning for enhancing grid resiliency has been proposed in paper [21]. Further, in [21, 22] resilience improvement is obtained via infrastructure and minimization of outages duration.

Based on the above discussion, in the existing researches, charging/discharging programs of EVs has been rarely devised with the aim of network resilience improvement. In the view of such shortcoming, this paper proposes a novel methodology for optimal charging/discharging program of the EVCS which through it benefits of both DSO and EVCS owner are optimally maximized. In the proposed methodology, as per effective role of the EVCS in improving grid resiliency, the idea of profit sharing between DSO and EVCS owner is applied to incentivize the EVCS owner to implement the devised charging/discharging schedule; and to increase the resiliency of the network against extreme weather conditions. In this regards, firstly, a stochastic framework, on the basis of Monte Carlo simulation, is proposed to forecast probability of weather based line outages and also to model random variables considering related uncertainties. In the next step, a formulation for optimal charging/discharging schedule of the EVCS is devised. In the proposed formulation, while optimizing power purchases from the utility, bus voltage deviation, power loss, grid resilience in the extreme weather condition is also maximized. However, to incentivize the EVCS owner to implement the optimal charging/discharging schedule and to participate in improving plan of resiliency, the idea of benefit sharing on the basis of energy price modification is applied. Moreover, the coordination of wind turbine, EV management and Demand Response Programs (DRP) is performed.

The resilience oriented multi-objective optimization algorithm of this paper is solved using a Modified Particle Swarm Optimization algorithm (MMPSO) and Pareto front solutions are obtained. Applying hybrid sequential Monte Carlo simulation and MMPSO algorithm increases the accuracy of achieving optimal solutions set. Finally, the proposed methodology is evaluated using ΦΛΕΠ metrics which through a multi-phase resilience trapezoid method all disturbance progress, post-disturbance degraded and restorative state are assessed. In summary, taxonomy of the most related research works is reported in Table I.

TABLE I
TAXONOMY OF THE LITERATURE REVIEW

Contribution	Ref	5	6	7	9	10	11-16 -18	13	1-15	17-19 -8	20	21-22- 24	27	31 32	This paper
optimal EVCS allocation		yes	no	no	yes	no	no	no	no	no	yes	no	no	yes	no
integration of the DERs into EVCSs		no	yes	no	yes	no	no	yes	no	no	no	no	no	yes	yes
coordination of DERs and EVs for optimal operation of EVCS and grid		no	yes	no	yes	no	no	yes	no	no	no	no	no	yes	yes
management of EVCS for load profile flattering		yes	yes	yes	no	yes	yes	yes	no	yes	yes	no	yes	yes	yes
optimal charging/discharging schedule of the EVs		yes	yes	yes	no	yes	yes	yes	yes	yes	yes	no	yes	no	yes
profit sharing between DSO and EVCS owner		no	no	no	no	yes	no	yes	yes	yes	yes	no	no	no	yes
resilience improvement of the grid		no	no	no	no	no	no	no	no	no	no	yes	no	no	yes
simultaneous investigation of effect of charging/discharging schedule and extreme weather on the grid resilience		no	no	no	no	no	no	no	no	no	no	yes	no	no	yes

II. MATHEMATICAL MODELLING AND FORMULATION OF THE PROBLEM

In this section, first, the mathematical model for all influencing components is presented, and then the proposed formulation for solving the problem is described.

A. EV and EVCS Models

As explained earlier, EVs are parked within the EVCS in the charging/or discharging intervals. However, since the EV owners might not care about their effects on the grid operation, the do not specifically connect EVs to the grid. Hence, the operation time of the EVCS within the grid is uncertain unless an appropriate planning is made. Therefore, the uncertainties, like duration time each EV is connected, distance traveled by each EV, the State of Charge (SOC) level of each EV at the charging/discharging time should be considered in the modeling of EVs and EVCS [31].

In this respect, this paper employ the Truncated Normal distribution function for modelling independent random variables, including EVs battery capacity, the distance and duration time of the trip, the parking time of the EV within the EVCS. Further, remaining dependent variables such as time of arrival/ departure of the EV to/from the EVCS is calculated. The details of such stochastic modeling are given in the [20].

Another parameter which affects the charging/discharging plan for the EV during the EV's presence at the EVCS, and is associated with uncertainty is the SOC level of EVs when connected to the grid. The SOC level of EVs while charging and discharging can be calculated according to the distance traveled (D_i) as follows [20]:

$$SOC_{\text{int}}^{i} = \left(1 - \frac{D_i}{D_{Total}}\right) \times 100\% \quad , \forall i \in N_{EVs} \tag{1}$$

$$SOC_t^i = X_1\left(SOC_{t-1}^i + \Delta t.\left(ch_{rate}\right)\right) \times 100\% \ , \forall i \in N_{EVs}, \forall t \in T \tag{2}$$

$$SOC_t^i = X_2\left(SOC_{t-1}^i - \Delta t.\left(disch_{rate}\right)\right) \times 100\% \ , \forall i \in N_{EVs}, \forall t \in T \tag{3}$$

Where SOC_{int}^{i} is the initial SOC of EV, the charge/discharge rate of EV batteries in the time step of Δt are specified with ch_{rate} / $disch_{rate}$. Also, the simultaneous charging/discharging of the EVs is avoided by using binary variables X_1 and X_2.

As per above e equations, charging/discharging time of EVs, and the total injected or absorbed energy of the EVCS can be modeled as follows:

$$t_{ch\,\text{arge}}(i) = \frac{(SOC_{\max} - SOC_t^i) \times ES_i}{P_v} \tag{4}$$

$$t_{disch\,\text{arge}}(i) = \frac{(SOC_t^i - SOC_{\min}) \times ES_i}{P_v} \tag{5}$$

$$E_{EVCS}^{disch\,\text{arge}} = \sum_{i}^{N_{EVs}} \text{Pre}T(i) \times C_i \times (SOC_{\text{int}}^{i} - SOC_{\min}) \ \forall \Delta t_{disch\,\text{arge}} \tag{6}$$

$$E_{EVCS}^{ch\,\text{arge}} = \sum_{i}^{N_{EVs}} \text{Pre}T(i) \times C_i \times (SOC_{\max} - SOC_{\text{int}}^{i}) \ \forall \Delta t_{ch\,\text{arge}} \tag{7}$$

Where $\text{Pre}T(i)$ is the presence time of each EV at the EVCS, C_i is battery capacity of EV number i.

In the field of modeling probabilistic parameters of EV /EVCS, in addition to the above equations, there are other stochastic variables, like time of arrival/departure of EV, duration time of the EV's trip, presence time of EVs inside the EVCS, that have been avoided to rewrite here due to the fact that they exist in the references like [13, 20]. However, utilization of the sequential Monte Carlo simulation for calculation of final model of such parameter is required. Hence, after formulating the probabilistic model, the Monte Carlo simulation with repeated replications is utilized to obtain the mean values during the simulation period. To this

end, the stopping criterion is satisfaction of the Coefficient of Variation (CV) which is assumed to be less than 4%.

B. Load and energy Price

As per probabilistic behavior of the demand, daily demand variation in each year of the planning period can be obtained by multiplying base load ($P_{i,base}$ and $Q_{i,base}$) and Demand Level Factor (*DLF*) [8, 32]. In addition, by considering the rate of yearly load growth, the amount of active and reactive power, is modeled as follows:

$$P^{e}_{i,t,h} = P_{i,base} \times DLF^{e}_{i,t,h} \times (1+\alpha)^{t} \quad (8)$$

$$Q^{e}_{i,t,h} = Q_{i,base} \times DLF^{e}_{i,t,h} \times (1+\alpha)^{t} \quad (9)$$

$$S^{D}_{i,h} = P^{D}_{i,h,s} + jQ^{D}_{i,h} \quad (10)$$

Where DLF is obtained by using the Probability Density Function (PDF) as:

$$DLF^{e}_{i,t,h} = \mu^{D}_{i,t,h} + \lambda^{D,e}_{i,t,h} \times \sigma^{D}_{i,t,h} \quad (11)$$

Where λ is a random variable and is generated using the normal PDF with an average value of zero and standard deviation of one for each demand level. $\mu^{D}_{i,t,h}$ is the predicted values for the load demand level with standard deviation of $\sigma^{D}_{i,t,h}$, and α and t are the load growth rate and number of year, respectively.

The power price is cleared depending on the wholesale market price and demand level, and is obtained as follows [33, 34]:

$$\rho_{h} = \rho_{base} \times PLF_{h} \quad (12)$$

where ρ_{base} is the basic electricity price and PLF_h stands for price level factor at demand level h_{th}.

Due to the importance of network resilience, the actual price should be obtained according to power purchasing cost and probable costs caused by line outages, due to extreme weather condition. In this paper, the actual price, which will be used as a signal price for DSO, is derived as follows:

$$\rho_{h} = \frac{\rho_{base} PLF_{h} + \rho_{ENS} ENS_{h}}{PLF_{h}} \quad (13)$$

In this equation, ENS cost is formulated as follows:

$$ENS\ \text{Cost} = \sum_{i=1}^{N_L} \lambda_{Line} L_{Line} \rho_{ENS} \left(\sum_{i=1}^{N_{bus}} P_{res} \mu_{Line}\right) + \text{C}_{repair} \quad (14)$$

Where, ρ_{ENS} presents ENS penalty cost for each load level, N_L stands for numbers of lines with length of L_{Line}. λ_{Line} and μ_{Line} are the failure and repair rate of the line. P_{res} states restored power once line is repaired.

C. Demand Response Program (DRP) Modeling

DRP is generally used to transfer demand from peak hours to off-peak, and on this way, the operational costs of DSO are reduced [35]. It this study, it is assumed that only ±15 % of demand could be transferred. Below is the relevant model for the applied DRP:

$$S^{DR}_{i,h} = S^{D}_{i,h} + \Delta S_{DRP} \quad (15)$$

$$\Delta S_{DRP} = \text{K}_{DRP} \times S^{D}_{i,h} \quad (16)$$

$$\sum_{h=1}^{24} \Delta S_{DRP} = 0 \quad (17)$$

(18)

$$\text{K}^{\min}_{DRP} < K_{DRP} < K^{\max}_{DRP} \quad (19)$$

$S^{DR}_{i,h}$ is apparent power after applying DRP at demand level number *h*. ΔS_{DRP} is the values of apparent power transferred by DRP. K_{DRP} is amount of participation in the load response plan.

D. Model of Wind Turbine Output

With utilization of hybrid EVs and DERs, like wind turbine, inside the EVCS, determining coordinated stochastic models becomes important. Power output of a wind turbine mainly depends on the wind speed parameter which is not generally specific and should be considered randomly. In this paper, the Rayleigh probability density function, which is a special case of the Weibull distribution, is applied for modeling random behavior of the wind speed (see Fig. 1) [24, 36].

$$f_{wg}(v) = \left(\frac{2v}{c^{2}}\right) \exp\left(-\left(\frac{v}{c}\right)^{2}\right) \quad (20)$$

Where v and c are the wind speed and scale index in the Weibull distribution, respectively. With knowing the average value of the wind velocity for the study site, the scale index is calculated as follows:

$$v_{m} = \int_{0}^{\infty} v f_{wg}(v) d_{v} = \int_{0}^{\infty} \left(\frac{2v^{2}}{c^{2}}\right) \exp\left[-\left(\frac{v}{c}\right)^{2}\right] d_{v} = \frac{\sqrt{\pi}}{2} c \quad (21)$$

$$c \cong 1.128 v_{m} \quad (22)$$

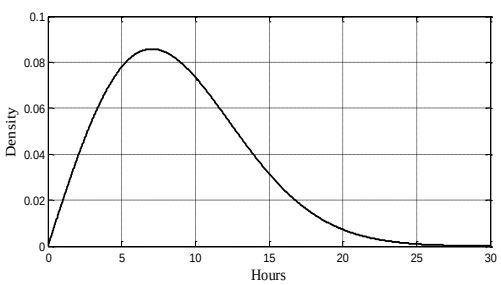

Fig. 1. Probability density function considered for modelling wind speed during 24 hours

Based on the above equations and considered PDF, power output of the wind turbine (WT) is obtained as follows:

$$P_{i,t,h}^{WT}=\begin{cases}0 & \text{if } v\le v_{in}^{cut} \text{ or } v\ge v_{out}^{cut}\\ P_{i,r}^{WT}\dfrac{v-v_{in}^{cut}}{v_{rated}-v_{in}^{cut}} & \text{if } v_{in}^{cut}\le v\le v_{rated}\\ P_{i,r}^{WT} & \text{else}\end{cases} \quad (23)$$

Where $P_{i,r}^{WT}$ is the permitted capacity for power generation. v_{in}^{cut}, v_{out}^{cut}, and v_{rated} are cut-in, cut-out and rated speed in the wind turbine, respectively.

As per the above equations, wind speed affects performance of the wind turbines, particularly, in the extreme weather conditions that the wind turbines may stop working. On the other hand, this issue, by increasing the outage rate of lines, affects the resiliency of the network and, consequently, the operation of the EVCS.

E. Resilience- oriented operation of the network

It is proved that extreme weather conditions (such as high speed wind and lightning) are the main reason (about 65%) for inception of various faults [23]. In such cases, line outage may occur and therefore network resiliency with increasing ENS is greatly reduced. As a side note, the main differences between reliability and resiliency depend upon types of event, its impact timing and the method of assessment. Reliability usually focuses on high probability events that have little impact on the network operation, but resiliency focuses on high-impact and rare events, like line outages due to extreme weather conditions [22, 29]. Further, reliability studies are commonly conducted by considering all possible events and providing a long-term solution to minimize the amount of energy not supplied (ENS) is the first goal. On the contrary, resiliency focuses on a specific incident category and can provide short-term to long-term solutions to reduce ENS.

In this respect and in order to have a proper analysis to evaluate weather condition effect on outage rate, weather-caused (wind or lightning) faults are considered in this paper. In paper [24] correlation between number of events (N_{wind} and $N_{lightning}$) and wind speed (W)/numbers of thunder (L) are formulated for short-time intervals.

$$N_{wind}=0.0012W_{speed}^{2}-0.0131W_{speed} \quad (24)$$

$$N_{lightning}=0.0001L+0.7014 \quad (25)$$

In this paper, it is assumed that average wind speed and lighting probability could be predicted in one hour time intervals, and for each time interval the medium quantity of wind speed and the number of thunders are used. Then, by considering the forecasted wind speed, probability of outages is modeled.

In this respect, the resiliency index (based on ENS) is calculated; however, for evaluation the effectiveness of the proposed strategy on resiliency, the evaluation metrics should be also introduced. In this paper, ΦΛΕΠ metrics proposed in paper [23] are used, based on which a multi-phase resilience trapezoid associated to the extreme weather is considered (see Fig. 2). Three phases can be clearly seen in the resilience trapezoid of Fig. 2 as: disturbance progress (Φ and Λ–metrics), post-disturbance degraded (E -metric) and restorative state (Π -metric). ΦΛΕΠ metrics would be defined to the operational and infrastructure resilience. Mathematical expression and measuring units for ΦΛΕΠ metrics are shown in Table II.

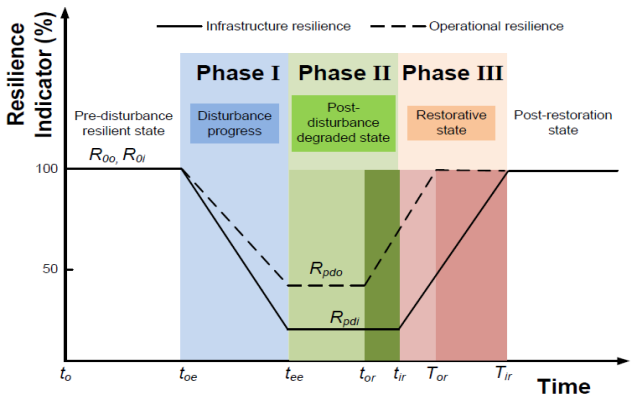

Fig. 2. Resilience indicator and the multi-phase resilience trapezoid [23]

TABLE II
MATHEMATICAL OPERATIONAL AND INFRASTRUCTURE FORMULATION OF RESILIENCE METRICS

Metric	Mathematical Expression		Measuring Unit	
	Operational	Infrastructure	Operational	Infrastructure
Φ	$\frac{R_{pdo}-R_{0o}}{t_{ee}-t_{oe}}$	$\frac{R_{pdi}-R_{0i}}{t_{ee}-t_{oe}}$	MW/hour	number of lines tripped/hours
Λ	$R_{0o}-R_{pdo}$	$R_{0i}-R_{pdi}$	MW	number of lines tripped
E	$t_{or}-t_{ee}$	$t_{ir}-t_{ee}$	hours	hours
Π	$\frac{R_{0o}-R_{pdo}}{T_{or}-t_{or}}$	$\frac{R_{0i}-R_{pdi}}{T_{ir}-t_{ir}}$	MW/hour	number of lines restored/hours
Φ	$\frac{R_{pdo}-R_{0o}}{t_{ee}-t_{oe}}$	$\frac{R_{pdi}-R_{0i}}{t_{ee}-t_{oe}}$	MW/hour	number of lines tripped/hours

F. Proposed methodology for Resilience- oriented operation of the grid

In the face of natural disasters, resiliency improvement of the network, i.e., its ability to prepare, survive, and rapidly recover, is a vital action. As explained earlier, one of the influencing solutions for resiliency enhancement is rescheduling of DERs, DRP implementation, appropriate management of EV's charging/discharging schedule. On the other hand, the uncertainty of weather based outages, available EVs in stations and their SOC level affect DER scheduling and DRP program. As a result, the application of these solutions, given their impact on the operation of the EVCS, must also be economically justified for the EVCS owner. In other words, an optimal balance between economic profits and resiliency should be made.

As a side note, the adopted charging/ discharging schedule for EVs are generally based on price signals offered by market, so that, the EV is charged during off-peak intervals. On the contrary, discharging of extra power in the EV's battery is done during peak intervals when the energy price is higher. Accordingly, it can be concluded that if the DSO locally increase reference for signal price in some intervals in order to improve the resilience, the EVCS owner will be encouraged to change the charging/discharging schedule and gain more profits. Based on this fact, in the proposed strategy of the paper, the real operation cost for each time interval is calculated by considering weather condition and uncertainty of outages.

In this regard, this paper proposes a novel resilience-oriented strategy, which with optimal interaction between rescheduling of DERs energy and EV's charging/discharging management, increase resiliency of the grid and decreases total ENS during normal operation and extreme weather conditions. In the proposed optimization method, profits of both EVCS and DSO are modeled as objective functions which must be maximized during daily operation planning. To do so, the outage rate of lines, power generation of wind turbine, movement of EVs and their available energy depend on weather conditions. In the following proposed formulation related to both DSO an EVCS owner are presented.

1) DSO Benefit Formulation

DSO, in supplying the network demand, must pay some costs, like cost of purchasing energy from the upstream or utility ($S_h^{Utility}$) or the cost of purchasing energy from the wind turbine and EVCS in the discharging intervals. It also earns revenue from the sale of energy to the customers or to the EVCS in the charging intervals. As a result, the DSO benefits, which should be maximized during next 24 hours in the proposed algorithm, is obtained by subtracting cost (C_{DSO}) and revenue (R_{DSO}).

$$R_{DSO} = \sum_{i=1}^{N_{load}} \rho_{sell}^{P} .P_{i,t,h}^{e} + \frac{1}{T(i)} \sum_{i=1}^{N_k} \rho_{sell}^{P} .E_{EVCS}^{charge} \tag{26}$$

$$C_{DSO} = \lambda_h .S_h^{Utility} + ENS\ \mathrm{Cost}_h + \rho_{sell}^{WT} .P_{i,t,h}^{WT} + \frac{1}{T(i)} \sum_{i=1}^{N_k} \rho^{P} .E_{EVCS}^{discharge} \tag{27}$$

$$OF_{DSO} = R_{DSO} - C_{DSO} \tag{28}$$

In the above equations, ρ_{sell}^{P}, λ_h, and ρ^{WT}_{sell}, are the price of sold energy to consumers, the price of purchasing energy from utility and the price of energy purchasing from wind units. It should be noted that the amount of purchased power from utility or form EVCS depends on the market electricity price. The purchased active and reactive power can be easily obtained from $S_h^{Utility}$.

Note that DSO has the ability to sell energy to market when $S_h^{Utility}$ become negative. In equation (27) the ENS cost due to line outage is also modelled. In addition, the power exchanged with the EVCS depends on the charge/discharge schedule, which is presented in the next section as a method for its optimal programming.

2) EVCS Benefit Formulation

Usually, the EVCS owner's profit is in increasing the presence of EVs and purchasing energy from the DSO at the lowest price. In other words, for the EVCS, the DSO profit (due to load characteristic correction and resilience improvement) is not important, unless it receives a profit from participating in these programs. Further, as mentioned, factors such as charge/discharge rate (ch_{rate} and $disch_{rate}$) and charging/discharging time are effective in modifying the load characteristic. Therefore, the following objective is suggested to optimize the above parameters. In fact, in this paper, first, the EV's charging/discharging planning is optimally calculated. In this respect, the following formulation with the purpose of peak shaving, valley filling and flattening the load curve is used. In this way, the optimal charging and discharging times, in which attractive price signals are given, are calculated.

$$OF_1 = a \times \sum_{t=1}^{T} \left(\frac{P_{L-Peak}}{P_{L-peak}^{Corrected}} - 1 \right) \Delta t_{discharge} + b \times \sum_{t=1}^{T} \left(\frac{P_{L-Min}^{Corrected}}{P_{L-Min}} - 1 \right) \Delta t_{charge} + \left(c \times MSE \right) \tag{29}$$

$$MSE = \sum_{t=1}^{24} (P^{Load}(t) - \sum_{i=1}^{N_{EVs}} P^{EVCS}(i) - P_{ref})$$

The above objective function is modeled based on the weighted sum model. In this function, a, b and c are applied for normalizing different terms of the OF and converting them to intervals [0-1]. The load power, predicted by the load curve, is stated by $P_{Load}(t)$, based on which and modified load profile the mean square error (MSE) is calculated. In other words, charge/discharge schedule is achieved in such a way that effective peak shaving and load profile flattering are achieved by tracking P_{ref} minimizing MSE. Δt_{charge} and $\Delta t_{\text{discharge}}$ are the total time when the EVs are charged and discharged, respectively.

Although the implementation of the above optimal schedule will make both DSO and the EVCS owner profitable, but as mentioned, if network resilience in bad weather conditions is considered, the charging/discharging program will change. In other words, the EVCS owner's profit function needs to be formulated again. In this respect, the cost and revenue function of the EVCS have been modelled as follows. Moreover, the EVCS benefit, which should be maximized during next 24 hours in the proposed algorithm, is obtained by subtracting cost and revenue.

$$R_{EVCS} = \rho_{sell}^{WT} . P_{i,t,h}^{WT} + \frac{1}{T(i)} \sum_{i=1}^{N_k} \rho^{P} . E_{EVCS}^{discharge} \quad (30)$$

$$C_{EVCS} = \frac{1}{T(i)} \sum_{i=1}^{N_k} \lambda_h . E_{EVCS}^{charge} + C_k^{deg} \left(\sum_{k=1}^{N_k} \frac{E_{EV}^{discharge}}{\eta_k^{discharge}} + \eta_k^{charge} . E_{EV}^{charge} \right) \quad (31)$$

$$OF_{EVCS} = R_{EVCS} - C_{EVCS} \quad (32)$$

The EVCS's revenue includes the sale of wind energy and the energy of EV batteries during discharge period, while charging EVs is costly for the owner. In this regard, C_k^{deg} and η_k^{charge} / $\eta_k^{discharge}$ are depreciation coefficient and efficiency of charging/discharging pattern of EV's battery, respectively.

Related Constraints

In the proposed formulation, constraints should also be considered, the most important of which is power balance in the network. This issue, as per implementation of DRP and also charging/discharging schedule can be formulated as follows. In addition, the bus voltage must be kept within its permissible ranges.

$$P_h^{Utility} - \left((1 - K_{DRP}) \times P_{i,h}^{D} + \Delta P_{DRP} \right) + \frac{1}{T(i)} \sum_{k=1}^{N_k} (E_{EVCS}^{discharge} - E_{EVCS}^{charge}) = V_{i,h} \sum_{j} V_{j,h} (G_{ij} \cos \delta_{i,h} + B_{ij} \sin \delta_{j,h}) \quad (33)$$

$$Q_h^{Utility} - \left((1 - K_{DRP}) \times Q_{i,h}^{D} + \Delta Q_{DRP} \right) = V_{i,h} \sum_{j} V_{j,h} (G_{ij} \cos \delta_{i,h} - B_{ij} \sin \delta_{j,h}) \quad (34)$$

$$\Delta S_{DRP} = \Delta P_{DRP} + j \Delta Q_{DRP} \quad (35)$$

$$V_i^{min} \le V_{i,h,s} \le V_i^{max} \quad (36)$$

$$0 \le S_{ij,h,s} \le S_{ij}^{max} \quad (37)$$

G. Approach overview

Management and control of charging/discharging of Electric vehicles (EVs) with the aim of profitability for the Distribution System Operator (DSO) and the private sector is one of the challenges of operating Electric vehicles Charging Stations (EVCS). This paper proposes a novel methodology for optimal planning of charging/discharging of the hybrid wind- EVCS which on the one hand, lead to correction of the load curve and on the other hand, improves the grid resilience in extreme weather conditions.

In this paper, first, the probabilistic model of influencing components, including EV, EVCS, load, energy price, DRP, wind turbine generation, is formulated and then final models using Monte Carlo simulation is extracted. Further, to have a proper analysis to evaluate resiliency of the test case, by considering the forecasted wind speed, probability of outages is modeled and the resiliency index (based on ENS) is calculated accordingly. In the next step, a methodology for resilience-oriented operation of the grid is presented, in which benefit formulation of both DSO and EVCS owner is calculated. In this respect, the benefit formulation of the EVCS is associated with optimal charging/discharging schedule of the EVs. Finally, the presented multi-objective optimization algorithm of the paper is solved using a Modified Particle Swarm Optimization algorithm (MMPSO) and the optimal solution is found.

III. TEST SYSTEM AND SIMULATION RESULTS

The proposed methodology of the paper for resiliency-oriented operation of grid is implemented on a 50-buses test case, which is part of the 69-bus IEEE radial test system [37] (see Fig.3). As a side note, the proposed methodology is devised in such a way that it can be implemented on any network; however, by selecting such network, which is one of the wide and large test systems, its efficiency is examined in large networks.

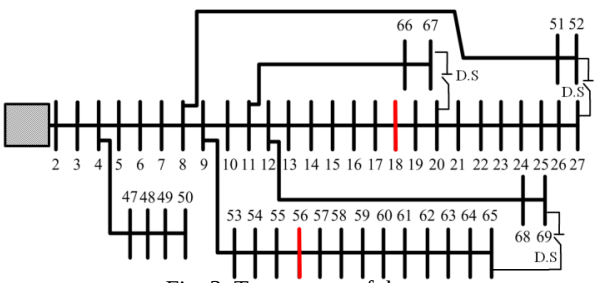

Fig. 3. Test system of the paper

First, modelling of the demand is done based on the load pattern (daily, weekly and annual) given in the standard Reliability Test System (RTS) [37]. However, it should be noted, in this study the load of a working day is considered to reduce the required time for execution of Monte Carlo. Then, the energy price model is also done according to section B.

As explained, the placement of the EVCS is not concern of this study, but due to the fact that their allocation affects the implementation of the proposed methodology, two EVCS with the capacity of 125 EVs are optimally allocated, based on the presented method of reference [20], in buses 18 and 56. Here, it is assumed that all EV drivers have almost the same pattern in driving, so that they park EV in a parking lot, and return home after work and park their car in another parking. These two EVCSs are called Administrative EVCS and Residential EVCS, respectively. Moreover, capacity of the EV's battery is assumed to be 25 kWh, and they are charged/discharged in 5 hours. As a result, rated power of the batteries is 5kW on average. Battery life is also estimated to be approximately 10 years. On the other hand, the behavior of EVs (in fact EV driver) is probabilistic and uncertain. Therefore, by using sequential Monte Carlo method, which is on the basis of repeated replications of the simulation, the final model of stochastic parameter is calculated based on the mean value during the simulation period.

In the present study, a storm happens for a 4-hours interval (here 14 -18 p.m. of the studied day). In addition, it is assumed that weather condition, outage number and the repair time are similar. In this respect, the Monte-Carlo simulation approach is rerun to study probability of line outage (failure) which is subject to the extreme weather. By obtaining the stochastic models, the proposed multi-step optimization strategy, for jointly optimization of EVs charging/discharging schedule and DSO/EVCS profits is solved. Since the studied problem is complex and vast, the particles may trap in the local optimum as they move towards a false Pareto front. To deal with this issue, a Modified Multiobjective PSO (MMPSO) algorithm [38, 39] is used here for finding Pareto solution of the problem. In the MMPSO algorithm the exploration and exploitation of the algorithm and its convergence capability have been improved. In the utilized MMPSO of this paper, the pertinent parameters are set based on the values obtained in the [40].

In order to demonstrate the impact of the proposed methodology on the optimal charging/discharging schedule of the EVCS, two scenarios are defined as follows:

Scenario 1: Optimal charging/discharging schedule without considering grid resilience

Scenario 2: Optimal charging/discharging schedule with considering grid resilience

The optimal results for the above mentioned scenarios are reported in the Table III. Note that in both scenarios DR program are applied.

TABLE III
THE OPTIMAL RESULTS OF IMPLEMENTING CHARGING/DISCHARGING SCHEDULE FOR SCENARIOS 1 AND 2

Scenarios	EVCS (Administrative)		EVCS (Residential)		Charge/discharge intervals	
	ch_{rate}	$disch_{rate}$	ch_{rate}	$disch_{rate}$	Charge Hour	Discharge Hour
scenario 1	14.2	16.7	16.7	14.2	1-7 12-17	8-12 19-24
scenario 2	16.7	14.2	20	11.2	1-7	8-12 12-18 19-24

It is observed that the discharge rate is always less than the charge rate. This is to ensure the travel of EVs. In fact, the program has been designed so that the discharge of EVs batteries does not interfere with the daily travel of EVs.

Another noteworthy point is that the charge rate is higher in the residential EVCS than in the Administrative and the discharge rate is higher in the Administrative EVCS than in the residential parking lot. This is because when EVs are parked in a residential EVCS, the load characteristic is often low (at midnight) and it is more attractive for the aggregator (EVCS owner) to charge the EV battery at a high rate and discharge it at a low rate. In addition, when the EVs are in the Administrative EVCS, the load characteristic sometimes encounters peak demand, so the high discharge rate and low charge are more attractive to the aggregator.

On the other hand, in the second scenario where resilience improvement is considered, the discharge rate is reduced. Moreover, the charging/discharging hours are changed. In fact, in times of extreme weather conditions, the EVCS in the discharge cycle helps to supply network power and reduces ENS accordingly. In this study, the ENS is calculated as the resiliency index and also the penalty cost.

In the next step, by solving the proposed formulation related to benefit of DSO an EVCS owner, the optimal results are calculated. As already mentioned, contrary to the single-objective optimization scenario, there is an optimal set of solutions or alternatives, called Pareto optimal set, where each solution can be selected as final one. Table IV reports the five Pareto optimal solutions for each scenario. Further, every Pareto solution in repository is depicted in the Fig. 4.

In this paper, to find the best solution, the min-max method, on the basis of fuzzy satisfaction method, is employed. In this method, the minimum values for per-unit and normalized profits of both objective functions (OF_{DSO} and OF_{EVCS}) are obtained. Afterwards, the maximum value of min (OF_{DSO} and OF_{EVCS}) among Pareto set is calculated to select the best solution. In this way, solutions number 2 and 5 are selected for scenarios 1 and 2, respectively (as can be seen in the results of Table IV).

Table V reports the optimal benefits of DSO and EVCS related to the best non-dominated solutions, which through it the effectiveness of the proposed strategy can be evaluated. In this table, total benefits of DSO and EVCS owner, including benefits due to load profile correction, benefits of improving resiliency, and benefit of reducing power purchase from utility, benefits of power loss reduction in line with proposed strategy are separately given.

Table V reports the optimal benefits of DSO and EVCS related to the best non-dominated solutions, which through it the effectiveness of the proposed strategy can be evaluated. In this table, total benefits of DSO and EVCS owner, including benefits due to load profile correction, benefits of improving resiliency, and benefit of reducing power purchase from utility, benefits of power loss reduction in line with proposed strategy are separately given.

As can be seen in Table V, in the second scenario, the profit due to the resilience improvement is increased due to the participation of the EVCS in supplying the load (during discharge interval). In this way, the total benefit of the DSO will increase (4.821×10^{7}). It is worth saying that the cost of ENS in all-weather condition is a positive quantity; hence, the EVCS owner gains more benefits from price modification and is more interested in cooperation with DSO. In other words, this matter is also profitable for the EVCS due to the increase in energy prices in the time of extreme weather condition, so that the EVCS owner's profit has increased from

2.08×10^5 to 2.92×10^5. According to this table, the cost of purchasing energy from the upstream network has also decreased, which in turn leads to the profit of the DSO.

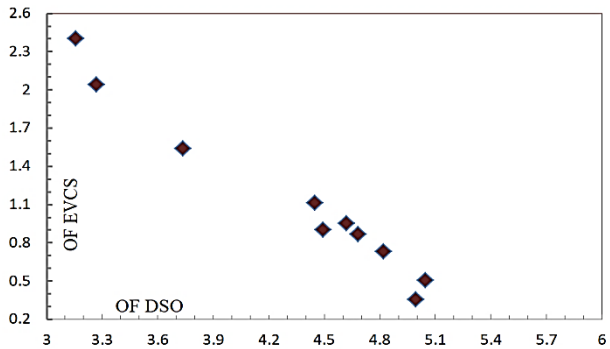

(a): Scenario 1

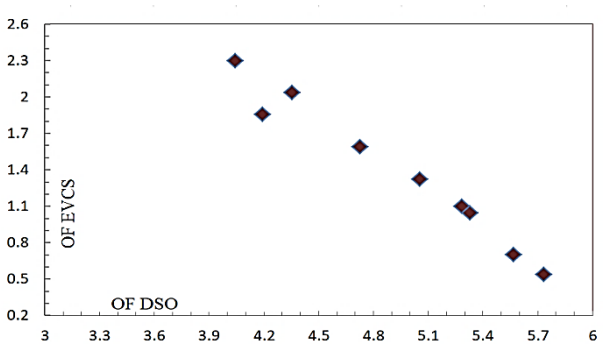

(b): Scenario 2

Fig. 4. Pareto front solutions for (a) scenarios 1 and (b) scenario 2

TABLE IV
OBJECTIVE FUNCTIONS FOR PARETO SOLUTIONS

Solution number		1	2	3	4	5
scenario 1	OF_{DSO}	3.158	**4.820**	4.620	4.449	4.682
	OF_{EVCS}	2.402	**0.732**	0.953	1.112	0.868
scenario 2	OF_{DSO}	4.356	5.283	3.495	5.054	**5.329**
	OF_{EVCS}	2.034	1.098	2.877	1.320	**1.046**

TABLE V
THE OPTIMAL VALUES OF OBJECTIVE FUNCTIONS FOR TWO SCENARIOS

Scenario	1	2
benefits of load profile correction ($)	2.153×10^6	1.830×10^6
benefits of improving resiliency ($)	8.232×10^5	9.729×10^5
benefit of reducing power purchase ($)	4.239×10^7	4.725×10^7
benefits of power loss reduction ($)	5.145×10^5	5.837×10^5
benefits of DSO ($)	4.073×10^7	4.821×10^7
benefits of EVCS ($)	2.08×10^5	2.92×10^5

In different circumstances, the effectiveness of the proposed methodology in grid resilience improvement is also evaluated through ΦΛΕΠ metrics and the pertinent results are calculated. In other words, to quantify the resilience improvement of applying proposed strategy, ΦΛΕΠ metrics in the operational and infrastructure are calculated and tabulated in Table VI.

The results of Table VI, that correspond to Fig. 2 and Table II, presents value of the key metrics for characterization the resilience trapezoid to evaluate how fast (Φ) and how low (Λ) resilience drops in Phase I, how extensive (E) is the post-event degraded state (Phase II) and how promptly (Π) the network recovers to its pre-event resilient state (Phase III), considering both operational and infrastructure resilience in each phase.

TABLE VI
ΦΛΕΠ METRICS TO OPERATIONAL AND INFRASTRUCTURE RESILIENCE

Metric	Scenario 1		Scenario 2	
	operational	infrastructure	operational	infrastructure
Φ	-1	-1	-0.72	-0.78
Λ	1	1	1.34	1.25
E	1	1	0.39	0.39
Π	1.23	1	3.42	3.20

As per the obtained results, the slope of the resilience degradation during the extreme weather is -1 for the first case, while in the second scenario that the corrective action are taken, the slope is decreased to -0.72. It should be noted that the grid reconfiguration, through isolating switch (shown with D.S in Fig. 3) change topology of the network. Also, in the second scenario, the value of Λ is obtained equal to 1.34, which proves that the resilience value in this scenario has dropped less compared to the first scenario. In accordance with Λ merit, the duration of the post disturbance is also degraded.

IV. CONCLUSIONS

During extreme weather conditions with high probability of fault inception, energy resources, charging/discharging schedule of the Electric vehicles Charging Stations (EVCS), flexible loads are rescheduled to improve grid resilience. In this paper, a novel two-stage

stochastic optimization method for optimal charging/discharging schedule of the EVCS is proposed. In this regard, the probabilistic and uncertain behavior of line outages due to extreme weather conditions, demand variation, EV driver pattern and State of Charge (SOC) of EV batteries are modeled by applying sequential Monte-Carlo simulation algorithm. Then, a new resilience-oriented multi-objective optimization algorithm for maximizing benefits of both DSO and EVCS owner is implemented for two hybrid wind-EVCS. One of the salient features of the proposed methodology is profit sharing between DSO and EVCS which not only lead to resiliency improvement of the grid, but also optimize benefits of the EVCS. Finally, the proposed methodology is evaluated using ΦΛΕΠ metrics which through a multi-phase resilience trapezoid method all disturbance progress, post-disturbance degraded and restorative state are assessed.

REFERENCES

[1] Z. Ding, Y. Lu, L. Zhang, W.-J. Lee, and D. Chen, "A stochastic resource-planning scheme for PHEV charging station considering energy portfolio optimization and price-responsive demand," *IEEE Transactions on Industry Applications*, vol. 54, no. 6, pp. 5590-5598, 2018.

[2] A. Ahmadian, B. Mohammadi-Ivatloo, and A. Elkamel, "A Review on Plug-In Electric Vehicles: Introduction, Current Status, and Load Modeling Techniques," *Journal of Modern Power Systems and Clean Energy*, vol. 8, no. 3, pp. 412-425, 2020.

[3] H. Soltani Gohari, K. Abbaszadeh, and J. Gholami Gorji, "A Controllable Bidirectional Rectifier for EV Home Charging Station with G2H/G2VH/V2H/V2G Functions," *International Journal of Industrial Electronics Control and Optimization*, vol. 4, no. 1, pp. 99-113, 2021.

[4] P. Chanhom, S. Nuilers, and N. Hatti, "A new V2G control strategy for load factor improvement using smoothing technique," *Advances in Electrical and Computer Engineering*, vol. 17, no. 3, pp. 43-50, 2017.

[5] K. Kasturi, C. K. Nayak, and M. R. Nayak, "Electric vehicles management enabling G2V and V2G in smart distribution system for maximizing profits using MOMVO," *International Transactions on Electrical Energy Systems*, vol. 29, no. 6, pp. e12013, 2019.

[6] S. Singh, P. Chauhan, and N. J. Singh, "Feasibility of Grid-Connected Solar-Wind Hybrid System with Electric Vehicle Charging Station," *Journal of Modern Power Systems and Clean Energy*, pp. 1-12, 2020.

[7] Y. Li, Z. Ni, T. Zhao, T. Zhong, Y. Liu, L. Wu, and Y. Zhao, "Supply Function Game Based Energy Management Between Electric Vehicle Charging Stations and Electricity Distribution System Considering Quality of Service," *IEEE Transactions on Industry Applications*, 2020.

[8] A. Sheikhi, S. Bahrami, A. M. Ranjbar, and H. Oraee, "Strategic charging method for plugged in hybrid electric vehicles in smart grids; a game theoretic approach," *International Journal of Electrical Power & Energy Systems*, vol. 53, pp. 499-506, 2013/12/01/, 2013.

[9] J. A. Domínguez-Navarro, R. Dufo-López, J. M. Yusta-Loyo, J. S. Artal-Sevil, and J. L. Bernal-Agustín, "Design of an electric vehicle fast-charging station with integration of renewable energy and storage systems," *International Journal of Electrical Power & Energy Systems*, vol. 105, pp. 46-58, 2019/02/01/, 2019.

[10] M. Zare Oskouei, B. Mohammadi-Ivatloo, M. Abapour, A. Anvari-Moghaddam, and H. Mehrjerdi, "Practical implementation of residential load management system by considering vehicle-for-power transfer: Profit analysis," *Sustainable Cities and Society*, vol. 60, pp. 102144, 2020/09/01/, 2020.

[11] S. Wang, N. Zhang, Z. Li, and M. Shahidehpour, "Modeling and impact analysis of large scale V2G electric vehicles on the power grid." pp. 1-6.

[12] A. Ul-Haq, C. Cecati, and E. El-Saadany, "Probabilistic modeling of electric vehicle charging pattern in a residential distribution network," *Electric Power Systems Research*, vol. 157, pp. 126-133, 2018.

[13] H. Chung, S. Maharjan, Y. Zhang, and F. Eliassen, "Intelligent Charging Management of Electric Vehicles Considering Dynamic User Behavior and Renewable Energy: A Stochastic Game Approach," *IEEE Transactions on Intelligent Transportation Systems*, pp. 1-12, 2020.

[14] A. S. Al-Ogaili, T. J. T. Hashim, N. A. Rahmat, A. K. Ramasamy, M. B. Marsadek, M. Faisal, and M. A. Hannan, "Review on Scheduling, Clustering, and Forecasting Strategies for Controlling Electric Vehicle Charging: Challenges and Recommendations," *IEEE Access*, vol. 7, pp. 128353-128371, 2019.

[15] Y. Cao, L. Huang, Y. Li, K. Jermsittiparsert, H. Ahmadi-Nezamabad, and S. Nojavan, "Optimal scheduling of electric vehicles aggregator under market price uncertainty using robust optimization technique," *International Journal of Electrical Power & Energy Systems*, vol. 117, pp. 105628, 2020/05/01/, 2020.

[16] K. M. Tan, S. Padmanaban, J. Y. Yong, and V. K. Ramachandaramurthy, "A multi-control vehicle-to-grid charger with bi-directional active and reactive power capabilities for power grid support," *Energy*, vol. 171, pp. 1150-1163, 2019.

[17] C. S. Ioakimidis, D. Thomas, P. Rycerski, and K. N. Genikomsakis, "Peak shaving and valley filling of power consumption profile in non-residential buildings using an electric vehicle parking lot," *Energy*, vol. 148, pp. 148-158, 2018/04/01/, 2018.

[18] A. Almutairi, and M. M. Salama, "Assessment and enhancement frameworks for system reliability performance using different PEV charging models," *IEEE Transactions on Sustainable Energy*, vol. 9, no. 4, pp. 1969-1984, 2018.

[19] M. Kamruzzaman, and M. Benidris, "Reliability-based metrics to quantify the maximum permissible load demand of electric vehicles," *IEEE Transactions on Industry Applications*, vol. 55, no. 4, pp. 3365-3375, 2019.

[20] E. Hadian, H. Akbari, M. Farzinfar, and S. Saeed, "Optimal Allocation of Electric Vehicle Charging Stations With Adopted Smart Charging/Discharging Schedule," *IEEE Access*, vol. 8, pp. 196908-196919, 2020.

[21] M. H. Amirioun, F. Aminifar, and M. Shahidehpour,

"Resilience-Promoting Proactive Scheduling Against Hurricanes in Multiple Energy Carrier Microgrids," *IEEE Transactions on Power Systems*, vol. 34, no. 3, pp. 2160-2168, 2019.

[22] S. Ma, S. Li, Z. Wang, and F. Qiu, "Resilience-Oriented Design of Distribution Systems," *IEEE Transactions on Power Systems*, vol. 34, no. 4, pp. 2880-2891, 2019.

[23] M. Panteli, P. Mancarella, D. N. Trakas, E. Kyriakides, and N. D. Hatziargyriou, "Metrics and Quantification of Operational and Infrastructure Resilience in Power Systems," *IEEE Transactions on Power Systems*, vol. 32, no. 6, pp. 4732-4742, 2017.

[24] A. Roudbari, A. Nateghi, B. Yousefi-khanghah, H. Asgharpour-Alamdari, and H. Zare, "Resilience-oriented operation of smart grids by rescheduling of energy resources and electric vehicles management during extreme weather condition," *Sustainable Energy, Grids and Networks*, pp. 100547, 2021.

[25] H. Khaloie, A. Abdollahi, and M. Rashidinejad, "Risk-averse Pre-Extreme Weather Events Self-Scheduling of a Wind Power Plant: A Hybrid Possibilistic-Scenario Model," *International Journal of Industrial Electronics, Control and Optimization*, vol. 1, no. 1, pp. 9-18, 2018.

[26] A. Arif, S. Ma, Z. Wang, J. Wang, S. M. Ryan, and C. Chen, "Optimizing Service Restoration in Distribution Systems With Uncertain Repair Time and Demand," *IEEE Transactions on Power Systems*, vol. 33, no. 6, pp. 6828-6838, 2018.

[27] W. Li, X. Xiong, and J. Zhou, "Incorporating fuzzy weather-related outages in transmission system reliability assessment," *IET generation, transmission & distribution*, vol. 3, no. 1, pp. 26-37, 2009.

[28] S. Sharma, and P. Jain, "Integrated TOU price - based demand response and dynamic grid - to - vehicle charge scheduling of electric vehicle aggregator to support grid stability," *International Transactions on Electrical Energy Systems*, vol. 30, no. 1, pp. e12160, 2020.

[29] F. Akhgarzarandy, H. Wang, and M. Farzinfar, " Optimal resiliency - oriented charging station allocation for electric vehicles considering uncertainties, " *International Transactions on Electrical Energy Systems*, vol. 31, no. 4, pp. e12799, 2021.

[30] A. Arjomandi-Nezhad, M. Fotuhi-Firuzabad, M. Moeini-Aghtaie, A. Safdarian, P. Dehghanian, and F. Wang, "Modeling and Optimizing Recovery Strategies for Power Distribution System Resilience," *IEEE Systems Journal*, pp. 1-10, 2020.

[31] M. Ramzanzadeh, M. Jafari Nokandi, T. Barforoushi, and J. Saebi, "Security-Constrained Unit Commitment in the Presence of Demand Response Programs and Electric Vehicles," *International Journal of Industrial Electronics, Control and Optimization*, 2020.

[32] B. Yousefi-Khangah, S. Ghassemzadeh, S. H. Hosseini, and B. Mohammadi-Ivatloo, "Short-term scheduling problem in smart grid considering reliability improvement in bad weather conditions," *IET Generation, Transmission & Distribution*, vol. 11, no. 10, pp. 2521-2533, 2017.

[33] S. Seyyedeh Barhagh, B. Mohammadi-Ivatloo, A. Anvari-Moghaddam, and S. Asadi, "Risk-involved participation of electric vehicle aggregator in energy markets with robust decision-making approach," *Journal of Cleaner Production*, vol. 239, pp. 118076, 2019/12/01/, 2019.

[34] Q. Chen, F. Wang, B.-M. Hodge, J. Zhang, Z. Li, M. Shafie-Khah, and J. P. Catalão, "Dynamic price vector formation model-based automatic demand response strategy for PV-assisted EV charging stations," *IEEE Transactions on Smart Grid*, vol. 8, no. 6, pp. 2903-2915, 2017.

[35] Y.-W. Chen, and J. M. Chang, "Fair demand response with electric vehicles for the cloud based energy management service," *IEEE Transactions on Smart Grid*, vol. 9, no. 1, pp. 458-468, 2016.

[36] M. Mazidi, A. Zakariazadeh, S. Jadid, and P. Siano, "Integrated scheduling of renewable generation and demand response programs in a microgrid," *Energy Conversion and Management*, vol. 86, pp. 1118-1127, 2014.

[37] P. M. Subcommittee, "IEEE Reliability Test System," *IEEE Transactions on Power Apparatus and Systems*, vol. PAS-98, no. 6, pp. 2047-2054, 1979.

[38] M. Farzinfar, M. Shafiee, and A. Kia, "Determination of Optimal Allocation and Penetration Level of Distributed Energy Resources Considering Short Circuit Currents," *International Journal of Engineering*, vol. 33, no. 3, pp. 427-438, 2020.

[39] Z. Moravej, M. Jazaeri, and M. Gholamzadeh, "Optimal coordination of distance and over-current relays in series compensated systems based on MAPSO," *Energy Conversion and Management*, vol. 56, pp. 140-151, 2012.

[40] A. Carlisle, and G. Dozier, "An off-the-shelf PSO." pp. 1-6.

Emad Hadian received the B.Sc. and M.Sc. degree in electrical engineering from Birjand University, Birjand, Iran, in 2015, and is currently working toward the Ph.D. degree in electrical engineering at the Azad University, Yazd Branch, Iran. His research interests include Microgrid, Electrical Vehicles, and Optimization

Hamidreza Akbari was born in Yazd, Iran, in 1980. He received the B.Sc. and M.Sc. degrees in electrical engineering from Amirkabir University of Technology, Tehran, Iran in 2001 and 2004, respectively and the Ph.D. degree in electrical engineering from Islamic Azad University, Science and Research Branch, Tehran, Iran in 2011. He is currently working as an Assistant Professor of Electrical Engineering in Islamic Azad University, Yazd Branch. His main research interests include modeling, analysis and design of electrical machines, power electronics and renewable energies.

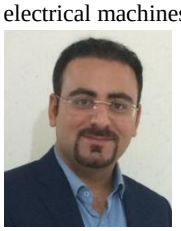

Mehdi Farzinfar received the B.Sc., in electrical engineering from Shahid Beheshti university, the Power and Water Institute of Technology Campus, Tehran, Iran, in 2008; and M.Sc., and Ph.D. degrees from Semnan University, Semnan, Iran, in 2010, and 2015 respectively. From 2013–2015 he was research assistant at the Power System Group

of the University of Auckland, Auckland, New Zealand, where he was engaged in the national project of Green Grid. He is currently an Assistant Professor with the School of Engineering, Damghan University, Damghan, Iran. His research interests include power system protection, Smart Grids, Microgrids, Electric vehicles.

Seyed Amin Saied received the M.Sc. and Ph.D. degrees in electrical engineering from the K. N. Toosi University of Technology, Tehran, Iran, in 2006 and 2012, respectively. He is currently with the Department of Electrical Engineering, Yazd Branch, Islamic Azad University, Yazd, Iran. His main research interests include the design and modeling of electrical machines, and electrical parameter estimation of electrical machines.

International Journal of Industrial Electronics, Control and Optimization © 2021 IECO
Vol. 4, No. 4, pp. 465-474, Sep (2021)

Optimization of a New Extended Cascaded Multilevel Inverter Topology to Reduce DC Voltage Sources and Power Electronic Components

Roya Naderi[1], Ebrahim Babaei[2,†], Mehran Sabahi[3], and Ali Daghigh[4]

[1,4]Department of Electrical Engineering, Shabestar Branch, Islamic Azad University, Shabestar, Iran
[2,3]Faculty of Electrical and Computer, Engineering, University of Tabriz, Tabriz, Iran

ABSTRACT

This work proposes a new multilevel inverter consisting of basic and sub-multilevel units. The basic unit is made up of four isolated dc voltage sources, two bidirectional switches, and ten unidirectional switches. To increase the number of output voltage levels, a cascaded architecture based on a series connection of sub-multilevel is proposed. The proposed inverter utilizes two algorithms to determine the values of dc voltage sources. The number of IGBTs, dc voltage sources, gate driver circuits, variety of dc voltage sources, and peak standing voltage on the switches are calculated and their optimization to produce the maximum number of levels in output voltage is investigated. To examine the advantages of the proposed inverter, the topology is compared with other topologies. The results show the superiority of the proposed topology over most conventional topologies in terms of the number of circuit components. Finally, to confirm the performance of the proposed multilevel inverter, the experimental results of a 25-level inverter prototype are provided.

Article Info

Keywords:
Cascaded multilevel inverter, Multilevel inverter, Optimization.
Article History:
Received 2020-24-11
Accepted 2021-21-06

I. INTRODUCTION

Multilevel inverters (MLI) have been used as one of the premier alternatives for medium to high power conversion utilizations, such as FACTS devices, renewable energy conversion systems, UPSs (uninterruptible power supply), electric vehicles, and HVDC [1-3]. One of famous topologies is Cascaded H-bridge (CHB) inverters. However, cascaded inverters require a greater quantity of input dc voltage sources and switches, and attempts to minimize the quantity of multi-level inverter circuit components have been one of the main goals of researchers. Based on these constraints, several topologies have been proposed to decrease the quantity of switches in [4-7] and H bridges are used to generate both positive and negative output voltage levels in all these topologies. However, H-bridge switches have a higher standing voltage, which limits their utilization in high-voltage systems. The topologies presented in [6, 7] are composed of diodes and have higher power losses in their asymmetric topologies. These limitations were resolved in [4, 8-9] where the structures can generate both polarities of output voltage levels without using H-bridge. However, they require more isolated dc voltage sources, which is another problem. A new MLI topology presented in [10,11] is a modified H-bridge multilevel inverter that can generate both polarities of output voltage levels using fewer switches. The topologies presented in [12-13] utilize bidirectional

[†]**Corresponding Author**: e-babaei@tabrizu.ac.ir
Tel: +98- 41-33393763, Fax: +98- 41-33300819, Faculty of Electrical and Computer Engineering, University of Tabriz, Tabriz, Iran

switches in which the number of gate driver circuits decreases due to the presence of one driver on each bidirectional switch. However, these topologies have a higher standing voltage than the CHB. New MLI topologies disadvantage of this converter is that it has a higher total standing voltage and the quantity of dc voltage sources in [15] is high. The use of a lower number of dc voltage sources in the switched cascaded MLI structure presented in [16] is one of the advantages of this topology. However, requiring a large number of ON switches is an unsolved problem and reduces the efficiency of the inverter. A new MLI topology with asymmetrical configuration was reported in [17], which can produce higher output voltage levels but still suffers from a large number of drivers and isolated sources of dc voltage sources. The MLI topologies introduced in [17, 18] generate both polarities of voltage levels without using an H-bridge. The nature of the bidirectional and unidirectional switches used in these architectures are common emitters where each unidirectional switch comprises of an antiparallel diode and an IGBT, while a bidirectional switch has two IGBTs and antiparallel diodes accordingly both of which require a single gate driver circuit. The basic structure of E-Type MLI in [17] generates 13 levels of output voltage using four asymmetric dc voltage sources and 10 gate driver circuits, but the ST-type topology in [18] requires the same number of dc voltage sources (four asymmetric dc voltage sources) and 12 gate driver circuits to produce 17 levels at the output. A new multilevel inverter topology comprising basic and sub-multilevel units is proposed in this work. This topology is also optimized for different purposes and is then compared with several multilevel inverters to evaluate the benefits of the advantages and disadvantages. Finally, the performance of the proposed 25-level inverter is evaluated by performing different test scenarios on the designed inverter prototype.

II. PROPOSED BASIC UNIT

The basic unit of the proposed multilevel inverter is shown in Fig. 1. The architecture of the proposed topology is a combination of ten unidirectional switches (individual switches are made up of an antiparallel diode and an IGBT), two bidirectional switches with a common-emitter topology (made of two IGBTs and two antiparallel diodes), and four isolated dc voltage sources with magnitudes of (U_1) and (U_2). The switching modes of the proposed 25-level MLI are presented in Table I in which '1' and '0' stand for ON and OFF states of the switches, respectively. The circuit layout of the proposed topology and the selection of the switching paths should be such that the dc voltage sources are never short-circuited by IGBTs or diodes. Clearly, the switches (Z_1, Z_2), (Z_1, S_Y, S_X), ⋯ are reported in [14, 15] have reduced the number of switches and used unidirectional switches. The amplitudes of dc voltage sources in these topologies are equal in which case it is named symmetric configuration. However, the main controlled in a complementary way to have a safe performance and to avoid short circuits across the voltage sources. The proposed MLI configurations shown in Fig. 1 can generate the following levels of voltage at the output:

$$0, \pm U_1, \pm 2U_1, \pm(U_2 - 2U_1), \pm(U_2 - U_1), \pm U_2,$$
$$\pm(U_1 + U_2), \pm(2U_1 + U_2), \pm(2U_2 - 2U_1), \pm(2U_2 - U_1),$$
$$2U_2, \pm(U_1 + 2U_2), \pm(2U_1 + 2U_2).$$

Due to the importance and impact of dc voltage source values on the quantity of output voltage levels, the amplitude of the dc voltage sources is chosen to produce maximize the number of output voltage levels as follows:

$$U_1 = U_{dc}, \; U_2 = 2U_{dc}$$

As mentioned before, this topology is capable of generating 25 levels of output voltage: zero output voltage level and 12 output levels for each polarity of voltage without using any voltage polarity generator such as H-bridges. Another issue regarding the proposed basic structure is the design and selection of switches. For this purpose, it is necessary to specify the nominal values of voltage and current of all switches. Table II summarizes the nominal values of voltage and current of all switches. Due to the fact that the switches that are on always have a series connection with the output load, the rated current of all switches will be equal to the maximum load current (I_m).

III. PROPOSED CASCADE MULTILEVEL INVERTER

The extended topology, which is referred to as sub-multilevel, is capable of producing higher levels of output voltage as shown in Fig. 2. The proposed sub-multilevel is made up of n dc voltage sources with magnitude (U_1) and n equal dc voltage sources with magnitude (U_2).

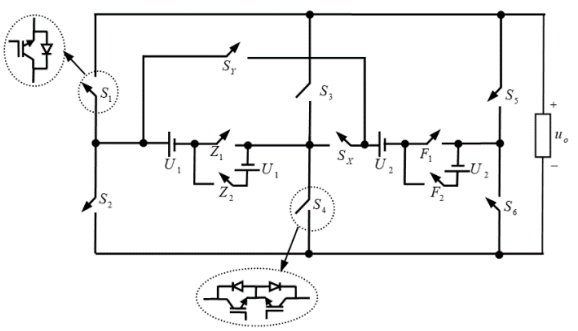

Fig. 1. The proposed basic unit topology.

Table III indicates the switching modes of the proposed sub-multilevel. Deriving expression for the quantity of

power electronic components used in the sub-multilevel topology is the focus of this section. The quantity of dc voltage sources (N_{source}^{sub}), the quantity of IGBTs (N_{IGBT}^{sub}), the quantity of gate driver (N_{drive}^{sub}), and the quantity of a variety of dc voltage sources ($N_{variety}^{sub}$) in the sub-multilevel topology can be calculated using the following equations:

$$N_{source}^{sub} = 2n \quad (1)$$

$$N_{drive}^{sub} = 2n + 8 \quad (2)$$

$$N_{IGBT}^{sub} = 4n + 6 \quad (3)$$

$$N_{variety}^{sub} = 2 \quad (4)$$

The total number of dc voltage sources used in the topology as shown in Fig. 2 is equal to 2n. As per Table III, the maximum output voltage of the proposed sub-multilevel ($U_{o,\max}^{sub}$) and the number of output voltage levels can be derived from the following equations:

$$U_{o,\max}^{sub} = n(U_1 + U_2) \quad (5)$$

$$N_{level}^{sub} = 2n(U_1 + U_2) + 1 \quad (6)$$

TABLE I
SWITCHING STATES OF THE PROPOSED BASIC UNIT

S_1	S_2	S_3	S_4	S_5	S_6	S_X	S_Y	Z_1	Z_2	F_1	F_2	U_o
1	1	0	0	0	0	0	0	0	0	0	0	**0**
1	0	0	1	0	0	0	0	1	0	0	0	U_1
1	0	0	1	0	0	0	0	0	1	0	0	$2U_1$
0	0	1	0	0	1	0	1	0	1	1	0	U_2-$2U_1$
0	0	1	0	0	1	0	1	1	0	1	0	U_2-U_1
1	0	0	0	0	1	0	1	0	0	1	0	U_2
1	0	0	0	0	1	1	0	1	0	1	0	U_1+U_2
1	0	0	0	0	1	1	0	0	1	1	0	$2U_1$+U_2
0	0	1	0	0	1	0	1	0	1	0	1	$2U_2$-$2U_1$
0	0	1	0	0	1	0	1	1	0	0	1	$2U_2$-U_1
1	0	0	0	0	1	0	1	0	0	0	1	$2U_2$
1	0	0	0	0	1	1	0	1	0	0	1	U_1+$2U_2$
1	0	0	0	0	1	1	0	0	1	0	1	$2U_1$+$2U_2$
0	1	1	0	0	0	0	0	1	0	0	0	-U_1
0	1	1	0	0	0	0	0	0	1	0	0	-$2U_1$
0	0	0	1	1	0	0	1	0	1	1	0	-(U_2-$2U_1$)
0	0	0	1	1	0	0	1	1	0	1	0	-(U_2-U_1)
0	1	0	0	1	0	0	1	0	0	1	0	-U_2
0	1	0	0	1	0	1	0	1	0	1	0	-(U_1+U_2)
0	1	0	0	1	0	1	0	0	1	1	0	-($2U_1$+U_2)
0	0	0	1	1	0	0	1	0	1	0	1	-($2U_2$-$2U_1$)
0	0	0	1	1	0	0	1	1	0	0	1	-($2U_2$-U_1)
0	1	0	0	1	0	0	1	0	0	0	1	-$2U_2$
0	1	0	0	1	0	1	0	1	0	0	1	-(U_1+$2U_2$)
0	1	0	0	1	0	1	0	0	1	0	1	-($2U_1$+$2U_2$)

Another key characteristic of multilevel inverters is the total standing voltage on the switches (TSV_{sub}). This criterion is obtained by summing the maximum standing voltage on the switches in their OFF state. TSV_{sub} is calculated as:

$$TSV_{sub} = \sum_{j=1}^{n} U_{Z,j} + \sum_{i=1}^{n} U_{F,j} + \sum_{i=1}^{6} U_{S,j} + U_{S,X} + U_{S,Y} \quad (7)$$

where $U_{Z.j}$, $U_{F.j}$, $U_{S.j}$, $U_{S.X}$, and $U_{S.Y}$ are the values of standing voltages for switches $Z_1, Z_2, Z_3, \cdots, Z_n$, switches $F_1, F_2, F_3, \cdots, F_n$, switches $S_1, S_2, \cdots, S_6$, switch S_X and switch S_Y, respectively. Based on the peak standing voltage values for individual switches, TSV_{sub} can be calculated for each switch as follows:

$$U_{S,1} = U_{S,2} = U_{S,5} = U_{S,6} = n(U_1 + U_2) \quad (8)$$

$$U_{S,3} = U_{S,4} = nU_2 \quad (9)$$

$$U_{S,X} = U_{S,Y} = nU_1 \quad (10)$$

$$\sum_{j=1}^{n} U_{Z,j} = \begin{cases} (\frac{3n^2}{4} - \frac{n}{2})U_1 & ,n = even \\ (\frac{3n^2}{4} - \frac{n}{2} - \frac{1}{4})U_1 & ,n = odd \end{cases} \quad (11)$$

$$\sum_{j=1}^{n} U_{F,j} = \begin{cases} (\frac{3n^2}{4} - \frac{n}{2})U_2 & ,n = even \\ (\frac{3n^2}{4} - \frac{n}{2} - \frac{1}{4})U_2 & ,n = odd \end{cases} \quad (12)$$

$$TSV_{sub} = \begin{cases} (\frac{3n^2}{4} + \frac{11n}{2})(U_1 + U_2) & ,n = even \\ (\frac{3n^2}{4} - \frac{11n}{2} - \frac{1}{4})(U_1 + U_2) & ,n = odd \end{cases} \quad (13)$$

To generate higher levels of output voltage whiles utilizing fewer components, m sub-multilevels can be connected in series as shown in Fig. 3. The output voltage of the proposed cascade multilevel inverter topology (u_o) is obtained by:

$$u_o = u_{o,1} + u_{o,2} + u_{o,3} + \cdots + u_{o,m} \quad (14)$$

According to Table III, the equation of the maximum output voltage of the proposed cascade multilevel inverter is expressed as:

$$u_{o,\max,1} = \left[\frac{(4n+1)^m - 1}{2}\right] U_{dc} = \frac{(N_{level,1} - 1)}{2} U_{dc} \quad (15)$$

Fig. 3 consists of m sub-multilevel units and each sub-multilevel comprises ($n_{j,1} + n_{j,2}$) dc voltage sources in which $n_{j,1}$ and $n_{j,2}$ are the number of voltage sources on the left and right sides of the *j*th sub-multilevel, respectively. To maximize the number of generated voltage levels in the output, with constant device quantity, the number of voltage sources on both sides of each sub-multilevel unit should be equal, and this number must be the same on all sub-multilevel inverters as:

$$n_{j,1} = n_{j,2} = n \quad (16)$$

Using Eq. (16), we have:

$$N_{source} = 2nm \quad (17)$$

$$N_{driver} = m(2n + 8) \quad (18)$$

$$N_{IGBT} = m(4n + 6) \quad (19)$$

TABLE II
NOMINAL VALUES OF VOLTAGE AND CURRENT OF SWITCHES

Switches	S_1	S_2	S_3	S_4	S_5	S_6	S_X	S_Y	Z_1	Z_2	F_1	F_2
Standing voltage	$2(U_1+U_2)$	$2(U_1+U_2)$	$2U_2$	$2U_2$	(U_1+U_2)	$2(U_1+U_2)$	$2U_1$	$2U_1$	U_1	U_1	U_2	U_2
Current rating	I_m	I_m	I_m	I_m	I_m	I_m	I_m	I_m	I_m	I_m	I_m	I_m

The total standing voltage of switches in the proposed MLI (TSV) for $n \geq 2$ is computed using the equations below:

$$TSV = \sum_{u=1}^{m}\left[(\sum_{j=1}^{n} U_{Zk,j} + \sum_{j=1}^{n} U_{Fk,j} + \sum_{j=1}^{6} U_{Sk,j}) + (U_{Sk,X} + U_{Sk,Y})\right] \quad (20)$$

Considering Fig. 3, it is clear that:

$$\sum_{k=1}^{m} U_{Sk,1} = \sum_{k=1}^{m} U_{Sk,2} = \sum_{k=1}^{m} U_{Sk,5} = \sum_{k=1}^{m} U_{Sk,6} = n\sum_{k=1}^{m}(U_{K,1} + U_{K,2}) \quad (21)$$

$$\sum_{k=1}^{m} U_{Sk,3} = \sum_{k=1}^{m} U_{Sk,4} = n\sum_{k=1}^{m} U_{K,2} \quad (22)$$

$$\sum_{k=1}^{m} U_{Sk,X} = \sum_{k=1}^{m} U_{Sk,Y} = n\sum_{k=1}^{m} U_{K,1} \quad (23)$$

$$\sum_{k=1}^{m}\sum_{j=1}^{n} U_{Zk,j} = \begin{cases} (\frac{3n^2}{4} - \frac{n}{2})\sum_{k=1}^{m} U_{k,1} & ,n = even \\ (\frac{3n^2}{4} - \frac{n}{2} - \frac{1}{4})\sum_{k=1}^{m} U_{k,1} & ,n = odd \end{cases} \quad (24)$$

$$\sum_{k=1}^{m}\sum_{j=1}^{n} U_{Fk,j} = \begin{cases} (\frac{3n^2}{4} - \frac{n}{2})\sum_{k=1}^{m} U_{k,2} & ,n = even \\ (\frac{3n^2}{4} - \frac{n}{2} - \frac{1}{4})\sum_{k=1}^{m} U_{k,2} & ,n = odd \end{cases} \quad (25)$$

TSV for $n \geq 2$ is calculated as follows:

$$TSV = \begin{cases} (\frac{3n^2}{4} + \frac{11n}{2})\sum_{k=1}^{m}(U_{k,1} + U_{k,2}) & n = even \\ (\frac{3n^2}{4} - \frac{11n}{2} - \frac{1}{4})\sum_{k=1}^{m}(U_{k,1} + U_{k,2}) & n = odd \end{cases} \quad (26)$$

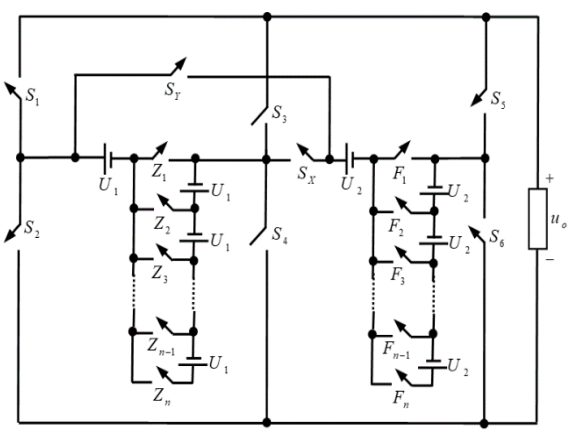

Fig. 2. The proposed sub-multilevel topology.

IV. Determining DC Voltage Source Magnitudes

A. First Algorithm

First sub-multilevel:

$$U_{1,1} = U_{1,2} = U_{dc} \quad (27)$$

The peak output voltage is obtained by:

$$U_{o\max,1} = n(U_{1,1} + U_{1,2}) = 2nU_{dc} \quad (28)$$

Second sub-multilevel:

$$U_{2,1} = U_{2,2} = 2U_{o\max,1} + U_{dc} = (4n+1)U_{dc} \quad (29)$$

The peak output voltage is expressed as:

$$U_{o\max,2} = n(U_{2,1} + U_{2,2}) = 2n(4n+1)\,U_{dc} \quad (30)$$

m^{th} sub-multilevel:

$$U_{m,1} = U_{m,2} = 2\sum_{j=1}^{m-1}(U_{o\max,j}) + U_{dc} = (4n+1)^{m-1}U_{dc} \quad (31)$$

Based on this algorithm, the number of output voltage levels ($N_{level,1}$) is calculated as:

$$N_{level,1} = (4n+1)^m \quad (32)$$

Based on the first algorithm and using Equs. (14), (26), and (32), the maximum generated output voltage ($u_{o,\max,1}$) and the total value of standing voltage on the switches (TSV_1) could be computed by:

$$u_{o,\max,1} = \left[\frac{(4n+1)^m - 1}{2}\right]U_{dc} = \frac{(N_{level,1} - 1)}{2}U_{dc} \quad (33)$$

$$TSV_1 = \begin{cases} (\frac{3n^2}{4} + \frac{11n}{2})\left(\frac{(4n+1)^m - 1}{2n}\right)U_{dc} \\ \quad = \left[\frac{3n^2 + 22n}{8n}\right](N_{level,1} - 1)U_{dc} & n = even \\ (\frac{3n^2}{4} + \frac{11n}{2} - \frac{1}{4})\left(\frac{(4n+1)^m - 1}{2n}\right)U_{dc} \\ \quad = \left[\frac{3n^2 + 22n - 1}{8n}\right](N_{level,1} - 1)U_{dc} & n = odd \end{cases} \quad (34)$$

The number of the variety of dc voltage sources for this algorithm $N_{variety,1}$ is equal to:

$$N_{variety,1} = m \quad (35)$$

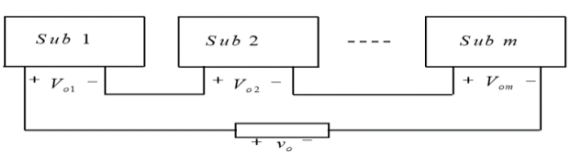

Fig. 3. The topology of the proposed multilevel.

Table III
SWITCHING STATES OF THE PROPOSED SUB-MULTILEVEL.

S_1	S_2	S_3	S_4	S_5	S_6	S_X	S_Y	Z_1	…	Z_{n-1}	Z_n	F_1	…	F_{n-1}	F_n	U_o
1	1	0	0	0	0	0	0	0		0	0	0		0	0	0
1	0	0	1	0	0	0	0	0	…	1	0	0	…	0	0	$(n-1)U_1$
1	0	0	1	0	0	0	0	0		0	1	0		0	0	nU_1
1	0	0	0	0	1	1	0	0		0	1	0		0	1	$n(U_1+U_2)$
							⋮									⋮
0	1	1	0	0	0	0	0	0		1	0	0		0	0	$-(n-1)U_1$
0	1	1	0	0	0	0	0	0		0	1	0		0	0	$-nU_1$
0	1	0	0	1	0	1	0	0		0	1	0		0	1	$-n(U_1+U_2)$

B. Second Algorithm

Unlike the first algorithm, each sub-multilevel has a different dc voltage source magnitude in the second algorithm, as summarized below:

First sub-multilevel unit:

$$U_{1,1} = U_{dc} \tag{36}$$

$$U_{1,2} = (2n+1)U_{1,1} \tag{37}$$

The peak output voltage for the first sub-multilevel is given by:

$$U_{o,\max,1} = n(U_{1,1} + U_{1,2}) = 2n(n+1)U_{dc} \tag{38}$$

Second sub-multilevel:

$$U_{2,1} = 2U_{o,\max,1} + U_{dc} = (2n+1)^2 U_{dc} \tag{39}$$

$$U_{2,2} = (2n+1)U_{2,1} = (2n+1)^3 U_{dc} \tag{40}$$

From Eq. (15), (39), and (40), the peak output voltage for the second sub-multilevel is obtained by:

$$U_{o,\max,2} = n(U_{2,1} + U_{2,2}) = 2n(1+n)(1+2n)^2 U_{dc} \tag{41}$$

*m*th sub-multilevel:

$$U_{m,1} = 2\sum_{j=1}^{m-1}(U_{o\max,j}) + U_{dc} = (2n+1)^{2(m-1)} U_{dc} \tag{42}$$

$$U_{m,2} = (2n+1)\,U_{m,1} = (2n+1)^{2m-1} U_{dc} \tag{43}$$

$$U_{o,\max,2} = n(U_{m,1} + U_{m,2}) = 2n(1+n)(1+2n)^{2(m-1)} U_{dc} \tag{44}$$

Considering the second algorithm, the output voltage levels $(N_{level,2})$ is computed as:

$$N_{level,2} = (2n+1)^{2m} \tag{45}$$

Considering Equs. (14), (26), and (45), the peak output voltage magnitude $(u_{o,\max,2})$ and the total magnitude of the standing voltage on the switches based on the second algorithm (TSV_2) are obtained from the following equations:

$$u_{o,\max,2} = \left(\frac{(2n+1)^{2m}-1}{2}\right)U_{dc} = \frac{(N_{level,2}-1)}{2}U_{dc} \tag{46}$$

$$TSV_2 = \begin{cases} \left(\frac{3n^2}{4}+\frac{11n}{2}\right)\left(\frac{(2n+1)^{2m}-1}{2n}\right)U_{dc} \\ \quad = \left[\frac{3n^2+22n}{8n}\right](N_{level,2}-1)U_{dc}\ ,\ n = even \\ \left(\frac{3n^2}{4}+\frac{11n}{2}-\frac{1}{4}\right)\left(\frac{(2n+1)^{2m}-1}{2n}\right)U_{dc} \\ \quad = \left[\frac{3n^2+22n-1}{8n}\right](N_{level,2}-1)U_{dc}\ ,\ n = odd \end{cases} \tag{47}$$

The variety of the dc voltage sources used $(N_{variety,2})$ is expressed by:

$$N_{variety,2} = 2m \tag{48}$$

V. Optimal Topology

This section analyzes the number of components and standing voltage on the switches, and the minimum number of components and *TSV* are calculated to attain the maximum quantity of the output voltage levels.

A. *Optimal topology for a minimum quantity of IGBTs with constant quantity of output voltage levels*

To identify the configuration that can create a constant number of output voltage levels ($N_{level,1}$) and ($N_{level,2}$) for the minimum quantity of IGBTs, using Eq. (19), (32), and (45), the number of IGBTs are determined as follows:

$$N_{IGBT} = \ln(N_{level,1}) \times \frac{(4n+6)}{\ln(4n+1)} \qquad for\ n \geq 2 \tag{49}$$

$$N_{IGBT} = \ln(N_{level,2}) \times \frac{(4n+6)}{2\ln(2n+1)} \qquad for\ n \geq 2 \tag{50}$$

Fig. 4(a) illustrates the differences of $\frac{(4n+6)}{\ln(4n+1)}$ and $\frac{(4n+6)}{2\ln(2n+1)}$ versus n. According to Fig. 4 (a), it is clear that $n=2$ minimizes the number of IGBTs for $n \geq 2$ for both proposed algorithms to achieve a constant number of output

voltage levels.

B. *Optimal topology for a minimum quantity of gate drivers with a constant quantity of output voltage levels*

Minimizing the number of gate drivers to generate a constant number of output voltage levels ($N_{level,1}$) and ($N_{level,2}$) is the very focus of this section. From (18), (32), and (45), the quantity of gate driver circuits are obtained as follows:

$$N_{driver} = \ln(N_{level,1}) \times \frac{(2n+8)}{\ln(4n+1)} \qquad for\ n \geq 2 \qquad (51)$$

$$N_{driver} = \ln(N_{level,2}) \times \frac{(2n+8)}{2\ln(2n+1)} \qquad for\ n \geq 2 \qquad (52)$$

Fig. 4(b) illustrates the differences of $\frac{(2n+8)}{\ln(4n+1)}$ and $\frac{(2n+8)}{2\ln(2n+1)}$ versus n. From Fig. 4(b), it is clear that the minimum quantity of gate drivers for the first and second proposed algorithms are derived by $n=3$.

C. *Optimal topology for a minimum number of variety of magnitudes of dc voltage sources with a constant number of output voltage levels*

Assuming ($N_{level,1}$) and ($N_{level,2}$) are constant in this section, the focus is to find the best topology that can generate the mentioned number of output voltage levels, using a minimum quantity of variety of dc voltage sources. According to (32) and (35), $N_{variety}$ for the first and second proposed algorithms can be derived as follows, respectively:

$$N_{variety} = \ln(N_{level,1}) \times \frac{1}{\ln(4n+1)} \qquad for\ n \geq 2 \qquad (53)$$

Using (45) and (48), the following equation is calculated:

$$N_{variety} = \ln(N_{level,2}) \times \frac{1}{\ln(2n+1)} \qquad for\ n \geq 2 \qquad (54)$$

Fig. 4(c) illustrates the differences of $\frac{1}{\ln(4n+1)}$ and $\frac{1}{\ln(2n+1)}$ versus n. According to this figure, it is clear that the number of variety of dc voltage sources for a constant $N_{level,1}$ and $N_{level,2}$ will be reduced at the least point of these figures. The least (minimum) points are obtained at $n=\infty$ for the first and second proposed algorithms, which means that the bigger the number of dc sources in series in one sub-multilevel, the less requirement for the variety of dc sources utilized. So, to minimize the variety of dc voltage sources, it is enough to use one sub-multilevel inverter in the optimum topology.

D. *Optimal topology for a minimum number of dc voltage sources with a constant number of output voltage levels*

The main focus of this part is to obtain the value of n to generate maximum $N_{level,1}$ and $N_{level,2}$ with a constant number of dc voltage sources. As it was already indicated in (16), the maximum quantity of voltage levels is generated when the quantity of dc voltage sources in each sub-multilevel is equal. Generally, the quantity of voltage levels is constant, from (17), (32), and (45), N_{source} for the first and second proposed algorithms is expressed accordingly by:

$$N_{source} = \ln(N_{level,1}) \times \frac{2n}{\ln(4n+1)} \qquad for\ n \geq 2 \qquad (55)$$

$$N_{source} = \ln(N_{level,2}) \times \frac{n}{\ln(2n+1)} \qquad for\ n \geq 2 \qquad (56)$$

Fig. 4(d) presents the variations of $\frac{2n}{\ln(4n+1)}$ and $\frac{n}{\ln(2n+1)}$ versus n. Accordingly, the number of dc voltage sources for a constant $N_{level,1}$ and $N_{level,2}$ will be minimized at $n=\infty$ for the initial and second proposed algorithms. So, to minimize the number of dc voltage sources, there will be one sub-multilevel inverter in the optimum topology.

E. *Optimal topology for a maximum number of output voltage levels with a constant number of IGBTs*

In this section, the number of IGBTs is assumed to be constant. Considering (19), (32), and (45), $N_{level,1}$ and $N_{level,2}$ are obtained as follows:

$$N_{level,1} = (4n+1)^{\frac{N_{IGBT}}{(4n+6)}} \qquad for\ n \geq 2 \qquad (57)$$

$$N_{level,2} = (2n+1)^{\frac{2N_{IGBT}}{(4n+6)}} \qquad for\ n \geq 2 \qquad (58)$$

Fig. 4(f) compares $(4n+1)^{\frac{1}{(4n+6)}}$ and $(2n+1)^{\frac{2}{(4n+6)}}$ versus n. It is clear that the maximum number of output voltage levels for the first and second proposed algorithms are generated when $n=2$.

F. *Optimal topology for a maximum number of output voltage levels with a constant number of gate drivers*

In this section, the optimization goal would be to maximize the number of output voltage levels that can be generated using a constant number of gate driver circuits. Considering (18), (32), and (45), $N_{level,1}$ and $N_{level,2}$ can be obtained as follows:

$$N_{level,1} = (4n+1)^{\frac{N_{driver}}{(2n+8)}} \qquad for\ n \geq 2 \qquad (59)$$

$$N_{level,2} = (2n+1)^{\frac{2N_{driver}}{(2n+8)}} \quad for\ n \geq 2 \qquad (60)$$

In this inverter, the output voltage level count will be maximized when $(4n+1)^{\frac{1}{(2n+8)}}$ and $(2n+1)^{\frac{2}{(2n+8)}}$ reach their maximum value. Fig. 4(g) compares $(4n+1)^{\frac{1}{(2n+8)}}$ and $(2n+1)^{\frac{2}{(2n+8)}}$ versus n according to which the number of output voltage levels will be maximized when $n=3$ for both proposed algorithms.

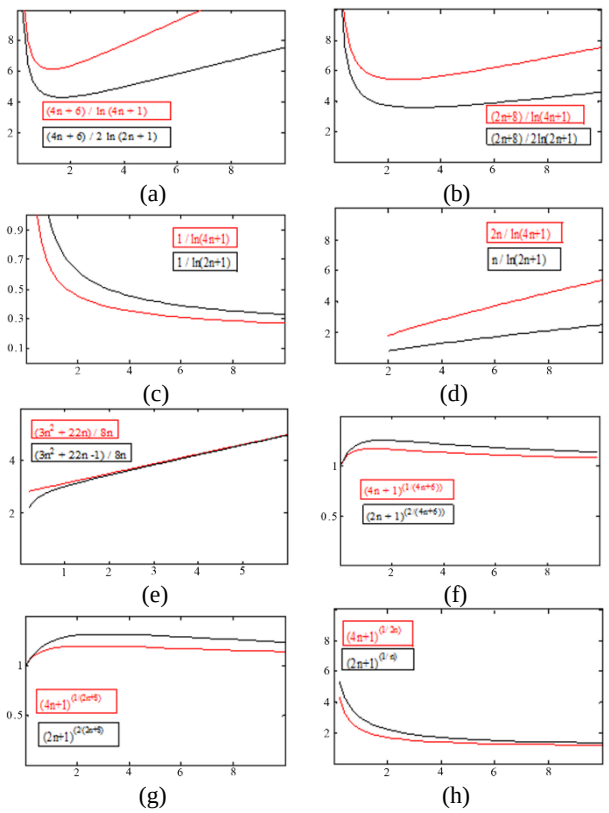

Fig. 4. Variations of different functions versus n.

VI. COMPARISON RESULTS

Fig. 5(a) shows the number of IGBTs versus the number of output voltage levels for the proposed topology with other references. Based on this figure, the proposed topology developed by the second algorithm uses the least amount of IGBT when compared to other structures in [19-30]. The number of the gate drivers required for the proposed topology is compared to other topologies in Fig. 5(b). This comparison indicates that when using the second algorithm for dc voltage source magnitude calculation, the proposed topology needs a minimum number of gate drivers compared to other references. The number of IGBTs, gate driver circuits, dc voltage sources, diodes, and capacitors required to generate at least 69 levels of voltage at the output of 19-30 asymmetric unit structures is summarized in Table IV. According to this table, to generate 69 output voltage levels, the proposed inverter based on the second algorithm requires 16 gate drivers and these numbers are equal to 16, 22, 36, 20, 70, 70, 61, 106, 40, 32, 22, and 21 to produce at least 69 levels in 19-30 topologies, respectively. The number of dc voltage sources is also studied and compared in Fig. 5(c), based on which when using the second algorithm for dc voltage source magnitude calculation, the recommended topology requires fewer dc voltage sources compared to the topologies in [19, 21-29].

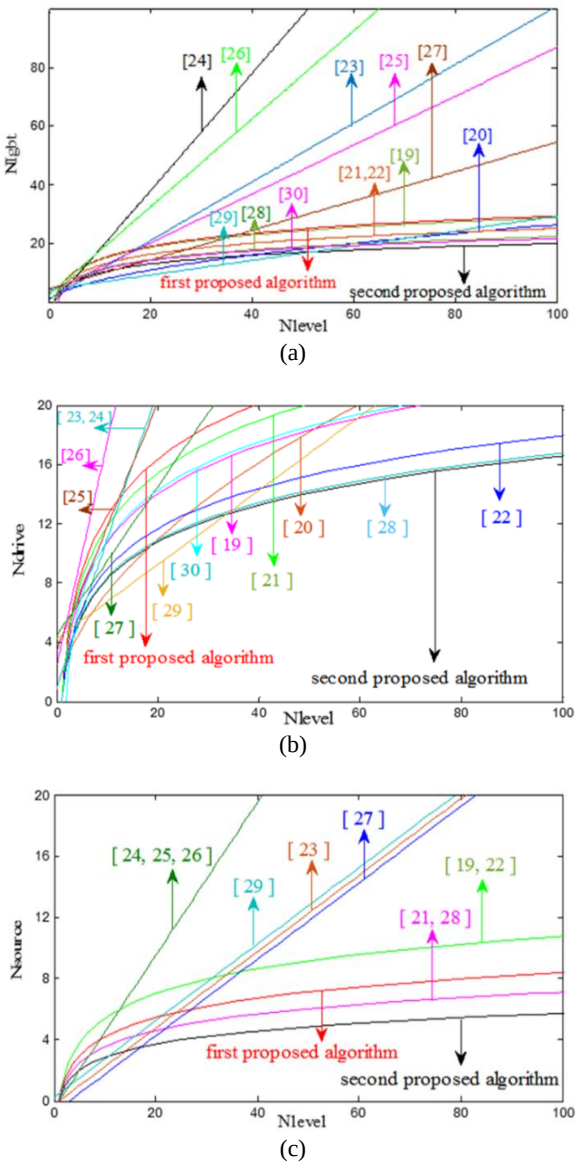

Fig. 5. Variation of (a) N_{IGBT} (b) N_{driver} (c) N_{source} versus N_{level}.

For example, according to Table IV, 69-level inverter based on the second algorithm requires eight dc voltage sources, and this number to produce at least 69 levels is equal to 10, 2, 18, 10, 17, 34, 34, 35, 17, 10, 18, and 1 for the topologies

presented in [19-30], respectively.

Table IV
COMPARISON OF THE PROPOSED INVERTER WITH OTHER STRUCTURES TO PRODUCE AT LEAST 69-LEVEL

Reference	NIGBT	Ndriver	Nsource	Capacitors	Diodes	Standing voltage
19	24	16	10	-	-	**266Vdc**
20	22	22	8	4	8	**9Vdc**
21	36	36	18	-	-	**136Vdc**
22	22	20	10	-	-	**231Vdc**
23	70	70	17	-	-	**138Vdc**
24	136	70	34	-	-	**1802Vdc**
25	61	61	34	-	-	**435Vdc**
26	109	109	35	-	-	-
27	40	40	17	-	16	-
28	32	32	10	-	-	-
29	37	22	18	-	-	**340Vdc**
30	21	21	1	8	4	**524Vdc**
2nd Proposed Algorithm	22	16	8	-	-	**289Vdc**

VII. EXPERIMENTAL RESULTS

This section presents the experimental results for 25 levels of the output voltage (n=2, m=1) based on the second algorithm. As per Fig. 1, this structure consists of four dc voltage sources, 14 IGBTs, and 12 driver circuits. Fig. 6 shows a circuit-built prototype in which values of U_1 and U_2 are selected as 30V and 150V, respectively.

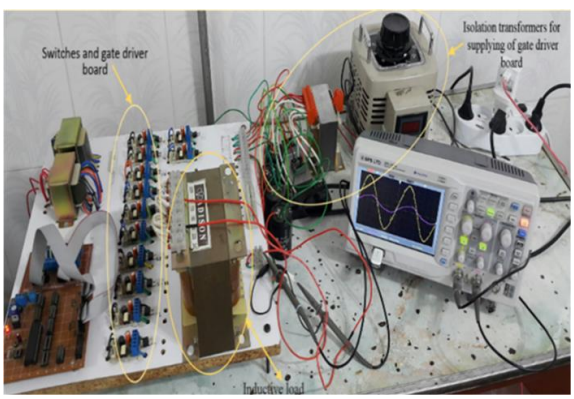

Fig. 6. Laboratory prototype

According to Fig. 7, the maximum output voltage and current are 360V and 4.4A, respectively and an R–L load of $R=85.6\Omega$ and $L=88.6mH$ is utilized to represent the load with an output voltage frequency of 50 Hz. Different control methods can be used to control multi-level inverters. In this paper, the fundamental frequency switching (least error method) is considered the control method. In this control method, switching is done in such a way that according to Fig. 8, the closest step waveform to the desired sinusoidal waveform is created. Fig. 9 shows the voltage on the switches of $S_1, S_2, \cdots, S_6, S_X, S_Y, Z_1, Z_2, F_1, F_2$, which have the maximum voltage of 360, 360, 300, 300, 360, 360, 60, 60, 30, 30, 150, 150 volts, respectively. The total value of standing voltage of the switches for a 25-level inverter (the sum of standing voltage on the switches) is 2520 V, which corresponds to Eq. (26) for $n=2$.

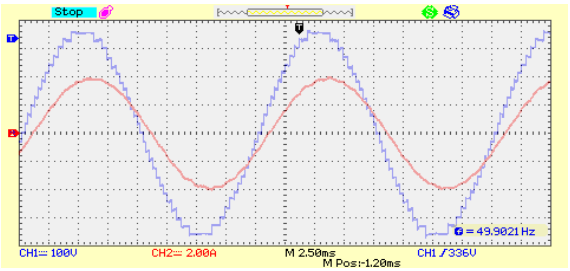

Fig. 7. Experimental results; output 25-level voltage (100V/div), and output 25-level current (2A/div).

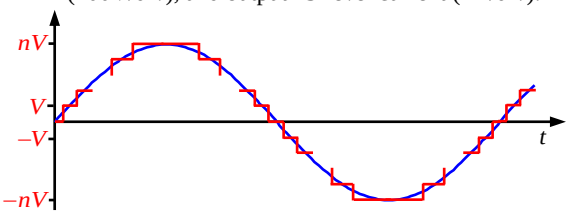

Fig. 8. Fundamental frequency switching control method

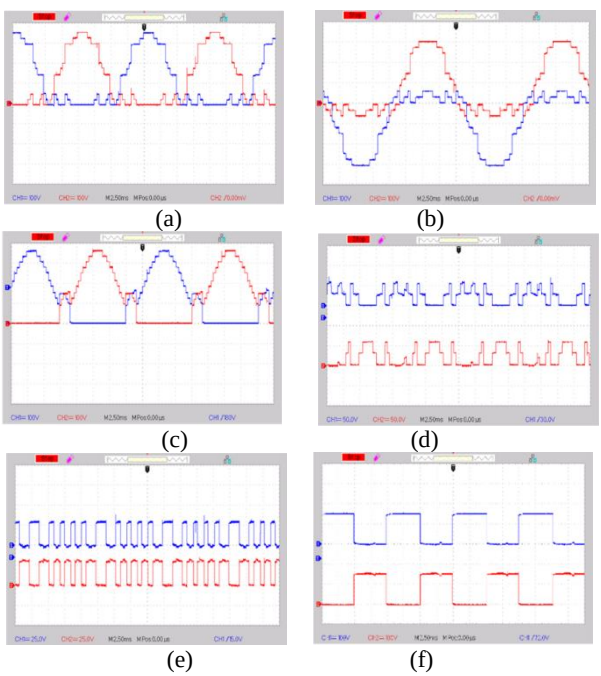

Fig. 9. Voltage waveforms for different switches of the prototype; (a) S1(100 V/div), S2(100 V/div), (b) S3(100 V/div), S4(100 V/div), (c) S5(100 V/div), S6(100 V/div), (d) Sx(50 V/div), Sy(50 V/div), (e) Z1(25 V/div), Z2(25 V/div), (f) F1 (100 V/div), F2 (100 V/div).

VIII. CONCLUSION

A new basic architecture of cascaded multilevel inverter is proposed in this research. The proposed basic unit is comprised of four isolated dc voltage sources and 10

unidirectional and two bidirectional switches with a common-emitter topology. Afterward, the expansion of the basic unit and finally its cascaded variants were examined. To determine the amplitude of dc voltage sources, two algorithms were presented to generate all levels (even and odd) in the output voltage. The optimal extensive topology configuration for different purposes is investigated. For example, it is established that the units with two dc voltage sources and two dc voltage sources are the optimal structure for having a maximum voltage level count at output per specific quantity of IGBTs for both algorithms. The proposed structure was compared with several recently proposed inverter topologies in different aspects. According to the results of the comparison, it is evident that the recommended topology reduced manufacturing cost, volume, and control complexity of the circuit in comparison to the conventional topologies due to having the lowest quantity of IGBTs, gate driver circuits, and dc voltage sources. A 69-level proposed inverter based on the second algorithm requires 22 IGBTs, 16 gate driver circuits, 8 dc voltage sources, no diodes, and no capacitors. To generate the same output voltage level quantity, structures in [23, 26] require 70 and 109 IGBTs, 70 and 109 gate driver circuits, and 17 and 35 dc voltage sources, respectively. The feasibility performance of the proposed structure, for which the dc voltage source magnitudes are calculated with the second algorithm and are controlled with the fundamental frequency control method, is verified through experimental tests performed on a single-phase 25-level prototype.

REFERENCES

[1] H. Abu-Rub, J. Holtz, J. Rodriguez, and G. Baoming, "Medium-voltage multilevel converters—State of the art, challenges, and requirements in industrial applications," *IEEE Trans. Ind. Electron.*, vol. 57, no. 8, pp. 2581-2596, 2010.

[2] M. Ayari, M. M. Belhaouane, X. Guillaud, and N. B. Braiek, "Global advanced control strategy for modular multilevel converter integrated in a HVDC link," *International Transactions on Electrical Energy Systems*, vol. 28, no. 4, p. e2511, 2018.

[3] G. E. Gowd and D. Sreenivasarao, "Nonlinear controller for maximum power extraction in asymmetric multilevel DC link reduced switch count inverter-based grid connected PV system," *International Trans. Electrical Energy Systems*, vol. 30, no. 2, p. e12206, 2020.

[4] E. Babaei, S. Laali, and Z. Bayat, "A single-phase cascaded multilevel inverter based on a new basic unit with reduced number of power switches," *IEEE Trans. Ind. Electron.*, vol. 62, no. 2, pp. 922-929, 2014.

[5] H. Samsami, A. Taheri, and R. Samanbakhsh, "New bidirectional multilevel inverter topology with staircase cascading for symmetric and asymmetric structures," *IET Power Electronics*, vol. 10, no. 11, pp. 1315-1323, 2017.

[6] F. Sedaghati, and S. N. Hashemipour. "Symmetric and asymmetric congurations for a multilevel inverter using less number of power switches," International Journal of Industrial Electronics, Control and Optimization, Vol. 1, No. 2, pp. 91-101, September, 2018.

[7] F. Sedaghati, S. H. Latifi. Majareh , and. H. Dolati. "A single-phase extendable topology for multilevel inverters," *International Journal of Industrial Electronics, Control and Optimization*, Vol. 2, No. 3, pp. 207-220, July 2019.

[8] M. D. Siddique, S. Mekhilef, N. M. Shah, A. Sarwar, and M. A. Memon, "A new single-phase cascaded multilevel inverter topology with reduced number of switches and voltage stress," *International Transactions on Electrical Energy Systems*, vol. 30, no. 2, p. e12191, 2020.

[9] B. Mahato, S. Majumdar, and K. C. Jana, "Reduction in controlled power switches for a single-phase novel multilevel inverter," *International Journal of Electronics*, vol. 106, no. 8, pp. 1200-1215, 2019.

[10] E. Babaei, S. Alilu, and S. Laali, "A new general topology for cascaded multilevel inverters with reduced number of components based on developed H-bridge," *IEEE Trans. Ind. Electron*, vol. 61, no. 8, pp. 3932-3939, 2013.

[11] M. Ghodsi, and S.M. Barakati, "New generalized topologies of asymmetric modular multilevel inverter based on six-switch H-bridge," *International Journal of Circuit Theory and Applications*, *48*(5), pp.789-808., vol. 48, no. 5, pp. 789-808, 2020.

[12] E. Babaei, S. Hosseini, G. Gharehpetian, M. T. Haque, and M. Sabahi, "Reduction of dc voltage sources and switches in asymmetrical multilevel converters using a novel topology," *Electric Power Systems Research*, vol. 77, no. 8, pp. 1073-1085, 2007.

[13] E. Babaei, "A cascade multilevel converter topology with reduced number of switches," *IEEE Trans. Power Electron.*, vol. 23, no. 6, pp. 2657-2664, 2008.

[14] S. H. Hosseini, S. N. Ravadanegh, M. Karimi, Y. Naderi, and M. R. J. Oskuee, "A new scheme of symmetric multilevel inverter with reduced number of circuit devices," in *Proc. ELECO*, 2015, Turkey, pp. 1072-1078.

[15] R. Rasulkhani, and A. Taheri. "A New Multilevel Inverter Topology with Component Count Reduction," International Journal of Industrial Electronics, Control and Optimization, Vol. 2, No. 4, pp. 355-364, Oct 2019.

[16] M. Ghodsi, and S. M. Barakati, "A Generalized Cascade Switched-Capacitor Multilevel Converter Structure and Its Optimization Analysis," *IEEE Journal of Emerging and Selected Topics in Power Electronics.*, vol. 8, no. 4, pp. 4306-4317, 2019.

[17] E. Samadaei, S. A. Gholamian, A. Sheikholeslami, and J. Adabi, "An envelope type (E-Type) module: asymmetric multilevel inverters with reduced components," *IEEE Trans. Ind. Electron.*, vol. 63, no. 11, pp. 7148-7156, 2016.

[18] E. Samadaei, A. Sheikholeslami, S. A. Gholamian, and J. Adabi, "A square T-type (ST-Type) module for asymmetrical multilevel inverters," *IEEE Trans. Power Electron.*, vol. 33, no. 2, pp. 987-996, 2017.

[19] R. S. Alishah, S. H. Hosseini, E. Babaei, and M. Sabahi, "A new general multilevel converter topology based on cascaded connection of submultilevel units with reduced

switching components, DC sources, and blocked voltage by switches," *IEEE Trans. Ind. Electron.*, vol. 63, no. 11, pp. 7157-7164, 2016.

[20] T. Roy and P. K. Sadhu, "A step-up multilevel inverter topology using novel switched capacitor converters with reduced components," *IEEE Trans. Ind. Electron.*, 2020.

[21] J. Ebrahimi, E. Babaei, and G. B. Gharehpetian, "A new topology of cascaded multilevel converters with reduced number of components for high-voltage applications," *IEEE Trans. Power Electron.*, vol. 26, no. 11, pp. 3109-3118, 2011.

[22] R. S. Alishah, S. H. Hosseini, E. Babaei, and M. Sabahi, "Optimal design of new cascaded switch-ladder multilevel inverter structure," *IEEE Trans. Ind. Electron.*, vol. 64, no. 3, pp. 2072-2080, 2016.

[23] J. S. M. Ali, R. S. Alishah, and V. Krishnasamy, "A new symmetric multilevel converter topology with reduced voltage on switches and DC source," *in 2018 International Conference on Power, Instrumentation, Control and Computing (PICC)*, 2018, pp. 1-6.

[24] R. S. Alishah, S. H. Hosseini, E. Babaei, M. Sabahi, and J. F. Ardashir, "An improved symmetric H-bridge multilevel converter topology; an attempt to reduce power losses," *Journal of Circuits, Systems and Computers*, vol. 27, no. 12, p. 1850187, 2018.

[25] Y. Naderi-Zarnaghi, M. Karimi, M. Jannati-Oskuee, S. Hosseini, and S. Najafi-Ravadanegh, "A Developed Asymmetric Multilevel Inverter with Lower Number of Components," *AUT journal of Electrical Engineering*, vol. 50, no. 2, pp. 197-206, 2018.

[26] M. T. Khosroshahi, "Crisscross cascade multilevel inverter with reduction in number of components," *IET Power Electronics*, vol. 7, no. 12, pp. 2914-2924, 2014.

[27] Y. Hinago and H. Koizumi, "A single-phase multilevel inverter using switched series/parallel dc voltage sources," *IEEE Trans. Ind. Electron*, vol. 57, no. 8, pp. 2643-2650, 2009.

[28] F. Masoudinia, E. Babaei, M. Sabahi, and H. Alipour, "New basic unit and cascaded multilevel inverters with reduced power electronic devices," *International Journal of Electronics*, pp. 1-18, 2020.

[29] M.R.J. Oskuee, M. Karimi, Y. Naderi, S. N. Ravadanegh, and S. H. Hosseini, "A new multilevel voltage source inverter configuration with minimum number of circuit elements," *Journal of Central South University*, vol. 24, no. 4, pp. 912-920, 2017.

[30] T. Roy, P. K. Sadhu, and A. Dasgupta, "Cross-switched multilevel inverter using novel switched capacitor converters," *IEEE* Trans. Ind. Electron., vol. 66, no. 11, pp. 8521-8532, 2019.

Roya Naderi was born in Tabriz, Iran in 1980. received her B.Sc. and M.Sc. degrees in Electronics Engineering both from Islamic Azad University of Tabriz in 2003 and 2009, respectively and her Ph.D. degree in Electrical Engineering (power electronics) from Islamic Azad University of Shabestar in 2020. She joined Islamic Azad University of Heris in 2012. She is the author of two books and 8 journal and conference papers. Her current research interests include the analysis and control of power electronic inverters and multilevel inverters.

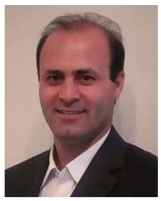

Ebrahim Babaei (M'10, SM'16) received the Ph.D. degree in Electrical Engineering from the University of Tabriz, in 2007. In 2007, he joined the Faculty of Electrical and Computer Engineering, University of Tabriz. He has been a Professor since 2015. He is the author and co-author of one book and more than 580 journal and conference papers. He also holds 25 patents in the area of power electronics. His current research interests include the analysis, modelling, design, and control of Power Electronics Converters and their applications, Renewable Energy Sources, and FACTS Devices. Prof. Babaei has been the Editor-in-Chief of Tabriz Journal of Electrical Engineering since 2013. He is also currently an Associate Editor of the IEEE Transactions on Industrial Electronics, IEEE Transactions on Power Electronics, Open Journal of the Industrial Electronics Society, and Iranian Journal of Science and Technology, Transactions of Electrical Engineering. He has been the Corresponding Guest Editor for two special issues in the IEEE Transactions on Industrial Electronics. In addition, Prof. Babaei has been the Technical Program Chair, Track Chair, organizer of different special sessions and Technical Program Committee member in most important international conferences organized in the field of Power Electronics. Several times, he was the recipient of the Best Researcher Award from the University of Tabriz. He received the Prize Winner and Distinguished Researcher all over Engineering Faculties of all Universities of East Azarbaijan, Iran, in 2020. He also received the Prize Winner and Award of 2016 Outstanding Reviewer from IEEE Transactions on Power Electronics. Prof. Babaei has earned inclusion on the list of the Top One Percent of the World's Scientists and Academics according to Thomson Reuters' list since 2015.

Mehran Sabahi was born in Tabriz, Iran in 1968. He received his B.Sc. degree in Electronic Engineering from the University of Tabriz, his M.Sc. degree in Electrical Engineering from Tehran University, Tehran, Iran, and his Ph.D. degree in Electrical Engineering from the University of Tabriz in 1991, 1994, and 2009, respectively. In 2009, he joined the Faculty of Electrical and Computer Engineering at the University of Tabriz where he has been an associate professor since 2015. His current research interests include power electronic converters and renewable energy systems.

Ali Daghigh was born in Tabriz, Iran in 1983. He received his B.Sc. degree in Power Electrical Engineering from the Sharif University of Technology, Tehran, Iran in 2007, his M.Sc. degree in Power Electrical Engineering from Tabriz University, Tabriz, Iran in 2010, and his Ph.D. degree in Power Electrical Engineering from Shahid Beheshti University, Tehran, Iran in 2016. He is currently an Assistant Professor with the Department of Electrical Engineering, Shabestar Branch, Islamic Azad University, Shabestar, Iran. His research interests include Electrical machines design and drives, wind generators, and the application of the finite-element method.

International Journal of Industrial Electronics, Control and Optimization IECO
Vol. 4, No. 4, pp. 475-484, Sep (2021)

An Operational Matrix Method Based on the Gegenbauer Polynomials for Solving a Class of Fractional Optimal Control Problems

Farzaneh Soufivand [1], Fahimeh Soltanian [2,†], and Kamal Mamehrashi [3]

[1,2,3] Department of Mathematics, Payame Noor University, Tehran, Iran.

ABSTRACT

One of the most important classes of fractional calculus is the fractional optimal control problem (FOCP), which arises in engineering. This study presents a direct and efficient numerical method for solving a class of (FOCPs) in which the fractional derivative is in the Caputo sense and the dynamic system includes the fractional- and integer-order derivatives. For this purpose, we use the operational matrix of fractional Riemann-Liouville integration based on the shifted Gegenbauer polynomials. First, the fractional- and integer-order derivatives in the given problem are approximated based on the shifted Gegenbauer polynomials with unknown coefficients. Then by substituting these approximations and the equation derived from the dynamic constraint into the cost functional, an unconstrained optimization problem is obtained. The main advantage of this approach is that it reduces the FOCP given to an unconstrained optimization problem and using the necessary optimality conditions yields a system of algebraic equations which can be easily solved by Newton's iterative method. In addition, the convergence of the method is proved via several theorems. Finally, some numerical examples are presented to illustrate the validity and applicability of the proposed technique.

Article Info

Keywords:
Caputo fractional derivative, Numerical method, Optimal control problems, Riemann-Liouville fractional integration, Shifted Gegenbauer polynomials, Operational matrix.

Article History:
Received 2021-08-15
Accepted 2021-10-28

I. INTRODUCTION

Optimal control theory has a wide range of applications in different science and engineering fields [1], such as physics and quantum dynamics [2, 3].

Nowadays, fractional calculus is a very important branch of mathematics and the dynamics of many systems can be described more precisely using fractional order derivatives rather than integer-order derivatives, such as dynamical procedures containing heat conduction and gas diffusion in fractal porous media [4].

Moreover, fractional calculus has numerous real applications in science and engineering fields, such as physics [5], medicine [6], electromagnetism [7], and the dynamic of viscoelastic materials [8]. One of the important topics in fractional calculus is the fractional optimal control problem (FOCP), in which the dynamic constraints as well as the cost functional might entail not only integer-order derivatives but also fractional-order derivatives or integrals [9]. FOCPs can be established with respect to different types of fractional derivatives. However, the most important types of fractional derivatives are the Riemann-Liouville and the Caputo fractional derivatives. Solving FOCPs was first accomplished by Agrawal [10]. Then, in [11], he presented a direct numerical method for solving Riemann-Liouville FOCPs. In the last two decades, orthogonal polynomials have been used for solving different problems [12, 13, 14]. In addition, solving FOCPs with polynomials and

[†]**Corresponding Author**: f_soltanian@pnu.ac.ir
Tel: +98-9131051361, Department of Mathematics, Payame Noor University, Tehran, Iran

operational matrices has received great attention from researchers and thus numerous studies have been conducted in this field. For instance, Legendre polynomials [15, 16], Jacobi polynomials [17, 18], Bernoulli polynomials [19], Bernstein polynomials [20, 21], and Genocchi polynomials [22] have been used for solving different models of FOCPs so far. In [23], by employing an indirect method and the necessary optimality conditions, the FOCP is converted to a two-point boundary value problem, which is solved by the collocation method based on Bernoulli hybrid functions. The Gegenbauer polynomials have many beneficial and important properties and the theory of these polynomial approximations has received considerable attention in recent years [24, 25, 14]. In [26], the Gegenbauer polynomials were employed to solve FOCPs with the Riemann-Liouville fractional derivative. In this paper, we consider the following FOCP in the Caputo sense [20, 21]

$$\min J = \int_0^1 f\big(t, x(t), u(t)\big)dx \tag{1}$$

subject to the dynamic constraint with fractional- and integer-order derivatives

$$Mx'(t) + ND^{\nu}x(t) = a\big(t, x(t)\big) + b(t)u(t), \tag{2}$$

with the boundary conditions

$$x(0) = x_0, \quad x(1) = x_1, \tag{3}$$

where $1 < \nu \leq 2$.

Moreover, we assume that $f\big(t, x(t), u(t)\big), a(t, x(t))$ and $b(t) \neq 0$ are smooth functions, D^{ν} is the Caputo fractional derivative of order ν, and M, and N are constant numbers. The aim of this article is to take the Caputo fractional derivative in the dynamic constraint by constructing the shifted Gegenbauer operational matrix of the Riemann-Liouville fractional integration. To do this and for the optimality of the cost functional, first, we approximate the fractional derivative in the dynamic constraint based on the shifted Gegenbauer polynomials with unknown coefficients. Then, the equation derived from the dynamic constraints is put into the cost functional. In this manner, by applying the necessary optimality conditions, a system of algebraic equations will be obtained that can be easily solved by Newton's iterative method. The remaining part of this paper is organized as follows: In section 2, we introduce some basic definitions of fractional calculus, as well as definitions of shifted Gegenbauer polynomials and their properties, which are required for the subsequent development. In section 3, a new function approximation of FOCPs is constructed. Section 4 presents the shifted Gegenbauer operational matrix of fractional integration. In section 5, we describe the numerical treatment of the proposed method. In section 6, the convergence of the method is given and some theorems are proved. Section 7 reports the numerical results and demonstrates the accuracy of the proposed method through several numerical examples, Moreover, in this section, the numerical results obtained by our method are compared with those found by other methods. Finally, the conclusion is given in section 8.

II. BASIC PRELIMINARIES

In this section, we explain some basic definitions that are required in the following part of the paper.

Definition 1. The Riemann-Liouville fractional integral operator I of order $\nu \geq 0$ on the interval $[0, \infty)$ of a function $g(t)$ is given by [13].

$$I^{\nu}g(t) = \begin{cases} \dfrac{1}{\Gamma(\nu)} \displaystyle\int_0^t (t-y)^{\nu-1} g(y)dy, & \nu > 0, \quad t > 0 \\ g(t), & \nu = 0 \end{cases} \tag{4}$$

The Riemann-Liouville fractional integral has the following properties:

$$I^{\nu}t^k = \frac{\Gamma(k+1)}{\Gamma(k+1+\nu)}t^{k+\nu}, \tag{5}$$

$$I^{\nu}\big(\lambda_1 g_1(t) + \lambda_2 g_2(t)\big) = \lambda_1 I^{\nu} g_1(t) + \lambda_2 I^{\nu} g_2(t) \tag{6}$$

where λ_1, and λ_2 are constants.

Definition 2. The Caputo fractional derivative of order ν of $g(t)$ is given by [13].

$$D^{\nu}g(t) = \frac{1}{\Gamma(n-\nu)}\int_0^t (t-y)^{(n-\nu-1)} \frac{d^n}{dy^n} g(y)dy, \tag{7}$$
$$n-1 < \nu \leq n, n \epsilon N$$

The Caputo fractional derivative D^{ν} has the following properties:

$$D^{\nu}t^n = \begin{cases} \frac{\Gamma(n+1)}{\Gamma(n+1-\nu)} t^{n-\nu}, & n \epsilon N \cup \{0\}, \ n \geq [\nu] \\ 0, & n \epsilon N \cup \{0\}, \ n < [\nu] \end{cases} \tag{8}$$

$$D^{\nu}\big(\lambda_1 g_1(t) + \lambda_2 g_2(t)\big) = \lambda_1 D^{\nu} g_1(t) + \lambda_2 D^{\nu} g_2(t) \tag{9}$$

where λ_1, and λ_2 are constants.

$$D^{\nu}I^{\nu}g(t) = g(t), \quad g(t) \epsilon C^n[0,1] \tag{10}$$

$$I^{\nu}D^{\nu}g(t) = g(t) - \sum_{i=0}^{n-1} g^i(0^+)\frac{t^i}{i!}, \tag{11}$$

$$g(t) \epsilon C^n[0,1], t > 0 \tag{12}$$

We first introduce the Gegenbauer polynomials, and then with a given variable change, we obtain the shifted Gegenbauer polynomials. The Gegenbauer polynomials $C_n^{(\beta)}(t)$ are a set of real-valued polynomials of the degree $n \epsilon Z^+$ associated with the parameter $\beta > -\frac{1}{2}$ in the domain $[-1, 1]$. These polynomials are defined by [14].

$$C_n^{(\beta)}(t) = \sum_{k=0}^{\left[\frac{n}{2}\right]} \frac{(-1)^k \Gamma(n-k+\beta)}{k!\,\Gamma(\beta)(n-2k)!}(2t)^{n-2k} \tag{13}$$

Another way to generate the Gegenbauer polynomials is to use the following recurrence formula:

$$(n+2\beta)C_{n+1}^{(\beta)}(t) = 2(n+\beta)tC_n^{(\beta)}(t) - nC_{n-1}^{(\beta)}(t), \quad (14)$$

Starting with

$$C_0^{(\beta)}(t) = 1, \quad C_1^{(\beta)}(t) = t. \quad (15)$$

The Gegenbauer polynomials are orthogonal with respect to L^2-space on the interval $[-1,1]$. The orthogonality relation is given by:

$$\int_{-1}^{1} C_m^{(\beta)}(t)C_n^{(\beta)}(t)\,\omega_n^{(\beta)}(t)dt = \eta_n^{(\beta)}(t)\delta_{m,n}, \quad (16)$$

where $\omega_n^{\beta}(t)$ and $\eta_n^{\beta}(t)$ are the weight function and the normalizing factor, respectively, and defined by:

$$\omega_n^{(\beta)}(t) = (1-t^2)^{\left(\beta-\frac{1}{2}\right)}, \quad (17)$$

$$\eta_n^{(\beta)}(t) = ||C_n^{(\beta)}(t)||^2 = \frac{2^{1-2\beta}\pi\Gamma(n+2\beta)}{n!(n+\beta)\Gamma^2(\beta)}, \quad (18)$$

and $\delta_{m,n}$ is the Kronecker delta function. In order to use the Gegenbauer polynomials on the interval $[0,1]$, we define the shifted Gegenbauer polynomials by replacing the variable t with $2t-1$, $t\epsilon[0,1]$ [14]. Let us define the shifted Gegenbauer polynomial $C_n^{(\beta)}(2t-1)$ of the degree n by $C_{S,n}^{(\beta)}(t)$, so

$$C_{S,0}^{(\beta)}(t) = 1, \quad C_{S,1}^{(\beta)}(t) = 2t-1. \quad (19)$$

The explicit form of the shifted Gegenbauer polynomial of the degree n is given by [14]:

$$C_{S,n}^{(\beta)}(t) = \frac{\Gamma\left(\beta+\frac{1}{2}\right)}{\Gamma(2\beta)}\sum_{k=0}^{n}\frac{(-1)^{(n-k)}\Gamma(n+k+2\beta)}{(n-k)!\,k!\,\Gamma\left(k+\beta+\frac{1}{2}\right)}(t)^k \quad (20)$$

The orthogonality condition of these polynomials with respect to L^2-space on the interval $[0,1]$ can be obtained by [14]:

$$\int_0^1 C_{S,m}^{(\beta)}(t)C_{S,n}^{(\beta)}(t)\,\vartheta^{\beta}(t)dt = \lambda_n^{(\beta)}(t)\delta_{m,n}, \quad (21)$$

where

$$\vartheta^{\beta}(t) = (t-t^2)^{\left(\beta-\frac{1}{2}\right)}, \quad (22)$$

and

$$\lambda_n^{(\beta)}(t) = \frac{\left(\Gamma\left(\beta+\frac{1}{2}\right)\right)^2\Gamma(n+2\beta)}{\left(\Gamma(2\beta)\right)^2(2n+2\beta)n!} \quad (23)$$

The shifted Gegenbauer polynomials are interrelated with the other polynomials by the following relations:

$$L_n(t) \equiv C_{S,n}^{\left(\frac{1}{2}\right)}(t), \; T_n(t) \equiv C_{S,n}^{(0)}(t), \; U_n^*(t) \equiv C_{S,n}^{(1)}(t), \quad (24)$$

where $L_n(t)$, $T_n(t)$, and $U_n^*(t)$ are the shifted Legendre polynomials, the shifted Chebyshev polynomials of the first kind, and the shifted Chebyshev polynomials of the second kind, respectively.

III. FUNCTION APPROXIMATION

In this section, we will construct an approximate function based on shifted Gegenbauer polynomials with unknown coefficients. Suppose that $H = L^2[0,1]$ is a Hilbert space and define

$$Z = Span\left\{C_{S,0}^{(\beta)}(t), C_{S,1}^{(\beta)}(t), \dots, C_{S,n}^{(\beta)}(t)\right\}. \quad (25)$$

Z is a finite-dimensional and closed subspace of H and therefore Z it is a complete subspace of H. Hence, for every arbitrary element $g(t)$ in H, there exists the unique best approximation out of Z such as $g_n(t)$ that

$$\forall\, z(t)\epsilon Z, \; \left|\left|g(t)-g_n(t)\right|\right|_2 \le \left|\left|g(t)-z(t)\right|\right|_2. \quad (26)$$

We can write, $H = Z \oplus Z^{\perp}$ where $Z^{\perp}$ is the orthogonal complement of Z. So, $g(t) = z(t) + z^{\perp}(t)$ where $z^{\perp}(t) = g(t) - z(t)$. It implies that $g(t) - g_n(t)\epsilon Z^{\perp}$ and therefore

$$\forall\, z(t)\epsilon Z, \; < g(t)-g_n(t), z(t) > = 0, \quad (27)$$

where <: > denotes the inner product. Since $g_n(t)\epsilon Z$, there are unique coefficients $c_0, c_1, \dots, c_n \epsilon R$ such that

$$g(t) \simeq g_n(t) = \sum_{j=0}^{n} c_j\, C_{S,j}^{(\beta)}(t) = C^T\phi(t), \quad (28)$$

where $C = [c_0, c_1, \dots, c_n]^T$,

$$\phi(t) = \left[C_{S,0}^{(\beta)}(t), C_{S,1}^{(\beta)}(t), \dots, C_{S,n}^{(\beta)}(t)\right]^T. \quad (29)$$

Using Eq. (27) and Eq. (28), we have

$$< g(t) - C^T\phi(t), C_{S,i}^{(\beta)}(t) > = 0 \;\; i = 0,1,\dots,n, \quad (30)$$

or equivalently

$$< g(t), \phi(t) > = C^T < \phi(t), \phi(t) > \quad (31)$$

where $< \phi(t), \phi(t) >$ is the following $(n+1)\times(n+1)$ matrix

$$Q = < \phi(t), \phi(t) > = \int_0^1 \phi(t)\phi^T(t)\,\vartheta^{\beta}(t)dt. \quad (32)$$

From Eq. (30) and Eq. (32), we obtain

$$C = Q^{-1} < g(t), \phi(t) >, \quad (33)$$

where

$$c_i = (\lambda_i^{\beta})^{-1}\int_0^1 g(t)\,\vartheta^{\beta}(t)C_{S,i}^{(\beta)}(t)dt\,, i = 0,1,\dots,n. \quad (34)$$

IV. SHIFTED GEGENBAUER OPERATIONAL MATRIX OF FRACTIONAL INTEGRATION

In this section, in order to solve FOCPs (1)-(3) based on shifted Gegenbauer polynomials, we will construct an operational matrix with a given theorem.

Theorem 1: Suppose $\phi(t)$ is the shifted Gegenbauer vector given with Eq. (29) and let $\nu > 0$. Then

$$I^{\nu}\phi(t) \simeq F^{\nu}\phi(t), \quad (35)$$

where F^{ν} is the $(n+1)\times(n+1)$ operational matrix of fractional integration of order ν in the Riemann-Liouville sense, given by:

$$F^{\nu}=\begin{bmatrix} \theta_{0,0,0} & \theta_{0,1,0} & \cdots & \theta_{0,n,0} \\ \sum_{j=0}^{1}\theta_{1,0,j} & \sum_{j=0}^{1}\theta_{1,1,j} & \cdots & \sum_{j=0}^{1}\theta_{1,n,j} \\ \sum_{j=0}^{2}\theta_{2,0,j} & \sum_{j=0}^{2}\theta_{2,1,j} & \cdots & \sum_{j=0}^{2}\theta_{2,n,j} \\ \vdots & \vdots & \cdots & \vdots \\ \sum_{j=0}^{n}\theta_{n,0,j} & \sum_{j=0}^{n}\theta_{n,1,j} & \cdots & \sum_{j=0}^{n}\theta_{n,n,j} \end{bmatrix}$$

where $\theta_{i,r,j}$ is as follows:

$$\theta_{i,r,j}=\sum_{j=0}^{i}\frac{(-1)^{i-j}\Gamma\left(\beta+\frac{1}{2}\right)\Gamma(i+j+2(\beta))}{(i-j)!\,\Gamma\left(j+\beta+\frac{1}{2}\right)\Gamma(2\beta)\Gamma(j+\nu+1)}\times$$

$$\sum_{j=0}^{i}\frac{(-1)^{r-k}r!\,(r+\beta)\Gamma^{2}(\beta)\Gamma^{2}\left(\beta+\frac{1}{2}\right)\Gamma\left(\nu+j+k+\beta+\frac{1}{2}\right)}{2^{(1-4\beta)}\pi(r-k)!\,k!\,\Gamma(r+2\beta)\Gamma(2\beta)\Gamma\left(k+\beta+\frac{1}{2}\right)}$$
$$\times\frac{\Gamma(r+k+2\beta)}{\Gamma(\nu+j+k+2\beta+1)} \quad (36)$$

Proof: See [26].

V. NUMERICAL TREATMENT

In this section, we describe our numerical method for solving FOCPs (1)-(3). In Eq. (2), we approximate $D^{\nu}x(t)$ by Gegenbauer polynomials as

$$D^{\nu}x(t)=C^{T}\phi(t), \quad (37)$$

here $\phi(t)$ and C are $(n+1)\times 1$ matrices by Eq. (29). By integrating from (37) and using (35), we obtain

$$I^{\nu}D^{\nu}x(t)=C^{T}F^{\nu}\phi(t), \quad (38)$$

and from (11), we have

$$I^{\nu}D^{\nu}x(t)=x(t)-tx'(0)-x(0), \quad (39)$$

Thus, $x(t)$ can be represented by

$$x(t)=C^{T}F^{\nu}\phi(t)+tx'(0)+x_0, \quad (40)$$

Therefore, the boundary condition $x(1)=x_1$ yields

$$x_1=x(1)=C^{T}F^{\nu}\phi(1)+x'(0)+x_0, \quad (41)$$

or equivalently

$$x'(0)=x_1-x_0-C^{T}F^{\nu}\phi(1), \quad (42)$$

Substituting Eq. (42) into Eq. (40), gives

$$x(t)=C^{T}F^{\nu}\phi(t)+t\left(x_1-x_0-C^{T}F^{\nu}\phi(1)\right)+x_0, \quad (43)$$

and by deriving Eq. (43), we estimate the ordinary derivative of $x(t)$ as

$$x'(t)=C^{T}F^{\nu}D\phi(t)+x_1-x_0-C^{T}F^{\nu}\phi(1), \quad (44)$$

where D is the operational matrix of differentiation. Using Eq. (2), Eq. (37), and Eq. (44), the control function is approximated as

$$u(t)=\frac{1}{b(t)}\left[Mx'(t)+ND^{\nu}x(t)-a\left(t,x(t)\right)\right]=$$
$$\frac{1}{b(t)}\left[M\left(C^{T}F^{\nu}D\phi(t)+x_1-x_0-C^{T}F^{\nu}\phi(1)\right)+NC^{T}\phi(t)\right.$$
$$\left.-a(t,C^{T}F^{\nu}\phi(t)+t\left(x_1-x_0-C^{T}F^{\nu}\phi(1)\right)+x_0)\right], \quad (45)$$

substituting the approximate functions (43) and (45) into the cost functional (1), the following unconstrained optimization problem is obtained

$$\min J=\int_0^1 f(t,C^{T}F^{\nu}\phi(t)+t\left(x_1-x_0-C^{T}F^{\nu}\phi(1)\right)+x_0\,\frac{1}{b(t)}[M\left(C^{T}F^{\nu}D\phi(t)+x_1-x_0-C^{T}F^{\nu}\phi(1)\right)+NC^{T}\phi(t)-a(t,C^{T}F^{\nu}\phi(t)+t\left(x_1-x_0-C^{T}F^{\nu}\phi(1)\right)+x_0)])dt, \quad (46)$$

which can be written as

$$\min J=\int_0^1\Psi(t,C)dt, \quad (47)$$

where

$$\Psi(t,C)=f(t,C^{T}F^{\nu}\phi(t)+t\left(x_1-x_0-C^{T}F^{\nu}\phi(1)\right)+x_0,$$
$$\frac{1}{b(t)}[M\left(C^{T}F^{\nu}D\phi(t)+x_1-x_0-C^{T}F^{\nu}\phi(1)\right)+NC^{T}\phi(t)$$
$$-a(t,C^{T}F^{\nu}\phi(t)+t\left(x_1-x_0-C^{T}F^{\nu}\phi(1)\right)+x_0)]). \quad (48)$$

In order to approximate the integral (47), we use the Legendre-Gauss quadrature rule

$$J[C]\simeq\frac{1}{2}\sum_{j=0}^{l}w_j\Psi\left(\frac{\tau_j+1}{2},C\right), \quad (49)$$

where τ_j and w_j for $j=0,1,\dots,l$ are $l+1$ zeros of the Legendre polynomial and the corresponding weight, respectively [27]. To find the unknown coefficients $C=[c_1,c_2,\dots,c_n]$, the following necessary conditions of optimality should be satisfied

$$\frac{\partial J}{\partial c_i}=0, \quad i=0,1,\dots,n. \quad (50)$$

In this manner, FOCPs (1)-(3) are reduced to a system of algebraic equations (50), which can be solved by Newton's iterative method, and then the approximate functions x(t) and u(t) are obtained by (43) and (45), respectively.

It should be noted that, if the control function cannot be directly derived from Eq. (2), we must approximate it in terms of the Gegenbauer polynomials with unknown coefficients. Then by substituting the approximated state and control functions in the cost functional and applying the optimality conditions, we can obtain the unknown coefficients.

VI. THE CONVERGENCE OF THE METHOD

In the previous section, a new technique for solving a class of FOCPs based on shifted Gegenbauer polynomials was provided. In this section, the convergence of the proposed method is investigated. It is shown that by increasing the number of shifted Gegenbauer polynomials, the approximation error approaches zero. The following lemma presents the upper bound of the error by considering that the function g is $n+1$ times continuously differentiable.

Theorem 2: Consider the function $g:[0,L]\to R, g\epsilon C^{n+1}[0,1]$. Suppose that g_n is the best approximation of g toward Z, then

$$|g-g_n|| \le \frac{H}{(n+1)!}\sqrt{\frac{L^{3+2n}}{3+2n}} \quad (51)$$

where $H = max_{x\in[0,L]}|g^{n+1}(x)|$

Proof: Taylor polynomial of g at zero is defined by

$$z_1(t) = g(0) + g'(0)t + \cdots + g^n(0)\frac{t^n}{n!}, \quad (52)$$

and the upper bound of the error of the Taylor polynomial is written as

$$\left||g(t)-z_1(t)\right|| \le \frac{Ht^{n+1}}{(n+1)!}, \quad \forall t\in[0,1] \quad (53)$$

where $H = max_{x\in[0,L]}|g^{n+1}(x)|$. Since $g_n \in Z$ is the best approximation of g out of Z and $z_1 \in Z$, then

$$\left||g-g_n|\right|_2^2 \le \int_0^L \left(g(t)-z_1(t)\right)^2 dt \le \int_0^L \left(\frac{Ht^{n+1}}{(n+1)!}\right)^2 dt$$

$$= \left(\frac{H}{(n+1)!}\right)^2 \int_0^L t^{2n+2}dt = \left(\frac{H}{(n+1)!}\right)^2 \frac{L^{3+2n}}{3+2n}, \quad (54)$$

By taking the square roots, the upper bound is achieved.

Corollary1: From Theorem 2, we can conclude that since $g\epsilon C^{n+1}[0,L]$, then $\lim_{n\to\infty} g_n = g$.

Theorem 3: If $g_n(t)$ is the nth approximation of the function $g\epsilon L^2_{\omega_L}[0,L]$, and

$$K_n(g) = \int_0^L [g(x)-g_n(x)]^2 \omega_L^{(a,b)}(x)dx \quad (55)$$

Then we have

$$\lim_{n\to\infty} K_n(g) = 0 \quad (56)$$

Proof: See [28].

Let e_{I^ν} denote the error value for the operational matrix of integration in a Riemann-Liouville sense achieved by using $(n+1)$ orthogonal polynomials in $L^2_\omega[0,1]$, then

$$e_{I^\nu} = F^\nu\phi(t) - I^\nu\phi(t) \quad (57)$$

where $e_{I^\nu} = [e_{I^\nu,0}, e_{I^\nu,1}, \dots, e_{I^\nu,n}]^T$ is an error vector The term $t^{j+\nu}$ based on shifted Gegenbauer polynomials is approximated as

$$t^{j+\nu} \approx \sum_{r=0}^n \tilde{\beta}_r C_{S,r}^{(\nu)}(t). \quad (58)$$

Now by applying Theorem 2 for the term $t^{j+\nu}$, we have

$$||t^{j+\nu} - \sum_{r=0}^n \tilde{\beta}_r C_{S,r}^{(\nu)}(t)||_2 \le \left(\frac{H}{(n+1)!}\right)^2 \frac{L^{3+2n}}{3+2n} \quad (59)$$

and the error norm is calculated as

$$||e_{I^\nu}||_2 = \left\| I^\nu C_{S,i}^{(\beta)}(t) - \sum_{r=0}^i \sum_{j=0}^n \theta_{i,r,j} C_{S,j}^{(\beta)}(t) \right\| =$$

$$||\sum_{j=0}^i \frac{\Gamma\left(\beta+\frac{1}{2}\right)\Gamma(i+j+2\beta)}{(i-j)!\,j!\,\Gamma\left(j+\beta+\frac{1}{2}\right)\Gamma(2\beta)(-1)^{i-j}} I^\nu(t^j) -$$

$$\sum_{r=0}^i \sum_{j=0}^n \frac{(-1)^{i-r}\Gamma\left(\beta+\frac{1}{2}\right)\Gamma(i+r+2\beta)}{\Gamma\left(r+\beta+\frac{1}{2}\right)\Gamma(2\beta)(i-r)!\,\Gamma(\nu+r+1)} \tilde{\beta}_j C_{S,j}^{(\beta)}(t)||$$

$$\le \sum_{r=0}^n \omega_{ij}^\nu \left|\left| t^{j+\nu} - \sum_{r=0}^n \tilde{\beta}_r C_{S,r}^{(\beta)}(t) \right|\right|_2$$

$$\le \sum_{r=0}^n \omega_{ij}^\nu \left(\frac{H}{(n+1)!}\right)^2 \frac{L^{3+2n}}{3+2n}, \quad (60)$$

Note that $\theta_{i,r,j}$ has been defined as $\theta_{i,r,j} = \sum_{r=0}^n \tilde{\beta}_r \omega_{ij}^\nu$, for $i,j = 0,1,\dots,n$. Therefore, we provide an error upper bound for the fractional Riemann-Liouville operational matrix of shifted Gegenbauer polynomials as:

$$||e_{I^\nu}||_2 \le \sum_{r=0}^n \omega_{is}^\nu \left(\frac{H}{(n+1)!}\right)^2 \frac{L^{3+2n}}{3+2n}. \quad (61)$$

Using Theorems 2 and 3 and Eq. (61), it is concluded that by increasing the number of shifted Gegenbauer basis, the error norm approaches zero. The set of shifted Gegenbauer polynomials forms a basis for the space

$C^n[0,1] =$

$\{f(t)|f$ is continuously differentiable on the interval $[0,1]\}$

with the uniform norm defined by

$$||x||_n = ||x||_\infty + ||x'||_\infty + \cdots \left||x^n|\right|_\infty. \quad (62)$$

Let Y_m be a subspace of Banach space $(C^n[0,1], ||.||_n)$ generated by the following shifted Gegenbauer polynomials

$$Y_m = span < C_{S,0}^{(\nu)}(t), C_{S,1}^{(\nu)}(t), \dots, C_{S,n}^{(\nu)}(t) >. \quad (63)$$

Thus, an arbitrary element of Y_m is in the form

$$\eta_0 C_{S,0}^{(\nu)}(t) + \eta_1 C_{S,1}^{(\nu)}(t) + \cdots + \eta_n C_{S,n}^{(\nu)}(t), \quad (64)$$

where η_0, $\eta_1, \dots, \eta_n$ are arbitrary real numbers. Furthermore, on each set Y_m the functional J leads to the function

$$J\left[\eta_0 C_{S,0}^{(\nu)}(t) + \eta_1 C_{S,1}^{(\nu)}(t) + \cdots + \eta_n C_{S,n}^{(\nu)}(t)\right] \quad (65)$$

of n variables η_1, $\eta_2, \dots, \eta_n$. we find η_1, $\eta_2, \dots, \eta_n$ in such a way to minimize the cost functional J. The continuity of the performance index J on the defied space is provided by the following theorem.

Theorem 4: The performance index $J: C^n[0,L]\to R$ given in Eq. (46) is uniformly continuous on the Banach space $(C^n[0,1], ||.||_n)$.

Proof: By the definition of the Riemann-Liouville integral, we have

$$I^\nu g(t) = \frac{1}{\Gamma(\nu)}\int_0^t (t-y)^{\nu-1} g(y)dy \quad (66)$$

$$||I^\nu g(t)||_\infty \le \frac{||g||_\infty}{\Gamma(\nu+1)} \quad (67)$$

$\epsilon > 0$ is given. Suppose that $g(t)\epsilon C^n[0,L]$ and $\delta > 0$. We take $m(t)\,\epsilon\, C^n[0,1]$ such that

$$||g-m||_n \le \sum_{i=0}^n \left||g^i - m^i|\right|_\infty < \delta \quad (68)$$

By considering Eq. (67), we have

$$||I^\nu g(t) - I^\nu m(t)||_\infty \le \frac{||g^n - m^n||_\infty}{\Gamma(\nu+1)} \le \frac{\delta}{\Gamma(\nu+1)} \quad (69)$$

According to our assumption on FOCP (1), $f(t,x,u)$ is a continuous function, so for sufficiently small values of $\delta > 0$,

$$|| f(t,g(t),\frac{1}{b(t)}\left(Mg'(t)+ND^{v}g(t)-a(t,g(t))\right) \quad (70)$$
$$-f(t,m(t),\frac{1}{b(t)}(Mm'(t) \ +ND^{v}m(t)-a(t,m(t)))||_{\infty}<\epsilon,$$

provided that $||g-f||<\delta$. Therefore, we obtain

$$||J(g(t))-J(m(t))||<\epsilon. \quad (71)$$

Now, suppose that μ_n is the optimum of the functional J on the subspace Y_m of the Banach space $(C^n[0,1],||.||_n)$.

The next theorem shows the convergence of the proposed method.

Theorem 5: Let μ be the optimum of the functional J on $C^n[0,1]$, then

$$\lim_{n\to\infty}\mu_n = \mu \quad (72)$$

Proof: See [12]

VII. ILLUSTRATIVE EXAMPLES

In this section, we will provide some examples by using the presented scheme. The numerical results will compare to analytical solutions or some other similar schemes in terms of accuracy.

Example 1: Consider the FOCP [21, 22]

$$\min J = \int_0^1 [t^2u^2(t)-(v+2)^2x^2(t)]^2dt$$

subject to the dynamical system

$$x'(t)+D^{v}x(t)=u(t)+t^2$$
$$x(0)=0, \qquad x(1)=\frac{2}{\Gamma(3+v)}.$$

Table I

ABSOLUTE ERROR FOR $x(t)$ OF THE PRESENT METHOD AND THE RESULTS OF [21] WITH v = 1.7 IN EXAMPLE 7.1

	Present method		Method used in [21]	
t	n=2	n=7	n=2	n=7
0.1	3.9e-03	3.3459e-08	9.31e-03	1.15e-6
0.2	5.92e-04	-2.1566e-06	1.27e-02	6.25e-06
0.3	1.4e-03	3.4198e-06	1.23e-02	1.02e-05
0.4	6.79e-04	3.4928e-06	9.89e-03	1.23e-05
0.5	4.5e-03	3.3671e-06	6.82e-03	1.20e-05
0.6	8.9e-03	3.3406e-06	4.06e-03	1.01e-05
0.7	1.23e-02	2.9359e-06	2.13e-03	8.74e-06
0.7	1.32e-02	2.0678e-06	1.12e-03	6.98e-06
0.9	9.8e-03	1.4861e-06	6.87e-04	3.37e-06

Table II

ABSOLUTE ERROR FOR $u(t)$ OF THE PRESENT METHOD AND THE RESULTS OF [22] WITH v = 1.7 IN EXAMPLE 7.1

	Present method		Method used in [22]	
t	n=2	n=7	n=5	n=7
0.1	1.42e-01	2.6412e-04	2.26529e-03	5.61726e-05
0.2	9.02e-02	7.4883e-05	2.52298e-03	2.99579e-05
0.3	4.32e-02	4.0204e-05	3.48464e-03	9.42639e-06
0.4	3.40e-03	3.1686e-05	2.41502e-03	5.26797e-06
0.5	2.71e-02	2.5444e-05	7.42558e-04	9.73733e-06
0.6	4.63e-02	2.0457e-05	5.49078e-04	7.75208e-06
0.7	5.24e-02	1.5456e-05	9.62006e-04	4.64625e-06
0.7	4.36e-02	9.6630e-06	5.09244e-04	6.49362e-07
0.9	1.18e-02	6.0227e-06	2.68469e-04	1.64844e-05

Table III

APPROXIMATE VALUE OF FUNCTIONAL J^* IN EXAMPLE 7.1

J	n=2	n=7
Present Method	4.58×10^{-5}	5.77×10^{-16}
Method used in [21]	2.18×10^{-4}	4.41×10^{-13}

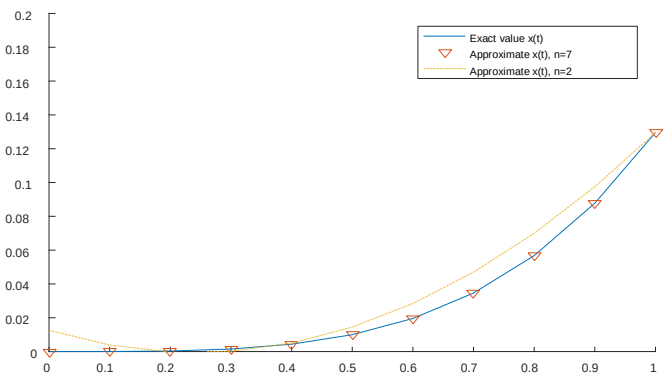

Fig. 1. Exact and approximate solutions of the state function $x(t)$ for n = 2, and n = 7 with v = 1.7 in Example 7.1.

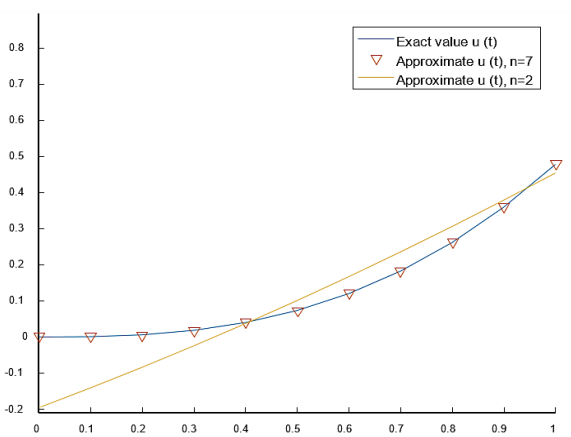

Fig. 2. Exact and approximate solutions of the control function

$u(t)$ for n = 2, and n = 7 with ν = 1.7 in Example 7.1

For the above problem, the exact solutions for the state and control functions are given as

$$x(t) = \frac{2t^{\nu+2}}{\Gamma(\nu+3)},$$

and

$$u(t) = \frac{2t^{\nu+1}}{\Gamma(\nu+2)}$$

the minimum value for the cost functional is $J = 0$. To implement the numerical technique by using the suggested approach, we employ theorem 1 to compute the elements of the operational matrix. Then, we apply Eq. (39) and Eq. (42) to approximate the state and control functions. Finally, by substituting the approximated values in the cost functional and imposing the necessary condition for optimization the unknown coefficients will be calculated. The obtained operational matrix for $\nu = 1.7$ and n = 2 is as follows:

$$F^{\nu} = \begin{bmatrix} 0.2398 & 0.3305 & 0.0820 \\ -0.1102 & -0.1071 & 0.0290 \\ 0.0164 & -0.0171 & -0.0346 \end{bmatrix}$$

Table I demonstrates the comparison of the error approximation for $x(t)$ between the Ritz method along with the Bernstein operational matrix applied in [21] and the present method with n = 2, and n = 7. It can be observed that the present method has significantly reduced the error. Also, the comparison of the obtained values for $u(t)$ by the present method and the method used in [22] is shown in Table II. Our results are comparable with those of the method applied in [22], which used Genocchi polynomials. Table III shows the of J achieved by the present method and the method in [21] for n = 2, and n = 7 with $\nu = 1.7$. The cost functional obtained in this paper is improved in comparison with that of [21]. In addition, the state and control functions for the values of n = 2, n = 7, and $\nu = 1.7$ along with the exact solutions are shown in Fig. 1 and 2, respectively. Based on these figures, it is clear that when the number of terms in the approximations increases, the numerical solutions approach the exact values.

Example 2: Consider the following problem [16, 20]:

$$\min J = \int_0^1 \left(u(t) - x(t)\right)^2 dt$$

subject to the dynamical system

$$x'(t) + D^{\nu}x(t) = u(t) - x(t) + \frac{6t^{\nu+2}}{\Gamma(\nu+3)} + t^3$$

$$x(0) = 0, \quad x(1) = \frac{6}{\Gamma(\nu+4)}.$$

The exact solutions for the state and control functions are given by

$$x(t) = \frac{6t^{\nu+3}}{\Gamma(\nu+4)},$$

and

$$u(t) = \frac{6t^{\nu+3}}{\Gamma(\nu+4)}$$

Table IV demonstrates the comparison of the approximated value for cost functional J between the method in [20] and the present method with n = 5, ν = 1.5, 1.8, and the exact solution. The performance index obtained in this paper is improved in comparison with the results of [20]. In Fig. 3 and Fig. 4, the exact and approximate state functions, as well as the control function, for different values of ν and n = 5 are plotted.

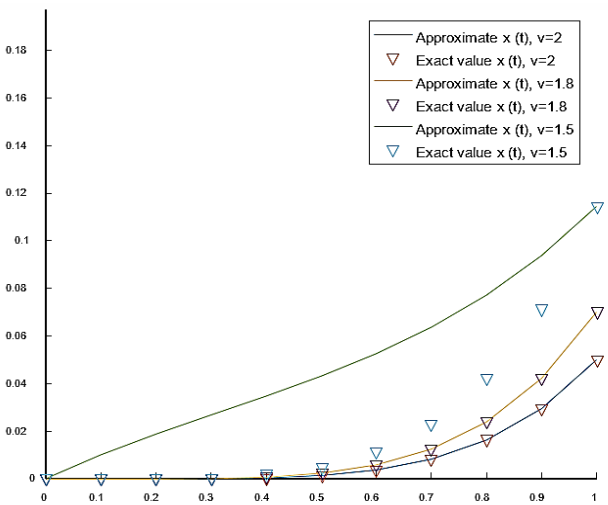

Fig.3. Comparison of the approximate and exact solutions of x(t) for v= 1.5, 1.8, 2 and n = 5 in Example 7.2

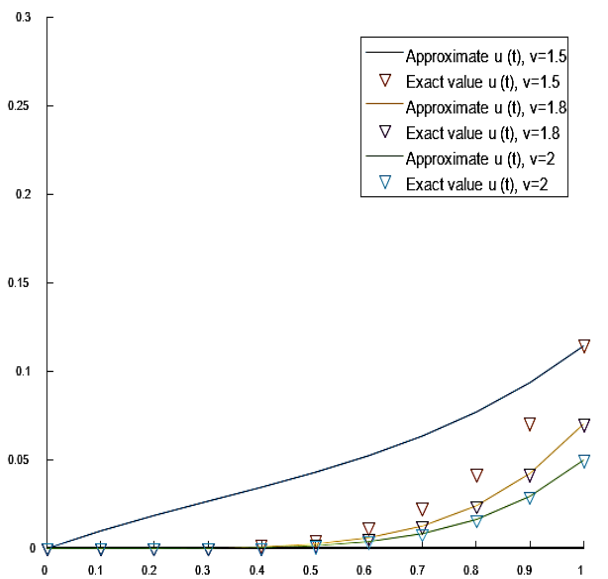

Fig.4. Comparison of the approximate and exact solutions of u(t)for v = 1.5, 1.8, 2 and $n = 5$ in Example 7.2.

Table IV
APPROXIMATE VALUE OF COST FUNCTIONAL J^* WIIH $n = 5$ FOR EXAMPLE 7.2

J	$\nu = 1.5$	$\nu = 1.8$
Exact value	0	0
Present method	4.84×10^{-12}	4.57×10^{-13}
Method used in [20]	8.5×10^{-11}	1.1×10^{-11}

Example 3: Consider the FOCP [22,29]

$$\min J = \int_0^1 e^t(x(t) - t^4 + t - 1)^2 + (t^2 + 1)(u(t) + 1 - t + t^4 - \frac{8000t^{\frac{21}{10}}}{77\left(\frac{1}{10}\right)})^2 dt$$

subject to the dynamical system

$$D^{1.9}x(t) = u(t) + x(t)$$
$$x(0) = 1, \quad x(1) = 1.$$

The exact solutions of x(t) and u(t) are given by

$$x(t) = 1 - t + t^4,$$

$$u(t) = -1 + t - t^4 + \frac{8000t^{\frac{21}{10}}}{77\left(\frac{1}{10}\right)}$$

The minimum value for the cost functional is $J = 0$. This example is numerically solved by the provided method for different values of n = 5, n = 6, n = 8, and $\nu = 1.9$. The value of cost functional by applying the present method, and the methods in [22, 29] for n = 5,6,8 with $\nu = 1.9$ and the exact value are shown in Table V. The value obtained for J by the suggested numerical scheme is more accurate than the values obtained by the methods in [22, 29]. The absolute errors of the control and state functions for different values of n and $\nu = 1.9$ are plotted in Fig. 5 and 6.

Fig. 7 and 8 display the plot of the approximate and exact, state and control functions for n = 5, 6, 8 and $\nu = 1.9$.

Table V
APPROXIMATE VALUE OF COST FUNCTIONAL J^* IN EXAMPLE 7.3

n	n=5	n=6	n=8
Exact value	0	0	0
Present method	6.78×10^{-8}	1.2×10^{-8}	7.8×10^{-10}
Method in [22]	2.062×10^{-7} 6.7775×10^{-8}	4.8×10^{-8}	2.9×10^{-9}
Method in [29]		_	8.22283×10^{-10}

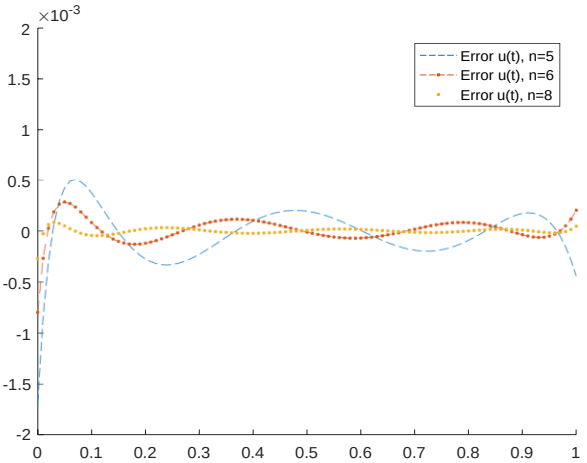

Fig. 5. Comparison of the errors of $u(t)$ for n = 5, 6, 8 and $\nu = 1.9$ in Example 7.3.

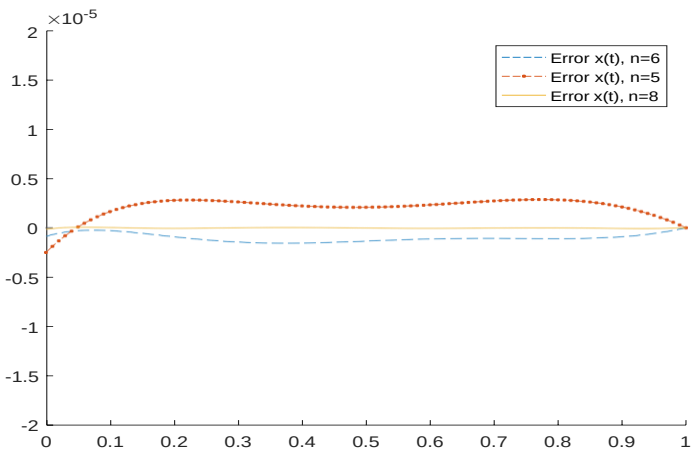

Fig. 6. Comparison of the errors of $x(t)$ for n =5, 6, 8 and ν= 1.9 in Example 7.3.

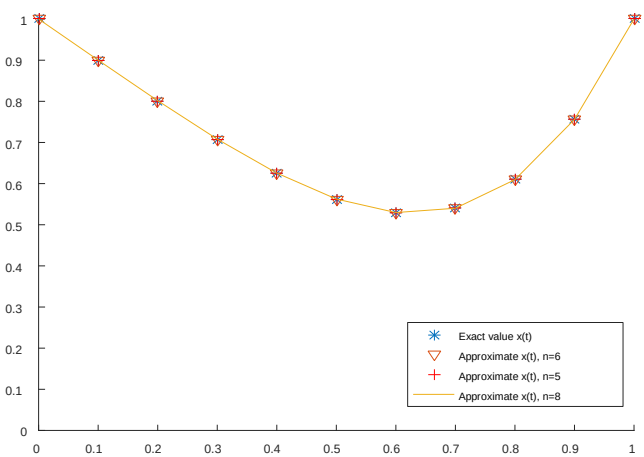

Fig. 7. Comparison of the exact and approximate solutions of $x(t)$ for n = 5, 6, 8 and $\nu = 1.9$ in Example 7.3.

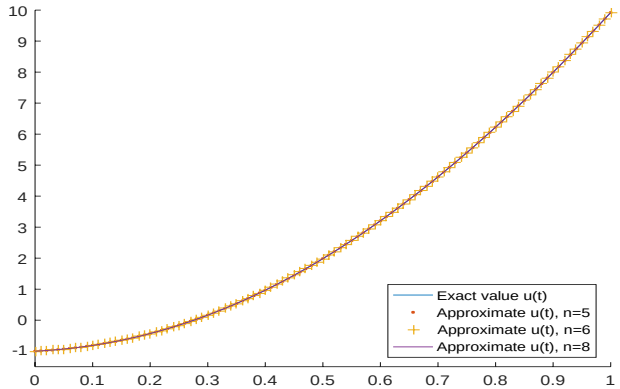

Fig. 8. Comparison of the exact and approximate solutions of $u(t)$ for n =5, 6, 8 and $\nu = 1.9$ in Example 7.3.

VIII. CONCLUSIONS

In this paper, we developed a new numerical scheme for solving a class of FOCPs based on the shifted Gegenbauer polynomials. The shifted Gegenbauer polynomials along with the operational matrix of fractional Riemann-Liouville integration and the Caputo fractional derivative were used to approximate the unknown state and control functions. Thereupon, an unconstrained optimization problem was achieved. Next, by imposing the necessary conditions of optimality, we obtained a system of algebraic equations. Furthermore, we extensively discussed the convergence of the proposed technique. At the end, three illustrative examples were solved and compared with the results in the literature to demonstrate the effectiveness and applicability of the method.

Acknowledgment

The authors are very grateful for all the constructive comments and suggestions by the reviewers to improve the paper.

REFERENCES

[1] H.P. Geering, "Optimal Control with Engineering Applications," *SpringerVerlag Berlin Heidelberg*, 2007

[2] B. Bonnard, and D. Sugny, "Optimal Control with Applications in Space and Quantum Dynamics, American Institute of Mathematical Sciences," 2012

[3] P. Doria, T. Calarco, and S. Montangero, "Optimal control technique for many-body quantum dynamics," *Phys. Rev. Lett.*, Vol. 106, 190501, 2011

[4] M. Zamani, M. Karimi-Ghartemani, and N. Sadati, "Fopid controller design for robust performance using particle swarm optimization," *Fractional Calculus and Applied Analysis*, Vol. 10, pp. 169–188, 2007

[5] R.T. Baillie, "Long memory processes and fractional integration in econometrics," *J. Econ*., Vol. 73 pp. 5–59, 1996

[6] M.G. Hall, and T.R. Barrick, "From diffusion-weighted MRI to anomalous diffusion imaging," *Magn. Reson. Med*., Vol. 59, pp. 447–445, 2008

[7] N. Engheta, "On fractional calculus and fractional multipoles in electromagnetism," *IEEE. T. Antenn Propag*, Vol. 44 , pp. 554–566, 1996

[8] C. Lederman, J.M. Roquejoffre, and N. Wolanski, "Mathematical justification of a nonlinear integro differential equation for the propagation of spherical flames, "*Annali di Matematica Pura ed Applicata*, Vol. 183, pp. 173–239, 2004

[9] A.H. Bhrawy, E.H. Doha, J.A. Tenreiro Machado and S.S. Ezz-Eldien, "An efficient numerical scheme for solving multi-dimentional fractional optimal control problems with a quadratic performance index," *Asian J. Control*., Vol. 17, No. 6, pp. 2389–2402, 2015

[10] O.P. Agrawal, "A general formulation and solution scheme for fractional optimal control problem," *Nonlinear Dynam*, Vol. 38, pp. 323–337, 2004

[11] O.P. Agrawal, and D. *A.* Baleanu, "Hamiltonian formulation and a direct numerical scheme for fractional optimal control problems," *Journal of Vibration and Control*, Vol. 13, No. (9-10), pp. 1269–1281, 2007

[12] K. Mamehrashi, and F. Soltanian, "numerical technique for solving a class of 2D variational problems using Legendre spectral method," *Computational Methods for Differential Equations*, Vol. 6, No. 4, pp. 471–482, 2018

[13] S. Sabermahani, Y. Ordokhani, and S.A. Yousefi, "Numerical approach based on fractional-order Lagrange polynomials for solving a class of fractional differential equations," *Comp. Appl. Math.*, Vol. 37, pp. 3846–3868, 2018

[14] M. Usman, M. Hamid, T. Zubair, R.U. Haq, W. Wang, and M.B. Liu, "Novel operational matrices-based method for solving fractional-order delay differential equations via shifted Gegenbauer polynomials," *Applied Mathematics and Computation*, Vol. 372, pp. 1249–1285, 2020

[15] S.S. Ezz-Eldien, E.H. Doha, D. Baleanu, and A.H. Bhrawy, "A numerical approach based on Legendre orthonormal polynomials for numerical solutions of fractional optimal control problems," *J. Vib. Ctrl*., Vol. 23, pp. 16–30, 2015

[16] N.H. Sweilam, and T.M. Al-Ajami, "Legendre spectral-collocation method for solving some types of fractional optimal control problems," *Journal of Advanced Research*, Vol. 6, No. 3, pp. 393–403, 2015

[17] A.H. Bhrawy, M.M. Tharwat, and M.A. Alghamdi, "A new operational matrix of fractional integration for shifted Jacobi polynomials," *Bull. Malays. Math. Sci. Soc*., Vol. 37, pp. 983–995, 2014

[18] E.H. Doha, A.H. Bhrawy, D. Baleanu, S.S. Ezz-Eldien, and R.M. Hafez, "An efficient numerical scheme based on the shifted orthonormal Jacobi polynomials for solving fractional optimal control problems," *Advances in Difference Equations*, Vol. 1, pp. 1–17, 2015

[19] E. Keshavarz, Y.Ordokhani, and M. Razzaghi, *"A numerical solution for fractional optimal control problems*

via Bernoulli polynomials," *Journal of Vibration and Control*, Vol. 22, No. 18, pp. 3889–3903, 2016

[20] M. Behroozifar, and N. Habibi, "A numerical approach for solving a class of fractional optimal control problems via operational matrix Bernoulli polynomials," *Journal of Vibration and Control*, pp. 1–18, 2017

[21] A. Nemati,.A. Yousefi, and F. Soltanian, "An efficient numerical solution of fractional optimal control problems by using the Ritz method and Bernstein operational matrix," *Asian Journal of Control*, Vol. 18, No. 6, pp. 2272–2282, 2016

[22] P. Chang, I.F. Noratiqah, and I. Abdulnasir, "A new efficient numerical scheme for solving fractional optimal control problems via a Genocchi operational matrix of integration," *Journal of Vibration and Control*, pp.11–13, 2017

[23] S. M. Shafiof, J. Askari, M. Shams Solary, "Hybrid Functions to Solve Fractional Optimal Control Problems Using the Collocation Method," *International Journal of Industrial Electronics, Control and Optimization, Vol. 4, No. 3, pp. 299-311, 2021*

[24] I. Area, D.K. Dimitrov, E. Godoy, and A. Ronveaux, "Zeros of Gegenbauer and Hermite polynomials and connection coefficients," *Mathematics of Computation*, Vol. 73, No. 248, pp. 1937–1951, 2004

[25] K.T. Elgindy, "High order numerical solution of second order one dimensional hyperbolic telegraph equation using a shifted Gegenbauer pseudospectral method," *Num. Meth. Part. Differ. Equ*., Vol. 32, pp.1-16, 2015

[26] H.F. Ahmad, and M.B. Melad, "A new approach for solving fractional optimal control problems using shifted ultrasperical polynomials," *Progr. Fract. Differ. App*, Vol. 4, No. 3, pp. 179–195, 2018

[27] R.A. DeVore, and L.R. Scott, "Error bounds for Gaussian quadrature and weighted-L1 polynomial approximation," *SIAM Journal on Numerical Analysis*, Vol. 21, No. 2, pp. 400–412, 1984

[28] T.J. Rivlin, "An Introduction to the Approximation of Function," *Blaisdell Publishing Company, New York*, 2003

[29] A. Lotfi,, S.A. Yousefi, and M.Dehghan, "Numerical solution of a class of fractional optimal control problems via the Legendre orthonormal basis combined with the operational matrix and the Gauss quadrature rule," *Journal of Computational and Applied Mathematics*, Vol. 250, pp. 143–160, 2013

[30] W.M. Abd-Elhameed, and Y.H. Youssri, "New ultraspherical wavelets spectral solutions for fractional Riccati differential equations," *Abstr. Appl. Anal*, 626275, 2014

[31] T. Akbarian, and M. Keyanpour, "A new approach to the numerical solution of fractional order optimal control problems," *J. Appl. Math*, Vol. 8, No. 2, pp. 523-534, 2013

[32] R. Almeida, and F.M. Torres, "Necessary and sufficient conditions for the fractional calculus of variations with caputo derivatives," *Commun. Nonlinear Sci.*, Vol. 16, pp. 1490–1500, 2011

[33] R. Archibald, K. Chen, A. Gelb, and R. Renaut, "Improving tissue segmentation of human brain MRI through preprocessing by the Gegenbauer reconstruction method, *Journal of the Neurolmage*," Vol. 20, No. 31, pp. 489–5022, 2003

[34] D. Baleanu, and J.I. Trujillo, "A new method of finding the fractional eulerlagrange and hamilton equations within caputo fractional derivatives," *Commun. Nonlinear Sci. Numer. Simul*., Vol. 15, pp. 1111–1115, 2010

[35] A.H. Bhrawy, E.H. Doha, D. Baleanu, and, S.S. Ezz-Eldien "An accurate numerical technique for solving fractional optimal control problems," *Proceedings of The Romania Academy*, Vol. 16, No. 1, pp. 47–54, 2015

[36] A. Lotfi, and S.A. Yousefi, "A generalization of Ritz-variational method for solving a class of fractional optimization problems," *Journal of Optimization Theory and Applications*, Vol. 174, pp. 238–255, 2017

[37] B. Mandelbrot, "Some noises with 1/f spectrum, a bridge between direct current and white noise," *IEEE Trans. Inform. Theory*, Vol. 13, pp. 289–289, 1967

Farzaneh Soufivand received the B.S. degree in Pure Mathematics from Lorestan University, Lorestan, Iran, in 200٤ and M.S. degree in Applied Mathematics from the Yazd University, Yazd, Iran, in 2006, she joined the Islamic Azad University as an educator in the Department of Mathematics, Doroud Branch, Doroud, Iran. Her current research interests include fractional optimal control problems and fractional differential equations.

Fahimeh Soltanian received the B.S. degree from the Faculty of Mathematics, Isfahan University of Technology, Isfahan, Iran, in 2000, the M.S. and Ph.D. degrees in Applied Mathematics from the Yazd University, Iran, in 2003 and 2009, respectively. Currently she is an Assistant Professor at Department of Mathematics of Payame Noor University, Iran. Her research interests are numerical analysis, optimal control, differential-algebraic equations and numerical optimization.

Kamal Mamehrashi received his B.S. degree in Pure Mathematics from Kharazmi University, Tehran in 2000, his M.S. degree in Applied Mathematics from IASBS, Zanjan in 2003, and his Ph.D. in Applied Mathematics (Control & Optimization) from PNU, Tehran in 2016 under the supervision of Professor Sohrab Ali Yousefi at the University of Shahid Beheshti, Tehran, Iran. He joined the Department of Mathematics at the University of Payame Noor in 2005 as a Lecturer and was promoted to Assistant Professor in 2016. His current research interests include (2D, delay) optimal control problems, (2D, delay) fractional optimal control problems and numerical methods.